Biomechanical Evaluation of Total Ankle Replacements

Atichart Kwanyuang

Submitted in accordance with the requirements for the degree of
Doctor of Philosophy

The University of Leeds
School of Mechanical Engineering

October, 2016

The candidate confirms that the work submitted is his own and that appropriate credit has been given where reference has been made to the work of others.

Acknowledgements

Being a member of the Institute of Medical and Biological Engineering (iMBE) at the University of Leeds is such a great honour and privilege. I would like to thank to whatever brought me to be a part of the best research community here. When this part of the thesis was written, this means that my time in the iMBE will be ending soon. Leaving the iMBE is a sad thing. However, in this sadness, there is a hidden feeling of happiness of finishing a long journey in the PhD study.

Completing the PhD was only a dream and was always a very difficult task for me. Without contributions from many people, I would not be submitting this thesis today. Therefore, in no particular order, I would like to extend my thanks to:

Phil, Keith, Lee, Camille, and all the rest of the technical staff, whose technical expertise and advice made my experiment work like a charm.

Debra, Cheryl, and the administrative support officers, who have always given me a hand whenever I needed help throughout my study.

Ashley, Martin, Robert, Alex, Ama, and all the rest of the PhD colleagues within the iMBE, whose shared experience and encouragement always made me aware that I am not the only one on the long journey of PhD and I must not give up.

Alison, Marlene, Nagitha, Martin, Tony, Xijin, Sebastien, Lee, and all the rest of the senior colleagues, whose academic experiences and comments made various problems easier and my PhD work better.

Prof Anthony Redmond who has provided many useful suggestions and encouragement since the transfer in the first year of my study until the viva in the final year.

My co-supervisors, Dr Qingen Meng, Dr Claire Brockett, and Prof John Fisher, without whose academic expertise, useful suggestions, the best support, and encouragement, I would almost certainly not be reaching this state now. Continued learning from experiences of Dr Meng in finite element analysis and Dr Brockett in ankle made my study much easier.

Most importantly, I offer my thanks to my primary supervisor, Prof Ruth Wilcox. Without her seemingly inexhaustible patience and encouragement, this work would never have been possible. Her academic expertise always made various difficulties solved like a charm. Not only the contents in the thesis, but also the grammatical errors that have been corrected by her throughout my study. I do know that she needed to work harder with foreign student like me. I will be forever in her debt.

Moreover, I would like to give particular thanks to my family for unconditional love and encouragement that helped me to face whatever problems in my life.

Lastly, I would like to thank the Office of The Civil Service Commission (OCSC) who provided the funding that enabled my studies.

Some people might not be named in this list. For those people, please do accept my apologies and please do acknowledge that this error is occurred because of my poor brain not my heart.

Abstract

Globally, 1% of the population is affected by arthritis of the foot and ankle. Total ankle replacement (TAR) was developed as an alternative to fusion to treat end-stage arthritis, however failure rates are relatively high and are often related to bony damage.

The purpose of this PhD was to develop a finite element (FE) model of a TAR to examine the risk of bone failure, and how this is affected by component alignment.

An experimental model of a TAR implanted into synthetic bone was first created as a means to validate an initial FE model under known conditions. Location and size of the plastic deformation were compared and good agreement was found.

A FE model of the natural ankle was then created from cryosectional images obtained from the Visible Human Project®. It was analysed in the natural state and after virtual implantation with a TAR. Both the cortical stiffness and the surgical positioning of the TAR were varied to represent relevant ranges seen clinically.

In the TAR models, the location of the highest stress was shifted from the region of high strength to a region of lower strength of bone. The maximum von Mises stress on the cancellous bone was primarily affected by the stiffness of cortical structure and the distance between the stem and the outer surface of the cancellous bone. In some misalignment cases, the yield stress for cancellous bone was likely to be exceeded under loads representing standing.

The results indicated that the quality of the bone and the thickness of the trabecular bone surrounding the TAR stem are important factors in governing the risk of bony failure following TAR, and should be taken into account clinically. The methods developed in this thesis can now be extended to examine other TAR designs and surgical approaches.

Table of Contents

Acknowledgements ..... **iii**
Abstract ..... **v**
Table of Contents ..... **vi**
List of Tables ..... **x**
List of Figures ..... **xii**
Abbreviations ..... **xix**
Abaqus Glossary ..... **xix**
NX Glossary ..... **xx**
Terminology ..... **xxi**
Chapter 1 Literature Review **1**
1.1 Introduction 1
1.2 Ankle Joint 2
1.2.1 Anatomy of Ankle Joint Complex 3
1.2.2 Biomechanics of Ankle Joint Complex 16
1.3 Injuries and Disorders of Ankle 22
1.3.1 Sprains 22
1.3.2 Fractures 22
1.3.3 Arthritis 23
1.4 Total Ankle Replacement 25
1.4.1 Indications and Contraindications for TAR 25
1.4.2 Designs of TAR 26
1.4.3 Discussion of TAR Design, Usage, and Outcomes 43
1.5 Finite Element Analysis in Total Ankle Replacement 47
1.5.1 Introduction to the Finite Element Method 47
1.5.2 General Description of the Finite Element Method 47
1.5.3 Finite Element Analysis in Orthopaedic Applications 48
1.5.4 Discussion 57
1.6 Conclusion 58
1.7 Aims and Objectives 59
Chapter 2 Experimental Studies of TAR with Synthetic Bone **60**
2.1 Introduction 60
2.2 Material and Methods 60
2.2.1 Mechanical Testing of Synthetic Bone 60
2.2.2 Mechanical Testing of TAR with Synthetic Bone 62

2.3 Results 71
2.3.1 Mechanical Testing of Synthetic Bone 71
2.3.2 Mechanical Testing of TAR with Synthetic Bone....74
2.4 Discussion 80
2.4.1 Mechanical Testing of Synthetic Bone 80
2.4.2 Mechanical Testing of TAR with Synthetic Bone....81
2.5 Summary 86
Chapter 3 Verification, Validation, and Sensitivity Studies of the FE Model of the TAR with Synthetic Bone 87
3.1 Introduction....87
3.2 Material and Methods 87
3.2.1 FE Model of TAR with Synthetic Bone 87
3.2.2 Verification, Validation, and Sensitivity Studies....93
3.3 Results 102
3.3.1 Verification: Code....102
3.3.2 Sensitivity Study: Geometry 103
3.3.3 Verification: Mesh Convergence Study 105
3.3.4 Sensitivity Study: Material Properties....105
3.3.5 Sensitivity Study: Interactions 107
3.3.6 Sensitivity Study: Bone Structure 108
3.3.7 Validation: Plastic Deformation of Synthetic Bone 109
3.4 Discussion 111
3.4.1 Verification 111
3.4.2 Validation 112
3.4.3 Sensitivity Studies 113
3.5 Summary 116
Chapter 4 Construction of the FE Model of the Natural Ankle Geometry 117
4.1 Introduction....117
4.2 Material and Methods 117
4.2.1 3-D Model Construction of Natural Ankle 117
4.2.2 Finite Element Analysis of Natural Ankle 138
4.3 Results 141
4.4 Discussion 143
4.5 Summary 144

Chapter 5 Finite Element Analysis of TAR with Natural Ankle Geometry 145

5.1 Introduction.....145

5.2 Materials and Methods 145

5.2.1 FE Model of TAR with Natural Ankle Geometry 145

5.2.2 Mesh Convergence Study.....149

5.2.3 Sensitivity Study – Tibial Geometry.....149

5.2.4 Sensitivity Study – Elastic Modulus of Cortical Shell.....150

5.2.5 Initial FEA of TAR with Natural Ankle Geometry 151

5.2.6 FEA of TAR with Different Positions of Implantation 151

5.3 Results 153

5.3.1 Mesh Convergence Study.....153

5.3.2 Sensitivity Study – Tibial Geometry.....156

5.3.3 Sensitivity Study – Elastic Modulus of Cortical Shell.....158

5.3.4 FEA of TAR for Comparison with FEA of Natural Ankle.....159

5.3.5 FEA of TAR with Different Positions of Implantation 161

5.4 Discussion 167

5.4.1 Mesh Convergence Study.....167

5.4.2 Removing of the Tibial Malleolus Geometry.....168

5.4.3 Changing of the Stiffness of the Cortical Structure.....168

5.4.4 Comparison between the Results of FEA of TAR and FEA of Natural Ankle.....169

5.4.5 Effect of Misalignment of TAR.....170

5.5 Summary.....176

Chapter 6 Overall Discussion and Conclusions 177

6.1 Overall Discussion.....177

6.1.1 Experimental Studies and Initial FE Model of a TAR with Synthetic Bones 177

6.1.2 Sensitivity Studies of Initial FE Model 178

6.1.3 Stress Distribution in Natural Ankle FE Model.....179

6.1.4 Effect of Misalignment of TAR on Stress Distribution in Bone 180

6.2 Overall Conclusions 182

6.3 Future Work.....183

References.....186

Appendix A Engineering Drawings 199

A.1 Engineering Drawings of Synthetic Bones.....199

A.1.1 Tibial Synthetic Bone 199
A.1.2 Talar Synthetic Bone 200
A.1.3 Cutting of Sawbones Block 201
A.2 Engineering Drawings of Jigs 202
A.2.1 Assembly of Jigs 202
A.2.2 Upper Jig 203
A.2.3 Lower Jig 204
Appendix B Conference Proceedings and Presentations 211
B.1 Conference Proceedings 211
B.2 Conference Oral Presentations 211
B.3 Conference Poster Presentations 211
B.4 Conference Abstracts 212
B.4.1 6th International Ankle Symposium 212
B.4.2 FOOT International Congress 2016 213
B.4.3 22nd Congress of the European Society of Biomechanics (ESB 2016) 214

List of Tables

Table 1-1 Number of revision ankle procedures performed each year from 2011 to 2014, as reported in the National Joint Registry for England, Wales, Northern Ireland, and the Isle of Man (http://www.njrcentre.org.uk) 44

Table 1-2 Indications for the 49 first revisions following primary ankle replacement for the procedures shown in Table 1-1 44

Table 1-3 Complications following implantation in various designs of TAR 46

Table 1-4 Parameters used in finite element analysis studies in total ankle replacement 52

Table 2-1 Material properties of Sawbones® Solid Rigid Polyurethane foam block #1522-03 (Data taken from the manufacturer's website http://www.sawbones.com [cited 5 Jul 2014]) 60

Table 2-2 The options of sensitivity adjustment chosen before performing equilibration and calibration 66

Table 2-3 The elastic modulus of synthetic bone obtained from mechanical testing 72

Table 2-4 The compressive yield strength of synthetic bone obtained from mechanical testing 73

Table 2-5 The concordance correlation coefficient (CCC) values obtained from 18 tests used to determine the agreement between loads measured by the electromechanical testing machine and the pressure mapping sensor 74

Table 2-6 The depth of deformation (mm) measured from three destructive tests 79

Table 3-1 The dimensions of the simplified bones 88

Table 3-2 Meshing information of the initial FE model of the TAR with synthetic bone 91

Table 3-3 Material properties assigned to the FE model 91

Table 3-4 Meshing information of the simplified talar and the bearing components 94

Table 3-5 Meshing information for the FE models with and without fillets 96

Table 3-6 Meshing information for each of the FE models used in the mesh convergence study 97

Table 3-7 The density (g/cc) and the compressive modulus (MPa) of each model of Sawbones® Polyurethane foam block (Data taken from the manufacturer's website http://www.sawbones.com [cited 5 Jul 2014]) 98

Table 3-8 Different interface properties assigned to the five FE models in the interaction sensitivity tests 99

Table 3-9 Meshing information of the FE model with and without cortical structure 101

Table 3-10 The output data predicted by the Hertzian contact theory and FE model 102

Table 3-11 The output variables measured at the node in the tibial bone obtained from the analyses of the FE model with and without cortical structure 109

Table 3-12 The depth of deformation measured from both experimental and FE models 110

Table 3-13 The output data predicted by the Hertzian contact theory and FE model 112

Table 4-1 Meshing information of the initial FE model of the natural ankle 136

Table 4-2 Various FE models of cartilage analyzed to identify optimum loads and boundary conditions and their results 139

Table 4-3 All output variables measured at the locations of interest on the tibial cancellous bone in the mesh convergence study, showing the magnitude and location of the variables.....141

Table 5-1 Changing of three outputs on cancellous bone after reducing elastic modulus of cortical bone 158

List of Figures

Figure 1-1 Posterior view of the ankle (Image taken from Netter 2010) .3

Figure 1-2 Anterior views of the right tibia and fibula (Image taken from Martini et al. 2012, page 203) 4

Figure 1-3 The bones of the foot (Image taken from Netter 2010) 5

Figure 1-4 The trochlea tali as a part of cone, as illustrated by Zwipp and Randt 1994, page 22 6

Figure 1-5 (a) The screw shape of the lateral facette of the talus and (b) the direction of the ankle joint axes, as illustrated by Zwipp and Randt 1994, page 23 7

Figure 1-6 Axis of the talocrural joint in the transverse plane (Image adapted from Isman and Inman 1969, page 117) 8

Figure 1-7 Axis of the talocrural joint in the frontal plane (Image adapted from Isman and Inman 1969, page 116)) 8

Figure 1-8 The ligaments of the ankle (Image taken from Martini et al. 2012, page 236) 10

Figure 1-9 Anterior and posterior views of bones and attachments of muscles of the foot, ankle, and leg (Image taken from Netter 2010) 13

Figure 1-10 Anterior view of muscles of the foot, ankle, and leg (Image taken from Netter 2010) 14

Figure 1-11 Lateral view of muscles of the foot, ankle, and leg (Image taken from Netter 2010) 15

Figure 1-12 The motion of ankle joint complex in three different planes during a single gait cycle (Image adapted from Benedetti et al. 2013, page 4) 17

Figure 1-13 Sagittal plane joint angle during a single gait cycle (Image taken from Whittle 2007, page 59) 18

Figure 1-14 Sagittal plane joint moment during a single gait cycle (Image taken from Whittle 2007, page 60).....18

Figure 1-15 Sagittal plane joint power during a single gait cycle (Image taken from Whittle 2007, page 60) 19

Figure 1-16 An example of free-body diagrams of the ankle segment for a typical posture during quasi-static walking (Image adapted from Seireg and Arvikar 1975, page 92).....20

Figure 1-17 Mean patterns of compressive ankle force (Image taken from Stauffer et al. 1977, page 194).....20

Figure 1-18 Illustration showing an arthrodesis technique (Image taken from Giannini et al. 2007, page 25).....24

Figure 1-19 Illustration showing a three-component ankle prosthesis (Image taken from Giannini et al. 2007, page 23) 25

Figure 1-20 The Smith total ankle (Image taken from Vickerstaff et al. 2007, page 1057) 28

Figure 1-21 The Newton ankle implant (Image taken from Bauer et al. 1996, page 123) 29

Figure 1-22 The low contact stress (LCS) TAR (Image taken from Buechel et al. 2004, page 20) 29

Figure 1-23 The Scandinavian total ankle replacement (STAR) (Image taken from Heuvel et al. 2010, page 155) 32

Figure 1-24 The Agility total ankle system (Image taken from Heuvel et al. 2010, page 156) 33

Figure 1-25 The Buechel-Pappas total ankle replacement (Image taken from Heuvel et al. 2010, page 155) 35

Figure 1-26 The MOBILITY total ankle system (Image taken from Wood et al. 2010, page 959) 36

Figure 1-27 The Zenith total ankle replacement (Image taken from Mckenzie et al. 2012, page 1) 37

Figure 1-28 The BOX total ankle replacement (Image taken from Giannini et al. 2013, page 2) 38

Figure 1-29 The Salto total ankle prosthesis (Image taken from Bonnin et al. 2004, page 7) 40

Figure 1-30 The HINTEGRA total ankle prosthesis (Image taken from http://www.integralife.eu [cited 19 Dec 2013]) 41

Figure 1-31 The INBONE total ankle replacement (Image taken from Ellis and DeOrio 2010, page 202) 42

Figure 1-32 The Taric ankle system (Image taken from http://www.implantcast.de [cited 19 Dec 2013]) 42

Figure 1-33 Number of primary ankle procedures performed in each year 43

Figure 2-1 The polyurethane foam specimens used for mechanical testing 61

Figure 2-2 Compressive load (N) versus compressive extension (mm) of a non-destructive mechanical testing of the Sawbones® polyurethane foam #1522-03 62

Figure 2-3 The Zenith™ total ankle replacement (Image adapted from Mckenzie et al. 2012, page 1) 63

Figure 2-4 The tibial and talar synthetic bones 63

Figure 2-5 The experimental specimen of synthetic bones with TAR installed 64

Figure 2-6 The Tekscan® Pressure Mapping Sensor model 5076 65

Figure 2-7 The I-Scan® system (Image taken from http://www.tekscan.com [cited 19 Jun 2016]) 65

Figure 2-8 The 2-point power law calibration curve for the sensor 67

Figure 2-9 The experimental construct loaded in the electromechanical testing machine 68

Figure 2-10 The complete experimental set-up for testing the TAR in synthetic bone, showing the pressure transducers inserted between the tibial and bearing components 69

Figure 2-11 Compressive load (N) versus compressive extension (mm) of a non-destructive mechanical testing of the Sawbones® polyurethane foam #1522-03 with linear regression line fitted.....71

Figure 2-12 Compressive load (N) versus compressive extension (mm) of a destructive mechanical testing of the Sawbones® polyurethane foam #1522-03.....73

Figure 2-13 Average contact pressure (kPa) versus measuring time (sec) of a mechanical testing of the TAR with synthetic bone with linear regression line fitted 75

Figure 2-14 Contact pressure (kPa) between tibial and bearing component experienced by the pressure mapping sensor on either side of the mid-plane when a compressive load of 3416 N was applied 75

Figure 2-15 Average contact pressure (kPa) versus measuring time (sec) of a mechanical testing of the TAR with synthetic bone on either side of the mid-plane with linear regression line fitted 76

Figure 2-16 The inclination between the articular surfaces of tibial and bearing components 77

Figure 2-17 Bar chart illustrating the average contact pressures (MPa) measured from each specimen 77

Figure 2-18 The deformation of the talar synthetic bone after destructive testing.....78

Figure 2-19 The location of the measurement of the depth of deformation.....79

Figure 2-20 The method of quantifying the vertical deformation 84

Figure 2-21 The method of quantifying the angle of inclination.....85

Figure 3-1 The 3-D models of simplified tibial and talar bones 88

Figure 3-2 The layout of cutting the simplified bone from the original block 89

Figure 3-3 The 3-D models of Zenith™ TAR components.....89

Figure 3-4 The CAD model of TAR with synthetic bone 90

Figure 3-5 The FE model of TAR with synthetic bone 92

Figure 3-6 The simplified talar and the bearing components of the Zenith™ TAR.....93

Figure 3-7 The FE model of simplified talar and the bearing components of the Zenith™ TAR 94

Figure 3-8 The FE model of the Zenith™ TAR with and without fillets 96

Figure 3-9 The plot of compressive modulus (MPa) against density (g/cc) for the Sawbones® polyurethane foam block data in Table 3-7 showing the power trendline fitting 98

Figure 3-10 Weight-bearing and non-weight-bearing cortical structures with their section views showing where there was overlapping between cortical bone and the tibial component.....100

Figure 3-11 von Mises stress (MPa) measured at all locations of interest on the models with and without fillets 103

Figure 3-12 Minimum principal strain measured at all locations of interest on the models with and without fillets 104

Figure 3-13 Vertical displacement (mm) measured at all locations of interest on the models with and without fillets 104

Figure 3-14 All output variables measured at the locations of interest on the tibial synthetic bone in the mesh convergence study 105

Figure 3-15 von Mises stress (MPa) measured at all locations of interest on the models with different elastic moduli 106

Figure 3-16 Minimum principal strain measured at all locations of interest on the models with different elastic moduli 106

Figure 3-17 Vertical displacement (mm) measured at all locations of interest on the models with different elastic moduli 107

Figure 3-18 All output variables measured at the locations of interest on the tibial synthetic bone in the models with different bone-implant interface conditions (from Table 3-8) 108

Figure 3-19 The locations of deformation of talar synthetic bone obtained from both experimental and FE models.....109

Figure 4-1 Sample of medical imaging data collected from database of the Visible Human Project® showing a section through the ankle bone 118

Figure 4-2 The process for creating the 3-D surface model (a) imported cryosectional image, (b) manual segmentation using 'paint' tool, (c) 'morphological erode' filter applied on segmentation, (d) 3-D surface model of ankle joint 121

Figure 4-3 3-D surface model of tibial and talar cartilages.....121

Figure 4-4 Point cloud data of ankle joint.....122

Figure 4-5 3-D solid model creating process showing the imported point cloud (a), the wrapped point data (b), the enhanced polygon object (c), and the NURBS surfaces patched 3-D solid model (d) 124

Figure 4-6 Comparison between ankle images collected from anatomical book (Martini et al. 2012) and exported from CAD software, (a) before rotating, (b) after rotating in 5° adduction ...125

Figure 4-7 Comparison between ankle images collected from anatomical book (Martini et al. 2012) (a) and exported from CAD software (b) in the sagittal plane 126

Figure 4-8 3-D solid model of the ankle before (a) and after (b) rotating in 5° adduction 126

Figure 4-9 Axis of rotation of the ankle joint (Image taken from Zwipp and Randt 1994, page 23).....127

Figure 4-10 Location of axis of rotation of the ankle joint measured from 46 cadaver legs (Image taken from Isman and Inman 1969, page 124 and 126).....128

Figure 4-11 The process of identifying the axis of rotation of the ankle joint showing the straight lines created over the talar trochlea (a), the three points created on each projected curve (b), the circles created to fit each set of the three points (c), the rotational axis of the ankle joint created to connect between the centres of the circles (d).....129

Figure 4-12 3-D solid model of the ankle before (a) and after (b) rotating in 10° dorsiflexion.....130

Figure 4-13 Cortical structure creating process using NX software ..131

Figure 4-14 Ankle cartilage creating process using NX software.....133

Figure 4-15 Cortical structure after applying 'Cut Instances' tool (a) and 'Merge Instances' tool (b) 134

Figure 4-16 Assembly of all instances 135

Figure 4-17 FE model of natural ankle 138

Figure 4-18 The contour plots of the von Mises stress (MPa) distribution in the tibial cancellous bone, showing in the frontal plane 142

Figure 4-19 The contour plots of the von Mises stress (MPa) distribution in the tibial cancellous bone, showing in the sagittal plane 142

Figure 5-1 Defining implant position process, (a) defining joint line using spacer to adjust the implant position vertically, (b) and (c) installing the tibial-talar block and the tibial alignment jig to adjust the implant position horizontally (Image taken from http://www.coringroup.com [cited 25 May 2015]) 146

Figure 5-2 Cutting the tibia and talus to conform to the surfaces of tibial and talar components 147

Figure 5-3 FE model of TAR with natural ankle geometry.....148

Figure 5-4 Model of the tibia, (a) with malleolus, (b) without malleolus 150

Figure 5-5 FE model of TAR with whole component misalignment, (a) medial and lateral translation, (b) anterior and posterior translation, (c) medial and lateral rotation, (d) anterior and posterior rotation.....152

Figure 5-6 FE model of TAR with partial component misalignment, (a) medial and lateral translation, (b) anterior and posterior translation, (c) medial and lateral rotation, (d) anterior and posterior rotation.....153

Figure 5-7 Mesh convergence study (measuring at tibial bone).....154

Figure 5-8 Location of maximum von Mises stress (a) and the highest magnitude of minimum principal strain (b) on tibial bone.....154

Figure 5-9 Mesh convergence study (measuring at bearing component) 155

Figure 5-10 Location of maximum von Mises stress (a) and the highest magnitude of minimum principal strain (b) on bearing component 156

Figure 5-11 Plot of von Mises stress (MPa) distribution in the model with and without tibial malleolus.....156

Figure 5-12 Plot of minimum principal strain distribution in the model with and without tibial malleolus.....157

Figure 5-13 Plot of vertical displacement (mm) distribution in the model with and without tibial malleolus 157

Figure 5-14 Relationship between reducing elastic moduli and increasing of the outputs (maximum von Mises stress, highest magnitude of minimum principal strain, and vertical displacement) with linear regression line.....159

Figure 5-15 The contour plots of the von Mises stress (MPa) distribution in the tibial cancellous bone of the FE model of natural ankle, (a) showing the cross section in the frontal plane, and (b) showing the cross section in the sagittal plane.....160

Figure 5-16 The contour plots of the von Mises stress (MPa) distribution in the tibial cancellous bone of the FE model of TAR with natural ankle geometry, (a) showing the cross section in the frontal plane, and (b) showing the cross section in the sagittal plane 160

Figure 5-17 von Mises stress (MPa) in cancellous bone around the tip of the stem, (a) well aligned position, (b) medial misalignment, (c) lateral misalignment, (d) anterior misalignment, (e) posterior misalignment.....162

Figure 5-18 The maximum von Mises stress (MPa) versus the shortest distance between the stem and the outer surface of cancellous bone (mm) measured at the region surrounding the tip of the stem, with linear regression line.....163

Figure 5-19 Distribution of von Mises stress (MPa) in cancellous bone around the tip of the stem, (a1) and (a2) well aligned position, (b) medial misalignment, (c) lateral misalignment, (d) anterior misalignment, (e) posterior misalignment.....164

Figure 5-20 Distribution of von Mises stress (MPa) in cancellous bone around the tip of the stem, (a) medial misalignment, (b) lateral misalignment, (c) anterior misalignment, (d) posterior misalignment.....165

Figure 5-21 The maximum von Mises stress (MPa) versus the shortest distance between the stem and the outer surface of cancellous bone (mm) measured at the region surrounding the tip of the stem, with linear regression line.....166

Figure 5-22 Distribution of von Mises stress (MPa) in cancellous bone around the tip of the stem, (a) medial misalignment, (b) lateral misalignment, (c) anterior misalignment, (d) posterior misalignment.....167

Figure 5-23 The maximum von Mises stress (MPa) versus the shortest distance between the stem and the outer surface of cancellous bone (mm) measured at the region surrounding the tip of the stem, with linear regression line.....171

Figure 5-24 The bottom view shows the overlapping region between cortical structure (shown in dark red) and tibial component. There are two colors on the tibial component: light grey (with cortical structure support) and dark grey (without cortical structure support). The red dash line acts like a rotational axis.....172

Figure 5-25 The deformation plot (displacements have been exaggerated by a factor of 30 to highlight the deformation) of a posterior misalignment (whole TAR component) FE model showing the different degrees of deformation between the regions with and without cortical structure support 173

Figure 5-26 The deformation plot (displacements have been exaggerated by a factor of 30 to highlight the deformation) of a lateral misalignment (partial TAR component) FE model showing the different degrees of deformation between the regions that the bearing and talar component move toward and outward 175

Abbreviations

3-D	three-dimensional
CAD	computer-aided design
CaP	calcium phosphate
CT	computed tomography
E	elastic modulus, Young’s modulus
FE	finite element
FEA	finite element analysis
FEM	finite element method
MRI	magnetic resonance imaging
TAA	total ankle arthroplasty
TAR	total ankle replacement
Ti-6AL-4V	titanium alloy
TiN	titanium nitride
UHMWPE	ultra-high-molecular-weight polyethylene
v	Poisson’s ratio

Abaqus Glossary

Cut instances	Cuts the geometry of a selected part instance using the geometry of one or more other part instances to make the cut
Merge instances	Merges the geometry of parts created in the Part module
Mesh part instance	Creates meshes throughout part instances
Tie constraint	Ties two separate surfaces together so that there is no relative motion between them

NX Glossary

Bridge curve	Creates a tangent blend curve between two curves
Extract body	Creates a body by copying a face, a set of faces, or another body
Extract curve	Creates curves from the edges and faces of bodies
Extrude	Creates a feature by extruding a section along a vector
Join curves	Joins together a chain of curves to create a single spline curve
Move object	Moves or rotates selected objects
Offset face	Offsets a set of faces from their current location
Project curve	Projects curves, edges, or points onto faces or planes
Subtract	Subtracts the volume of one solid body from another, leaving a void
Thicken	Creates a solid body by adding thickness to a set of faces
Trim body	Trims off a portion of a body using faces, or a datum plane
Trimmed sheet	Trims off a portion of a sheet body using curves, faces, or a datum plane

Terminology

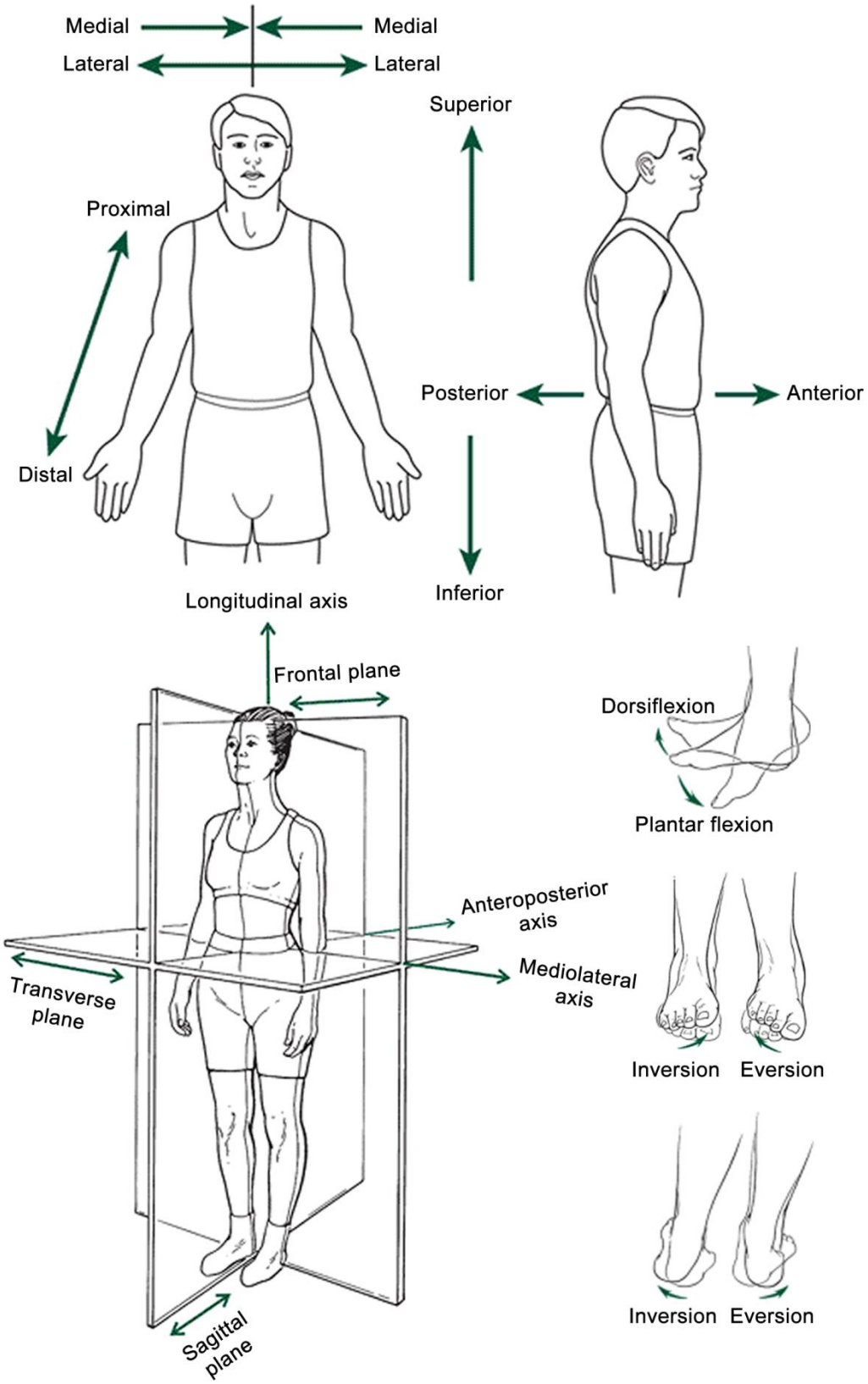

Image adapted from Hamill and Knutzen 2009

Chapter 1 Literature Review

1.1 Introduction

The work in this thesis concerns the examination of total ankle replacement performance using finite element analysis, with a focus on assessing the risk of failure in the surrounding bone.

Although the incidence of arthritis of the ankle is less common than other major joints of the lower extremity, approximately 1% of the global population is affected by this type of arthritis. Posttraumatic arthritis is the most common type of arthritis of the ankle, while secondary and primary arthritis are subordinate. The former aetiology of ankle osteoarthritis is reported in approximately 70% of cases (Saltzman et al. 2005, Valderrabano et al. 2009). Ankle arthrodesis or ankle fusion have been considered to be a gold standard to treat end-stage ankle arthritis, however, there are various complications associated with this treatment option. Total ankle replacement (TAR), or total ankle arthroplasty (TAA) was initially invented as an alternative to fusion to provide more functional ability for the patient (Hintermann et al. 2012).

TAR, or TAA, is a surgical procedure to replace the damaged articular surfaces of the human ankle joint with artificial joint components. The first total ankle arthroplasty was performed in 1970 by Lord and Marrotte. In the following decade, the use of the prosthesis was abandoned due to its high failure rate. More recently, ankle replacements have made a comeback because more modern designs have produced better results (Gougoulias et al. 2009, Saltzman et al. 2009). However, there are still some concerns over TAR performance and they are not yet as successful as hip or knee replacements.

Finite element analysis (FEA) is an advanced computer technique for structural stress analysis developed in engineering mechanics. It was introduced into orthopaedic biomechanics in the 1970s to measure stresses in human bones. Since then, this method has been applied with increasing frequency for stress analyses of not only various kinds of tissues but also orthopaedic devices. These investigations have aimed to evaluate relationships between load carrying functions and structure of the tissues, and to optimise designs and fixation techniques of implants (Huiskes and Chao 1983). Therefore, the application of FEA to investigate the stress in the bones around a TAR, and the device itself, would be useful in understanding performance and predicting potential failure in TAA.

In the following chapter, the ankle joint and related biomechanics are introduced. The literature concerning total ankle replacement and its clinical outcomes is reviewed, along with the use of finite element analysis to examine TAR performance. The chapter concludes with the overall aims and objectives of the work in this thesis.

1.2 Ankle Joint

The ankle is the region where the leg and the foot meet (Figure 1-1). Some authors define the ankle joint as only the talocrural joint (Cailliet 1968, Riegger 1988, Michael et al. 2008, Netter 2010, Hernández-Díaz et al. 2012), which functions as a uniaxial joint. However, others, especially from a biomechanical point of view, define it as a complex of up to three principal joint systems (Procter and Paul 1982, Zwipp and Randt 1994), which function as a multi-axial joint. Not only the talocrural joint (the ankle joint or the upper ankle joint), but the talocalcaneal joint (the subtalar joint or the posterior lower ankle joint) and the transverse tarsal joint (the midtarsal joint or the anterior lower ankle joint) are also included in this ankle complex. The movement of the foot takes place at more than one joint in the ankle region, for example, dorsiflexion and plantarflexion are mainly performed at the talocrural joint, while the subtalar, and the midtarsal joints are predominantly responsible for inversion and eversion. Therefore, to understand the ankle joint biomechanics, a review of some joints in addition to the talocrural joint is useful. In this study, the ‘ankle joint’ is used to refer to only the talocrural joint, while the whole joint system including the talocrural, the talocalcaneal, and the transverse tarsal joints will be defined as the ‘ankle joint complex’ (Michael et al. 2008).

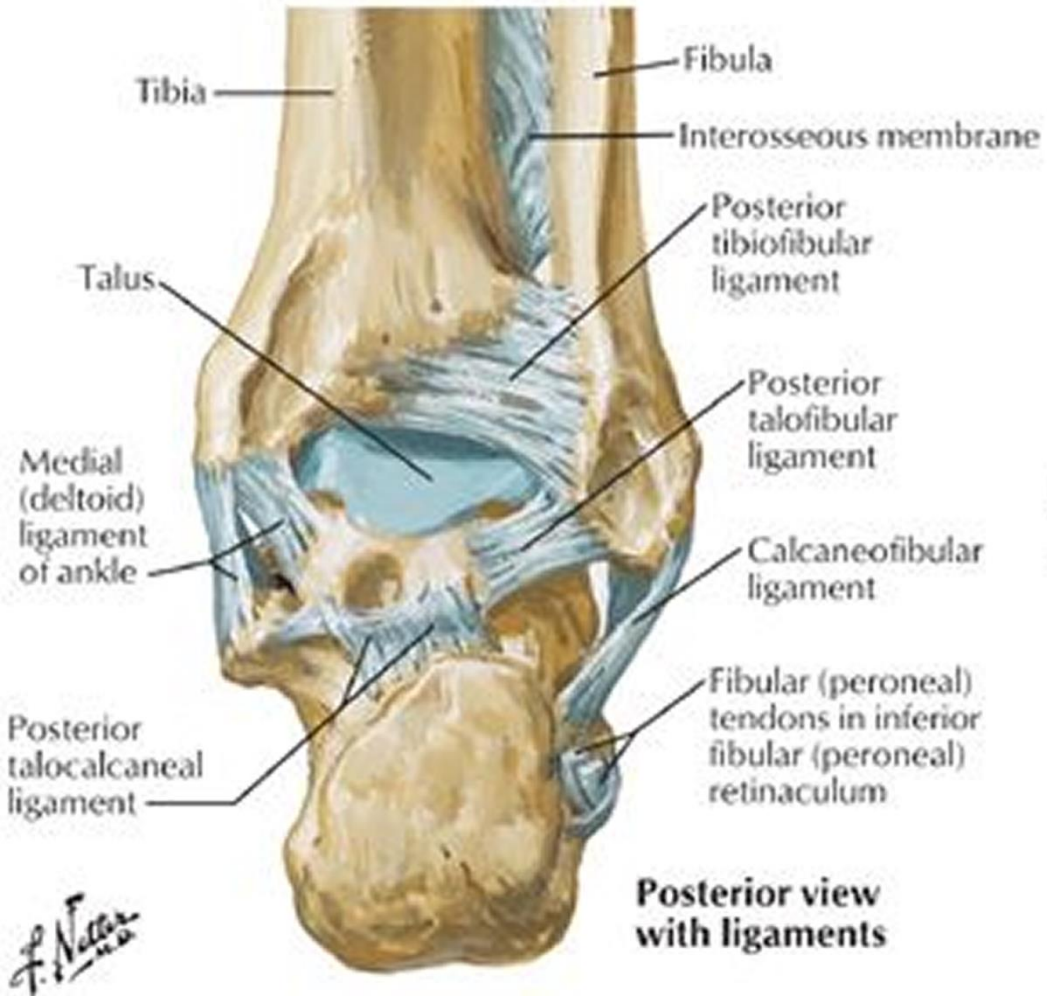

Figure 1-1 Posterior view of the ankle (Image taken from Netter 2010)

1.2.1 Anatomy of Ankle Joint Complex

1.2.1.1 Bony Anatomy of the Foot and Ankle

The lower leg includes a large and weightbearing bone called the tibia (located medially), and the fibula (located laterally), which is slender and bears little weight (Cailliet 1968, Behnke 2006, Netter 2010). There are enlargements at the distal ends of the shafts of both the tibia and the fibula. The enlargement at the distal end of the tibia is known as medial malleolus, while at the distal end of the fibula is known as the lateral malleolus. The distal ends of both the tibia and the fibula form a mortise that articulates with the talus, which is one of the bones of the foot, contributing to the talocrural joint (Figure 1-2).

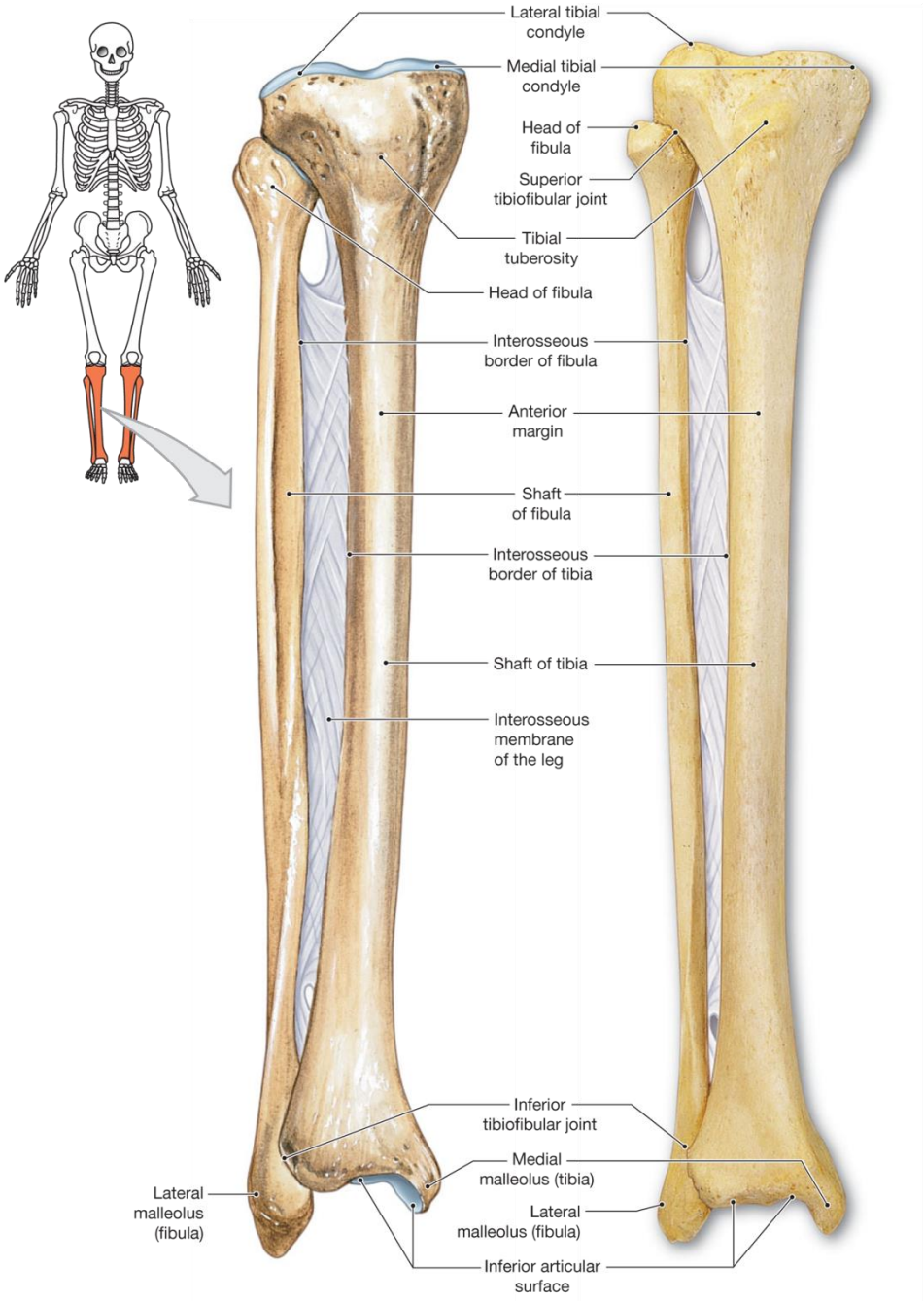

Figure 1-2 Anterior views of the right tibia and fibula (Image taken from Martini et al. 2012, page 203)

The foot's 26 bones include 14 phalanges, five metatarsals, and seven tarsal bones, which can be usually separated into three distinct segments: the anterior segment (the forefoot) which consists of 14 phalangeal bones forming the toes and five metatarsal bones, the middle segment (the midfoot) which contains five tarsal bones (the navicular, the cuboid, and the three cuneiforms), and the posterior segment (the hindfoot) which consists of two tarsal bones (the talus and the calcaneus) (Figure 1-3). The talus rests on top of the calcaneus,

which is in direct contact with ground. The articulation of the talus on the calcaneus forms the talocalcaneal joint, while on the distal ends of the tibia and the fibula forms the talocrural joint. The talus also articulates with the navicular in front at the talonavicular joint which combines with the calcaneocuboid joint, which is formed by the articulation between the calcaneus and the cuboid, to form the transverse tarsal joint (Hicks 1953, Cailliet 1968, Riegger 1988, Netter 2010).

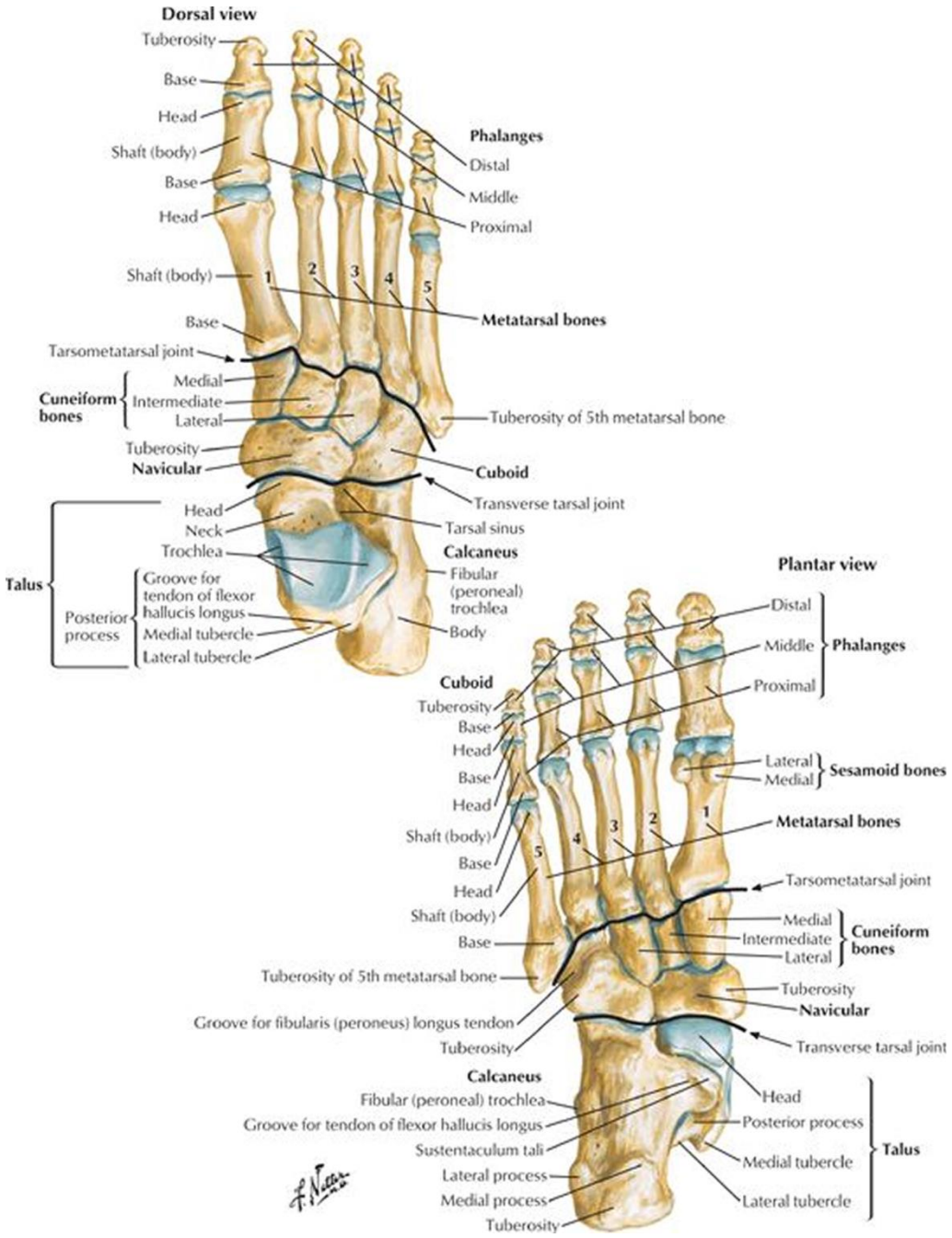

Figure 1-3 The bones of the foot (Image taken from Netter 2010)

1.2.1.2 Talocrural Joint

1.2.1.2.1 Bones of Talocrural Joint

The talocrural joint is composed of three bones: the tibia, the fibula, and the talus. The talus consists of a head, neck, and body with trochlea, and around 60% of its surface is covered with articular cartilage (Rockar Jr 1995, Dawe and Davis 2011). The trochlea, the dorsal surface, of the talus fits into the mortise formed loosely by the distal ends of the tibia and the fibula. The surface of the distal end of the tibia is concave anteroposteriorly and concave-convex-concave from medial to lateral, reciprocally fitting to the contact surface of the trochlea and allowing rotational gliding of the talus at the articulation (Cailliet 1968, Riegger 1988). The malleoli of the tibia and the fibula grip the talus, which functions as a hinge joint that permits movement in the sagittal plane (dorsiflexion and plantar flexion). However, some authors have stated that this movement does not act as a simple hinge due to the structure of the joint, for example, due to the cone-section geometry of the trochlea (Figure 1-4), the screw shape of the lateral facet of the talus, and the oblique axis of rotation of the talocrural joint (Figure 1-5) (Zwipp and Randt 1994, Michael et al. 2008).

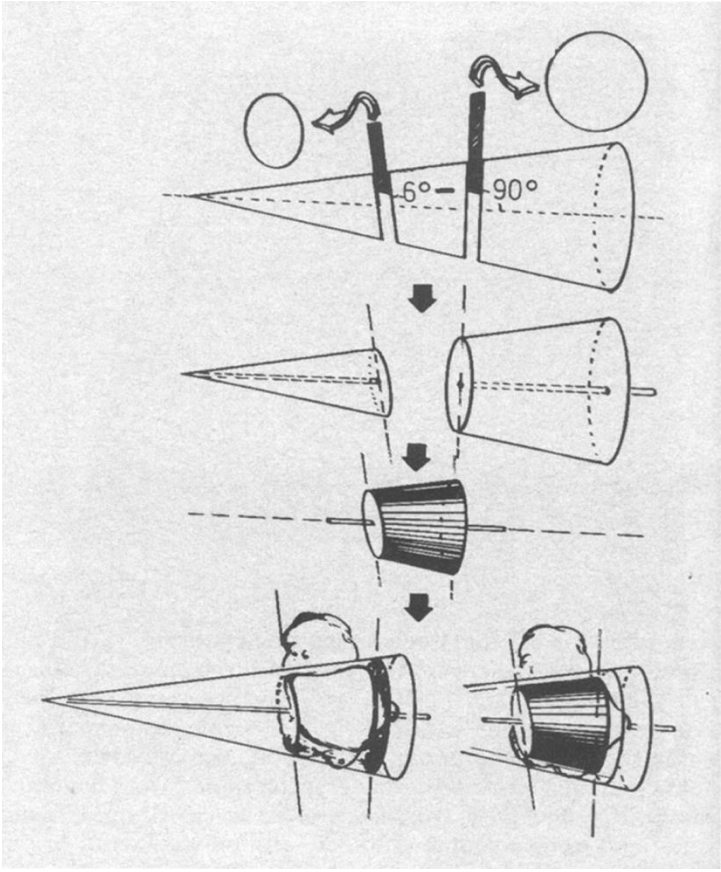

Figure 1-4 The trochlea tali as a part of cone, as illustrated by Zwipp and Randt 1994, page 22

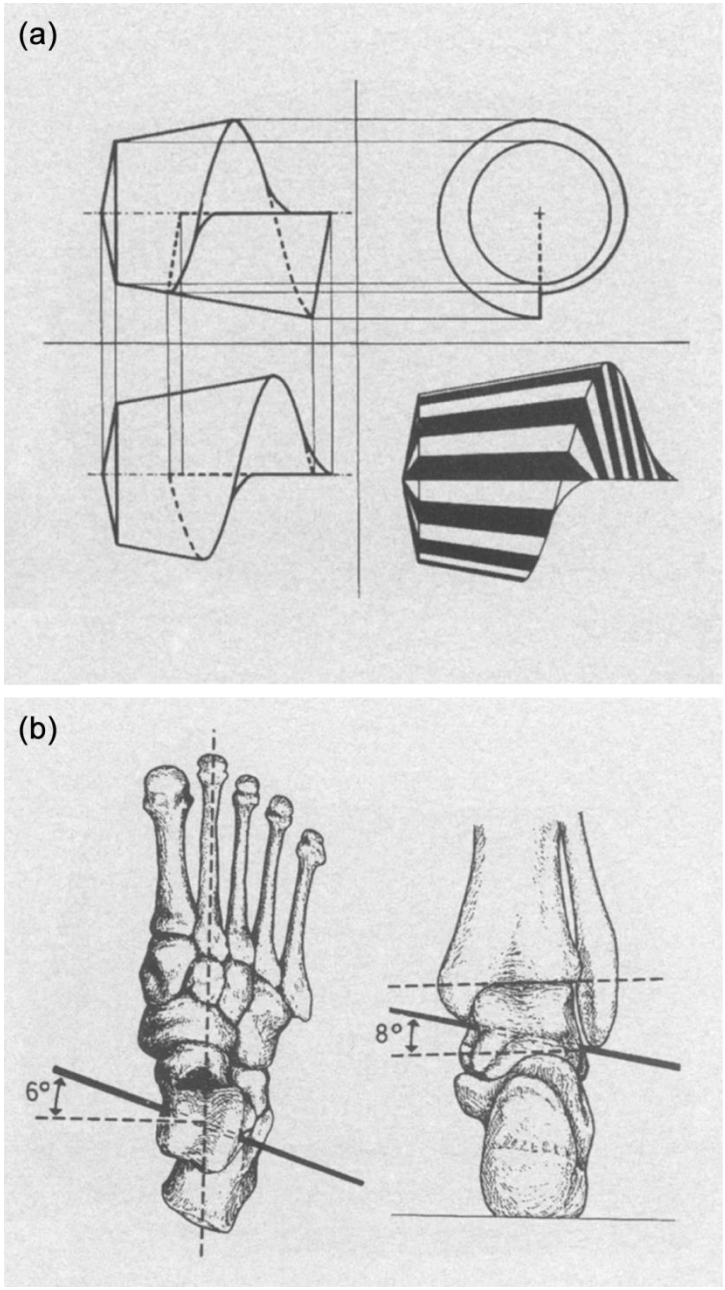

Figure 1-5 (a) The screw shape of the lateral facette of the talus and (b) the direction of the ankle joint axes, as illustrated by Zwipp and Randt 1994, page 23

The axis of the normal ankle joint passes below the tips of the lateral and medial malleoli, which runs from lateral to medial towards with six degree in the transverse plane (Figure 1-6) and ascending 10° in the frontal plane (Figure 1-7). This is because the medial malleolus is anterior and superior to the lateral malleolus (Isman and Inman 1969, Zwipp and Randt 1994, Michael et al. 2008). The joint is more stable when in dorsiflexion compared to in plantar flexion due to wedge shape with the widest portion anterior of the talus. The wider anterior part of the talus wedges between the two malleoli when in

dorsiflexion, while the narrower posterior part comes up into the mortise when in plantar flexion, which may permit some lateral motion to occur (Cailliet 1968, Riegger 1988, Netter 2010).

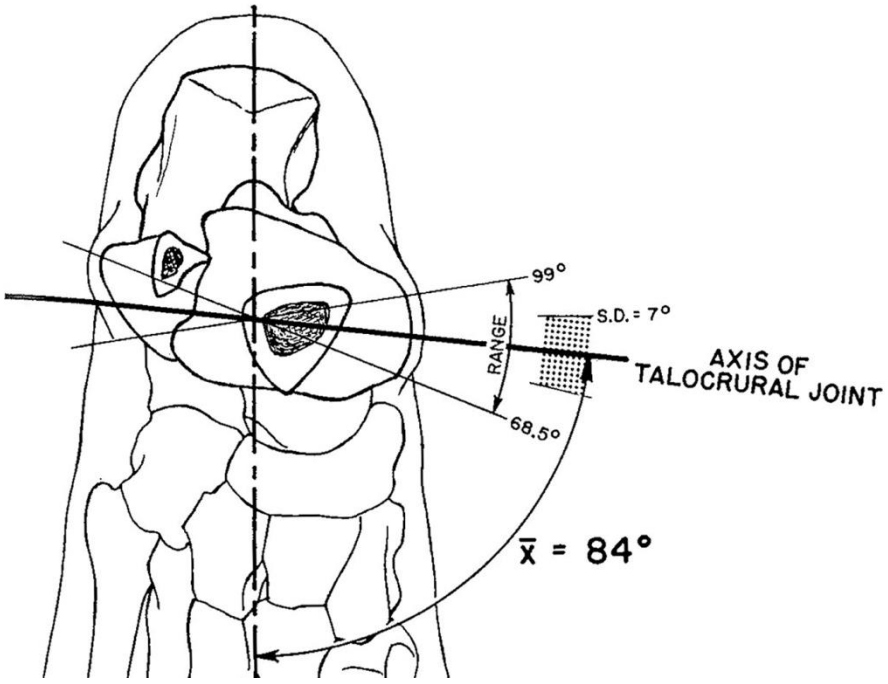

Figure 1-6 Axis of the talocrural joint in the transverse plane (Image adapted from Isman and Inman 1969, page 117)

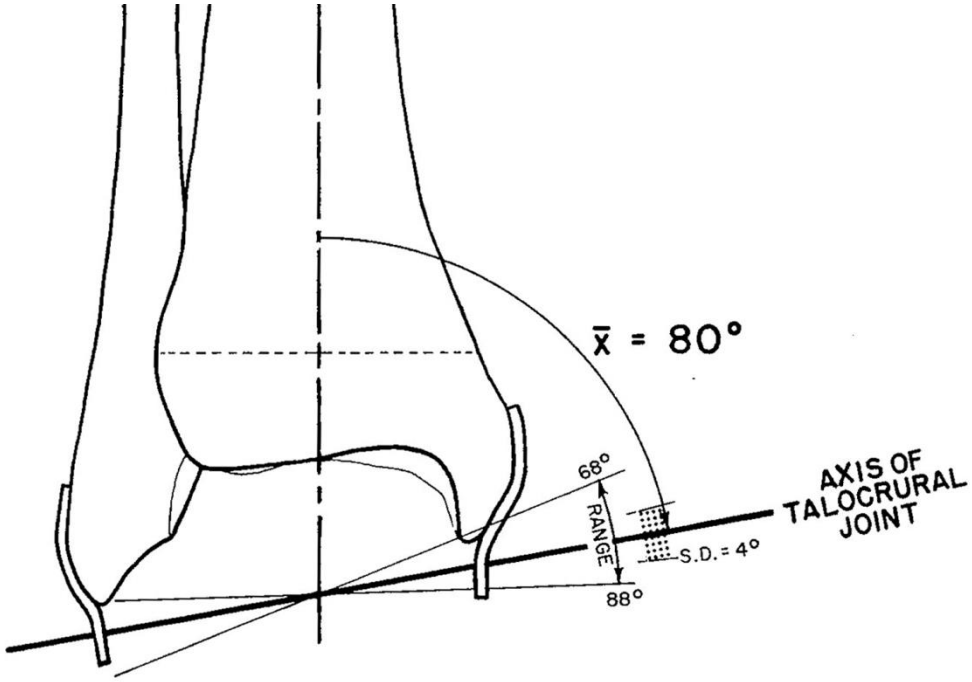

Figure 1-7 Axis of the talocrural joint in the frontal plane (Image adapted from Isman and Inman 1969, page 116))

1.2.1.2.2 Ligaments of Talocrural Joint

The talocrural joint is a diarthrosis (synovial joint), which is covered by a thin capsule attaching superiorly to the tibia and the malleoli, and inferiorly to the talus. The capsule is lined with synovial membrane, which secretes synovial fluid. This capsule is supported by the strong collateral ligament (Golanó et al. 2010, Netter 2010).

The ankle joint is strongly supported by three groups of surrounding ligaments that consist of the ligaments of tibiofibular syndesmosis, the medial collateral ligaments, and the lateral collateral ligaments. The tibiofibular syndesmotic ligaments maintain the stability between the distal end of the tibia and the fibula, and resist separation between the tibia and the fibula. These ligaments consist of three parts: the anterior or anteroinferior tibiofibular ligament, the posterior or posteroinferior tibiofibular ligarment, and the interosseous tibiofibular ligament (Figure 1-8). The medial collateral ligaments, or the deltoid ligament, support the medial aspect of the talocrural joint, and resist eversion strongly. These ligaments are composed of four parts: the anterior and posterior talotibial (the anterior and posterior tibiotalar), the tibionavicular, and the calcaneotibial (the tibiocalcaneal). The lateral collateral ligaments support the lateral aspect of the talocrural joint, and minimize inversion. These ligaments consist of three parts: the anterior talofibula ligament, the posterior talofibula ligaments, and the calcaneofibular ligament (Figure 1-8) (Cailliet 1968, Riegger 1988, Behnke 2006, Kong et al. 2007, Hamill and Knutzen 2009, Golanó et al. 2010, Netter 2010).

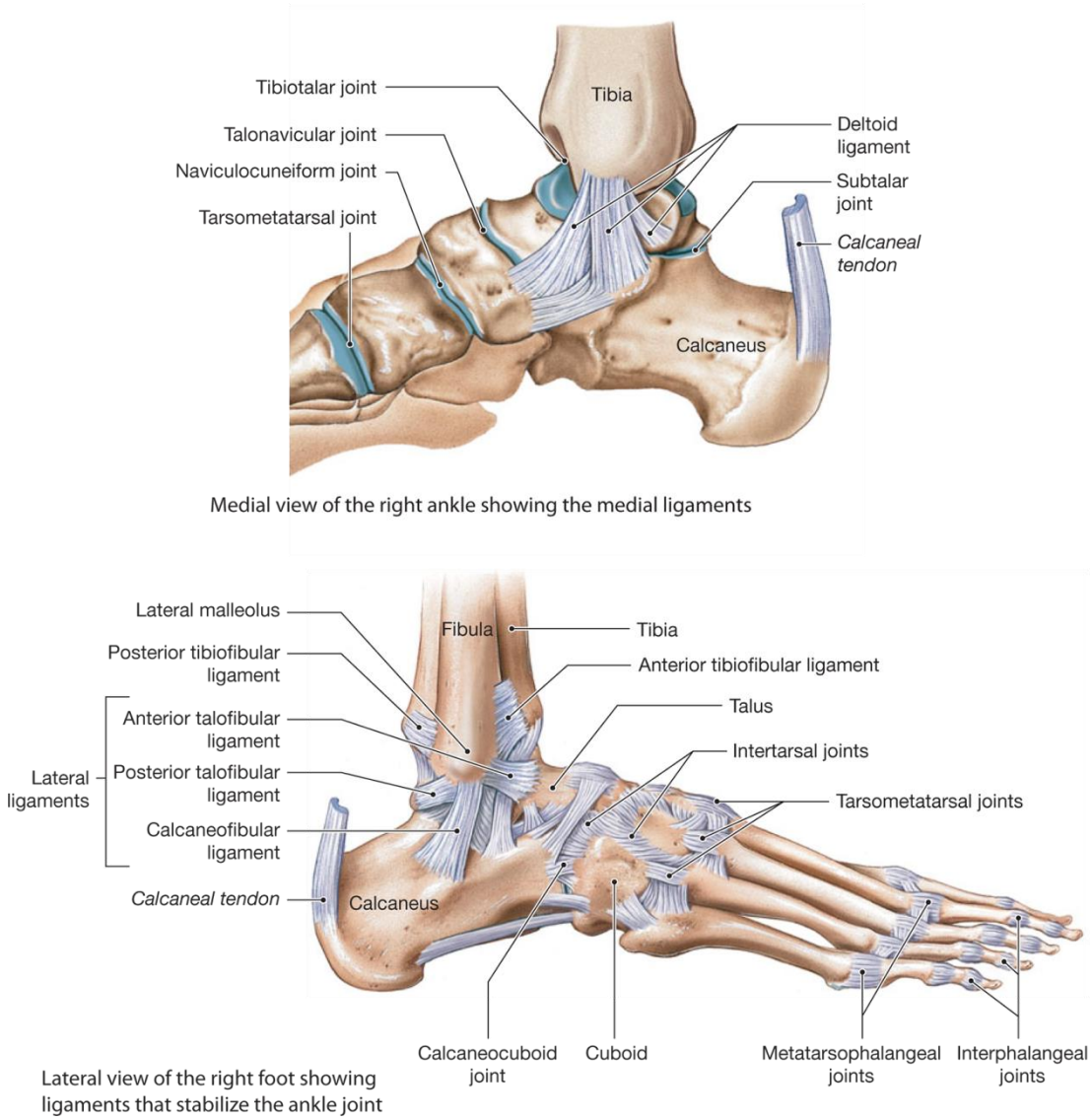

Figure 1-8 The ligaments of the ankle (Image taken from Martini et al. 2012, page 236)

1.2.1.3 Talocalcaneal Joint

1.2.1.3.1 Bones of Talocalcaneal Joint

The talocalcaneal joint consists of two bones: the talus superiorly and the calcaneus, the largest and strongest bone compared to other tarsal bones (Hall and Shereff 1993, Netter 2010), inferiorly. The majority of the talus rests on the anterior two thirds of the calcaneus, and projects slightly anteriorly to the calcaneus. The subtalar joint allows simultaneous movement in different directions due to several articulations in different planes contained in this joint. The two similar articulated facets of the anterior talocalcaneal joint on the inferior aspect of the talus are convex, and on the superior aspect of the calcaneus are concave, while the facets for articulation of the posterior

talocalcaneal joint on the inferior aspect of the talus are concave, and on the superior aspect of the calcaneus are convex. This relationship permits eversion and inversion, and most of eversion and inversion of the foot is provided by this joint. The posterior facet is separated from the middle facet by a deep groove termed the tarsal sinus, where the interosseous talocalcaneal ligament resides in (Cailliet 1968, Rockar Jr 1995).

The tarsal sinus divides the talocalcaneal joint into two parts: anterior and posterior. The anterior part of the talocalcaneal joint is termed as the talocalcaneonavicular joint, because this part shares a synovial cavity with the talonavicular joint. The posterior talocalcaneal joint is covered by another synovial cavity, and this articulation is known as the subtalar joint. However, the talocalcaneonavicular and the subtalar joints are considered to be one functional unit due to the fact that these two joints have a common axis of motion (Cailliet 1968, Rockar Jr 1995).

1.2.1.3.2 Ligaments of Talocalcaneal Joint

The talocalcaneal joint is more strongly supported by the two ligaments of ankle joint, which are the calcaneofibular part of the lateral collateral ligament and the calcaneotibial part of the deltoid, than by its own ligaments. This is because the two major ligaments linking between the talus and the calcaneus, which are the interosseous talocalcaneal and the lateral talocalcaneal ligaments, are relatively weak. Moreover, the long tendons of the peroneus longus, peroneus brevis, flexor hallucis longus, tibialis posterior, and flexor digitorum longus provide support to the talocalcaneal joint as well (Cailliet 1968).

1.2.1.4 Others in Ankle Joint Complex

The transverse tarsal joint (midtarsal joints or Chopart’s joint) is a combination of the talonavicular joint, where the convex facet of the talar head articulates with the concave facet on the posterior aspect of the navicular, and the calcaneocuboid joint, which is the articulation between the convex facet on the anterior aspect of the calcaneus and the concave facet on the posterior aspect of the cuboid. These joints allow similar movement of the foot, eversion and inversion (Cailliet 1968).

1.2.1.5 Muscles of the Foot, Ankle, and Leg

The muscles of the leg, the ankle, and the foot are typically divided into the extrinsic muscles, which originate outside the foot and insert within the foot, and the intrinsic muscles, which originate and insert within the foot. Most of the movement of the foot is produced by the 12 extrinsic muscles, which are contained in four compartments: the anterior, the lateral, the superficial posterior, and the deep posterior compartments of the leg (Figure 1-9, 1-10 and 1-11). The anterior compartment consists of the four muscles: the tibialis anterior, the extensor digitorum longus, the extensor hallucis longus, and the peroneus tertius. The tibialis anterior and the extensor hallucis longus produce dorsiflexion and inversion of the foot. The peroneus tertius produces dorsiflexion and eversion of the foot. The extensor digitorum longus only produces dorsiflexion of the foot. The lateral compartment is composed of the two muscles: the peroneus longus and the peroneus brevis, which produce plantarflexion and eversion of the foot. The superficial posterior compartment consists of the three muscles: the gastrocnemius, the soleus, and the plantaris, which produce plantarflexion of the foot. The deep posterior compartment is composed of three muscles: the tibialis posterior, the flexor digitorum longus, and the flexor hallucis longus, which produce plantarflexion and inversion of the foot (Cailliet 1968, Behnke 2006, Netter 2010).

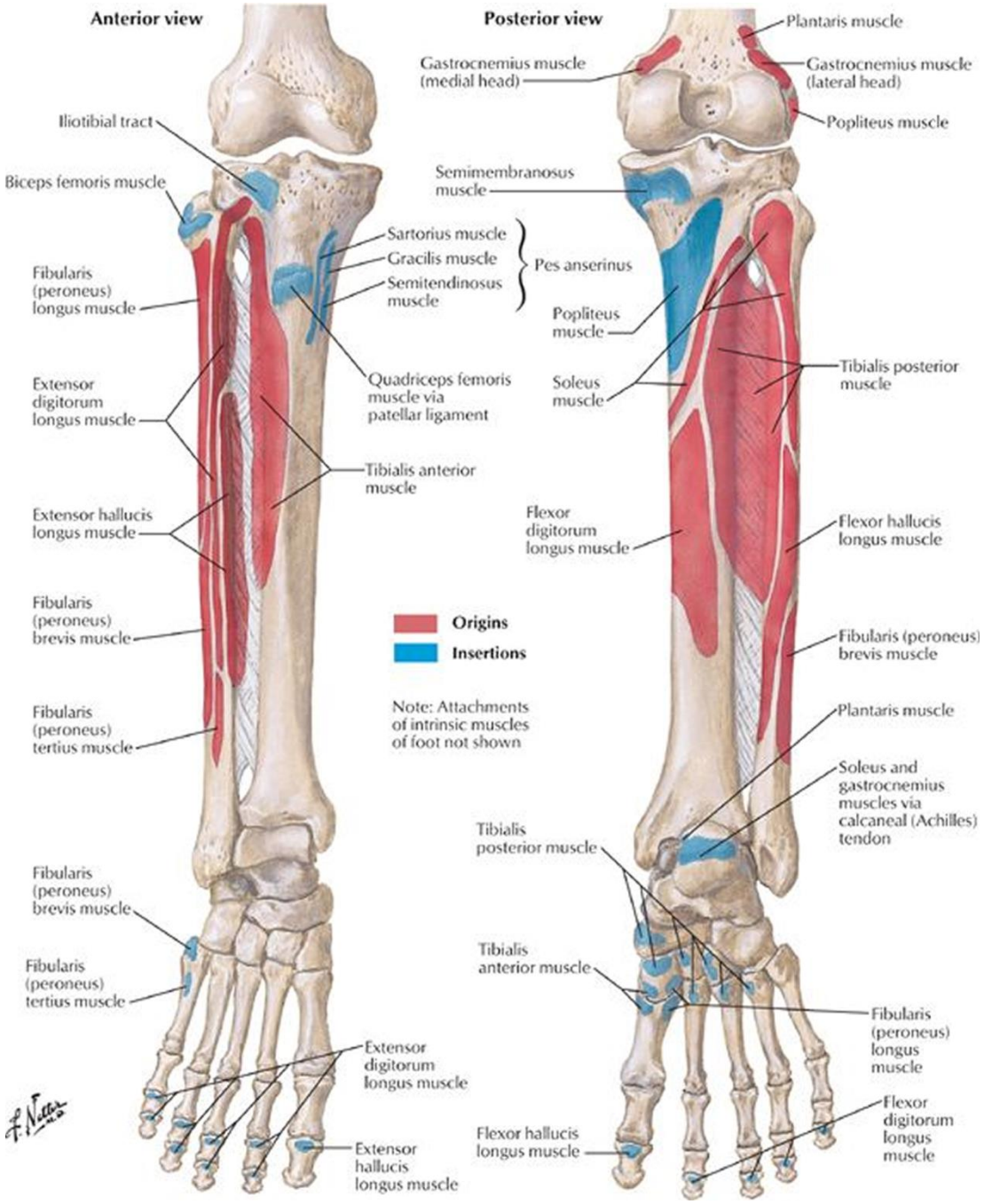

Figure 1-9 Anterior and posterior views of bones and attachments of muscles of the foot, ankle, and leg (Image taken from Netter 2010)

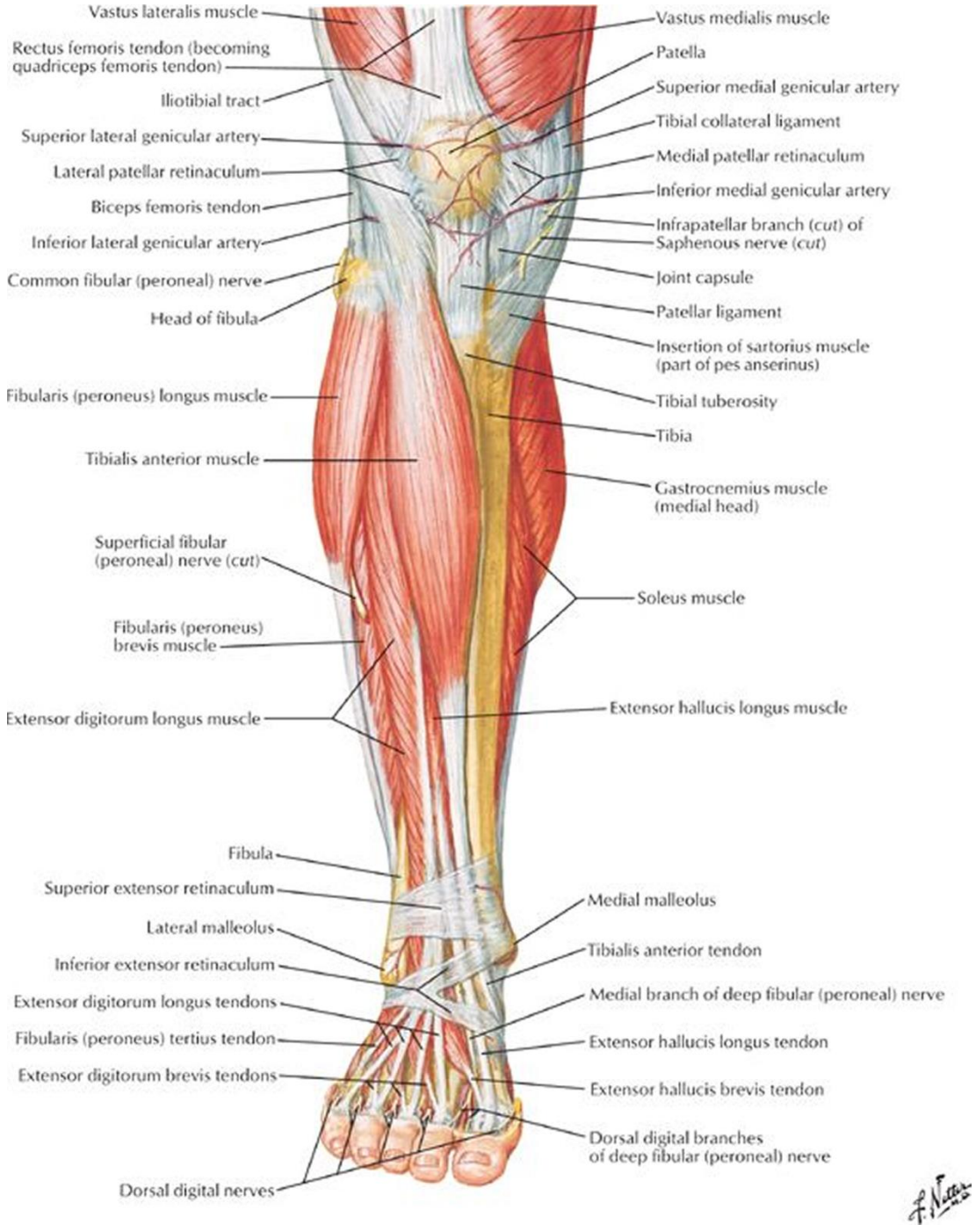

Figure 1-10 Anterior view of muscles of the foot, ankle, and leg (Image taken from Netter 2010)

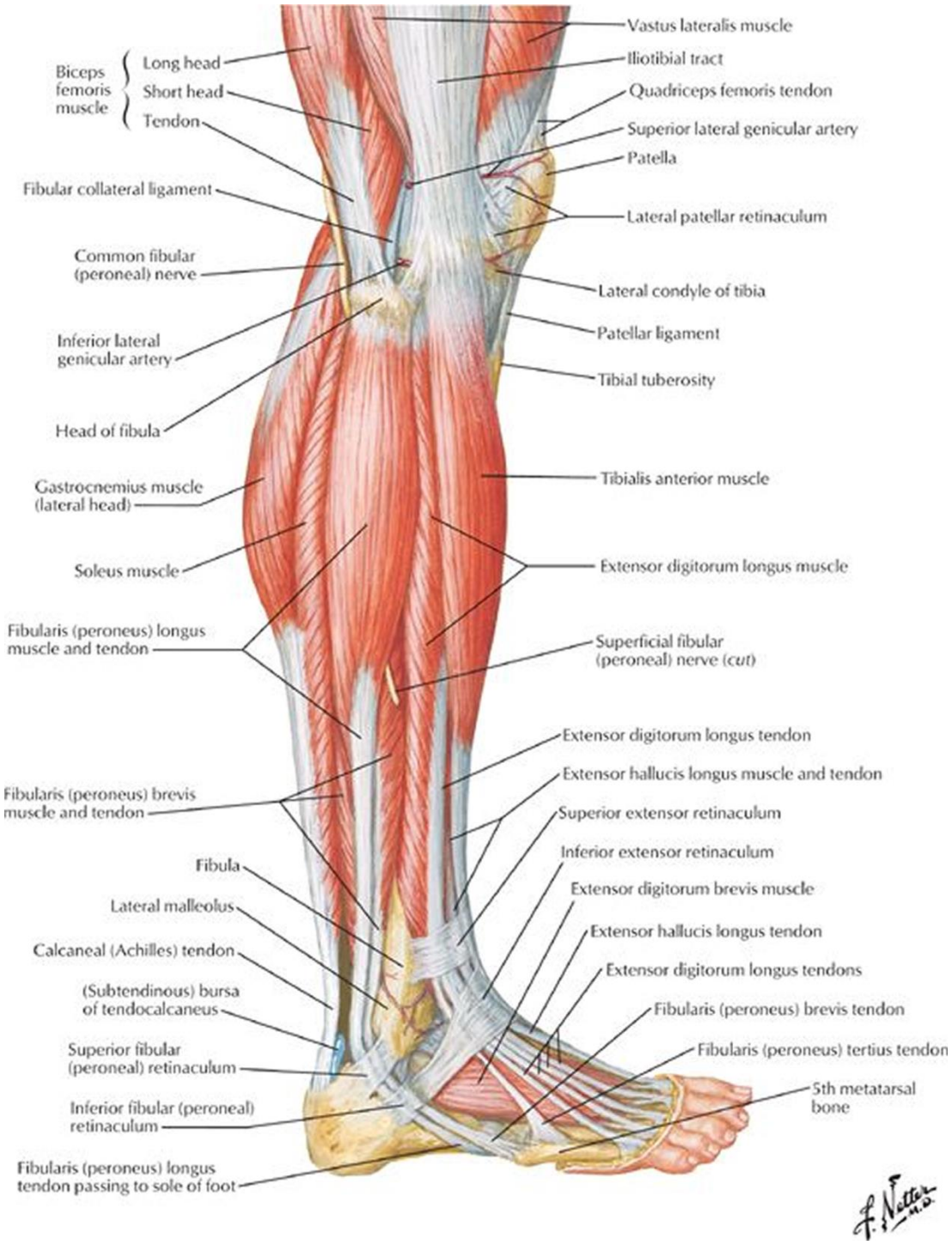

Figure 1-11 Lateral view of muscles of the foot, ankle, and leg (Image taken from Netter 2010)

1.2.2 Biomechanics of Ankle Joint Complex

1.2.2.1 Joint Biomechanics

The ankle joint is considered by several authors to be a hinge joint (Isman and Inman 1969, Procter and Paul 1982), while others suggested that it is not a simple hinge joint due to its simultaneous movements when performing a function. Some authors considered the ankle joint to be multi-axial (Barnett and Napier 1952, Lundberg et al. 1989). This is because the ankle joint also produces internal rotation during dorsiflexion, as well as external rotation generated during plantarflexion. However, there is some evidence to demonstrate that the talocrural joint is uniaxial, and its simultaneous movements occur as a result of its oblique axis (Zwipp and Randt 1994). The talocalcaneal joint usually generates eversion, abduction, and dorsiflexion during pronation, as well as inversion, adduction, and plantar flexion are produced during supination (Isman and Inman 1969, Procter and Paul 1982, Hamill and Knutzen 2009).

A study of Grimston et al. measured range of motion of the ankle joint complex of 120 subjects ranging in age from nine to 79 years in six movements: plantar flexion, dorsiflexion, inversion, eversion, abduction, and adduction. The results revealed that the average combined movement of the ankle joint complex in the sagittal plane was approximately 67°, from approximately 25° dorsiflexion to 42° plantar flexion, in the frontal plane approximately 35° (from approximately 23° inversion to 12° eversion), and in the transverse plane was about 71°, from approximately 38° abduction to 33° adduction (Grimston et al. 1993).

1.2.2.2 Gait Biomechanics

In everyday activities, the movement of the ankle joint in the sagittal plane has been found to be approximately 30° for walking, and 37° and 56° for ascending and descending stairs respectively (Michael et al. 2008). Moreover, a study of Stauffer et al. revealed that an average 24.4° combined movement of the ankle joint in the sagittal plane, which consists of 10.2° dorsiflexion and 14.2° plantar flexion, is required during stance phase of gait (Stauffer et al. 1977). The motion of ankle joint complex in three different planes: the frontal, sagittal, and transverse planes, over a corresponding to a single gait cycle was measured by Benedetti et al. These measurements were performed on a healthy single young adult subject (26 year-old male, 177cm, 70kg) with the aid of seven different acquisition devices in seven laboratories. The results are shown in Figure 1-12 (Benedetti et al. 2013).

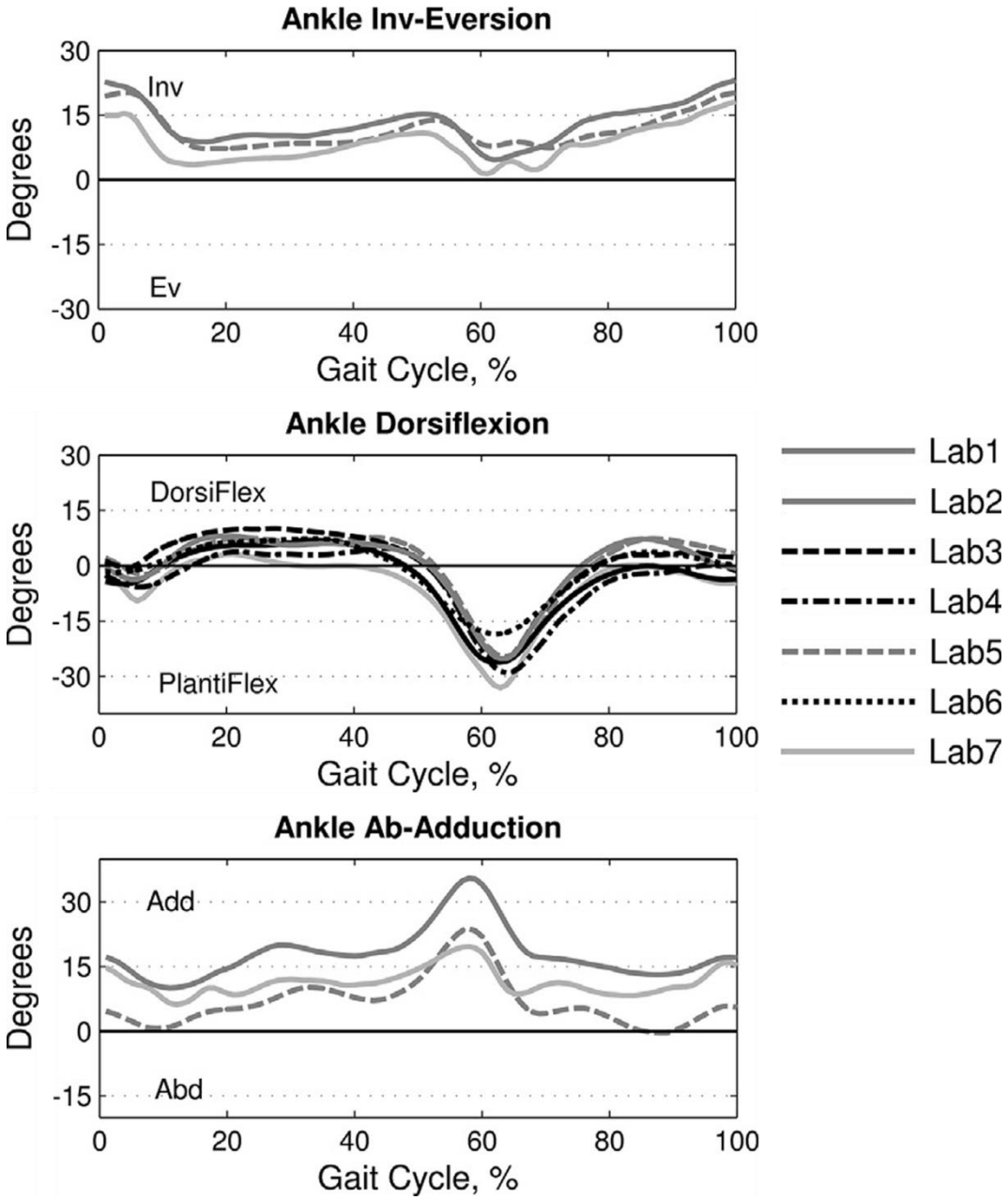

Figure 1-12 The motion of ankle joint complex in three different planes during a single gait cycle (Image adapted from Benedetti et al. 2013, page 4)

In addition, plots of joint angle (Figure 1-13), internal joint moment (Figure 1-14), and joint power (Figure 1-15) against a single gait cycle were also determined by Whittle (Whittle 2007). The maximum movement of the ankle joint complex in dorsiflexion occurred during heel off at about 40% of gait cycle, while in plantar flexion occurred during toe off at about 60% of gait cycle. The maximum internal joint moment of the ankle joint complex was produced during heel off at about 40% of gait cycle. The maximum joint power of the ankle joint complex was generated at 50% of gait cycle between heel off and toe off.

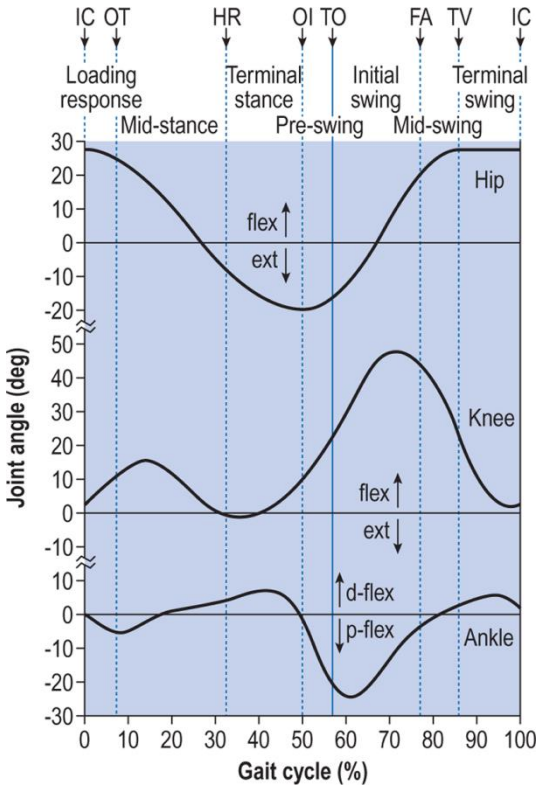

Figure 1-13 Sagittal plane joint angle during a single gait cycle (Image taken from Whittle 2007, page 59)

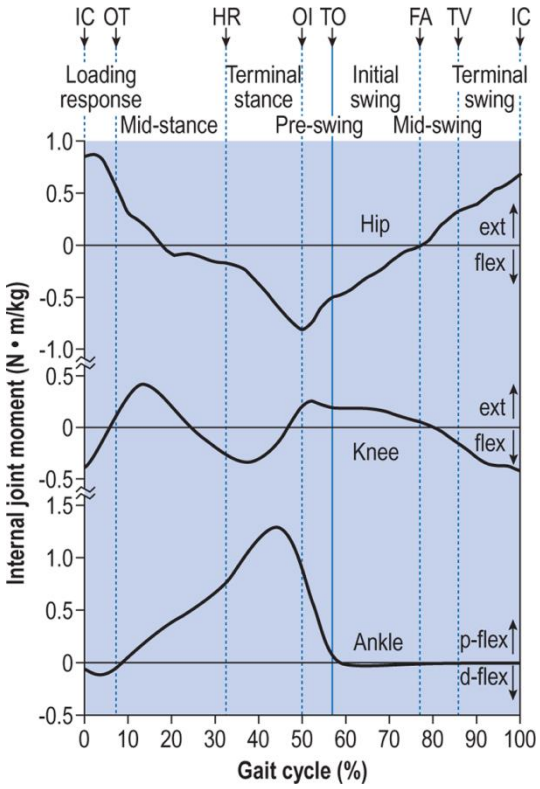

Figure 1-14 Sagittal plane joint moment during a single gait cycle (Image taken from Whittle 2007, page 60)

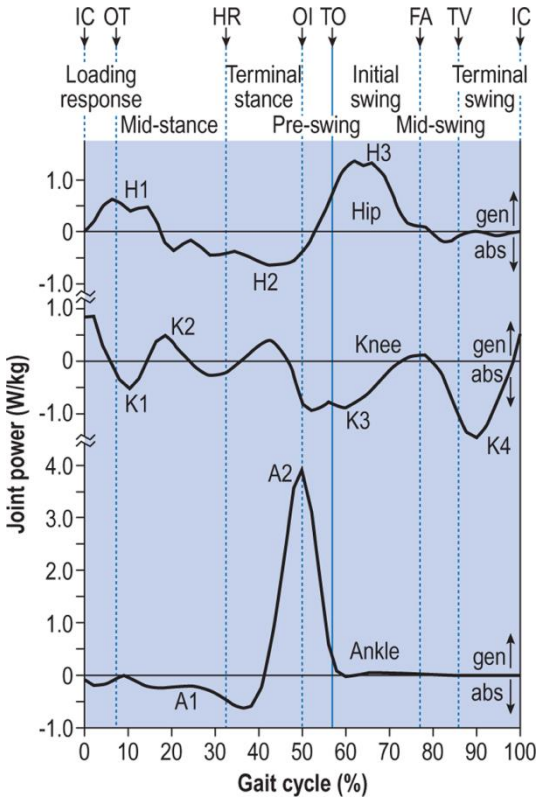

Figure 1-15 Sagittal plane joint power during a single gait cycle (Image taken from Whittle 2007, page 60)

An accurate knowledge of the forces imposed upon the ankle joint is important for understanding, treating, and preventing injuries to this area, and it is also useful for designing ankle joint prostheses. It is difficult to measure internal force at the ankle joint directly because this procedure requires surgical placement of the force transducers (Burdett 1982). Therefore, some authors have developed mathematical models of the ankle joint to predict the forces at the ankle during gait with the aid of cameras and force platforms (Figure 1-16) (Stauffer et al. 1977, Burdett 1982, Procter and Paul 1982).

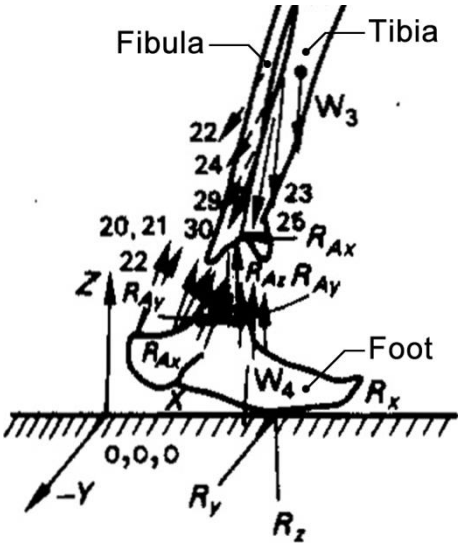

Figure 1-16 An example of free-body diagrams of the ankle segment for a typical posture during quasi-static walking (Image adapted from Seireg and Arvikar 1975, page 92)

Stauffer and collaborators found that normal (compressive) forces across the ankle during normal walking were raised to three times body weight between heel strike and foot flat phases of gait cycle, and reached a plateau until heel off. At the heel off phase, the Achilles tendon began to produce a large plantar flexion moment, this caused the force to increase to a maximum peak value of 4.5 to 5.5 (average 4.73) times body weight. They also claimed that, although walking rate was increased from 40 to 60 strides per minute, the magnitude of the peak force would not be significantly changed (Figure 1-17) (Stauffer et al. 1977).

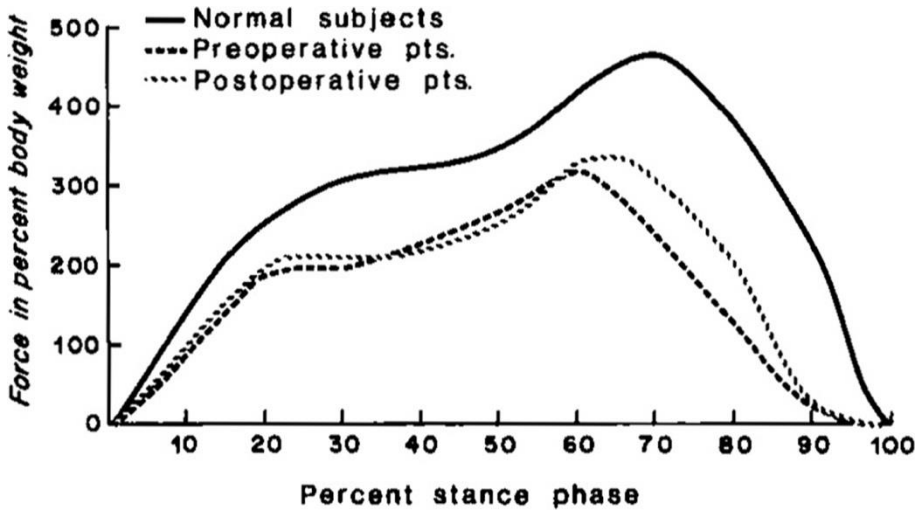

Figure 1-17 Mean patterns of compressive ankle force (Image taken from Stauffer et al. 1977, page 194)

The calculated ankle joint force against percentage of gait cycle was illustrated in the study of Seireg and collaborators (Figure 1-16), and showed the maximum value for the ankle joint reaction force was approximately 5.2 times the body weight during the heel off phase of the gait cycle (Seireg and Arvikar 1975). In the study of Procter and collaborators in 1982, in addition to the peak resultant forces at the joints, the maximum forces experienced by muscles were also determined. The average maximum resultant forces illustrated in this paper were: 3.88 times body weight at talocrural joint during heel off phase; 2.43 times body weight at anterior facet of talocalcaneonavicular joint during heel off; 2.84 times body weight at postterior facet of talocalcaneonavicular joint during heel off; 0.99 times body weight at anterior tibial muscle group during heel strike; 0.66 times body weight at posterior tibial muscle group during midstance; 2.46 times body weight at calf muscle group during heel off; and 1.06 times body weight at peroneal muscle group during heel off (Procter and Paul 1982). Arakilo and collaborators also showed forces applied on ankle joint and surrounding tendon and muscles calculated by musculoskeletal modeling software during toe off of gait cycle. These included 4.95 times body weight at ankle joint, 3.90 times body weight at Achilles tendon, 0.615 times body weight at peroneus muscle, and 0.719 times body weight at tibialis anterior muscle (Arakilo et al. 2009). In the study of Yalamanchili and collaborators, who studied kinetic and kinematic parameters in the foot during normal gait on twelve healthy male subjects, the average peak force acting at the ankle in the vertical plane was approximately three times body weight (Yalamanchili et al. 2009). Moreover, the peak resultant ankle joint and Achilles tendon forces during running at speed 4.47 m/s were mentioned in the study by Burdett. These value were 9.0 to 13.3 times body weight at ankle joint and 5.3 to 10.0 times body weight at Achilles tendon (Burdett 1982).

1.3 Injuries and Disorders of Ankle

The soft-tissues of the ankle (the ligaments, tendons, and muscles) can be damaged by even simple everyday activities. The most common soft-tissue injury is a sprain, which happens when a ligament is forced to stretch beyond its normal range. This is one of two common ankle problems. The other one is a fracture, which is a break in a bone (Ranawat and Positano 1999). Severe sprains, which have not been healed completely resulting in ankle instability, and fractures can lead to post-traumatic arthritis, which is an inflammation of a joint occurring when the cartilage, the smooth covering on the end of the bone, becomes damaged or worn (Hintermann 2005, Fong et al. 2009, DiStefano and Pinney 2010).

1.3.1 Sprains

An ankle sprain is one of the most common injuries, especially in many kinds of sport, and occurs in about one in 10,000 people per day (Fallat et al. 1998, Osborne and Rizzo Jr 2003, Fong et al. 2007, Hubbard and Cordova 2009, Schmitt et al. 2009, Struijs and Kerkhoffs 2010, Witjes et al. 2012). It results from abnormal movements of the ankle, especially in supination produced by adduction and inversion during plantar flexion of the foot (Ranawat and Positano 1999, Fong et al. 2009, Struijs and Kerkhoffs 2010, Witjes et al. 2012), forcing ligaments to stretch beyond their normal limit. A severe sprain causes complete rupture of the ligament. Without adequate treatment and rehabilitation, chronic problems of pain and instability may result (Osborne and Rizzo Jr 2003, Hubbard and Hertel 2006, Fong et al. 2009, Witjes et al. 2012, Petersen et al. 2013). Several studies have reported that approximately 19% of post-traumatic osteoarthritis of ankle cohort was initially caused by ankle sprains (Valderrabano et al. 2006, Valderrabano et al. 2009).

1.3.2 Fractures

An ankle fracture is among the most common injuries of the lower limb, constituting approximately 10% of all fractures (Berentey et al. 1994, Miller et al. 2010, Schie-Van der Weert et al. 2012).

Several factors affect the selection of an appropriate treatment for an ankle fracture, because each has unique characteristics. Some fractures can be best treated by a conservative technique, such as a plaster cast, while others require an operative treatment, but both have similar aims of reducing the fracture until union, and restoring the previous movement. (Schouwenaars and Mulier 1979, Fernandez 1984, Ranawat and Positano 1999, Kettunen and Kröger 2005, Bernstein and Ahn 2010, Miller et al. 2010, Hulsker et al. 2011).

Several studies have reported that approximately 80% of cases of post-traumatic ankle osteoarthritis were initially caused by ankle fractures (Valderrabano et al. 2006, Valderrabano et al. 2009).

1.3.3 Arthritis

Although the ankle joint is more commonly injured than any other major joint, ankle arthritis is relatively rare, being approximately nine times less prevalent than the hip or knee arthritis (Thomas and Daniels 2003, DiStefano and Pinney 2010, Ritterman et al. 2012, Baumhauer 2013, Labib et al. 2013). The articular cartilage of the ankle is more uniform, denser, stiffer, and has less diminution with aging compared to the cartilage in the hip and knee. This may explain the relatively low prevalence of ankle arthritis (DiStefano and Pinney 2010, Ritterman et al. 2012, Labib et al. 2013). In a study of 406 ankles with end-stage ankle osteoarthritis, Valderrabano et al. divided the aetiology of ankle osteoarthritis into three main groups: posttraumatic, secondary, and primary osteoarthritis, and found these represented 78%, 13%, and 9% of cases in this cohort respectively (Valderrabano et al. 2009). Posttraumatic arthritis consists of progressive hyaline cartilage alteration, subchondral sclerosis, and osteophyte development, which results from an ankle injury, such as bone fracture, isolated osteochondral damage, and ligament injury (Giannini et al. 2007). The direct cartilage injury, irregular joint loading due to fracture with joint incongruity, or altered loading due to malalignment may be factors resulting in the arthritis (DiStefano and Pinney 2010). Primary osteoarthritis of the ankle is relatively rare (Moskowitz 1987). The second most common cause of ankle arthritis is secondary arthritis, which includes a known associated event or disease, such as rheumatoid arthritis, hemochromatosis, and postinfectious arthritis. Rheumatoid arthritis, the most common aetiology in this category, is a systemic autoimmune disease that produces proteolytic enzymes that destroy the articular cartilage leading to joint instability (Canseco et al. 2011).

The treatment of osteoarthritis can be either nonoperative or operative, depending on the stage of the disease, the age of the patient, the level of motivation, the quality of joint alignment, and the range of motion of adjacent joint (Giannini et al. 2007, Berlet et al. 2008). Nonsurgical or conservative treatments may include medications, such as nonsteroidal anti-inflammatory drugs (NSAIDs), orthotic devices, such as custom-made shoes, orthoses, and braces, and injections, such as corticosteroids and hyaluronic acid. The aim of these treatments is to reduce inflammation and pain associated with arthritis. Likewise, orthotic devices are used with the aim of alleviating pain by modifying

or decreasing weight-bearing loads transmitted and limiting motion through the ankle joint.

In older patients, the most common surgical techniques prescribed are total ankle replacement and ankle arthrodesis or ankle fusion. In addition to use in older patients, the ankle arthrodesis is also used in younger patient who are very active. Ankle arthrodesis is a surgical technique which uses internal fixation, such as screws and plates, to fuse the bones of the ankle joint with the aim of relieving pain due to movement at the articulation, and restoring and maintaining alignment (Figure 1-18). Ankle fusion is the most common treatment for ankle arthritis, and is generally successful, however, there are problems due to this treatment including infection, nonunion, malunion, immobilisation, and development of arthritis in the adjacent joints. An orthotic device may be prescribed to improve gait biomechanics that are restricted postoperatively. This surgical option may also be considered as a treatment to salvage the ankle joint after the failure of the total ankle arthroplasty (Thomas and Daniels 2003, Giannini et al. 2007, Berlet et al. 2008, Rao et al. 2010, Lee et al. 2011, Ritterman et al. 2012, Labib et al. 2013, Weatherall et al. 2013).

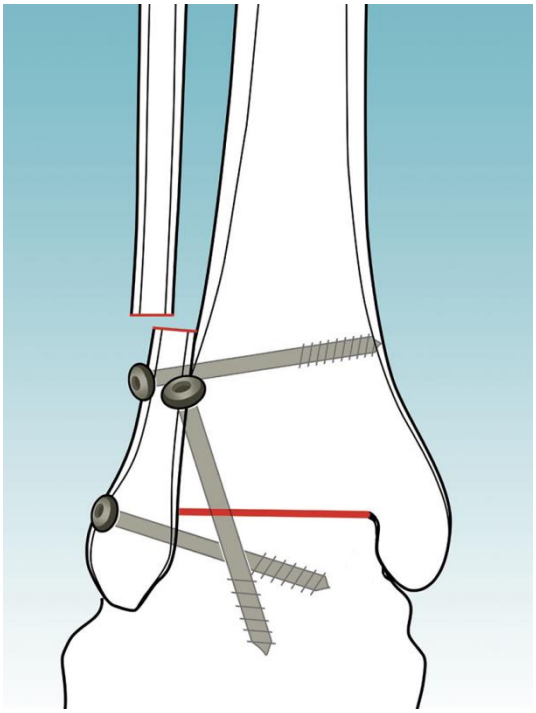

Figure 1-18 Illustration showing an arthrodesis technique (Image taken from Giannini et al. 2007, page 25)

1.4 Total Ankle Replacement

Total ankle replacement (TAR) or total ankle arthroplasty (TAA) was initially invented as an alternative to fusion for the treatment of end stage ankle osteoarthritis (Figure 1-19). Developed in the 1970s, the aim of the replacement was to reduce postoperative complications, whilst improving the range of motion compared with fusion. Early designs of TAR had unacceptably high failure and complication rates associated with fixation or due to the highly constrained designs, leading to procedure being abandoned in favour of ankle arthrodesis. However, modern designs of TAR have shown improved clinical performance, making them a viable surgical option (Van et al. 2010, Park and Mroczek 2011, Ritterman et al. 2012).

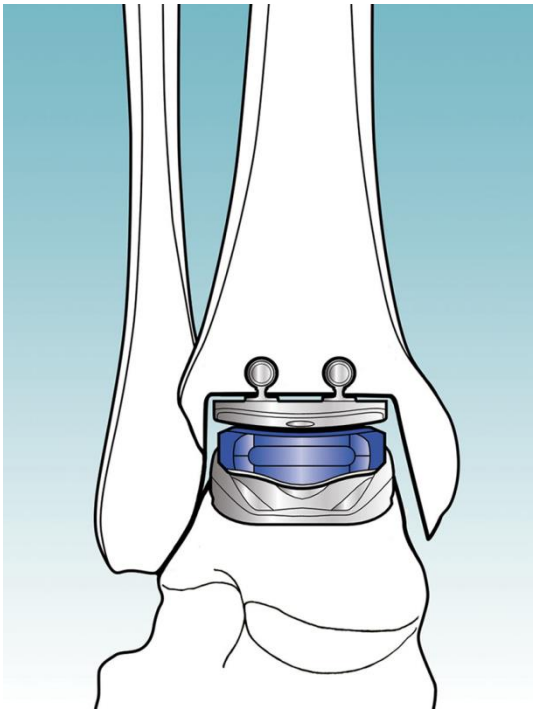

Figure 1-19 Illustration showing a three-component ankle prosthesis (Image taken from Giannini et al. 2007, page 23)

1.4.1 Indications and Contraindications for TAR

TAR is generally indicated in patients with severe, end stage primary osteoarthritis, posttraumatic osteoarthrosis, inflammatory arthritis, and other secondary osteoarthrosis (Van et al. 2010, Weatherall et al. 2013). A successful outcome in any joint replacement, including TAR, is significantly influenced by appropriate patient selection. Most authors advocate that the optimal candidate for TAR is the older patient (over 50 years of age), however,

some authors suggest that TAR may benefit younger patients as well (Jackson and Singh 2003, Easley et al. 2011). Other recommendations include non-obese patients with good bone stock, normal vascular status, minimal deformity, and low physical demand (Easley et al. 2002, Hintermann 2005, Guyer and Richardson 2008, Bonasia et al. 2010).

Most contraindications for TAR are derived from the factors associated with unacceptably high rates of failure and complications, which can be either relative or absolute contraindications. The relative contraindications include young age, obesity, high physical demand, previous severe trauma, severe osteoporosis, diabetes mellitus, and long-term use of steroids. While in the study of Weatherall et al., severe osteoporosis was also identified as an absolute contraindication. Further absolute contraindications include neuropathic arthritis (Charcot's joint), active or recent ankle infection, avascular necrosis (AVN) of the talus over more than 50% of the talar body, severe soft-tissue problems, severe neurological dysfunction, and non-reconstructable malalignment. Some authors suggest that previous ankle infection is an absolute contraindication (Hintermann 2005, Van et al. 2010), while many authors identify prior ankle infection as only a relative contraindication (Easley et al. 2002, Jackson and Singh 2003, Bonasia et al. 2010, Weatherall et al. 2013). Similarly, the studies of Easley et al. and Bonasia et al. identified severe lower extremity malalignment as a relative contraindication.

1.4.2 Designs of TAR

The development of the TAR has taken a long time compared to total hip and knee arthroplasties, mainly due to difficulties related to the biomechanics of the ankle, for example, the small size of the joint, high compressive forces and resultant moments, and the potential for malalignment and instability (Hintermann 2005). Early designs of TAR were initially introduced in the 1970s, but, as previously stated, had unsatisfactory outcomes. However, interest in the use of TAR was resumed in the 1990s due to improved designs. TARs can be classified according to six factors: the fixation type, number of components, constraint type, congruency type, component shape, and bearing type. The fixation of TAR can be categorised as cemented or uncemented. The cemented fixation method used in most of the first-generation TARs yielded high revision and failure rates, therefore, fixation of modern designs of TAR are typically uncemented. Based on the number of components, TARs can be divided as either two-component or three-component designs. Almost all TARs developed during the 1970s to 1980s were the two-component design. The two-component TARs can be further subdivided into three categories: constrained,

semi-constrained, and non-constrained. The constrained designs allow movement of ankle as a hinge joint; the range of motion is increasingly permitted in the semi-constrained and the non-constrained TARs respectively (Bauer et al. 1996). The articular surface shape can be either incongruent or congruent. The incongruent types resulted in early failure, whereas the congruent designs tended to provide better outcomes. This might be because the congruent articular surfaces provide greater stability and resistance to wear (Vickerstaff et al. 2007). According to the component shape, TARs can be classified as non-anatomic and anatomic type. The bearing type can also be used to classify TARs into two categories: fixed and mobile. The mobile bearing type establishes two separate articular surfaces between tibial and talar components, while the fixed bearing type creates only one (Hintermann 2005).

1.4.2.1 First-Generation TARs

TAR was initially used to replace the ankle joint by Lord and Marotte in France in 1970 (Park and Mroczek 2011). A ball and socket design of the first TAR was based on an inverted hip prosthesis implanting an inverted hip stem into the tibia and a cemented polyethylene acetabular cup in the calcaneus (Hintermann 2005). This technique involved completely resection of the talus leading to a subtalar arthrodesis (Bauer et al. 1996). 25 patients were treated with this procedure, but 12 arthroplasties failed and only seven patients could be considered satisfactory postoperatively at 10-year follow-up (Van et al. 2010). At the time, Lord and Marotte realized due to the complexity of ankle biomechanics that the amount of rotation required at the ankle could not be adequately mimicked by a simple hinge ankle prosthesis (Vickerstaff et al. 2007, Gougoulias et al. 2009).

Early generation TAR include three designs, the Smith total ankle, the Imperial College of London Hospital (ICLH) implant, and St Georg, which were all developed in 1972. The Smith total ankle was a two-component non-constrained type with incongruent articular surface. The tibial and talar components of this prosthesis were made of metal and polyethylene respectively, and were different from almost all other first generation TARs that used the polyethylene for the tibial part and the metal for the talar part (Figure 1-20) (Vickerstaff et al. 2007). The implant demonstrated loosening rates of 14% at 25-month follow-up and 29% at 84-month follow-up. Inherently poor wear and deformation resistance and poor stability were also reported (Giannini et al. 2000).

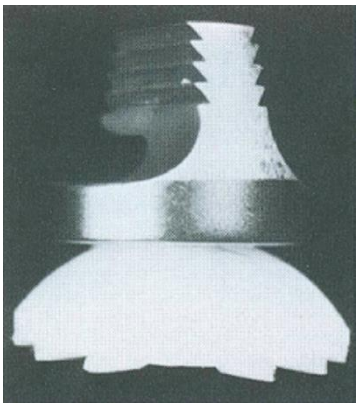

Figure 1-20 The Smith total ankle (Image taken from Vickerstaff et al. 2007, page 1057)

Kempson, Freeman, and Tuke developed the ICLH implant, which was a two-component constrained design with cemented fixation. Only 11 of 62 arthroplasties performed between 1972 and 1981 were reported with satisfactory outcomes at an average follow-up of 5.5 years, and 13 were salvaged using arthrodesis. This prosthesis was discontinued due to major complications including superficial wound healing problems, talar collapse, and loosening of the components (Hintermann 2005, Vickerstaff et al. 2007, Gougoulias et al. 2009). The St Georg, a semi-constrained prosthesis, was developed by Buchholz with the aim to minimise bone resection (Bauer et al. 1996). In 1973, this implant was abandoned after only eight ankle replacements in Sweden due to a high failure rate (Hintermann 2005). There were 11 early and 32 late complications identified with this type of replacement at average ten years of follow-up (Gougoulias et al. 2009).

In addition to the three designs of TAR introduced in 1972, several other TARs were developed during this first decade and are also classified as ‘first generation’ TARs (Giannini et al. 2000, Jackson and Singh 2003, Bonasia et al. 2010). In 1973, the Newton ankle implant, an unconstrained cemented two-component design with incongruous articular surface, was introduced (Figure 1-21). The shape of the articular surface of this prosthesis was different from most other pioneers, which featured a congruous articular surface. The incongruency led to very high polyethylene wear, and consequently discontinuation of use. The New Jersey cylindrical replacement (NJCR) consisted of a cylindrical surface ultrahigh molecular weight polyethylene (UHMWPE) talar component and a mortised cobalt-chromium alloy tibial component using dual fixation fins and cement for stabilisation, and was first implanted in 1974. Again, due to the incongruent design, poor wear performance, poor deformation resistance, and relatively poor inherent

instability were reported. The first three-component TAR was launched in 1978. The low contact stress (LCS) TAR, was evolved from the NJCR by adding a polyethylene mobile-bearing between metallic tibial and talar components (Figure 1-22).

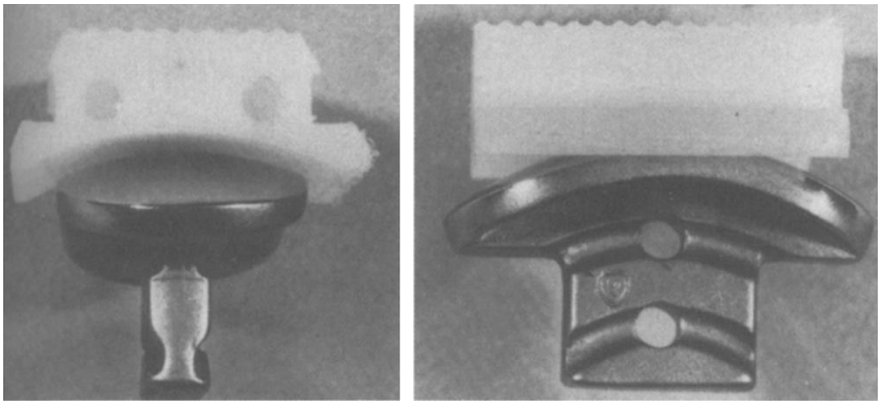

Figure 1-21 The Newton ankle implant (Image taken from Bauer et al. 1996, page 123)

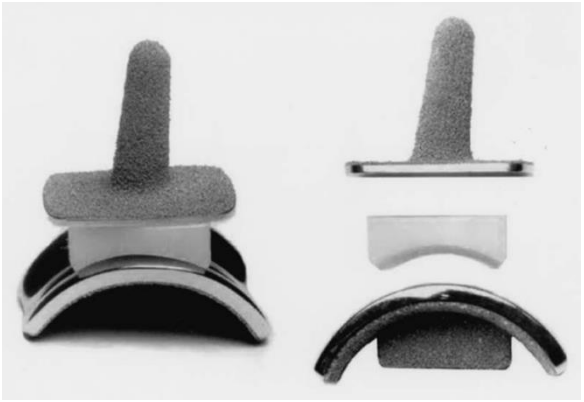

Figure 1-22 The low contact stress (LCS) TAR (Image taken from Buechel et al. 2004, page 20)

The Irvine ankle arthroplasty developed in 1975, a non-constrained type, was one of the few early prostheses that attempted to establish the morphology of the talus based on anatomical measurements of 32 tali. This implant was designed to allow movement in both sagittal and frontal planes and allow axial rotation, however, it was realised that the rotation of the talar component caused separation of the prosthesis and increased stress on the surrounding ligaments. The outcomes included two out of 28 prostheses had failed at nine month follow-up, and wound healing and malalignment problems were also reported (Hintermann 2005, Vickerstaff et al. 2007, Gougoulias et al. 2009).

Almost all first generation of TARs were two-component designs, with the exception of the LCS TAR. Most designs consisted of polyethylene concave tibial components and metallic convex talar components (except in the ICLH implant where the materials were inverted). These designs were either constrained or non-constrained, but all were fixed using a cemented method (Vickerstaff et al. 2007, Bonasia et al. 2010, Van et al. 2010). Poor results and high failure rates were presented for all designs. The constrained designs were associated with high rates of aseptic loosening due to increasing transmitted forces across the bone-prosthesis interface related to inability to dissipate the rotational forces of the prosthesis, while the nonconstrained designs involved instability due to applying of the excessive strain on surrounding soft tissues (Conti and Wong 2001, Bonasia et al. 2010). The cemented fixation, which was the only method available in the 1970s for fixing orthopaedic implants, was a major contributing cause of failure of the first generation of TARs. This procedure required large bone resection to fit both the implant and the cement resulting in rapid decreasing bony strength of both the tibia and the talus (Conti and Wong 2001, Van et al. 2010). These high failure rates led to the abandonment of the first generation of TARs in favour of fusion (Vickerstaff et al. 2007, Bonasia et al. 2010).

1.4.2.2 Second-Generation TARs

The second phase of ankle prosthesis design began in the 1980s with the launch of new designs of TARs (Bonasia et al. 2010). These were developed with cementless fixation, which reduced bone resection, and were designed to replicate the anatomy of the natural ankle. Further benefits of these cementless designs included the potential to reduce damage to surrounding soft tissue due to heat generated during cement setting period (Cook and O'Malley 2001). These cementless designs used a press-fit insertion technique to secure the implant into the bone instead of cemented fixation (Jackson and Singh 2003, Park and Mroczek 2011). The uncemented implant surface was covered in porous beads, normally coated with hydroxyapatite, with the aim of allowing and encouraging bone growth onto the prosthesis to form a solid bone-prosthesis interface as a biologic fixation (Cook and O'Malley 2001, Vickerstaff et al. 2007, Bonasia et al. 2010, Van et al. 2010). Another common feature of second generation prostheses was a semi-constrained design, which overcame clinical problems associated with the constrained and non-constrained devices (Jackson and Singh 2003, Vickerstaff et al. 2007, Bonasia et al. 2010, Seth 2011). Three second generation TARs, the Scandinavian Total Ankle Replacement (STAR), the Agility Total Ankle System, and the Buechel-Pappas Total Ankle Replacement, have demonstrated reasonable functional outcome

and have dominated the market (Easley et al. 2002, Jackson and Singh 2003, Van et al. 2010).

1.4.2.2.1 Scandinavian Total Ankle Replacement (STAR)

The Scandinavian total ankle replacement (STAR) was first introduced in 1978, and first implanted in 1981. This prosthesis was initially an unconstrained congruent two-component design, comprised of a polyethylene tibial component and a metallic talar component initially fixed by cement (Figure 1-23). The survival rate at 12 years was 70% (Kofoed 2004). A development of a polyethylene meniscus led to a design change from two to three-component with a mobile bearing in 1986. This prosthesis was further developed to a non-cemented design with a bioactive surface coating in 1990 (Gougoulias et al. 2009, Van et al. 2010). The UHMWPE mobile bearing articulates superiorly with a flat cobalt chrome (CoCr) tibial plate, and inferiorly with a curved CoCr talar component. This allows a good range of motion, whilst limiting motion at the inferior surface to anterior-posterior translation only. The tibial and talar components are secured to the bones by two and one fins respectively. The anatomically shaped talar component has wings, which replace the degenerate medial and lateral talar facets, allow additional load transfer, and resurface the talar dome (Easley et al. 2002, Vickerstaff et al. 2007, Gougoulias et al. 2009).

Henricson et al. reported that 71 of 303 uncemented STARs and 2 of 15 cemented STARs used in Sweden were revised due to aseptic loosening, technical error, instability, infection, intractable pain, polyethylene breakdown, painful varus, and fracture. Aseptic loosening was the most common reason for revision of this prosthesis (Henricson et al. 2007). The midterm results of 68 prostheses implanted into 65 patients at average 3.7-year follow-up showed 35 patients were totally pain-free, while 14 patients had secondary or additional operations. The overall clinical score was graded as excellent or good in 67 ankles (Valderrabano et al. 2004). Kofoed revealed the results of cemented technique used in 33 patients between 1986 and 1989, and uncemented technique used in 25 patients between 1990 and 1995 at the average 9.4-year follow-up. Nine of 33 patients and one of 25 patients required revision surgery or fusion. The survival rates for 12 years were 70% and 95.4% for the cemented and uncemented groups respectively. The average clinical scores for the cemented group was 74.2±19.3, and the uncemented group was 91.9±7.4 (Kofoed 2004). Both radiographically loose and revision were not found in all seven arthroplasties at 5.4-year follow-up (Wood et al. 2000). Wood et al. reported on 200 uncemented mobile bearing STARs implanted between 1993 and 2000. Eight prostheses required further surgery due to complication, and

14 implants required revision or fusion. The survival rate at five years was 92.7%, and the most frequent complications included delayed wound healing and fracture of malleolus (Wood and Deakin 2003).

Figure 1-23 The Scandinavian total ankle replacement (STAR) (Image taken from Heuvel et al. 2010, page 155)

1.4.2.2.2 Agility Total Ankle System

The Agility total ankle system was first implanted in 1984. This prosthesis was the first TAR to receive FDA (U.S. Food and Drug Administration) approval in 1992, and remained the only FDA approved TAR in the USA until 2007 (Van et al. 2010). This prosthesis is a semiconstrained porous-coated two-component design with fixed bearing. The Agility TAR consists of the modular tibial component, which includes a titanium tibial tray and a concave UHMWPE insert, and a convex CoCr talar component. The articular surface of the tibial component is larger than the articular surface of the talar component allowing axial rotation of the talus (Figure 1-24). To implant this TAR, fusion of the distal tibiofibular syndesmosis is required. This fusion increases the prosthesis-bone interface area of the tibial component to resist subsidence, and allows the fibula to share some of the load (Easley et al. 2002, Vickerstaff et al. 2007, Gougoulias et al. 2009).

Pyevich et al. reported on 100 Agility prostheses that were implanted into 95 patients between 1984 and 1993, but only 86 ankles were available at follow-up. Five ankles required revision and one ankle consequently required fusion. Twelve tibial and nine talar components had migrated, and some of these were consequently revised due to loosening. Twenty-eight ankles experienced delayed union and nine ankles experienced non-union of the syndesmosis.

Forty-seven and 24 of 85 ankles were not painful and mildly painful respectively at the average 4.8-year follow-up, and 79 of 85 ankles were satisfactory (Pyevich et al. 1998). The results of 106 prostheses performed between 1995 and 2001 were reported by Spirt et al.: 85 patients required 127 reoperations and eight patients experienced below-the-knee amputation at an average of 33 months after replacement (Spirt et al. 2004). A study of 132 prostheses, implanted in 126 patients by a single surgeon between 1984 and 1994 with an average follow up of nine years showed 33 patients had died, 14 patients required a revision or a fusion, and one patient experienced the leg amputation due to unrelated cause. 90% of 67 patients followed clinically reported decreasing of pain and satisfactory with the surgery outcome (Knecht et al. 2004). In another clinical study 37 of 38 patients followed up at average 44.5 months reported satisfactory with the outcome of the surgery (Kopp et al. 2006).

Figure 1-24 The Agility total ankle system (Image taken from Heuvel et al. 2010, page 156)

1.4.2.2.3 Buechel-Pappas Total Ankle Replacement

The Buechel-Pappas total ankle replacement, the first reported three-component prosthesis (Gougoulias et al. 2009), evolved from the LCS prosthesis by removing anterior-posterior constraint between the tibial and bearing components in 1989 (Vickerstaff et al. 2007). The Buechel-Pappas was designed to combine mobility and congruency to overcome wear and constraint problems. The talar component was changed from single fin fixation with a shallow sulcus, used in the LCS prosthesis, to two fins fixation with a deep sulcus used in the Mark II model to reduce rate of subsidence of the component. The longitudinal sulcus on the talar component articulates with a matching ridge on the UHMWPE bearing providing stability in medial and

lateral direction, and preventing dislocation. The sulcus also allows some inversion and eversion. The articulation between the tibial and bearing components provides unconstrained movement due to both flat articular surfaces (Figure 1-25) (Easley et al. 2002, Vickerstaff et al. 2007, Gougoulias et al. 2009).

Henricson et al. reported 16 of 92 Buechel-Pappas prostheses used in Sweden since 2000 were revised due to various reasons including aseptic loosening, technical error, instability, infection, intractable pain, polyethylene breakdown, painful varus, and fracture. The most common reason for revision of this implant was instability (Henricson et al. 2007). Giovanni et al. investigated efficacy of 31 Buechel-Pappas TARs implanted in 23 patients with rheumatoid arthritis between 1990 and 1997. Twenty-eight prostheses in 21 patients remained in-situ at an average 8.3 year follow-up because one patient had died and two ankles required fusion. Three patients were dissatisfied with the outcomes of their prostheses, while 18 patients with 25 implants were completely satisfied and experienced only mild to no pain. Radiographic analysis revealed that 23 prostheses were stable and well positioned with evidence of biologic ingrowth, while five implants had risk of imminent failure due to noticeable component subsidence. One ankle showed clear evidence of osteolysis. One of 10 intraoperative medial malleolar fractures had an adverse effect on treatment result. Nine postoperative complications included four wound ruptures, four stress fractures, and one medial malleolar nonunion occurred (San Giovanni et al. 2006). Buechel and colleagues evaluated their two consecutive designs of TAR, New Jersey LCS Total Ankle and Buechel-Pappas Total Ankle, at average 12-year and five-year follow-ups respectively. Both prostheses were cementless, porous-coated, congruent-contact, and mobile-bearing, but difference in their depth of sulcus and quantity of fixation fin of the talar components. There were 38 patients using 40 LCS designs, and 74 patients using 75 Buechel-Pappas designs. Clinical results demonstrated that 70% good to excellent, 5% fair, and 25% poor for the LCS design after 2-20 years of implantation, while 88% good to excellent, 5% fair, and 7% poor for the Buechel-Pappas design after 2-12 years of implantation. The overall survivorship for the LCS prosthesis was 74.2%, while the Buechel-Pappas prosthesis was 92% (Buechel et al. 2004).

Figure 1-25 The Buechel-Pappas total ankle replacement (Image taken from Heuvel et al. 2010, page 155)

1.4.2.3 Modern Designs of TAR

The third phase of TAR development began in the late 1990s with the launch of new designs of cementless three-component mobile bearing TAR including the Salto, HINTEGRA, MOBILITY, and BOX (Bologna Oxford) (Bonasia et al. 2010, Van et al. 2010). There are a wide range of third-generation TARs available on the marketplace worldwide. However, the England and Wales National Joint Registry (2013) reported a total of 549 implants of only nine different models of TAR throughout 2012; these were the MOBILITY, Zenith, BOX, Salto, HINTEGRA, STAR, Rebalance, INBONE, and Taric. Each design is discussed in this section, except the STAR, which has already been discussed, and Rebalance, due to no information being available clinically nor through the manufacturer. There is significant variation in the literature available for each device.

1.4.2.3.1 MOBILITY Total Ankle System

The MOBILITY total ankle system (DePuy International, Leeds, UK) was developed by a team of experienced ankle arthroplasty surgeons and is an uncemented fully congruent three-component prosthesis with a UHMWPE mobile bearing. The tibial and talar components are made of cobalt chrome and are porous coated. The articular surface of the tibial component is a flat surface, while the articular surface of the talar component is a deep sulcus. The tibial and talar components are fixed to the bones using a short conical intramedullary stem and two short deep anterior fins respectively (Figure 1-26) (Gougoulias et al. 2009, Wood et al. 2010, Sproule et al. 2013, Summers and Bedi 2013).

Summers et al. evaluated 58 prostheses implanted into 56 patients at the time of follow-up of average 32 months. The results demonstrated a relatively high rate of reoperation of 18 at a mean of 14 months mainly due to painful impingement, and eight of these underwent a second reoperation. Seven out of 58 ankles required revision, and four out of seven consequently required fusions due to aseptic loosening or chronic pain (Summers and Bedi 2013). In a clinical study of 100 prostheses, implanted in 96 patients, 94 were available for follow-up. Five out of 94 ankles required revision at six, 33, 34, 36, and 45 months with various reasons, and two consequently required fusion. The three-year and four-year survivals were 97% (91 ankles reviewed) and 93.6% (47 ankles reviewed) respectively (Wood et al. 2010). In the study by Muir et al., 178 prostheses performed by three surgeons between January 2004 and June 2009 were reviewed. Ten out of 178 ankles required revision, and two of the revised implants consequently required fusion (Muir et al. 2013). Sproule and colleagues investigated 88 prostheses implanted in 85 patients, and found that 10 of 88 ankles failed. Eight of 10 failures required revision due to various reasons including aseptic loosening of the tibial component (six ankles), talar migration (one ankle), and deep infection (one ankle). One failed prosthesis was converted to an arthrodesis due to malposition of component during edge-loading, and another underwent transtibial amputation due to chronic regional pain syndrome (Sproule et al. 2013).

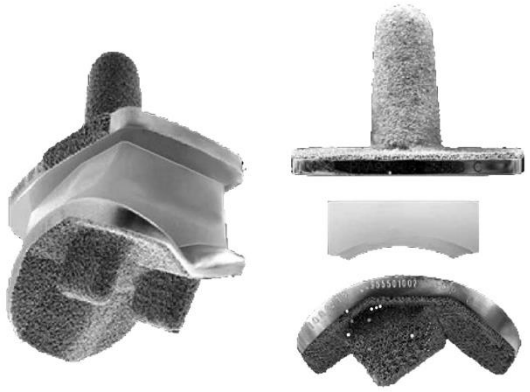

Figure 1-26 The MOBILITY total ankle system (Image taken from Wood et al. 2010, page 959)

1.4.2.3.2 Zenith Total Ankle Replacement

The Zenith total ankle replacement (Corin, Cirencester, UK) is an uncemented three-component prosthesis with a mobile bearing. This implant has evolved from the Buechel-Pappas total ankle replacement. The tibial and talar implant surfaces are coated by BONIT coating to encourage bone on-growth (Figure 1-27) (Gougoulias et al. 2009, Millar and Garg 2013).

Millar et al. evaluated 50 cases including 48 patients with osteoarthritis and two patients with rheumatoid arthritis, with an average follow-up of 30 months. One patient had died at 25 months following surgery from unrelated causes. There was one peri-operative malleolar fracture, which required fixation, and one fracture of the lateral malleolus highlighted at the six-week follow-up, which was treated non-operatively. 46 patients were satisfied and four patients were unsatisfied with the outcome of surgery. This study also demonstrated that the visual analogue scale (VAS) for pain and the American Orthopaedic Foot and Ankle Society (AOFAS) score had improved significantly (Millar and Garg 2013).

Figure 1-27 The Zenith total ankle replacement (Image taken from Mckenzie et al. 2012, page 1)

1.4.2.3.3 BOX Total Ankle Replacement

The BOX total ankle replacement (Finsbury Orthopaedics, Leatherhead, Surrey, UK), developed in collaboration with the Rizzoli Orthopaedic Institute, Bologna, Italy and the University of Oxford, is an uncemented three-component mobile bearing prosthesis. The tibial component has a lower spherical convex shape, and the talar component has an upper anticlastic shape. The meniscal component is bi-concave and fully conforming with the corresponding tibial and

talar surfaces. The tibial and talar components are fixed to the bones using two parallel cylindrical bars and two pegs respectively. Fixation surfaces of both components are porous coated with hydroxyapatite (Figure 1-28). The designers claim that the implant maintains complete congruency throughout arc of motion and closely resembles biomechanics of normal ankle (Gougoulias et al. 2009, Ingrosso et al. 2009, Giannini et al. 2011).

Giannini and colleagues evaluated 158 prostheses implanted in 156 patients at an average follow-up of 17 months. Seven out of 158 ankles required further secondary operations, and two cases required revisions at two and three years following surgery. The AOFAS score of 36.3 rose to 74.7, 78.6, 76.4, and 79.0 at 12, 24, 36, and 48 months respectively (Giannini et al. 2011). Giannini and collaborators also investigated 70 TARs implanted in 68 patients between July 2003 and April 2008 at an average follow-up of 6.4 years. Two out of 70 ankles required revision. The pre-operative AOFAS score of 38.4 rose to 77.9 at last follow-up (Giannini et al. 2013). In the study by Bianchi et al., 62 TARs implanted in 60 patients between 2004 and 2008 were reviewed at average follow-up of 42.5 months. Out of 62 TARs, five ankles required revision, and four out of five revisions consequently required fusions. The overall survival was 91.9%, and the AOFAS score of 35.1 pre-operatively rose to 78.0 at final follow-up (Bianchi et al. 2012).

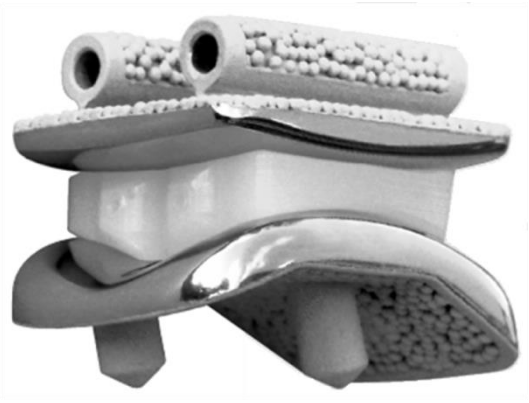

Figure 1-28 The BOX total ankle replacement (Image taken from Giannini et al. 2013, page 2)

1.4.2.3.4 Salto Total Ankle Prosthesis

The Salto total ankle prosthesis (Tornier, Saint Ismier, France) is an uncemented three-component prosthesis with an UHMWPE mobile bearing. The tibial and talar components are made of cobalt chrome and are porous coated by titanium and hydroxyapatite. The tibial component has a flat surface and a medial rim to prevent prosthetic impingement on the medial malleolus. The talar component replicates the anatomy of the talar dome, and covers the lateral aspect of the talus to articulate with either lateral malleolus or an optional cemented polyethylene lateral malleolar component. The meniscal bearing maintains full congruency with the corresponding tibial and talar surfaces in dorsiflexion and plantar flexion (Figure 1-29) (Bonnin et al. 2004, Gougoulias et al. 2009, Reuver et al. 2010, Bonnin et al. 2011).

Reuver and colleagues evaluated 64 prostheses implanted in 60 patients between 2003 and 2007. There were 59 TARs in 55 patients available at a time of follow-up of average 36 months. Seven out of 59 ankles required revisions due to aseptic loosening (five TARs) and deep infection (two TARs), and five out of seven revised ankle consequently required fusion. The mean AOFAS score was 75, and the overall survival rate with revision or ankle fusion as the end point was 86% at final follow-up (Reuver et al. 2010). Bonnin and collaborations reviewed 98 prostheses implanted in 96 patients between 1997 and 2000. There were 87 prostheses in 85 patients available at a time of follow-up of average 8.9 years. Six ankles were converted to fusions, and 18 ankles required reoperation without fusion. The common reasons for reoperation included bone cysts, fracture of the polyethylene, and unexplained pain. The survival rate was 65% with any reoperation of the ankle, and 85% with revision of a component as the end point. The mean AOFAS score was 79 at last follow-up (Bonnin et al. 2011). In the study by Nodzo et al., 75 prostheses implanted in 74 patients between January 2007 and April 2011 were evaluated at a time of follow-up of average 43 months. Of a total of 74 patients, 13 required reoperations with a total of 18 procedures performed. There was one patient required revision at three years following surgery, and no one required arthrodesis. The survival rate was 68% with any reoperation of the ankle, and 98% with revision of a component as the end point (Nodzo et al. 2014).

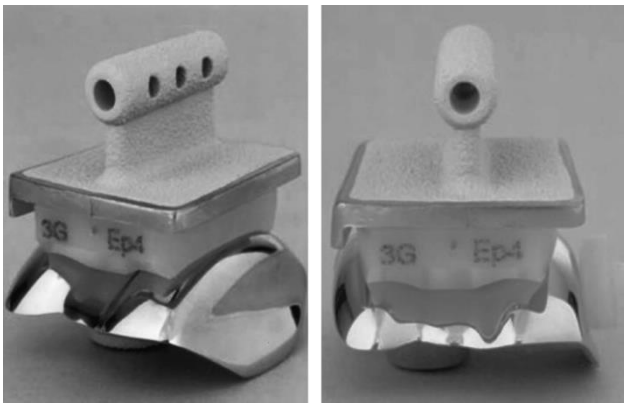

Figure 1-29 The Salto total ankle prosthesis (Image taken from Bonnin et al. 2004, page 7)

1.4.2.3.5 HINTEGRA Total Ankle Prosthesis

The HINTEGRA total ankle prosthesis (Integra LifeSciences/Newdeal, Lyon, France) is an uncemented non-constrained three-component mobile bearing prosthesis. The tibial component has a flat surface with pyramidal peaks on the fixation surface against the tibia, and an anterior shield for screw fixation, differing from other ankle systems that typically use intramedullary fixation. The talar component has a conical articulating surface with a larger lateral radius, and medial and lateral rims providing stability for meniscal bearing. The talar component also has anterior shield for placement of screws. Two pegs have been added to the fixation surface against the talus to maximise contact area. Both metallic components are coated with titanium and hydroxyapatite. The mobile bearing has a flat surface to the tibial side and a concave surface perfectly matching the talar surface (Figure 1-30) (Hintermann et al. 2004, Gougoulias et al. 2009, Hintermann et al. 2013).

Hintermann and collaborators evaluated 122 prostheses implanted in 116 patients at a time of follow-up of average 18.9 months. Of a total of 122 ankles, eight required revisions due to various reasons including loosening of component, impingement, dislocation of meniscal component, and pain and stiffness. The pre-operative AOFAS score of 40 rose to 85 at last follow-up. Patients were satisfied with 102 TARs, and unsatisfied with four ankle replacements. Eighty-three ankles were completely pain-free (Hintermann et al. 2004). In the study by Barg et al., 779 prostheses implanted in 741 patients between May 2000 and July 2010 were evaluated. There were 722 TARs in 684 patients available at an average follow-up of 6.3 years. Of a total of 722 ankles, 61 required revision arthroplasties and seven out of 61 prostheses were

consequently converted to arthrodesis. The overall survival rates were 94% and 84% after five and ten years respectively (Hintermann et al. 2013).

Figure 1-30 The HINTEGRA total ankle prosthesis (Image taken from http://www.integralife.eu [cited 19 Dec 2013])

1.4.2.3.6 INBONE Total Ankle Replacement

The INBONE total ankle replacement (Wright Medical Technologies, Arlington, TN) is a fixed bearing two-component design with a modular stem for both the tibial and talar components. Several small interconnecting segments are used to form the tibial stem, and the quantity of segments corresponds to stability of the components. Usually, four segments are used. The talar component is a saddle-shaped prosthesis resembling anatomy of superior articular surface of the talar body. The polyethylene bearing is locked into the tibial baseplate to prevent increased wear in comparison with mobile bearing designs, and to prevent dislocation of polyethylene (Figure 1-31). This prosthesis was approved for used by the FDA in 2005 (DeOrio 2010, Ellis and DeOrio 2010, Datir et al. 2013, Scott et al. 2013).

Datir and collaborators evaluated this prosthesis implanted in 30 patients, and reported 23 out of 30 patients had a successful clinical outcome with intact prosthesis at a follow-up of two years. Seven had failed due to deep wound infection or subsidence of the talar component. One patient with failed TAR was lost to follow-up, and six patients consequently required ankle fusions (Datir et al. 2013).

Figure 1-31 The INBONE total ankle replacement (Image taken from Ellis and DeOrio 2010, page 202)

1.4.2.3.7 Taric Ankle System

The Taric ankle system (Implant Cast, Buxtehude, Germany) is a cementless mobile bearing prosthesis. The tibial and talar components are porous coated by titanium and hydroxyapatite, and both components are fixed to the bones using two convergent fins. No clinical results are available (Figure 1-32) (Gougoulias et al. 2009).

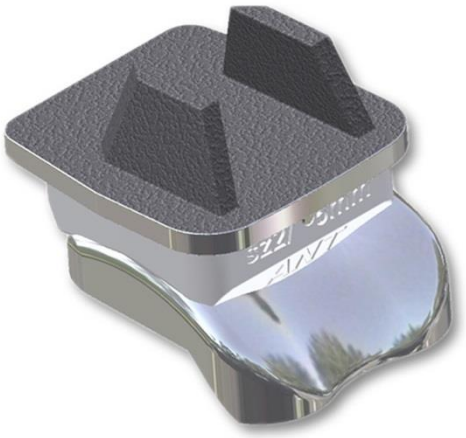

Figure 1-32 The Taric ankle system (Image taken from http://www.implantcast.de [cited 19 Dec 2013])

1.4.3 Discussion of TAR Design, Usage, and Outcomes

The number of primary ankle procedures performed in each year reported by the National Joint Registry (NJR) for England, Wales, Northern Ireland, and the Isle of Man is illustrated in Figure 1-33.

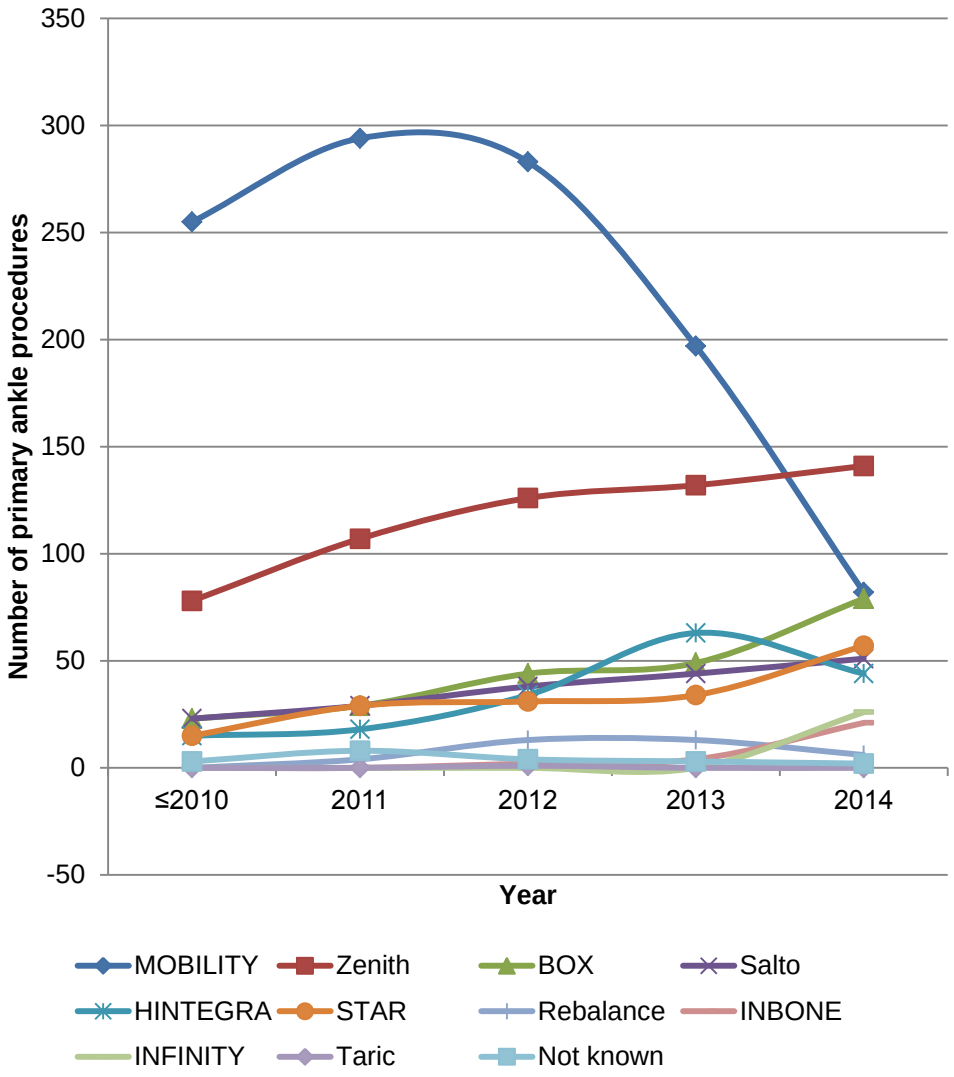

Figure 1-33 Number of primary ankle procedures performed in each year

The NJR also reported the number of revision ankle procedures performed in each year between 2011 and 2014 which are shown in Table 1-1. Forty-nine of the 2,554 reported procedures had been revised before the end of 2014, and their indications for revision are also shown in Table 1-2.

Table 1-1 Number of revision ankle procedures performed each year from 2011 to 2014, as reported in the National Joint Registry for England, Wales, Northern Ireland, and the Isle of Man (http://www.njrcentre.org.uk)

TAR model	Number of revision ankle procedures performed in each year			
	2011	2012	2013	2014
MOBILITY	4	10	5	3
Salto	1	-	-	-
Zenith	-	3	2	6
HINTEGRA	-	1	1	-
STAR	-	-	-	3
INBONE	-	-	-	2
BOX	-	-	-	1

Table 1-2 Indications for the 49 first revisions following primary ankle replacement for the procedures shown in Table 1-1

Indication		Number
Infection	High suspicion	1
	Low suspicion	12
Aseptic loosening	Tibial component	10
	Talar component	11
Lysis	Tibia	3*
	Talus	2*
Malalignment		7
Implant fracture	Tibial component	0
	Talar component	2
	Meniscal component	0
Wear of polyethylene component		1
Meniscal insert dislocation		1
Component migration/dissociation		3
Pain (undiagnosed)		16
Stiffness		9
Soft tissue impingement		7
Other indications for revision		12

*One patient had lysis of both tibial and talar component

The three-component TAR is the most common design chosen for implantation in this region, and the two most common ankle prostheses are the MOBILITY total ankle system and the Zenith TAR. The use of the MOBILITY total ankle system has reduced sharply since 2012, while the Zenith TAR has increased gradually each year. Aseptic loosening of both tibial and talar components has

been reported in the NJR as a reason for ankle revision in high numbers every year.

There are a lot of different designs of TAR (as shown in the figures in Section 1.4.2) on the marketplace worldwide. Each design feature has both pros and cons. For example, the constrained design provides better stability but increases transmitted forces across the bone-implant interface leading to loosening of the component; the non-constrained prosthesis provides better range of motion but applies excessive strain on surrounding soft tissues leading to ankle instability; and the incongruent articular surface may also provide a good range of motion but is poor in terms of wear and stability. The modern trend in ankle prosthesis design is attempting to balance between constrained and non-constrained approaches to reduce such complications. Therefore, almost all modern TARs are of a similar semi-constrained type. However, there has not been convergence to a single design concept. In particular, the method of attachment of the TAR components varies widely, especially in the tibial component.

Newer designs seem to have better clinical outcomes but are still less successful than hip/knee replacements. As reported in Section 1.4.2, aseptic loosening, subsidence, and bone fracture are common causes of failure. Malpositioning is also reported in some cases (Table 1-3). Excessive constraint may be a dominant factor in aseptic loosening. For example, the STAR has a feature at the articular surface between the bearing and talar components to prohibit some motions, the socket-like articular surface of the tibial component of the Agility total ankle system limits some motions of the talar component, and the rim feature on the tibial and talar components of the Salto and HINTEGRA total ankle prostheses respectively are used to limit the movements of the mobile bearing. These designs have all faced the problem of aseptic loosening. Inadequate fixation may be a main factor in subsidence. It was reported that the two fin fixation was used instead of a single fin fixation for the talar component of the Buechel-Pappas TAR specifically to reduce the rate of subsidence. The design of the fixation therefore needs not only to distribute loads to prevent subsidence, but also to appropriately cope with the degree of constraint to prevent loosening. Therefore, the bone-prosthesis interface is an important factor that may influence success or failure of the implant.

Table 1-3 Complications following implantation in various designs of TAR

TAR model	Design feature	Complication					
		Infection	Aseptic loosening	Polyethylene wear	Pain	Soft tissue impingement	Instability
Smith	Non-constrained, incongruent		✓	✓			✓
ICHL	Constrained		✓				
Newton	Non-constrained, incongruent			✓			
NJCR	Incongruent			✓			✓
Irvine	Non-constrained					✓	
STAR	Non-constrained, congruent	✓	✓	✓	✓		✓
Agility	Semi-constrained		✓	▪			
Buechel-Pappas	Non-constrained, congruent	✓	✓		✓		✓
MOBILITY	Non-constrained, congruent	✓	✓		✓	✓	
Salto	Non-constrained, congruent	✓	✓	✓	✓		
HINTEGRA	Non-constrained		✓		✓	✓	
INBONE	Non-constrained	✓			▪		

1.5 Finite Element Analysis in Total Ankle Replacement

The finite element method (FEM) plays an important role in computational analysis of the characteristics of complex structures and components in a wide variety of engineering problems. In orthopaedics, the FEM was initially used to evaluate stresses in human bones in the 1970s, and has been increasingly applied for the analysis of stress in various kinds of tissues and orthopaedic devices since then (Huiskes and Chao 1983).

1.5.1 Introduction to the Finite Element Method

The FEM is a numerical technique used to obtain approximate solutions of boundary value problems for the analysis of structures and continua in engineering (Hutton 2004, Jagota et al. 2013). It is often used to deal with complicated problems which cannot be satisfactorily solved by classical analytical methods. The method produces a number of simultaneous algebraic equations that usually require a computer to generate and solve. The results obtained from finite element analysis (FEA) are rarely exact, but they can be accurate enough for engineering purposes to be obtained at reasonable price. By processing more equations, the errors can be reduced but the computational expense may be increased.

The advantage of the FEM is its versatility that can be applied to various physical problems. Different types, shapes, and physical properties of elements can be meshed together, and the arbitrary shape, loads, and boundary conditions of the FE model can be analysed within a single FEA software package under many different conditions which are controlled by the user to quantify the desired analytical values (Cook et al. 1989).

1.5.2 General Description of the Finite Element Method

The finite element procedure divides the structure into smaller sections known as (finite) elements. The main characteristics of each finite element are represented in the element stiffness matrix. The stiffness matrix contains the information, such as geometry and material properties, that indicates the resistance of the element to change when subjected to external influences (Hutton 2004). The field variables are the basic unknowns in the engineering problems, which are the displacements of the structure in solid mechanics. If they are found, the behaviour of the whole structure can be predicted. The unknown field variables are expressed in terms of assumed approximating functions (interpolating functions) within each element with the aim of reducing an infinite number of unknowns to a finite number. The approximating functions

are defined in terms of the field variables at specified points known as nodes. The step of determining the element properties can be done by formulating the stiffness characteristics of each element. Mathematically this relationship is of the form

$$[k]_e\{\delta\}_e = \{F\}_e$$

where $[k]_e$ is element stiffness matrix, $\{\delta\}_e$ is nodal displacement vector of the element, and $\{F\}_e$ is nodal force vector. Each element stiffness matrix needs to be assembled into a global stiffness matrix to get system equations $[k]\{\delta\} = \{F\}$ representing the whole structure. Any boundary conditions then need to be taken into account. The simultaneous equations that make up the global stiffness equation can then be solved using mathematical techniques such as Gauss-elimination or Choleski's decomposition techniques. The resulting solutions will give the nodal displacements, from which additional calculations can be performed to quantify the required values, such as stresses, strains, etc., in the structure (Bhavikatti 2005).

1.5.3 Finite Element Analysis in Orthopaedic Applications

The FEM was first introduced in the orthopaedic literature in 1972 as a new method for studying the mechanical behaviour of a femur (Huiskes and Chao 1983). The results of this study indicated that the complex geometry and the variety of load situations posed no problems in analysis by the FEM (Brekelmans et al. 1972). Since then, this method has been increasingly used for analysing stress in bones, bone-prosthesis structures, fracture fixation devices, and various kinds of tissue other than bone. In most cases, the aims have been to investigate the relationships between load carrying functions and morphology of the tissues, and to optimise designs and fixation techniques for implants (Huiskes and Chao 1983).

Certain steps for analysis in orthopaedics using the FEM are common to all other types of FE analyses; these include the preprocessing, solution, and postprocessing phases. The preprocessing step is critical. The geometric and material properties, loadings, boundary conditions, element types, and meshes are defined in this step. The formulation in this step needs to be carefully performed because it affects the accuracy of the results significantly. During the solution phase, the FEA software generates algebraic equations in a matrix form and computes to quantify the desired values. The obtained analytical results are sorted, printed, and plotted in the postprocessing stage, where the solutions can be checked to ensure they are physically reasonable (Hutton 2004). Recommendations, which include verification, sensitivity studies, and validation, have been made for checking the validity of FE models in this field

(Henninger et al. 2010). Verification is the process of investigating that the computational implementation of the mathematical model and its associated solution are correct. Mesh convergence studies, which are a subset of verification, are recommended for reducing errors involved discretisation. If a change in solution output due to different discretisation (e.g. a doubling of the number of elements) is less than a predefined amount, dependent on the application, then the mesh convergence study can be assumed to be complete. Sensitivity studies are usually the procedures for determining the influence of material properties on the model predictions, which can be generally performed by sequentially altering a single material parameter. If the results are not changed significantly due to the difference in a given input parameter, the simulations can be identified as being insensitive to changes in that input. Conversely, a parameter that affects the output dramatically should be investigated to ensure appropriate characterisation. Validation is the process of investigating how accurately a model represents the physics of the real-world system, which can be performed either directly or indirectly. Although this procedure is often the most laborious aspect of computational analysis, it can ensure that the model predictions are robust (Henninger et al. 2010).

1.5.3.1 Finite Element Analysis in Total Ankle Replacement

Only a few published papers related to FEA of total ankle replacement are available compared to FEA on total hip and knee replacements. The ankle FEA studies can be mainly divided into two groups: those that model just the TAR and those that model the TAR and bone, with the objective being to investigate the failure mechanisms of TARs. The analysis of the failure of implantation due to the bone damage requires both bone and prosthesis to be modelled, while the bone may not be necessary for analysis of the prosthesis failure. In addition, there have been a limited number of studies that have analysed the natural ankle bones on the basis of FEM. For example, Bandak and collaborators developed an FE model of the human lower leg to investigate injury mechanisms of the major bones of the foot (Bandak et al. 2001), Anderson and collaborators used FEA to investigate contact stress distributions across the articular surface of ankle joint (Anderson et al. 2007), and Parr and collaborators developed two different FE models of the talus to reveal the influence of the trabecular bone on the mechanical performance (Parr et al. 2013).

When approaching the FEA, a number of factors that might significantly affect accuracy of the analysis results should be taken into account. Almost all of the critical factors are formulated in the preprocessing step including the geometric

and material properties, loadings, boundary conditions, element types, and meshes. These factors are discussed below. This section will focus on FEA studies of the ankle, but since a greater amount of work using the FEM has been undertaken in the analysis of hip and knee replacements, additional examples from these fields are also described.

1.5.3.1.1 Geometric Properties

Taddei and collaborators highlighted in their study that the errors in the geometric representation of the bone are always the dominant factors in the error in the predicted stresses (Taddei et al. 2006). To maintain the similarity to the skeletal object, the 3-D models used in several studies have been constructed from medical imaging data. To create the 3-D models of the bones, three common steps are required: extracting the contour of the bone from the medical imaging data slices, interpolating contour to obtain the surface, and meshing the surface (Taddei et al. 2006). In FE studies of the ankle, the 3-D data of a human tibia in the study of Terrier and collaborators was created using CT scanned images (Terrier et al. 2014). This approach has become more common place in studies of hip and knee replacement. For example, the solid models of the femur, patella, tibia, and fibula in the study of Halloran and collaborators were generated from a CT from the National Library of Medicine's Visible Human Project® (Halloran et al. 2005), and the 3-D models of tibial, femoral, and patellar bones in the study of Baldwin and collaborators were manually extracted from MR images by segmentation with the aid of image processing software (Baldwin et al. 2012). In other studies of the ankle, 3-D models of the ankle bones have been created based on direct measurement. For example, geometries of tibial cortical and cancellous bones in the study of Falsig and collaborators were constructed using the outline data measured directly from cross section of cadaveric bone at eight positions along the periphery (Falsig et al. 1986), and a total of 27 cross sections of cadaveric ankle bones were optically scanned to identify endosteal and periosteal boundaries for creating cortical and cancellous bones of tibia and fibula in the study of Miller and collaborators (Miller et al. 2004). Although the latter authors intended to investigate only the stresses in two different designs of polyethylene liner, the geometry of tibial bone was also created to mimic tibio-fibula load distribution. Moreover, a reverse-engineering technique may be required to create 3-D models of orthopaedic devices to maintain the similarity to the components where no computer-aided design (CAD) data is available. This technique was mentioned in generating the geometries of two different types of TAR prosthesis in the study of Espinosa and collaborators (Espinosa et al. 2010).

1.5.3.1.2 Material Properties

It is necessary to accurately assign the material properties to the FE model corresponding to the situation under consideration. Almost of all material properties for the metal components of the prosthesis are assumed to be linear, homogenous, and isotropic, however, the behaviors of the polyethylene inserts have been assigned non-linear material properties. The UHMWPE meniscal bearings in both studies of Reggiani and Espinosa and their collaborators were modeled as an elastic-plastic continuum (Reggiani et al. 2006, Espinosa et al. 2010), while the same material was defined as viscoelastic in the study of Elliot and collaborators (Elliot et al. 2014). The material properties of bones are non-linear, heterogeneous, and orthotropic, however, in several of the ankle FEA studies, the material properties of cortical bones are assumed to be homogenous and isotropic, as shown in Table 1-4.

Table 1-4 Parameters used in finite element analysis studies in total ankle replacement

Study	Geometry	Bone		Structure of material	Material properties		FE model	
		Site	Type		E (Gpa)	v	Element type	Load
Falsig et al. 1986		Tibia	Cortical	Homogeneous, Isotropic	15	0.28	8-node isoparametric	Theoretical
			Cancellous		0.3	0.32		
Chu et al. 1995		Bone	Cortical	Homogeneous, Isotropic	14*	0.35	Solid	Theoretical
			Cancellous		14*	0.35		
		Ligament			0.0115		Truss	
Miller et al. 2004	Digitiser	Tibia	Cortical	Homogeneous, Isotropic	17.58	0.3		Theoretical
			Cancellous		0.28	0.3		
		Fibula	Cortical		17.58	0.3		
			Cancellous		0.28	0.3		
Cheung et al. 2006	MRI	Bone	Cortical	Homogeneous, Isotropic	7.3*	0.3	Tetrahedral	Experimental
			Cancellous		7.3*	0.3		
		Cartilage			0.01	0.4		
		Ligament			0.26		Truss	
Terrier et al. 2013	CT	Tibia		Heterogeneous, Isotropic	Equation	0.3	Tetrahedral	
Ozen et al. 2013	CT	Bone	Cortical	Homogeneous, Isotropic	7.3*	0.3	Tetrahedral	Theoretical
			Cancellous		7.3*	0.3		
		Cartilage			0.01	0.4		
		Ligament			0.26	0.4	Truss	

*A common material property is used for both cortical and cancellous bones

For example, in the study of Falsig and collaborators, cortical bone was assumed to be homogeneous, isotropic, and linearly elastic, while cancellous bone was considered to be either homogeneous or heterogeneous (Falsig et al. 1986). The results were found to be affected by the heterogeneity, with lower stress in the heterogeneous model. The material properties of both cortical and cancellous bones in the study by Miller and collaborators were assumed to be homogeneous, isotropic, and linearly elastic (Miller et al. 2004), while the mechanical properties of both cortical and cancellous bones in the study by Terrier and collaborators were assigned on the basis of heterogeneity and isotropy (Terrier et al. 2014). To assign heterogeneous material properties of bones, CT scanned images are necessarily required. A common procedure to define material properties to the bones is to assign them element by element, depending on the bone density which is derived from the intensity of the greyscale of the pixels in the medical imaging data (Sawatari et al. 2005, Tuncer et al. 2013). The element-specific method is usually based on a single CT scan, so this method represents only one specific patient. This method is therefore good for validation against an experiment on the same specimen, but may not be representative of a wider population where each patient's bone density distribution may vary. In some studies, bones were assigned to be an orthotropic material such as the studies of Asgari and van Jonbergen and their collaborators. In addition to the Young's modulus and Poisson's ratio, the shear modulus is necessarily required to model this type of mechanical behavior of material (Asgari et al. 2004, van Jonbergen et al. 2012). Alternatively, components which are much stiffer than others and whose output variables are not the focus of the study, may be modeled as rigid bodies to reduce computational expense. For example, metal prosthesis components in both studies of Reggiani and Terrier and their collaborators were meshed with rigid quadrilateral elements (Reggiani et al. 2006, Terrier et al. 2014).

1.5.3.1.3 Element Choices

The selection of element type and size to represent the entire FE model corresponding to the desired situation is critical. There are no specific criteria for reference, since the choice is dependent on the model, loading scenario, and application. Triangular and tetrahedral elements used in many automatic meshing algorithms are geometrically versatile which can be used to mesh a complex shape conveniently, and they have widely been used in FE models of the ankle (as shown in Table 1-4). In the study of Miller and collaborators, the metallic prosthesis component and cancellous bone were meshed using ten-node tetrahedral elements, while the cortical structure was represented by four-node quadrilateral shell elements with a thickness of 1.0 mm. The polyethylene

liner was modeled using eight-node hexahedral elements (Miller et al. 2004). Eight-node hexahedral elements were initially used to mesh the mobile bearing in the study of Reggiani and collaborators, but consequently changed to tetrahedral elements because it was found easier to mesh (Reggiani et al. 2006). Quadratic 10-nodes tetrahedral elements were used to mesh the bone model in the study by Terrier and collaborators (Terrier et al. 2014).

It is known that in general the coarser the mesh is, the shorter the analysis duration is, but there is inherent loss of accuracy compared to a finer mesh. A mesh sensitivity study is usually used to quantify influence of mesh density on the analysis output (Henninger et al. 2010). An outcome of this procedure is to establish how fine a mesh needs to be for a particular model and is useful in supporting the decision of the selection of element size. Mesh convergence studies were reported by almost all authors in their published papers of the ankle FEA. For example, five different mesh schemes were analysed and compared for mesh sensitivity study in the study of Terrier and collaborators, while a similar test was not examined in the study of Falsig and collaborators due to reasons of economy (Falsig et al. 1986, Terrier et al. 2014). Acceptable percentage differences of stress output obtained between the FE model with chosen element size and the FE model with further mesh refinement in the studies of Miller and Elliot and their collaborators were less than 3% and 5% respectively (Miller et al. 2004, Elliot et al. 2014).

1.5.3.1.4 Boundary Conditions and Loads

Taddei and collaborators found that, among all the variables, the analysis results seemed to be highly dependent on the loading condition (Taddei et al. 2006). In the ankle FEA studies, loading and boundary conditions have been applied to represent either physiological conditions or a parallel experimental set-up. In the study of Miller and collaborators, the tibial component of a fixed bearing TAR was fully bonded into the tibia, which was connected to the fibula using two beam elements to mimic a fusion. All nodes of the tibial and fibular bones were constrained only in transverse plane, while the talar component was fixed in all directions. A load of five times body weight, which was assumed to be the maximum load applied to the joint during normal gait, was applied to the proximal ends of the tibia and fibula (Miller et al. 2004). Similarly, in the study of Espinosa and collaborators, the talar component was fully fixed at four different positions corresponding to four distinct phases of gait cycle, while allowing translational degree of freedom along the axis of the stem for the tibial component. Axial loads corresponding to each posture were collected from the literature and applied onto the tibial component in the normal direction

(Espinosa et al. 2010). In the study of Terrier and collaborators, a FE model was created corresponding to an experiment for a validation purpose. The construct was inverted, which was different from the real-world condition. The proximal part of the tibia was fully constrained, and an axial compressive force was applied through a point rigidly linked to the tibial component (Terrier et al. 2014). Contact properties between the metal and polyethylene component were assigned to be either frictionless or coefficient of friction of 0.04 in the study of Reggiani and collaborators, and either hard contact or normal penalty with coefficient of friction in a range of 0.12-0.15 depending on material types in the study of Elliot and collaborators (Reggiani et al. 2006, Elliot et al. 2014). However there has been limited evaluation of the sensitivity of the results to the boundary conditions and loads applied. Only a little detail, related to a study of five different loading positions, was reported in the study of Falsig and collaborators (Falsig et al. 1986).

1.5.3.1.5 Study Aims and Findings

Finite Element Analysis for Investigating Damage to Bone

Falsig and collaborators used FEA to evaluate three new different concepts of design of cemented tibial component to investigate their effects on bones. The normal and shear stresses on trabecular bone were found to be much reduced by an additional long intramedullary peg that bypass stresses to the cortical bone (Falsig et al. 1986).

Terrier and collaborators developed a FE model of TAR for future testing of hypotheses related to clinical issues. The objective reported in this initial published paper was to validate their model using a corresponding experimental study. The longitudinal and transverse strains on the outer surface of the tibial cortical bone were collected for validation using the corresponding experimental data, and the same strain types together with von Mises stress throughout the tibial bone were also collected to investigate the effect of the misalignment of the polyethylene insert (Terrier et al. 2014).

These two studies investigated either stress or strain applied directly onto the bone that was the effect of either different design of prosthesis or different position of implantation. The output variable obtained was able to be used for further prediction of risk of bone damage due to excessive stress or strain that can lead to success of failure of implantation.

Finite Element Analysis for Investigating Damage to Prosthesis

Although Miller and collaborators intended to investigate only the stresses in two different designs of polyethylene liner, the geometry of tibial bone was also

created to mimic tibio-fibula load distribution. This was different from other studies to investigate only the damage to prosthesis component. Two TAR model with different designs of talar component were created. As a result, the talar component with a wider articular surface was found to be able to reduce the stress on the polyethylene component (Miller et al. 2004).

Reggiani and collaborators developed a FE model of mobile bearing TAR that was able to be used for investigating overall kinematics, contact pressures, and ligament forces during functional activities. Consequently, the predictions of overall kinematics were found to be in good agreement with corresponding *in vivo* measurements. Contact pressures on both articular surfaces of the meniscal bearing were determined at several phases during the gait cycle, and most ligament reaction forces were found to be within corresponding physiological ranges (Reggiani et al. 2006).

Espinosa and collaborators developed two different FE models of TAR (two-component and three-component) to mainly investigate the contact pressures which were affected by component misalignment. For the misalignment of components, three possible and potentially important cases were identified. These included inversion-eversion of the tibial and talar components and external rotation. As a result, the three-component design showed lower contact pressures in the normal position, and was relatively less sensitive to misalignment (Espinosa et al. 2010).

Elliot and collaborators investigated contact stresses on polyethylene liners of seven different designs of TAR at various phases during the gait cycle for calculating wear rates. An equation for calculating wear rate was derived from Hertzian contact theory together with Archard wear law. Consequently, the important geometric parameters of TARs that affect the stress and wear were identified, which was useful for optimizing the design of a new generation of TARs (Elliot et al. 2014).

These four studies investigated either stress or contact pressure applied directly onto the polyethylene bearing and the effects of either different designs of prosthesis, different postures of the ankle, or different positions of implantation. The output variable obtained was able to be used for further prediction of the risk of polyethylene damage due to excessive stress or contact pressure, which could cause the success or failure of the implantation.

1.5.4 Discussion

There have been only a few studies of TARs compared to total hip and knee replacements, therefore, understanding of mechanisms by which TAR devices fail is also limited to date. FEA may provide insight into the reasons for failure under different patient and surgical conditions. In a development process of a FE model of TAR with natural ankle bone, the geometry of the bone is challenging to model, but image-based approaches are becoming more commonplace and may provide a solution. Several input parameters, such as material properties, boundary conditions, loads, and element choices, can have a dominant effect on the analysis results. Different material properties have been applied as shown in Table 1-4, and the bone has been assumed to be either homogenous or heterogeneous. An element-specific method for modeling non-homogenous bone is usually based on a single CT scan, so this method represents only one specific patient. This method is therefore good for validation against an experiment on the same specimen, but may not be representative of a wider population where each patient's bone density distribution may vary. Although, there are no specific criteria for choosing the most appropriate element type, the appropriate size of each element is always an important factor that affects the FEA results. Boundary conditions and loads are also often dominant factors. The more accurately that the boundary conditions and loads represent the intended situation in the real-world, the more accurate the FEA predictions will be. Therefore to ensure that the FE model can be used to make accurate predictions, some initial processes are necessarily required. These procedures include verification, validation, and sensitivity studies as described above. Whilst a number of the ankle FE models report some aspects of these processes, more evaluation is required for specific applications of the models. In summary, FEA is a useful tool that is expected to provide insight into the reasons for failure of TARs, however, this approach is only just starting to be used to study the ankle. The various problems that have been addressed during model development stages of previous studies may be useful for application in this study as well as the insight gained from the successful analysis results.

1.6 Conclusion

Early TARs introduced in the 1970s were abandoned due to unsatisfactory clinical outcomes. Improved designs and increasing patient demand led to the resumption in the 1990s. Nowadays, there are various designs of TAR, which are available on the market. These correspond to the increase in the demand of patients who suffer end state of arthritis that require TAR for treatment instead of conventional arthrodeses.

However, major challenges remain due to the small size of the joint compared to hip and knee, and high forces experienced by the joint. The potential for malalignment and instability appears to be high, with aseptic loosening and bone failure being common causes of device failure.

As can be seen, FEA can be applied to orthopaedic applications to investigate the biomechanical behavior of joint replacement systems either to reveal the mechanism of failure or evaluate new designs of devices. The majority of FEA studies in orthopaedics have been undertaken in the analysis of hip and knee arthroplasties, while only a few have examined ankle replacement.

FEA has several advantages over both *in vivo* and *in vitro* testing. These include the reduced analysis expense and duration of evaluation, the potential to compare between implants on a standardized model, as well as the lower risk of danger and fewer ethical issues. Due to the limited studies of TARs to date using FEM, there is potential for a wide variety of investigations in this field to fulfil the knowledge gap compared to the study of hip and knee replacements. FEA has the potential to be used to evaluate the mechanism of failure of the current TAR prostheses and inform clinical practice as well as to improve new designs to reduce the risk of failure. However, there is a need to develop robust models by studying the effect of the input variables and undertaking further validation to ensure the accuracy of the analysis results before this method can be utilized for new applications.

1.7 Aims and Objectives

The purpose of this PhD is to develop a finite element model of a total ankle replacement to evaluate general biomechanical characteristics and examine risk of bone failure, and how this is affected by component alignment.

In this work, a model of a single TAR design is used with a focus on developing a process that could be applied more widely in the future to understand mechanisms of failure of existing designs of prosthesis, and to predict likelihood of failure of novel designs.

The objectives of this study were as follows:

To create an experimental model of a TAR implanted within synthetic ankle bones, and to perform experimental studies to identify and measure parameters of interest for the purpose of FE model validation. This work is presented in Chapter 2.

To develop an initial FE model of the TAR and synthetic ankle bones corresponding to the experimental model, and to undertake various verification and sensitivity studies (i.e. to prove that the FE model is solved correctly, and to measure the effects of altering the input parameters upon the FEA results). Further, to

validate chosen output variables collected from the FEA against the same measurements obtained experimentally to determine the degree to which the model is a sufficiently accurate representation of the real-world for its intended use. This work is presented in Chapter 3.

To create 3-D models of natural ankle bones from medical imaging data, and to develop a FE model of natural ankle bones informed by the previous findings. This work is presented in Chapter 4.

To develop a FE model of a TAR implanted within the natural ankle geometry, initially following the ‘idealised’ surgical technique provided by the TAR manufacturer and use the model to investigate the stresses acting on the bone compared to the natural ankle, and hence predict the likelihood of bone damage. Further, to

use this FE model to represent various misalignment cases seen clinically and evaluate the effect of those misalignment cases on the stresses within the bones surrounding the implant. This work is presented in Chapter 5

Chapter 2 Experimental Studies of TAR with Synthetic Bone

2.1 Introduction

Experimental studies in which a total ankle replacement (TAR) is tested within synthetic bone are introduced in this chapter. Various tests are described to collect experimental data for comparison with the finite element (FE) models presented in Chapter 3, to determine the degree to which the FE model is a sufficiently accurate representation of the real-world for its intended use. This was the main purpose of the studies in this chapter. Some additional studies are also presented to determine the material properties of the experimental specimens, which were necessary to confirm the values to assign in the FE model.

2.2 Material and Methods

2.2.1 Mechanical Testing of Synthetic Bone

A synthetic polyurethane foam material (Sawbones® Solid Rigid Polyurethane #1522-03, Pacific Research Laboratories Inc, Washington USA) was chosen to be used to represent the tibial and talar bones in this experimental study. This material was originally developed to be used for testing orthopaedic devices and instruments, with properties that are representative of bone. The material properties of the polyurethane foam block quoted by the manufacturer are shown in the Table 2-1.

Table 2-1 Material properties of Sawbones® Solid Rigid Polyurethane foam block #1522-03 (Data taken from the manufacturer's website http://www.sawbones.com [cited 5 Jul 2014])

Density	**Compressive**		**Tensile**		**Shear**	
	Strength	**Modulus**	**Strength**	**Modulus**	**Strength**	**Modulus**
(g/cc)	(MPa)	(MPa)	(MPa)	(MPa)	(MPa)	(MPa)
0.32	8.4	210	5.6	284	4.3	49

Although the material properties of the polyurethane foam were available from the manufacturer, mechanical testing of the foam was undertaken to confirm the properties because there might be variation depending on the production lot.

The polyurethane foam block (original block size: 130.00 × 180.00 × 40.00 mm) was cut into a small rectangular prisms, with dimensions of 15.00 × 15.00 ×

30.00 mm (Figure 2-1). There were six specimens in total which were used for mechanical testing to quantify its compressive modulus and strength.

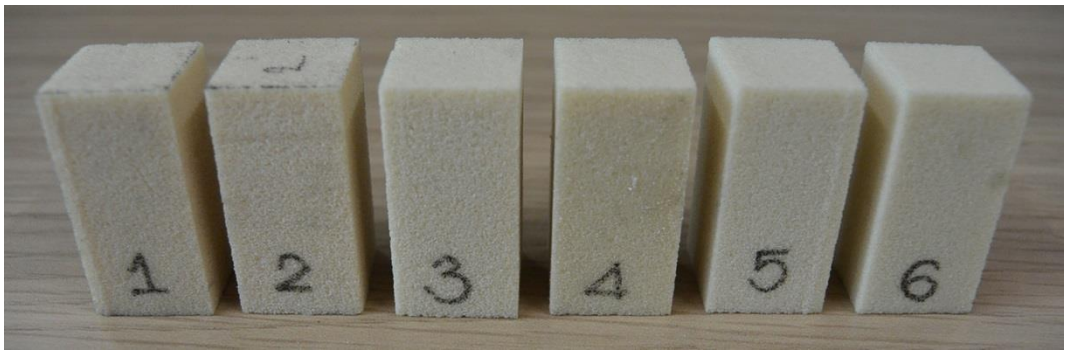

Figure 2-1 The polyurethane foam specimens used for mechanical testing

The polyurethane foam specimens were loaded in an electromechanical testing machine (Instron® model 3366 Dual Column Universal Testing System, Instron Corporation, Massachusetts USA). Each specimen underwent four test cycles, which included three non-destructive cycles and one test to failure. The compressive loads applied in these tests were 1000 N and 3500 N for the former and the latter tests respectively. The compressive load and compressive extension were collected from each test. These outputs were captured automatically using the manufacturer's software (Bluehill® version 2.35, Illinois Tool Works Inc, Massachusetts USA) at intervals of 100 ms, and were plotted by the software to show their relationship (Figure 2-2). The raw data collected during the mechanical testing was also exported as a CSV (comma separated values) file for further analysis. The compressive modulus and compressive yield strength of the material were calculated using equations 2-1 and 2-2 respectively.

$$E = \frac{F}{d} \times \frac{L}{A} \qquad \text{Equation 2-1}$$

Where E is the elastic modulus, F is the compressive load, d is the compressive extension, L is the original length of the specimen, and A is the cross sectional area of the specimen.

The $\frac{L}{A}$ term was approximately 0.13 mm^{-1} for the specific specimen used in this study. The stiffness term $\frac{F}{d}$ was defined as the gradient of the compressive load-extension plot and was obtained from the equation of the linear regression line used to fit those data (Microsoft® Excel® 2010 software, version 14.0, Microsoft Corporation, Washington USA). The data in the range of 200-1000 N

of compressive load, which was found to be the most linear, was used to calculate the stiffness.

$$\sigma_y = \frac{F_y}{A} \qquad \text{Equation 2-2}$$

Where σ_y is the compressive yield stress, F_y is the compressive load at the yield point, and A is the cross sectional area of the specimen (which was 225 mm^2).

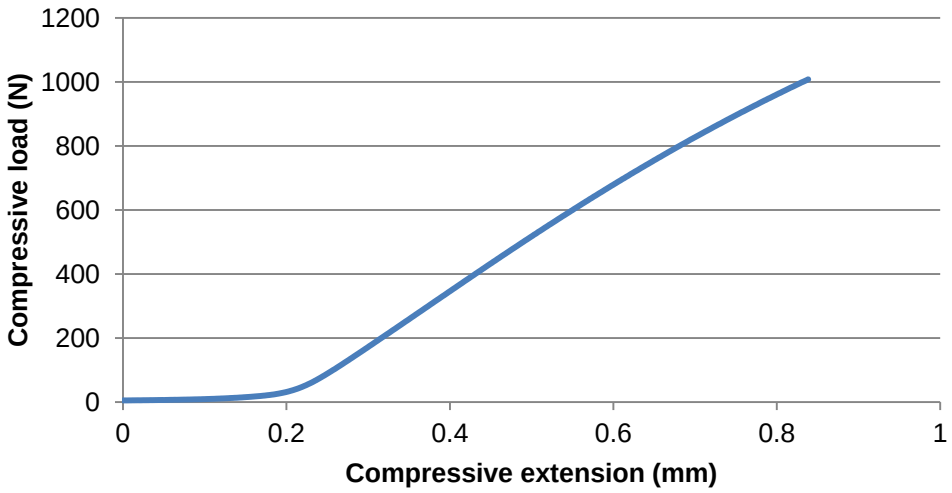

Figure 2-2 Compressive load (N) versus compressive extension (mm) of a non-destructive mechanical testing of the Sawbones® polyurethane foam #1522-03

2.2.2 Mechanical Testing of TAR with Synthetic Bone

The TAR used in this study was the Zenith™ TAR manufactured by Corin Group PLC (Cirencester UK) (Figure 2-3). The Zenith™ TAR is an uncemented three-component prosthesis (include tibial, bearing, and talar components) with a mobile bearing. The tibial and talar components are manufactured from biocompatible titanium alloy (Ti-6Al-4V), while the bearing component is made from the ultra-high-molecular-weight polyethylene (GUR1050 UHMWPE). The articulating surface of both tibial and talar components are coated with titanium nitride (TiN) to reduce polyethelene wear, and the bone contact area is coated with microcrystalline calcium phosphate (CaP) to encourage osseointegration. The tibial component is fixed onto the bone by one stem, while the talar component is fixed by two pegs. Several sizes of this TAR are available in the market, but the prosthesis used in this study was the Zenith™ TAR size 3.

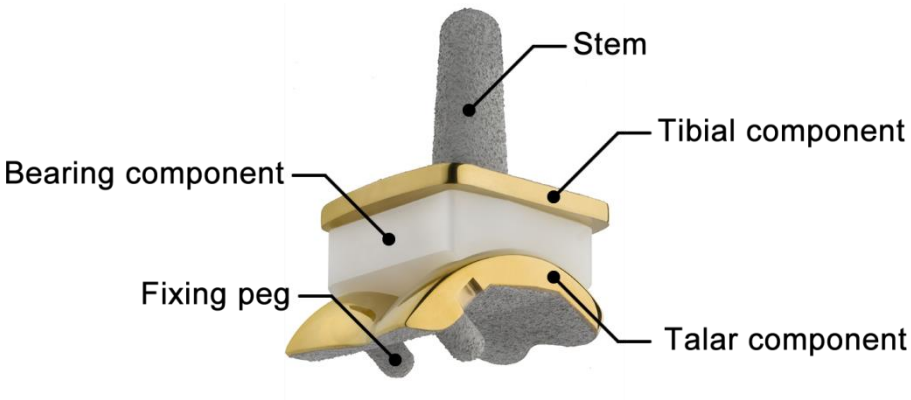

Figure 2-3 The Zenith™ total ankle replacement (Image adapted from Mckenzie et al. 2012, page 1)

The polyurethane foam block (original block size: 130.00 × 180.00 × 40.00 mm) was cut into small rectangular prisms to represent the tibial and talar bone in the experimental study, with dimensions of 40.00 × 50.00 × 50.00 mm and 40.00 × 50.00 × 35.00 mm respectively. The bottom surface of the tibial synthetic bone and the top surface of the talar synthetic bone were cut to match the surface of the corresponding prostheses to create conforming bone-implant interfaces (Figure 2-4). Fixing holes on the synthetic bone were cut to match the original dimensions of the stem and fixing pegs of the prosthesis, therefore, these were a little smaller than the CaP coated stem and fixing pegs. To insert the components into the synthetic bone, some compressive force was required to push both parts together, mimicking the press fit method used to install this type of prosthesis in the real clinical procedure (Figure 2-5). The needle-like structure of CaP coating increased the friction at the synthetic bone-implant interface and enhanced the fastening between these parts. The full engineering drawings of the synthetic bones are provided in Appendix A.1.

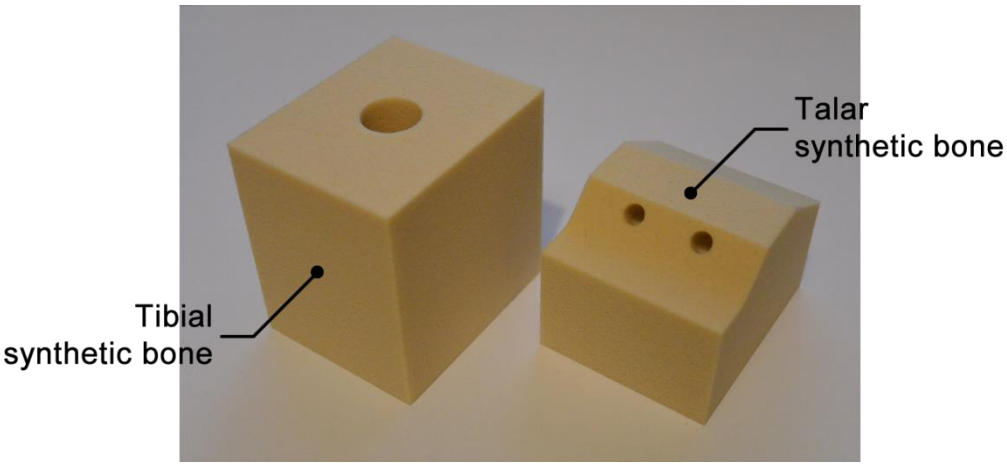

Figure 2-4 The tibial and talar synthetic bones

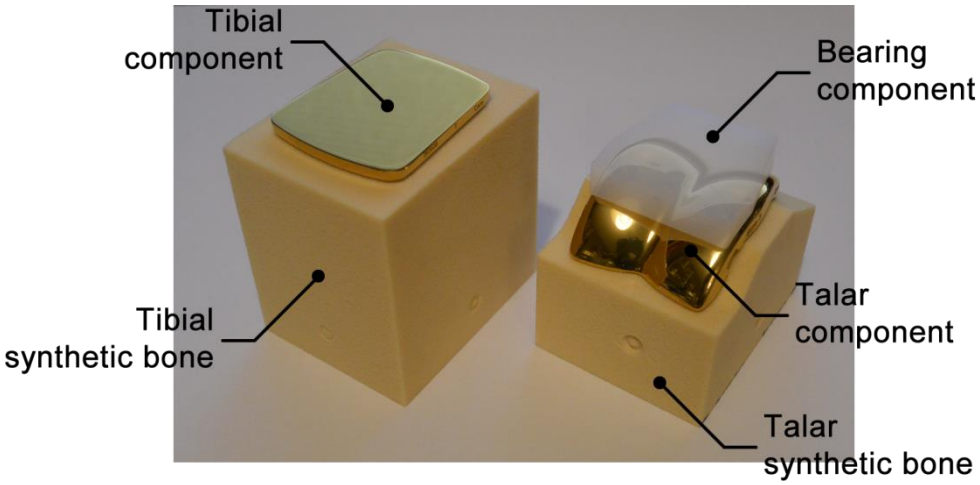

Figure 2-5 The experimental specimen of synthetic bones with TAR installed

2.2.2.1 Pressure Mapping Sensor Preparation

A pressure mapping sensor was required in this study for measuring the compressive load transmitted through the prosthesis, and investigating the contact pressure applied on the prosthesis component. The sensor used was a thin film pressure mapping transducer (Model 5076, Tekscan Inc, Massachusetts USA) (Figure 2-6). This type of sensor is made from two thin flexible polyester or polyamide sheets that are laminated together. An electrically conductive material is printed onto the inner surface of both sheets, but with different patterns of printing, with a row pattern on one sheet and a column pattern on the other. A semi-conductive material is printed to cover the rows/columns of the conductive material as a second layer before they are laminated together. The intersection of these rows and columns creates a sensing cell ('sensel™'). The load is measured in terms of the resistance at each sensel, and the value at the highest when no load is applied to it. There were 1,936 sensels (44 rows and 44 columns) in total for the sensor used in this study. Although the sensor model 5076 was available in a wide range of maximum pressure ratings, the sensor used in this study was suitable for the pressure that was not more than 6,895 kPa.

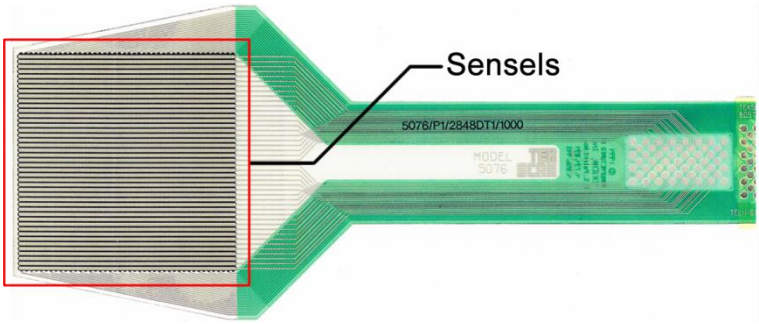

Figure 2-6 The Tekscan® Pressure Mapping Sensor model 5076

The I-Scan® system is a tool used to measure and analyze interface pressure between two surfaces. This system includes three main components: the pressure mapping sensor, the handle with attached USB cable (data acquisition electronics), and the computer with I-Scan® software installed (Figure 2-7). The pressure mapping sensor was inserted into the handle, which was used to gather and process the data from the sensor before sending to the computer, and the handle was connected to a USB port on computer via the attached USB cable. The data received from the handle was then analyzed using the I-Scan® software, version 6.03I (Tekscan Inc, Massachusetts USA).

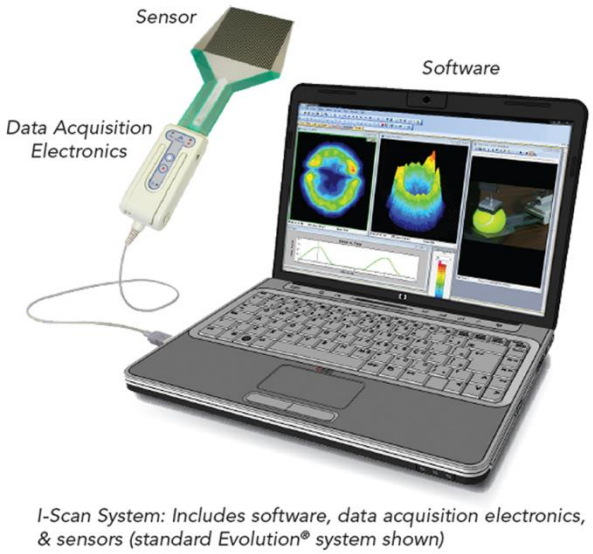

Figure 2-7 The I-Scan® system (Image taken from http://www.tekscan.com [cited 19 Jun 2016])

Two important procedures were undertaken to improve the accuracy of the sensor before using it to measure any loads. These procedures were the equilibration and calibration.

Prior to performing these procedures, it was necessary to set the sensitivity (gain) adjustment, that is the tuning between the range of the data output from the computer and the range of the actual force output from the system handle. This adjustment is also used to alter the range of the effective force of the sensor. In this study, six pre-set gains were applied as illustrated in Table 2-2. Although these were all required for the set-up processes, only one gain value was subsequently used for the tests in this study.

Table 2-2 The options of sensitivity adjustment chosen before performing equilibration and calibration

Option	High-1	Mid-2	Mid-1	Default	Low-3	Low-2
Gain	1.1	0.65	0.38	0.25	0.12	0.07

To compensate for slight differences in the inherent measurement property of each sensel within a range, an equilibration process was required. In this study, a uniform pressure applicator (PB100E equilibration device, Tekscan Inc, Massachusetts USA), was chosen to apply a pressure onto the sensor during equilibration process. This device was able to provide uniform pressure in a range of 0-100 psi. In this case, the sensor was equilibrated at four different pressures (20, 40, 60, and 80 psi) to ensure that the compensation was done appropriately at various pressure levels. The four-point equilibration was repeated at all sensitivity options chosen to create separated equilibration files, therefore, there were six equilibrations in total that were performed in this study.

The sensor was inserted into the equilibration device, and the desired uniform pressure loading was applied onto the sensor through the inflating of the bladder membrane. The equilibration device was connected to the pressure source via a control box, which had a pneumatic valve used to control the level of the compressed air. The measurement data was sent from the sensor to the computer and the output was enhanced by the software via an automatic ‘equilibration’ tool. This tool applied a digital compensation factor to the output of the sensor to make recorded uniform across all sensels.

Finally, a calibration process was undertaken to convert the digital output to a desired engineering unit. The I-Scan software allows users to perform two different types of calibration: linear and 2-point power law. The linear calibration is suitable for the limited range of load, but the 2-point power law calibration is better for measuring load that vary considerably during testing. Therefore, the 2-point power law calibration was chosen for this study. Calibration was

performed at 20% and 80% of the expected maximum test load (683.2 N and 2732.8 N) as recommended by the manufacturer (Figure 2-8). Although the calibration needed to be repeated at all sensitivity options, it was found only one option (Low-2) was suitable for the magnitude of the load used in this study. This was because other sensitivity options caused the sensor to be saturated at a lower load than desired. Therefore, the equilibration and calibration used for further studies were specific to the Low-2 sensitivity adjustment.

In this study, the sensor calibration was performed on the same set-up as the experimental study itself. The calibration system was started by setting the model for calibration in the same condition with the experimental model. The sensor was located into the same position as during actual measurements (between the tibial and bearing components), and aligned to maintain the symmetry of both the model and the sensor. The two different compressive loads were applied onto the model using the electromechanical testing machine. The sensor was loaded for approximately 75 seconds for the first calibration point and then allowed to relax for at least 6 minutes before applying the other load for the second calibration point, as recommended by the manufacturer to allow the sensor to be relaxed for 3-5 times the total time the sensor had been loaded after each load. The ‘calibration’ tool within the I-Scan software was used to perform a power law interpolation based on zero load and the two different applied loads and create a calibration file which was then used to convert the digital output to the desired engineering units throughout the subsequent experimental studies.

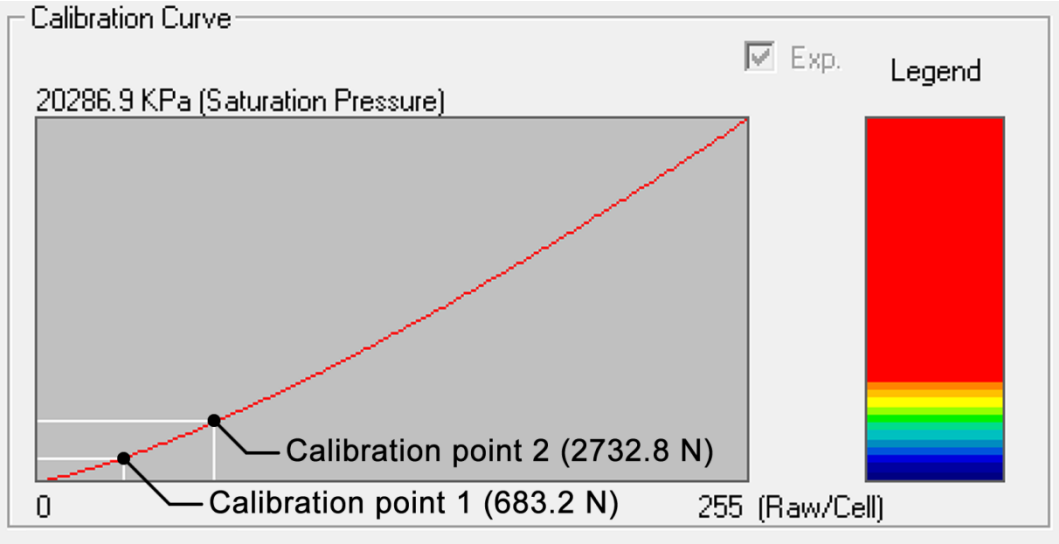

Figure 2-8 The 2-point power law calibration curve for the sensor

2.2.2.2 Experiment Setting

Following insertion of the prosthesis components into the corresponding polyurethane foam blocks, the model was loaded into a custom made jig that was designed specifically to act as a coupling between the electromechanical testing machine and the model. The jig included the two main parts, which were the upper and the lower jigs (Figure 2-9). The upper jig used to clamp the tibial synthetic bone with the tibial component inserted, while the lower jig used to clamp the talar synthetic bone with the talar component inserted, in both cases using four grub screws that were tightened to grip each side of the synthetic bone. This fixing method enabled adjustment of the alignment of the experimental model by tightening or loosening the grub screws. The bearing component was placed onto the conforming surface of the talar component without any constraint. The upper jig was mounted into the electromechanical testing machine at the load cell part, and secured using the clevis pin together with lock-nut to eliminate backlash. The lower jig was fixed onto an existing jig using five socket head cap screws, and that jig was attached to the electromechanical testing machine at the base part using clevis pin together with a lock-nut. The full engineering drawings of the custom made jig are provided in Appendix A.2.

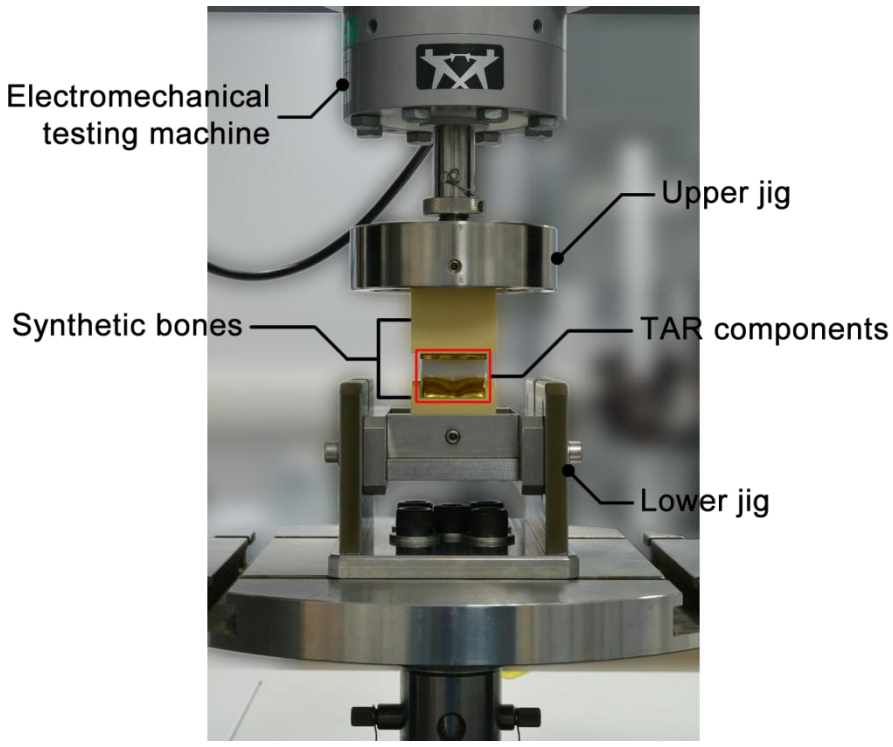

Figure 2-9 The experimental construct loaded in the electromechanical testing machine

The equilibrated and calibrated pressure sensor was placed between the tibial and bearing components, and adjusted to align between centerlines of both sensor and experimental model (Figure 2-10). The sensor was used to measure the compressive load transmitted through the prosthesis, and investigate the contact pressure applied on the prosthesis component.

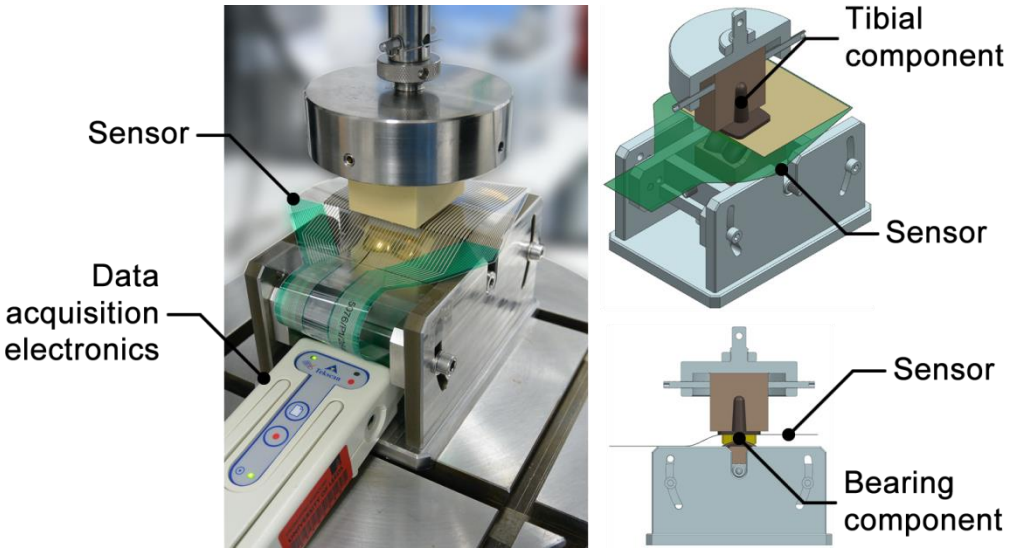

Figure 2-10 The complete experimental set-up for testing the TAR in synthetic bone, showing the pressure transducers inserted between the tibial and bearing components

Tests were undertaken on three experimental models in this study, and all models were tested using both non-destructive and destructive methods. For the non-destructive tests, a compressive load of 3416 N was applied at a rate of 0.5mm/min to the experimental construct. The test was repeated five times. Then, a destructive test was undertaken in which a load of 8000N was applied at a rate of 0.25mm/min. The contact pressure was measured only in the non-destructive testing.

2.2.2.3 Data Collection

From the electromechanical testing machine, two outputs of interest, the compressive load and compressive extension, were collected from each test via the Bluehill® software. Both the data of compressive extension and load were automatically collected at intervals of 100 ms, and were plotted by the software to show their relationship. The raw data collected during the mechanical testing was also exported for further analysis.

From the pressure mapping sensor, the contact pressure was captured in the form of a movie of the pressure contours with the aid of I-Scan® software. The

movie was recorded with the frame rate of 10 frames/sec corresponding to the data collecting rate of the electromechanical testing machine. The video recorded was able to be converted to either a plot or ASCII data for further analysis.

Both data were also compared to determine whether the pressure mapping sensor could reproduce the results based on the electro mechanical testing machine using the concordance correlation coefficient (CCC). This method evaluates the agreement by measure the correlation between the two outputs based on the 45° line through the origin. A perfect positive or inverse agreement occur when the CCC values are equal to 1 and -1 respectively, while there is no agreement when the value is equal to 0 (Lawrence and Lin 1989, Lin 2007).

The detail of the deformation of the synthetic bone following the destructive test, such as the location and the depth of the deformation, was also recorded for further validation of the finite element analysis results. The measurement of the deformation was performed at the region of the largest deformation which could be seen clearly. A vernier caliper was used to measure the depth of the deformation by measuring the difference in height between the deformation region and the adjacent area which was not plastically deformed.

2.3 Results

2.3.1 Mechanical Testing of Synthetic Bone

2.3.1.1 Elastic Modulus of Synthetic Bone

The compressive extension and load were collected from the non-destructive mechanical testing of the synthetic bone. A typical plot is shown in Figure 2-11, illustrating the linear regression fit used to calculate the elastic modulus using Equation 2-1.

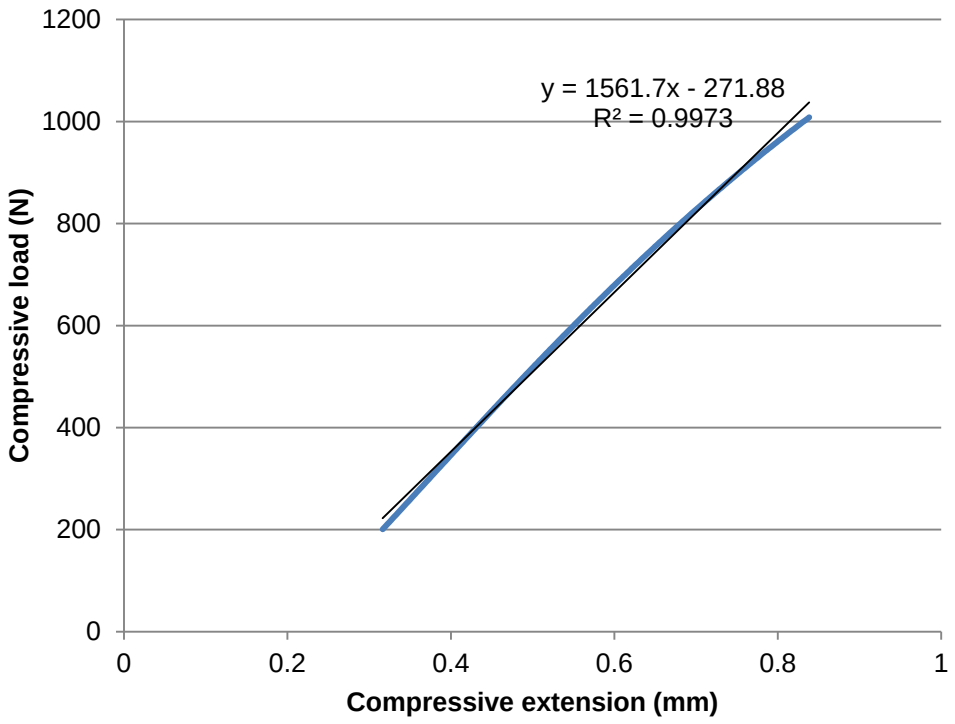

Figure 2-11 Compressive load (N) versus compressive extension (mm) of a non-destructive mechanical testing of the Sawbones® polyurethane foam #1522-03 with linear regression line fitted

The results of the 18 tests are shown in Table 2-3. The mean elastic modulus was 215.1±4.1 MPa (range 208.2-220.1 MPa). The high level of r^2 indicates that the load-displacement data was highly linear.

Table 2-3 The elastic modulus of synthetic bone obtained from mechanical testing

Specimen	Test	r^2	E (MPa)
1	1	0.9973	208.2
	2	0.9981	210.4
	3	0.9983	210.9
2	1	0.9974	208.6
	2	0.9981	210.6
	3	0.9983	212.1
3	1	0.9976	214.5
	2	0.9984	218.2
	3	0.9985	219.1
4	1	0.9976	214.5
	2	0.9983	219.1
	3	0.9985	220.1
5	1	0.9975	215.3
	2	0.9980	216.9
	3	0.9983	217.2
6	1	0.9977	217.7
	2	0.9982	219.5
	3	0.9983	219.6
		Average	215.1
		SD	4.1

2.3.1.2 Yield Stress of Synthetic Bone

A typical plot of the compressive load against extension from the destructive testing is shown in Figure 2-12.The graph illustrated a typical compressive deformation of the foam material. In the plot, a yield point was observed at which the curve leveled off, which divided the curve into two sections: the elastic and plastic regions. At this point, there was a sudden collapse without any increase in compressive load. The steepest gradient of the curve was seen before the yield point representing the elastic behavior, and the curve climbed gradually after the yield point representing the plastic behavior. However, to represent the material behavior in the FE model in Chapter 3, the properties would be simplified as elastic-perfectly plastic. The material behavior in the plastic region was described by a horizontal line at the same level as the yield point to represent perfectly plastic deformation such that there was no further resistance of the specimen to deformation when reaching the yield point. The compressive yield stress was obtained from the compressive load measured at the yield point and calculated using Equation 2-2.

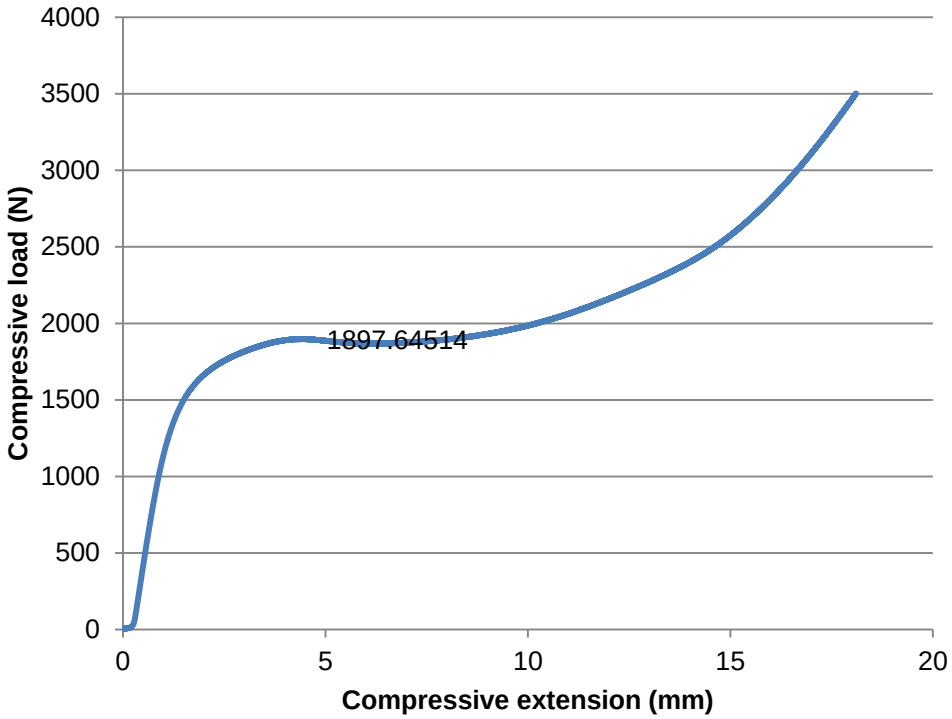

Figure 2-12 Compressive load (N) versus compressive extension (mm) of a destructive mechanical testing of the Sawbones® polyurethane foam #1522-03

The results of the six tests are given in Table 2-4. The mean yield strength was 8.44±0.07 MPa (range 8.35-8.53 MPa).

Table 2-4 The compressive yield strength of synthetic bone obtained from mechanical testing

Specimen	Compressive yield strength (MPa)
1	8.43
2	8.41
3	8.53
4	8.51
5	8.35
6	8.42
Average	8.44
SD	0.07

2.3.2 Mechanical Testing of TAR with Synthetic Bone

2.3.2.1 Concordance Correlation Coefficient for Measuring Agreement

The load data obtained from both the electromechanical testing machine and the pressure mapping sensor were plotted to investigate their relationship. Their concordance correlation coefficient (CCC) was quantified to determine the relationship between the loads measured by the two different methods.

There were 18 tests in total to quantify the significant parameters to determine the agreement between loads measured by two different methods. The CCC values are listed in Table 2-5. These values were in a range of 0.994-0.998, and their average value was 0.997±0.001, showing a very high level of agreement.

Table 2-5 The concordance correlation coefficient (CCC) values obtained from 18 tests used to determine the agreement between loads measured by the electromechanical testing machine and the pressure mapping sensor

Specimen	Test	Concordance correlation coefficient (CCC)
1	1	0.996925
	2	0.997733
	3	0.995244
	4	0.997174
	5	0.994134
	6	0.995917
2	1	0.995336
	2	0.997205
	3	0.998172
	4	0.996695
	5	0.997402
	6	0.997293
3	1	0.998489
	2	0.998267
	3	0.998354
	4	0.998217
	5	0.998308
	6	0.997922
	Average	0.997155
	SD	0.001256

2.3.2.2 Contact Pressure

As the load was applied to the TAR system, the mean contact pressure between the tibial and bearing components was seen to increase linearly (Figure 2-13). A typical pressure contour plot taken when a compressive load of 3416 N was applied, is shown in Figure 2-14. Although the sensor was placed between two flat surfaces, the contact pressure measured was not uniform. This might be because the surfaces were not perfectly flat.

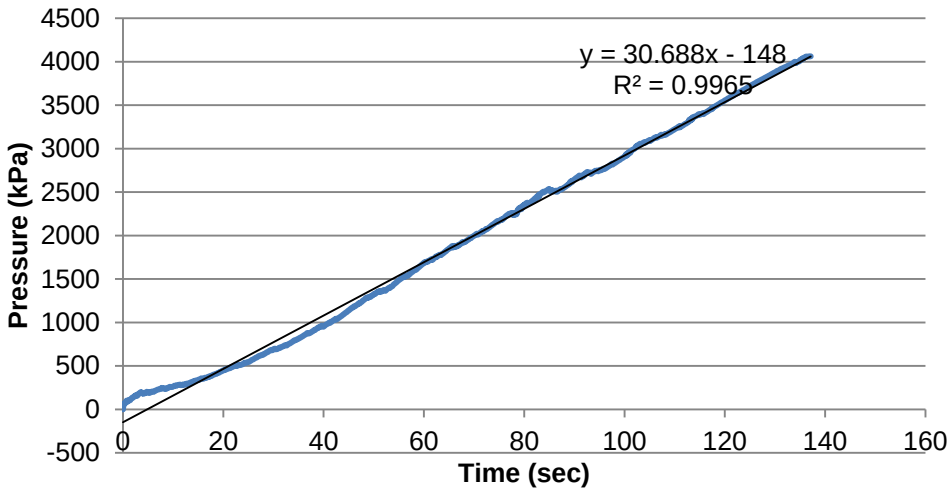

Figure 2-13 Average contact pressure (kPa) versus measuring time (sec) of a mechanical testing of the TAR with synthetic bone with linear regression line fitted

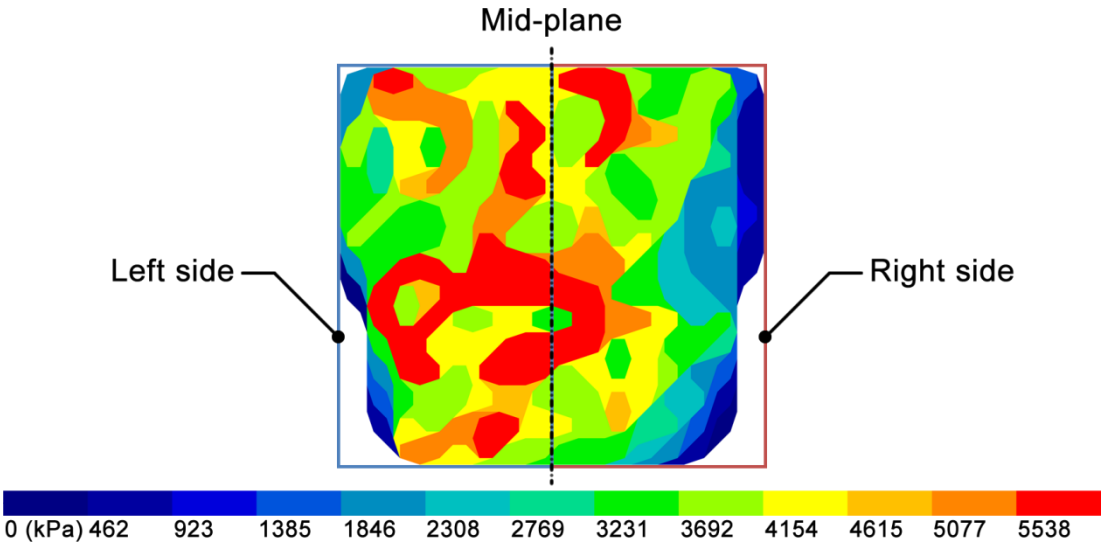

Figure 2-14 Contact pressure (kPa) between tibial and bearing component experienced by the pressure mapping sensor on either side of the mid-plane when a compressive load of 3416 N was applied

Moreover, if the articulating area was considered in two separate parts divided by the mid-plane, the contact pressure experienced by each side of the sensor was not the same. The contact pressure measured on the left side was consistently higher (Figure 2-15). This was likely because there was some inclination between the articular surfaces of tibial and bearing components in the frontal plane (Figure 2-16). Considering the frontal plane of the specimen, there was a gap between the tibial and bearing components at the extreme right hand side of the articulation, while no gap was observed at the same point on the left hand side. The average contact pressures measured of each specimen was plotted as a bar chart to illustrate the difference between the left and right sides contact pressures (Figure 2-17). The average contact pressure measured by the sensor from all tests was 3.997±0.077 MPa, and the average contact pressure on the left and right sides of the mid-plane were 4.534±0.124 MPa and 3.447±0.100 MPa respectively.

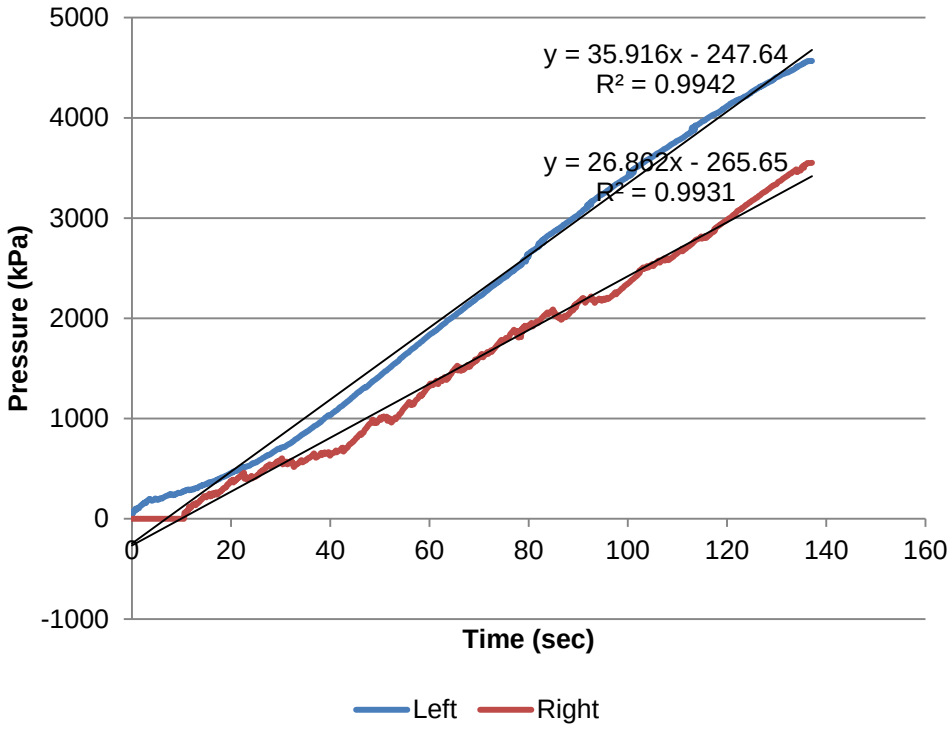

Figure 2-15 Average contact pressure (kPa) versus measuring time (sec) of a mechanical testing of the TAR with synthetic bone on either side of the mid-plane with linear regression line fitted

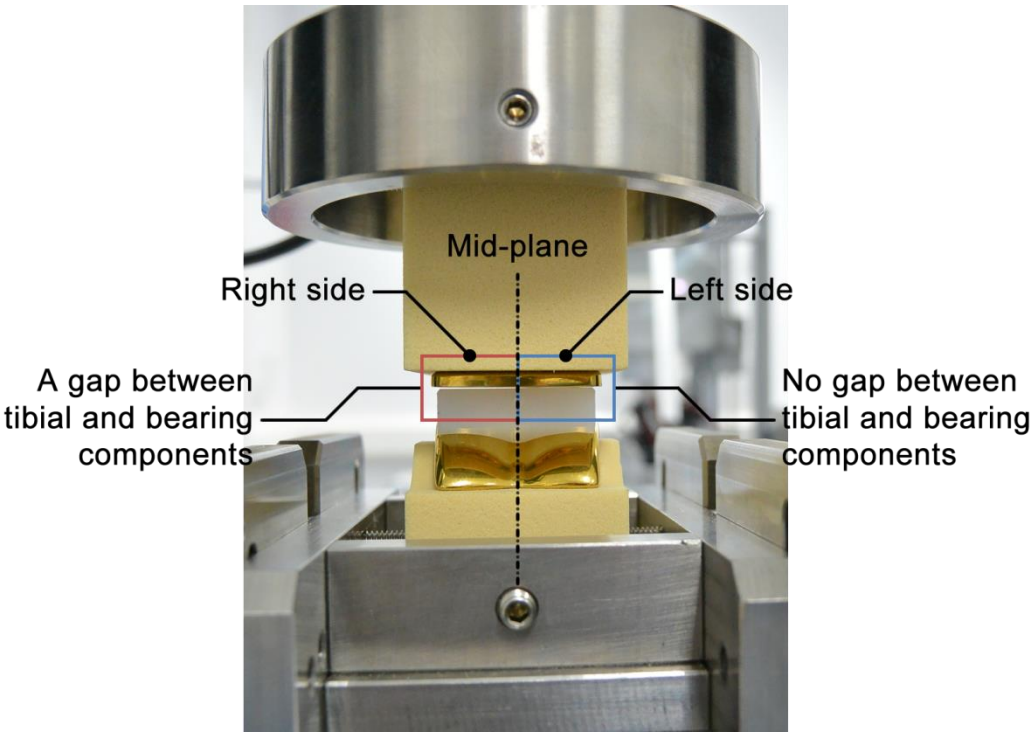

Figure 2-16 The inclination between the articular surfaces of tibial and bearing components

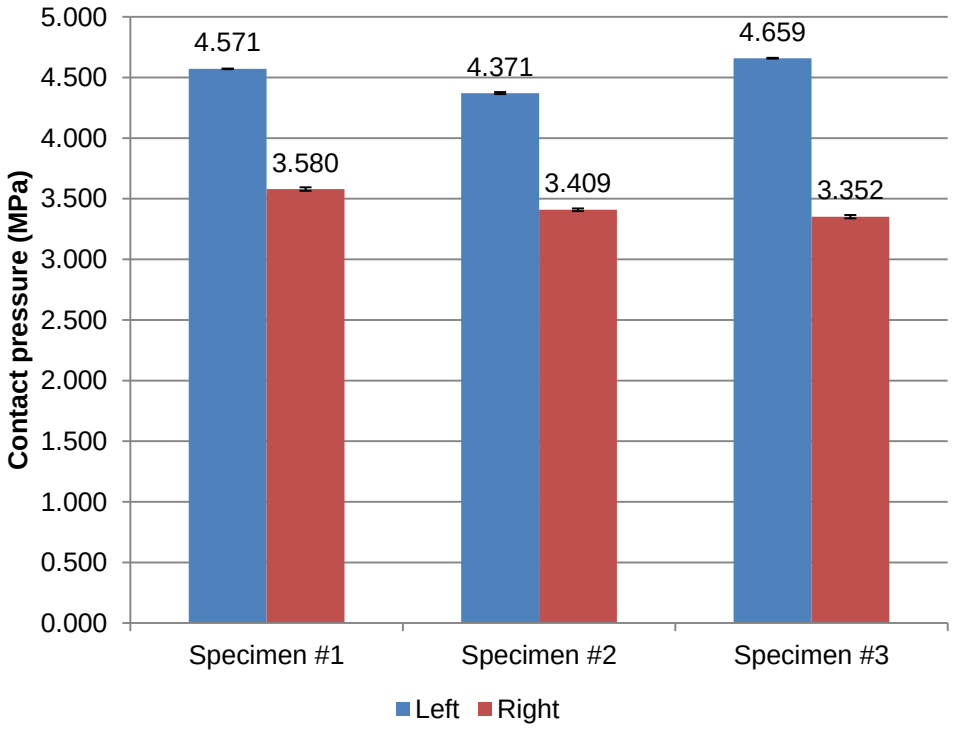

Figure 2-17 Bar chart illustrating the average contact pressures (MPa) measured from each specimen

2.3.2.3 Deformation

Following the destructive test, the deformation of the polyurethane foam block in the area of bone-component interface could be seen clearly. The largest observable deformation was found on the talar synthetic bone at the region where the most posterior edge of the talar component was located (Figure 2-18). The deformation depth at the most posterior region of the talar bone-implant interface of all experimental models was measured for further validation of the FE model. The measurement was performed at three measuring points at approximately 7 mm, 8mm, and 9 mm from the either side of the mid-plane (Figure 2-19). The deformation data measured are listed in Table 2-6. The deformation of the talar synthetic bone on the left side of the mid-plane was larger than the right side corresponding to the contact pressure measurement results. The average depths of deformation on the left and right sides from the three destructive tests were 0.2667±0.0050 mm and 0.2167±0.0050 mm respectively, and the average deformation on both sides was 0.2417±0.0025 mm. This can be also used to confirm the existence of the inclination between the experimental components.

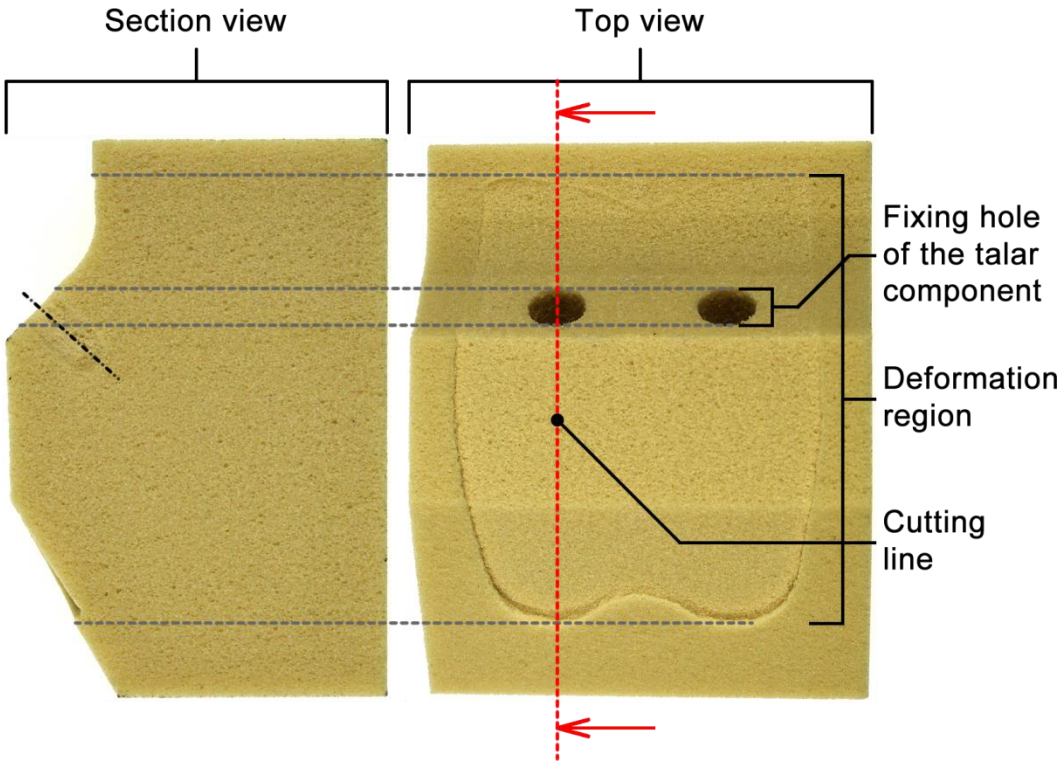

Figure 2-18 The deformation of the talar synthetic bone after destructive testing

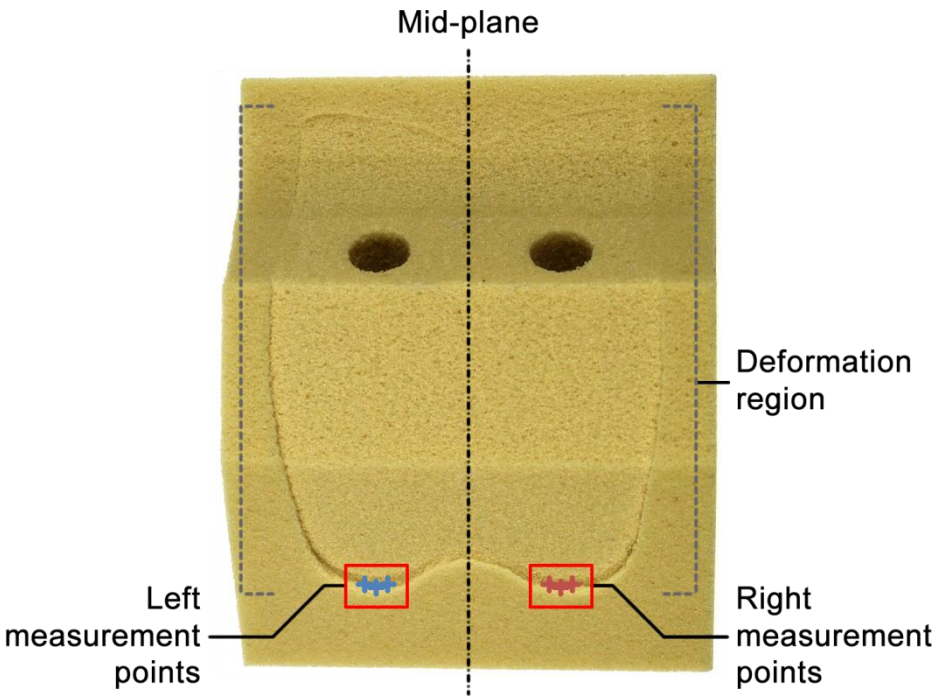

Figure 2-19 The location of the measurement of the depth of deformation

Table 2-6 The depth of deformation (mm) measured from three destructive tests

Specimen	Location of measurement - distance from the mid-plane (mm)	Depth of deformation (mm)		
		Left	Right	Average
1	7	0.2700	0.2200	0.2450
	8	0.2700	0.2200	0.2450
	9	0.2700	0.2200	0.2450
2	7	0.2600	0.2200	0.2400
	8	0.2600	0.2200	0.2400
	9	0.2600	0.2200	0.2400
3	7	0.2700	0.2100	0.2400
	8	0.2700	0.2100	0.2400
	9	0.2700	0.2100	0.2400
	Average	0.2667	0.2167	0.2417
	SD	0.0050	0.0050	0.0025

2.4 Discussion

2.4.1 Mechanical Testing of Synthetic Bone

The mechanical testing of synthetic bone was performed to ensure that the material properties quoted by the manufacturer were sufficiently accurate to be used in the subsequent finite element analysis. This process is important because the difference in material properties between the experimental and FE models will cause differences between the results that affect the result of validation directly. The difference in material properties would also affect further predictions. In this case, the difference of the values obtained between the manufacturer and the in-house testing was 2.4% for the compressive modulus, and 0.5% for the compressive strength. The material properties (compressive modulus and compressive strength) informed by the manufacturer were a little different compared to the in-house testing, therefore, those manufacturer's values will be used for material properties of synthetic bone in the further finite element analysis (FEA) studies.

Considering the mechanical testing results, the material seems to be stiffer when repeating the test on the same specimen. There were two factors that were likely to be causes of this stiffness changes. The first factor was an inadequate relaxation time for the specimen before repeating the test. The second factor was an occurrence of damage in the specimen, although the compressive test was done in the elastic region of the material. This might be because of the foam structure of the specimen. The strength of the solid material surrounding each hole might be difficult to control in real-world production, and some pockets might not be able to withstand load as much as others, leading to localized failure. Any collapsed cells could consequently make the specimen stiffer by replacing the gas pocket by solid material. This factor could also mean that the mechanical properties of the foam material might vary depending on its structure.

In the destructive test, the curve plotted between the compressive extension and compressive load showed the behavior of material in both elastic and plastic regions (Figure 2-12). This plot was a typical shape for the behavior of foam materials. In the elastic region, the graph rose linearly illustrating a proportional relationship between the parameters. At this stage, the load applied would cause bending of the cell walls, and this temporary deformation could be recovered when unloading. At the yield point, the graph levelled, representing a sudden collapse of the specimen that took place without an increase in the compressive load. The cell walls are thought to start to buckle at this stage. In the plastic region, the graph continued to plateau and the climb

gradually, showing some recovery in the capacity to withstand compressive load. At this stage, the cell walls are likely to have buckled and the collapsed cell walls were crushed together to close the pores, changing the density of specimen. The densification caused the specimen to be stiffer and could resist the compressive load again. However, for the subsequent FE model, the material properties were modeled using elastic-perfectly plastic material such that the behavior after the yield point was represented by a horizontal line in the same magnitude as the yield. This means that the model will not capture further resistance of the specimen to deformation when reaching the yield point, and will therefore not capture the larger strain plastic behaviour.

2.4.2 Mechanical Testing of TAR with Synthetic Bone

2.4.2.1 Concordance Correlation Coefficient for Measuring Agreement

Although the Tekscan® pressure mapping sensor was a commercial product, this type of sensor required some in-house adjustments to ensure an adequate accuracy of measurement. The sensitivity adjustment was performed for tuning between the range of the data output from the computer and the range of the actual force output from the sensor. The inherent different measurement property of each sensel on the sensor was digitally compensated for enhancing an accuracy of measurement through the equilibration process. The final step of preparation was the calibration which was used to convert the digital output from the sensor system to an actual desired engineering unit. After completing the adjustment of the sensor, some testing was necessarily required to ensure the accuracy of measurement. In this study, the measurement value obtained from the sensor system was compared with the similar value obtained from the load cell of the electromechanical testing machine based on the concordance correlation coefficient (CCC) analyses. In this case, the measurement data obtained from the load cell, which was calibrated and certified by the manufacturer, was thought to be reliable for comparison. The average CCC obtained from the correlation analysis of 18 tests of three specimens was 0.997155±0.001256. This analysis was not only used to confirm the correlation between both output variables, but also to confirm the precision of the two measurement methods. This was because the CCC measures agreement between the two variables by using a 45° line through the origin for reference. The CCC value that was close to 1 therefore illustrated that, at each load value applied, both the load cell and the pressure mapping sensor showed very similar measurement values.

This confirmed that the preparation processes (sensitivity adjustment, equilibration, and calibration) were done appropriately, and the sensor was

reliable and could be used for further contact pressure measuring with an adequate accuracy.

2.4.2.2 Contact Pressure

Considering the pressure contour plot from the sensor placed between the tibial and bearing components, the pressure distribution was not uniform even though the sensor was placed between two flat surfaces. This was thought to be an effect of placing the sensor between two hard surfaces, and both surfaces might not be perfectly flat. To solve this problem or enhance the pressure contour plot, a thin sheet of softer material (such as a sheet of paper or rubber) could be inserted together with the sensor between those two hard surfaces. The inserting material would lower the peak pressure areas, and increase the pressure in the low pressure areas to distribute the pressure throughout the articulating area. The pressure contour plot could be expected to display more uniform distribution of contact pressure consequently. However, this step was not undertaken here because the actual load distribution between the two sides of the component was important.

The measurement data was converted to be a plot between contact pressure experienced during loading and the measuring time. The increasing of the contact pressure throughout the sensor area corresponded to the increasing load applied. However, when dividing the contact area using the mid-plane into two equal areas, the contact pressures experienced by the two sides were different (approximately 27% difference in average contact pressure). This confirmed that there was some degree of inclination between the experimental components in the frontal plane.

A similar discrepancy in pressure occurred in all the experimental tests, therefore, the source of this misalignment was thought to be come from the permanent experimental parts (such as jigs or fixtures) instead of the experimental model. All custom made jigs were constructed using high precision machines, therefore, the method for installing these jigs might be the most likely to be the cause of the inclination. Considering the fixing method between the jig and the electromechanical testing machine, the jig was secured to the machine using the clevis pin together with lock-nut. There was a small clearance between the hole and the pin allowing the jig to be moved in a certain range. That is why the lock-nut was necessary to be installed together to eliminate the backlash. The thread that the lock-nut tightened to was thought to be the source of the inclination. Either a slightly mismatched profile of the thread or the existing clearance between the thread was likely to have caused

this misalignment, which in turn caused a difference in measured contact pressure between the left and right hand sides.

2.4.2.3 Deformation

Considering the deformation on the synthetic bone, the deformation occurred on both the tibial and talar synthetic bone in the region of bone-implant interface, but the largest deformation was located at the most posterior region of the talar bone-implant interface. At that location, the depth of deformation was measured for comparing with FEA result in the subsequent work. The reason why the deformation at this location was the largest might be because there was not any fixing peg located in this area to distribute the load. The two fixing pegs of the talar component were located in the anterior region, and the deformation of the synthetic bone in that region was considerably smaller. In the aspect of load bearing, the importance of the fixing peg might be comparable to that of pile in a building structure. The design of fixing parts was not only for constraining the component in any certain plane, but was also to increase area of bone-prosthesis interface with the aim of sharing load using both the tip and the skin friction. However, there was a limit for the design of fixing pegs of the talar component due to the clinical implantation. The TAR was inserted into the ankle at the anterior region, therefore, almost of all designs of the talar component have fixing parts located anteriorly for convenience to insert the component in to a narrow clearance between tibia and talus.

Moreover, there were other deformations that could not be observed easily by eye. These deformations occurred surrounding both the stem of the tibial component and the fixing pegs of the talar component. The component, which was installed using the press-fit method, was removed easily from the synthetic bone after the destructive test. The reason why the component could be removed easily might be because the polyethylene foam at the bone-implant interface had deformed plastically, causing expansion of the fixing hole.

Corresponding to the different contact pressure experienced by either side of the mid-plane, the deformation observed on both sides were also different. The difference between the average depths of deformation on each side of the mid-plane obtained from 18 measuring points of three specimens was approximately 21%. This can be also used to confirm the existence of the inclination between the experimental components.

In the ideal condition, the values between the percentage difference of the contact pressure measurement and the deformation measurement would be expected to be the same value. In this case, the percentage difference of the

deformation measurement was a little lower. This might be because the deformation was approximately in a range of 0.21-0.27 mm, and the measuring instrument, vernier caliper, only provided a precision to 0.01 mm. Therefore, the precision of the instrument was thought to be a factor that affected the percentage difference of the deformation measurement.

The depth of deformation collected from this experimental study was also used to quantify the degree of deformation. The highest degree of inclination occurred in specimen #3 where the difference between the values of the depth of deformation on either side of the mid-plane was maximum (0.06 mm). Because the measurement of the depth of deformation was perpendicular to the plane that was inclined at an angle of 30° to the horizontal plane, the actual vertical deformation was equal to the depth of deformation divided by the cosine of 30° (Figure 2-20). The shortest distance between the two measuring points on either side of the mid-plane (14.00 mm) was also used to calculate this inclination in the extreme condition. The angle of inclination was calculated by quantifying the arctangent of the difference of vertical deformation divided by the distance between two measuring points (Figure 2-21). The degree of inclination obtained from the calculation was approximately 0.28°.

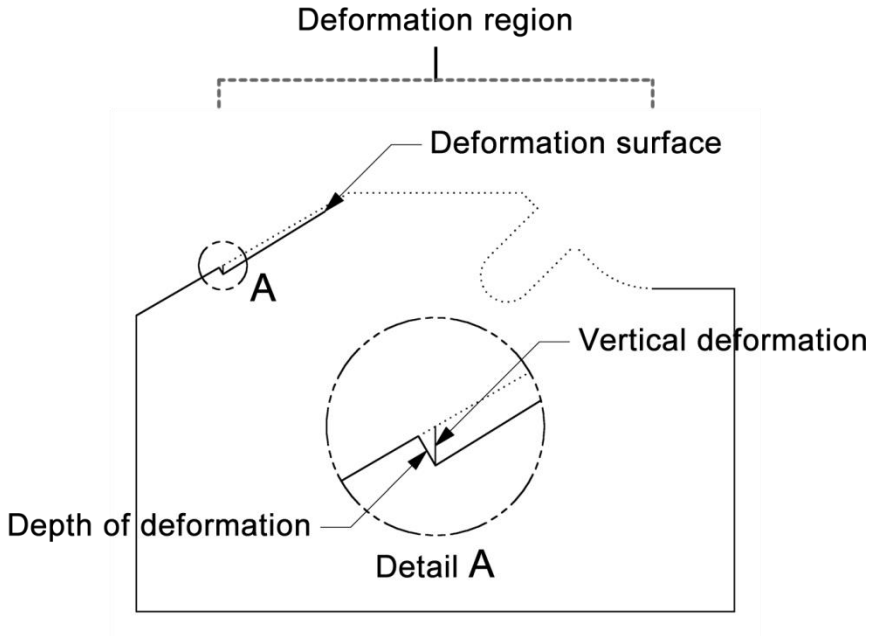

Figure 2-20 The method of quantifying the vertical deformation

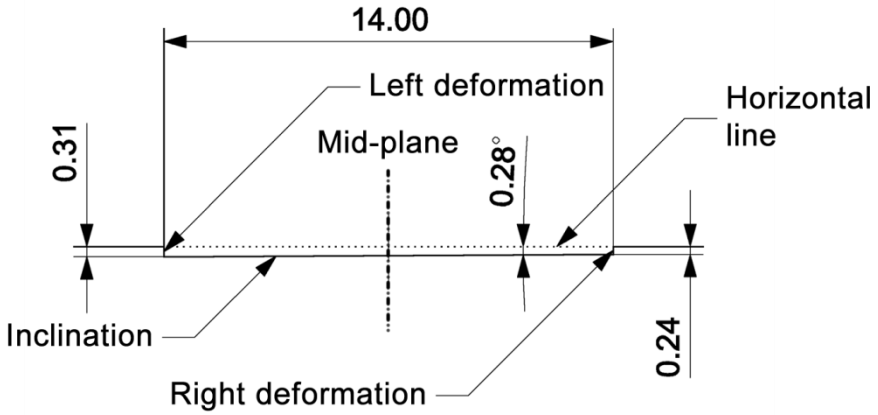

Figure 2-21 The method of quantifying the angle of inclination

The inclination of only 0.28° between the TAR components in the frontal plane made the difference of approximately 27% between the contact pressures experienced by either side of the mid-plane, therefore, the alignment of the TAR components is likely to be an important factor in the outcome of implantation due to the potential for excessive load to be applied. This indicates that maintenance of the alignment between each component of the prosthesis during surgery must be a priority to prevent an excessive loading problem.

Although a small inclination of the TAR caused a large effect in the experimental model, in the clinical implantation, the severity of the effect may be lower. This is because the movement of each instrument part was highly constrained, and each TAR component could not be moved to compensate for any inclination. The movement of each part of the human body is freer, the joint can slightly change its positioning to compensate a misalignment of the prosthesis and better share the load bearing, reducing the severity of either excessive contact pressure or excessive deformation. However, the patient may face associated problems due to alterations in physiological movement instead. Although not necessarily fully realistic, the results of this study illustrate the importance of alignment, and the need to evaluate in more realistic models, which will be considered further in Chapter 5

2.5 Summary

An experimental model of TAR with synthetic bone was used in a series of experimental studies. The material properties of the synthetic bone informed by the manufacturer were confirmed using the results obtained from in-house mechanical testing. The pressure mapping sensor was appropriately prepared for further measurement with an adequate accuracy. The experimental data, including the depth of deformation, was obtained successfully for comparing with the FEA results in the subsequent work. The following conclusions can be drawn from this study:

1 The results obtained from concordance correlation coefficient (CCC) analyses were used to confirm that the pressure mapping sensor was equilibrated and calibrated appropriately. The CCC values close to 1 can be described as the data measured by both the load cell and the sensor had a strong agreement. Therefore, the sensor can be used for further measurement with an adequate accuracy and reliability.

2 Experimentally, there was some difference in deformation laterally, which corresponded to a difference in contact pressures measured on either side of the mid-plane, illustrating that there was some degree of inclination between the interfaces of TAR. The experimental deformation data can be used for calculating the degree of inclination, which was approximately an angle of 0.28°. Only a little inclination between the TAR components can make an amount of difference of approximately 27% of contact pressure experienced by the components on either side of the mid-plane. This might leads to the failure of implantation due to the excessive loading.

Chapter 3 Verification, Validation, and Sensitivity Studies of the FE Model of the TAR with Synthetic Bone

3.1 Introduction

The initial processes of preparing the finite element (FE) model of the TAR in synthetic bone are introduced in this chapter. The FE model construction is described along with various processes for comparison of the outputs with theoretical data, experimental data (obtained from the Chapter 2), and with different model parameters. These procedures include verification, validation, and sensitivity studies. Verification is the process to prove that an FE model is solved correctly. Validation is the process to determine the degree to which a model is a sufficiently accurate representation of the real-world for its intended use. Sensitivity studies measure the impact of altering the input parameters upon the FEA results.

3.2 Material and Methods

3.2.1 FE Model of TAR with Synthetic Bone

3.2.1.1 Model Construction

A 3-D model of a TAR within synthetic bone was created for analysis using the finite element method (FEM), and the results were used to compare with those obtained from the experimental study performed previously in Chapter 2 as a validation step. Therefore, the 3-D model used in this study was constructed to match the geometry of the experimental model used in Chapter 2.

There were five parts in total that were included in the assembly. Two of them represented the tibial and talar bones, while the other three parts represented the TAR components.

The 3-D models of the simplified tibial and talar bones were created in NX software (version 7.5.4.4, Siemens Product Lifecycle Management Software Inc, Texas USA). Rectangular prisms were generated using the ‘Extrude’ command. Then, the ‘Trim Body’ and ‘Subtract’ commands were used for cutting the bottom surface of the simplified tibial bone and the top surface of the simplified talar bone to match with the bone contact area of the corresponding TAR components (Figure 3-1).

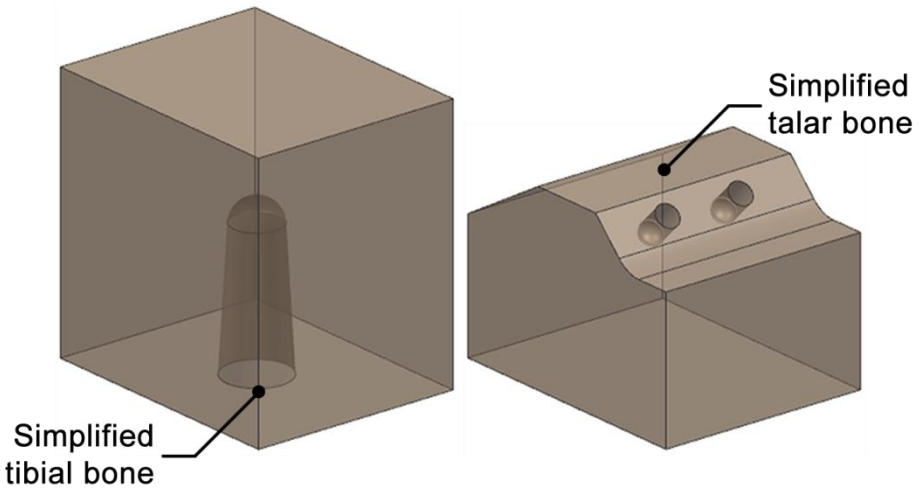

Figure 3-1 The 3-D models of simplified tibial and talar bones

The dimensions of the simplified bones used for verification and sensitivity studies were slightly different from the simplified bones used for validation, and their dimensions are shown in Table 3-1. This was because the verification and sensitivity studies were performed before the experimental study, and the assumed sectioning of the raw material was a little different from the actual process (Figure 3-2). The geometry of the 3-D model of the simplified bones used in the validation process was altered to be the exactly same as the geometry of the synthetic bone used in the experiment to reduce the risk of inaccuracy.

Table 3-1 The dimensions of the simplified bones

Type of study	**Site of simplified bone**	**Dimension (mm)**		
		Width	**Length**	**Height**
Verification and sensitivity studies	Tibia	40	40	43
	Talus	40	43	20
Validation	Tibia	40	50	50
	Talus	40	50	35

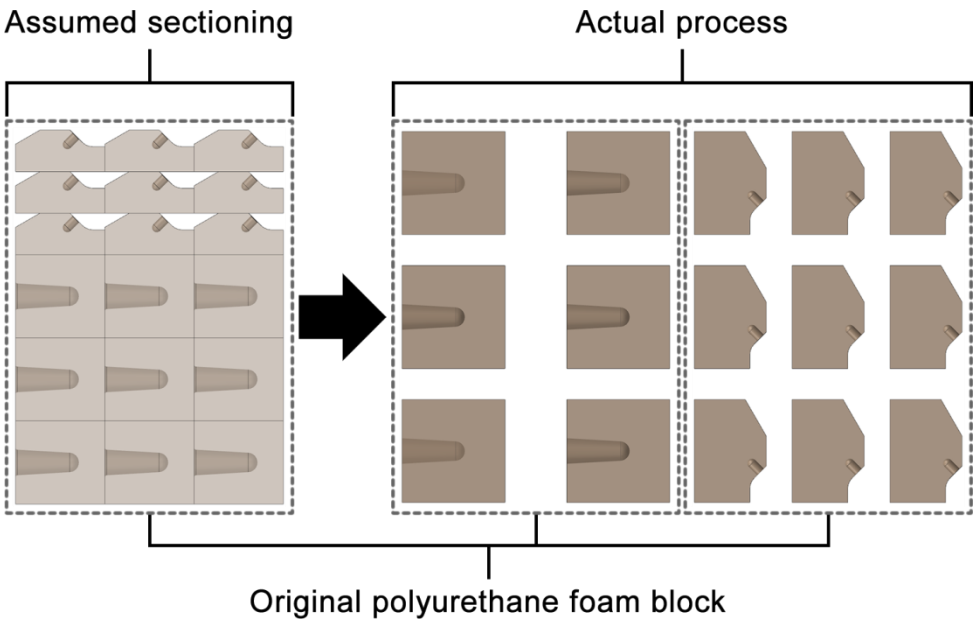

Figure 3-2 The layout of cutting the simplified bone from the original block

The 3-D model of the Zenith™ TAR, which was the same size as the real prosthesis used in the experimental study, was obtained from the manufacturer (Corin Group PLC, Cirencester UK) as a Parasolid file that was compatible with the NX software (Figure 3-3). This type of file can be imported directly into the software and used without any change from the original data. In the initial study, small details on the TAR components, such as the engraving and fillets, were removed. The fillets located in the region of bone-implant interfaces were maintained initially and their role investigated in a sensitivity study to ensure that the removal of these small details would not affect the analysis results.

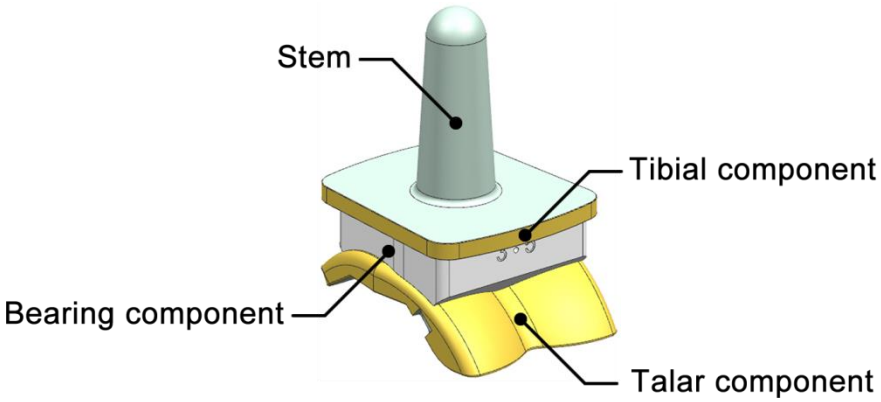

Figure 3-3 The 3-D models of Zenith™ TAR components

The TAR components were virtually inserted in to the corresponding simplified bones mimicking the position of the experimental set-up (Figure 3-4). This assembly was exported as a parasolid file for further construction using FEA software (Abaqus/CAE version 6.12-2, Dassault Systèmes Simulia Corp, Rhode Island USA).

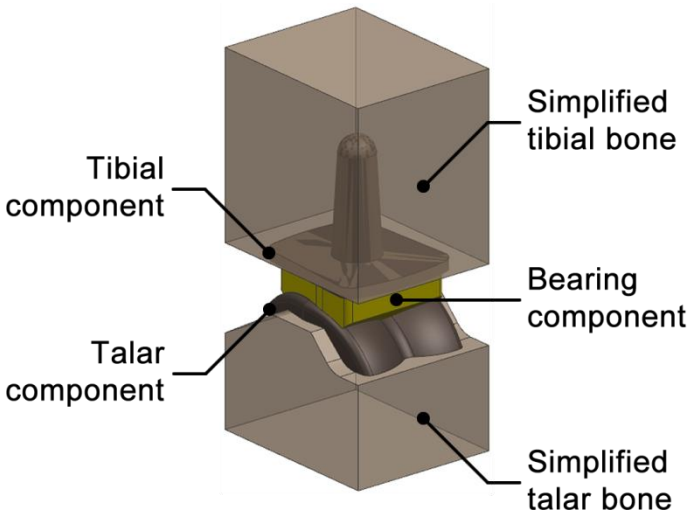

Figure 3-4 The CAD model of TAR with synthetic bone

An analytical rigid plate, with dimensions corresponding to those of the tibial synthetic bone, was created to enable loading over the whole of the cross section at the top of the tibial bone. A reference point was located at the center of the rigid plate, and the plate was aligned on the top of the simplified tibial bone.

In this study, ten-node quadratic tetrahedron (C3D10) elements were chosen to mesh both the synthetic bone and the TAR component. This was because the tetrahedral elements are geometrically versatile and suitable for automatic meshing of complex geometry. The meshing of the assembly was achieved through the standard automated meshing tool (‘Mesh Part Instance’). The approximate element size and the element number of each instance in the initial FE model are shown in the Table 3-2. For this initial model prior to the mesh convergence study, a relatively small element size was selected. The smallest approximate element size calculated by the software by default was 1.3 mm for meshing the bearing component. An approximate element size of 1.2 mm was therefore applied to mesh all the components at this initial study. The initial FE model was consequently represented by ~408,000 tetrahedral elements in total.

Table 3-2 Meshing information of the initial FE model of the TAR with synthetic bone

Instance	Element type	Approximate element size (mm)	Element number
Tibial synthetic bone	C3D10	1.2	217,081
Tibial component	C3D10	1.2	28,400
Bearing component	C3D10	1.2	20,191
Talar component	C3D10	1.2	26,023
Talar synthetic bone	C3D10	1.2	115,986

3.2.1.2 Material Properties and Interactions

Material properties of both synthetic bone and TAR component were assumed to be linear elastic, homogenous, and isotropic, and listed in Table 3-3. The synthetic bone used in this study (#1522-03, Sawbones®, Pacific Research Laboratories Inc, Washington, USA) was made from polyurethane foam and the properties reported by the manufacturer were used (as reported in Section 2.2.1). The tibial and talar components of the Zenith™ TAR were made from biocompatible titanium alloy (Ti-6Al-4V), while the bearing component was manufactured from the ultra-high-molecular-weight polyethylene (GUR1050 UHMWPE). The properties for these materials were taken from http://www.matweb.com, and published materials (Hopkins et al. 2010, Froes 2015).

Table 3-3 Material properties assigned to the FE model

Instance	Material	Young's modulus (MPa)	Poisson's ratio
Tibial synthetic bone	PU #1522-03	210	0.3
Tibial component	Ti-6Al-4V	113,800	0.342
Bearing component	UHMWPE	850	0.4
Talar component	Ti-6Al-4V	113,800	0.342
Talar synthetic bone	PU #1522-03	210	0.3

The tibial and talar components of the Zenith™ TAR were initially tied to the tibial and talar synthetic bone respectively to model the fully constrained bone-implant interfaces. The contacts between tibial, talar, and bearing components were assumed to be frictionless. These constraints were subsequently examined in sensitivity tests described in further detail in Section 3.2.2.5. The interface between the analytical rigid plate and the tibial synthetic bone was

defined as a tie constraint to represent the experimental set-up where the synthetic bone was clamped to the housing on the crosshead.

3.2.1.3 Loads and Boundary Conditions

A boundary condition was assigned to the bottom surface of the talar synthetic bone to fully fix the simplified talar bone in all directions. The displacement and rotation of the analytical rigid plate was constrained in all directions except the vertical displacement to match to the experimental set-up.

An axial concentrated force was applied to the reference point of the analytical rigid plate (Figure 3-5). The rigid plate was used to distribute concentrated force over the entire cross sectional area at the top of the simplified tibial bone. The force applied to the tibial synthetic bone used was a compressive axial load of 3416 N, which matched the maximum value applied in the non-destructive experimental tests.

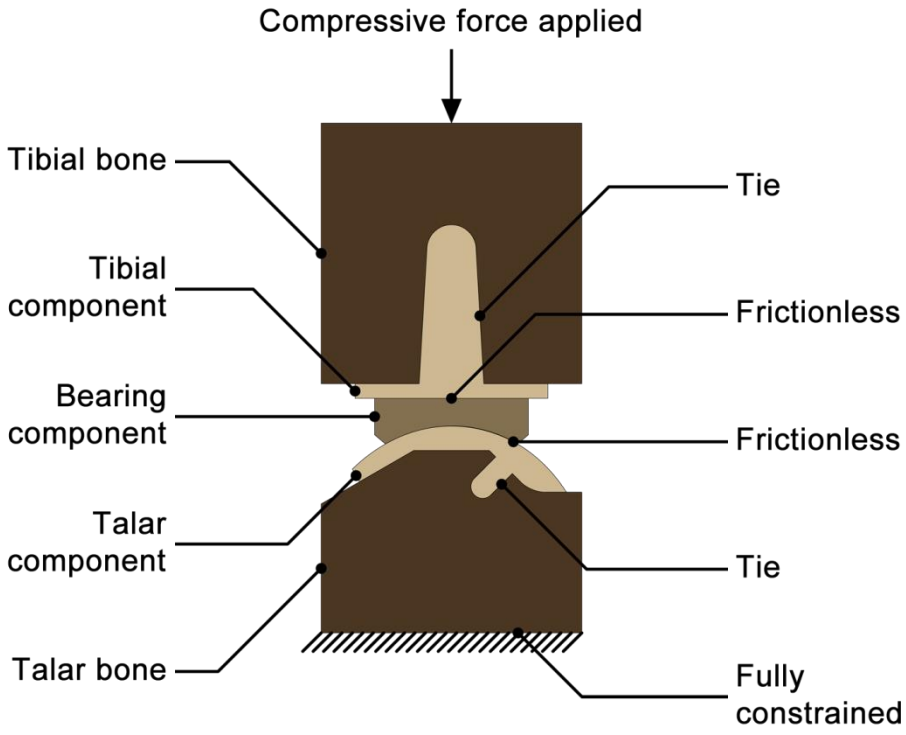

Figure 3-5 The FE model of TAR with synthetic bone

3.2.1.4 Output Data Measurements

In this study, three output variables: the von Mises stress (σ_{vm}), minimum principal strain (ε_{min}), and vertical displacement (u_y) were collected from FE models. These outputs were generally measured at three locations: one at the tip of the stem of the tibial component, and two at the tips of the two fixing pegs of the talar component. At each location, the values on both the synthetic bones and TAR components were measured. These measurements were used in the following studies except the validation.

3.2.2 Verification, Validation, and Sensitivity Studies

Two verification processes were performed in this study: code verification and a mesh convergence study. Three parameters (geometry, material properties, and interactions) were then evaluated through sensitivity studies to gain a better understanding of their effects on the analysis results. A comparison between the experimental results obtained from the Chapter 2 and the FE analysis results was subsequently performed as a method of validation.

3.2.2.1 Verification: Code

To verify that the contact algorithm employed in the Abaqus software was suitable for this study, a simplified articulation between the talar and the bearing components of the Zenith™ TAR was modelled and the results compared with those obtained from Hertzian contact theory. In the simplified model, the talar component was represented by a hemisphere with a diameter of 50 mm, while the bearing component was a rectangular prism with a spherical concavity (diameter = 60 mm) (Figure 3-6).

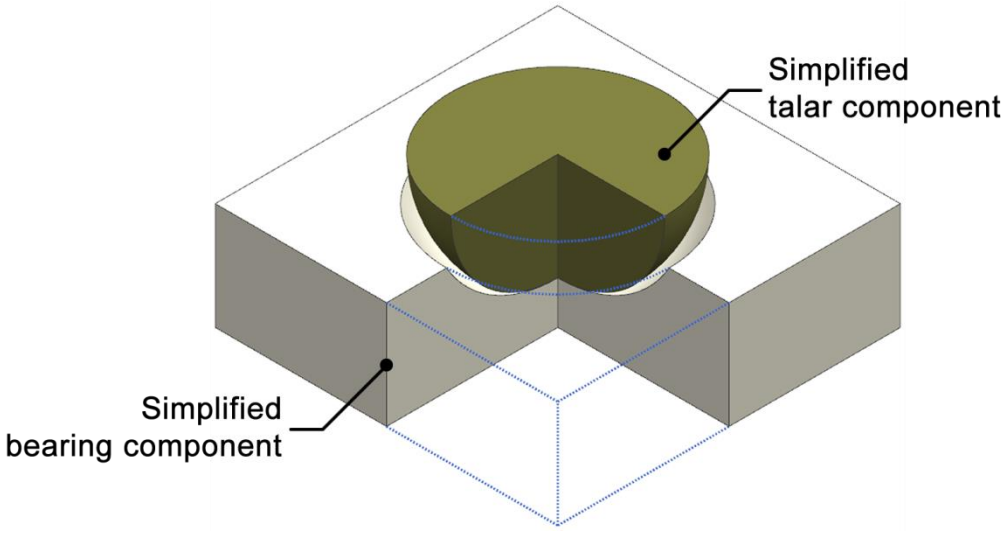

Figure 3-6 The simplified talar and the bearing components of the Zenith™ TAR

All simplified components were modelled as elastic materials. The talar component was assumed to be titanium alloy (Ti-6Al-4V) (Young's modulus of 113.8 GPa and Poisson's ratio of 0.342), while the bearing component ultra-high-molecular-weight polyethylene (UHMWPE) (Young's modulus of 850 MPa and Poisson's ratio of 0.4). The contact at the articulation was assumed to be frictionless.

The base of the simplified bearing component was fully fixed. As in the full model, a compressive force of 3416 N was applied to the simplified talar component through an analytical rigid plate (Figure 3-7). In the FE model, the total number of eight-node linear brick (C3D8R) elements used was approximately 200,000 as detailed in Table 3-4.

Table 3-4 Meshing information of the simplified talar and the bearing components

Instance	Element type	Approximate element size (mm)	Number of elements
Simplified talar component	C3D8R	1	61,590
Simplified bearing component	C3D8R	1	136,036

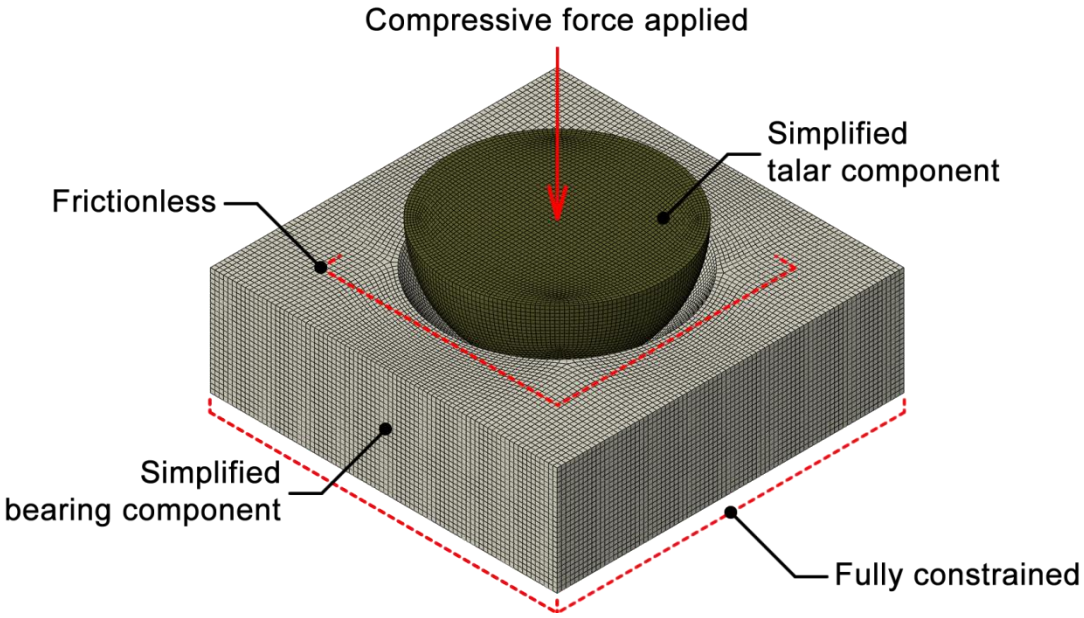

Figure 3-7 The FE model of simplified talar and the bearing components of the Zenith™ TAR

When the Hertzian contact theory was used to solve the above contact problem, the ball-in-socket articulation was assumed equivalent to a spherical indenter model, and the radius of the circle of contact (a) and maximum contact pressure (p) were calculated using the Equations 3-1 and 3-2 respectively (Fischer-Cripps 2007).

$$a^3 = \frac{3}{4}\frac{PR}{E^*} \qquad \text{Equation 3-1}$$

$$p = \frac{3}{2}\frac{P}{\pi a^2} \qquad \text{Equation 3-2}$$

Where P is the indenter load, R is the relative curvature of the indenter and the specimen, and E* is the combined modulus of the indenter and the specimen. R and E* can be obtained from calculation using the Equations 3-3 and 3-4 respectively.

$$\frac{1}{R} = \frac{1}{R'} + \frac{1}{R_S} \qquad \text{Equation 3-3}$$

Where R' is the radius of the indenter and R_S is the radius of the specimen. In this case, R_S is negative due to the concave surface of the specimen.

$$\frac{1}{E^*} = \frac{(1-\nu^2)}{E} + \frac{(1-\nu'^2)}{E'} \qquad \text{Equation 3-4}$$

Where E' and v', and E and v describe the elastic modulus and Poisson's ratio of the indenter and the specimen respectively.

In this study, the radius of the circle of contact and maximum contact pressure obtained between the FEA and calculation were compared to verify the FEA software.

3.2.2.2 Sensitivity Study: Geometry

At the development stage of the FE model of the Zenith™ ankle system, it was found that the mesh for the fillets of the tibial and talar components required an excessively large number of elements, and that removal of the fillets could substantially reduce the computational cost. A comparison between the predictions of the FEA of models with (Figure 3-8a) and without (Figure 3-8b) the edge fillets was therefore performed to evaluate the effect of such a simplification.

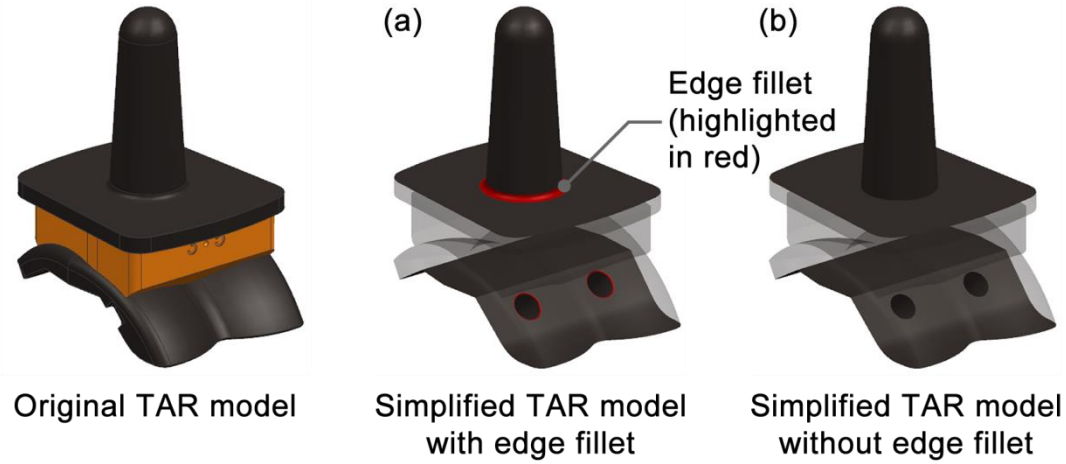

Figure 3-8 The FE model of the Zenith™ TAR with and without fillets

The quantities of the ten-node quadratic tetrahedral element used to mesh the synthetic bones and TAR components were approximately 408,000 and 370,000 for the models with and without the edge fillets, respectively. The detailed meshing information is shown in Table 3-5.

Table 3-5 Meshing information for the FE models with and without fillets

Instance	**Element type**	**Approximate element size (mm)**	**Element number**	
			FE model with edge fillet	**FE model without edge fillet**
Tibial synthetic bone	C3D10	1.2	217,081	211,248
Tibial component	C3D10	1.2	28,400	25,702
Bearing component	C3D10	1.2	20,191	20,191
Talar component	C3D10	1.2	26,023	19,534
Talar synthetic bone	C3D10	1.2	115,986	93,086
		Total	407,681	369,761

3.2.2.3 Verification: Mesh Convergence Study

A mesh convergence study was performed on the model without the edge fillet to choose an optimal mesh density for further studies. All parameters were the same as those reported in Section 3.2.2.2 except the quantity of elements. Seven mesh schemes were used with the element number approximately doubled each time from ~14,500 up to 900,000. More details of each mesh are shown in Table 3-6.

Table 3-6 Meshing information for each of the FE models used in the mesh convergence study

FE model #	Meshing information						
	Tibial bone		Tibial comp	Bearing comp	Talar bone	Talar comp	Total Qty
1	**Size**	8	4.4	2.2	3.9	4	-
	Qty	1,735	727	4,108	1,541	6,439	14,550
2	**Size**	5.8	3.2	1.7	2.5	3	-
	Qty	3,515	1,404	7,738	3,173	12,158	27,988
3	**Size**	4.3	2.7	1.3	1.9	2.2	-
	Qty	7,309	2,790	16,559	6,000	25,426	58,084
4	**Size**	3.2	2.1	1	1.4	1.6	-
	Qty	15,054	5,797	35,408	12,926	48,307	117,492
5	**Size**	2.5	1.6	0.8	1.1	1.2	-
	Qty	29,667	11,338	66,330	25,512	93,270	226,117
6	**Size**	2	1.3	0.6	0.88	0.9	-
	Qty	55,724	21,405	146,675	48,621	187,400	459,825
7	**Size**	1.5	1	0.48	0.7	0.67	-
	Qty	119,867	43,031	254,166	92,974	404,291	914,329

The results of the mesh convergence tests were used to determine the most optimum mesh size which was then used for all subsequent studies.

3.2.2.4 Sensitivity Study: Material Properties

Since the Young's modulus of the synthetic bone block may vary within a range, the effect of the material properties of the polyurethane foam on the FEA results was also investigated. This information will also be important for future studies representing real bone, where the range of Young's modulus will be greater.

Various models of Sawbones® Solid Rigid Polyurethane foam block are available in the market. Each model is differentiated by its density, and the manufacturer also informs that the density of each model may vary ± 10%. The density and the compressive modulus of each model provided by the manufacturer are shown in Table 3-7.

Table 3-7 The density (g/cc) and the compressive modulus (MPa) of each model of Sawbones® Polyurethane foam block (Data taken from the manufacturer's website http://www.sawbones.com [cited 5 Jul 2014])

Model	Density (g/cc)	Compressive modulus (MPa)
#1522-23	0.08	16
#1522-01	0.16	58
#1522-02	0.24	123
#1522-03	0.32	210
#1522-04	0.48	445
#1522-05	0.64	759
#1522-27	0.80	1148

The compressive modulus was plotted against the density, and it was found that the relationship was perfectly fitted ($R^2 = 1$) by a power law relationship, the equation of which was $E = 1737.8\rho^{1.8557}$ (Figure 3-9).

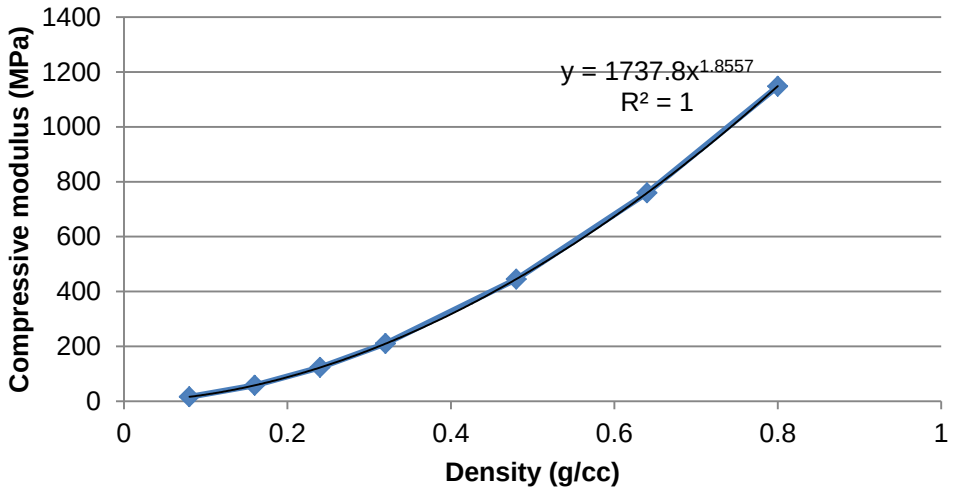

Figure 3-9 The plot of compressive modulus (MPa) against density (g/cc) for the Sawbones® polyurethane foam block data in Table 3-7 showing the power trendline fitting

The compressive modulus obtained from manufacturer for the chosen model was 210 MPa, but using the above relationship, the effect of varying of the density by - 10% might make the modulus as low as approximately 173 MPa. These two values were therefore used to investigate the effect of the Young's modulus of the synthetic bone on the analysis results.

3.2.2.5 Sensitivity Study: Interactions

The effect of different interactions at the bone-implant interfaces was investigated because the coefficient of friction at the bone-implant interfaces may vary and could not be easily characterised. In a previous study, friction tests between cancellous bone cubes and porous-surfaced metal plates have been conducted to determine the coefficient of friction at the time of implantation of non-cemented prostheses (Rancourt et al. 1990). The cubes were pressed against the porous surface by an adjustable normal force; the normal force applied and the friction resistance were then used to calculate the friction coefficient, which was found to vary within a range from 0.3 to 1.3. In the clinical case, there is expected to be bony ingrowth, so the interaction is likely to change over time. Therefore, to cover the range of different interface conditions, three cases were examined here. The three types of interaction, tied, frictionless, and using a coefficient of friction of 1.3, were simulated and compared. A total of five FE simulations were performed using the different interface interactions shown in Table 3-8.

Table 3-8 Different interface properties assigned to the five FE models in the interaction sensitivity tests

FE model #	**Interface property**	
	Tibial bone-implant interface	**Talar bone-implant interface**
1	Tie	Tie
2	Tie	Frictionless
3	Tie	Friction (μ = 1.3)
4	Frictionless	Frictionless
5	Friction (μ = 1.3)	Friction (μ = 1.3)

In this study, another reference point was especially created for the FE models with friction/frictionless tibial bone-implant interfaces. The reference point was coupled to the hemispherical section of the tip of the tibial stem in order to apply a boundary condition to constrain rotation of the component about the vertical axis, which was necessary to prevent a convergence problem in the model due to excessive movement.

3.2.2.6 Sensitivity Study: Bone Structure

Generally, long bones contain two distinct morphological types of bone: cortical and cancellous. In the previous studies in this chapter, the structure and material properties of the simplified bones represented only behavior of cancellous bones, mimicking the experimental set-up described in Chapter 2. To investigate the biomechanical importance of the cortical bone on the FEA results, as a precursor to modelling the whole natural bone, 3-D geometries including a simplified representation of this type of bone were therefore created by adding a uniform layer of cortical bone to the outer sides of the bone cuboid. Two different configurations of the cortical bones layers (weight-bearing and non-weight-bearing) were evaluated in this study (Figure 3-10). The weight-bearing cortical structure had an overlapping region at the bone-implant interface in transverse plane, while in the non-weight-bearing structure the cortical bone did not contact the implant.

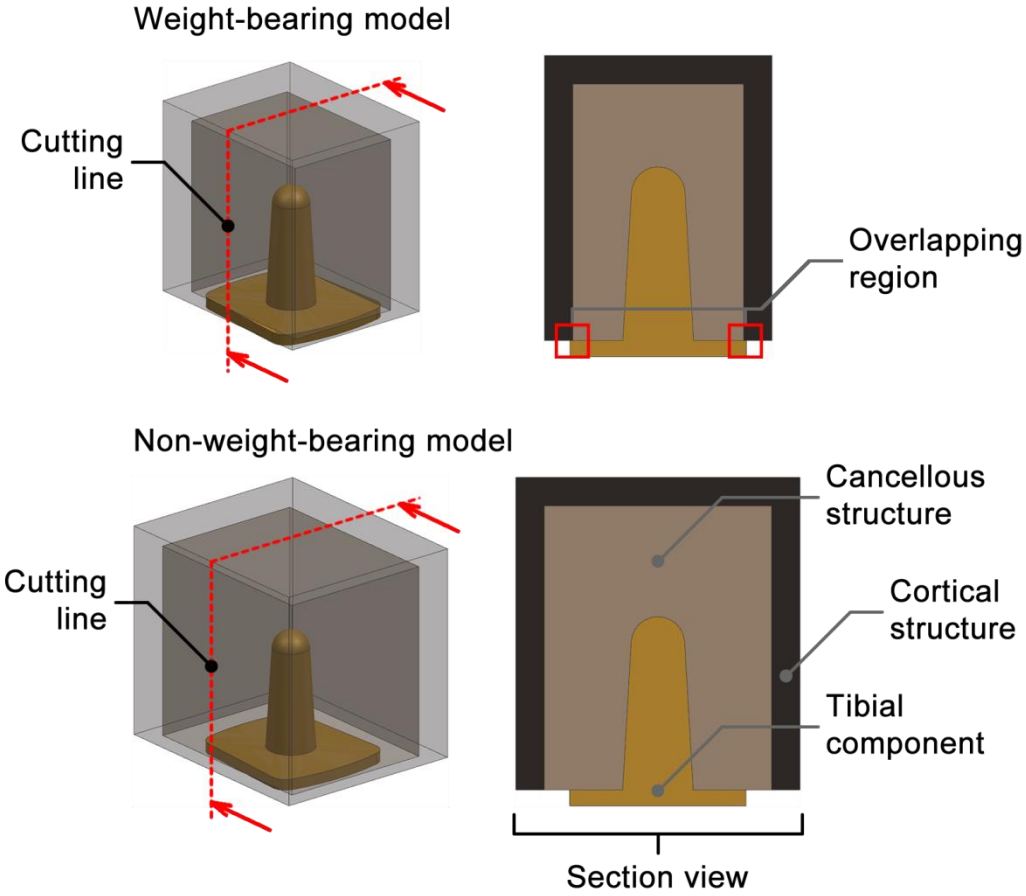

Figure 3-10 Weight-bearing and non-weight-bearing cortical structures with their section views showing where there was overlapping between cortical bone and the tibial component

The dimensions of the simplified bone were the same as the ones used in validation process (Section 3.2.1.1). The 3-D model of the cortical shell structure was created by thickening the duplicated outer surface of the original simplified bone on all external sides using the 'Offset Face' command in the NX software. The extension was performed in an inward and outward direction for the weight-bearing and non-weight-bearing structures respectively. The overlapping geometry between the original synthetic bone and the weight-bearing shell structure was then removed. The thickness of the shell structure was assigned to be 5 mm that was relatively thick compared to the natural structure of bone to determine the maximum likely effect of cortical structure on the FEA result.

As a first approximation, values for the cortical bone were taken from the literature (Chu et al. 1995, Tuncer et al. 2013). An elastic material model was used with a Young's modulus and Poisson's ratio of cortical structure were 14 GPa and 0.35 respectively. The cortical structure was tied to the synthetic cancellous bone to model the fully constrained single bone component. Again C3D10 elements were chosen to mesh the cortical shell structure, the approximate sizes of which were the same as the corresponding original synthetic bone. The approximate element size and the number of elements of each instance are shown in Table 3-9.

Table 3-9 Meshing information of the FE model with and without cortical structure

Instance	**Element type**	**Approx element size (mm)**	**Number of element**		
			Bone without cortical structure	**Bone with cortical structure**	
				Non-weight-bearing	**Weight-bearing**
Tibial cortical structure	C3D10	2.5	-	34,892	22,988
Tibial synthetic bone	C3D10	2.5	42,326	42,326	23,966
Talar synthetic bone	C3D10	1.2	156,395	157,358	103,870
Talar cortical structure	C3D10	1.2	-	165,028	116,537

Moreover, the bone-implant interface of each model was represented by each of the three different conditions described in Section 3.2.2.5. Therefore, there were nine FE models in total that were examined in this study.

3.2.2.7 Validation: Plastic Deformation of Synthetic Bone

The plastic deformation data (location and deformation depth) of the talar synthetic bone obtained from the FEA were validated using the corresponding experimental results undertaken previously (Section 2.3.2.3).

In this study, the fully constrained bone-implant interface model without cortical structure was used with the elastic material properties described previously. In addition, the plastic behavior of the polyurethane foam and UHMWPE were defined using an elastic-perfectly plastic material model. Compressive yield stresses of 8.4 MPa and 13.8 MPa were assigned to the foam and UHMWPE respectively. The compressive load applied was increase to 8,000 N to match the destructive experimental test undertaken in Chapter 2.

3.3 Results

3.3.1 Verification: Code

The contact radii and the maximum contact pressures predicted by the Hertzian contact theory and FE model are presented in Table 3-10. The relative error of the prediction for the former output variable was only 1.95%, but for the latter was relatively high at 16.46%. The reasons for these discrepancies are discussed in Section 3.4.

Table 3-10 The output data predicted by the Hertzian contact theory and FE model

Prediction method	**Output variable**	
	Radius of contact circle (mm)	**Maximum contact pressure (MPa)**
Hertzian contact theory	7.26	30.94
Finite element analysis	7.12	36.49

3.3.2 Sensitivity Study: Geometry

The removal of the fillets had little effect on the outputs. The differences in von Mises stress between the two models were less than 4% at all locations except the node located on the talar bone where the difference was 9.86% (Figure 3-11).

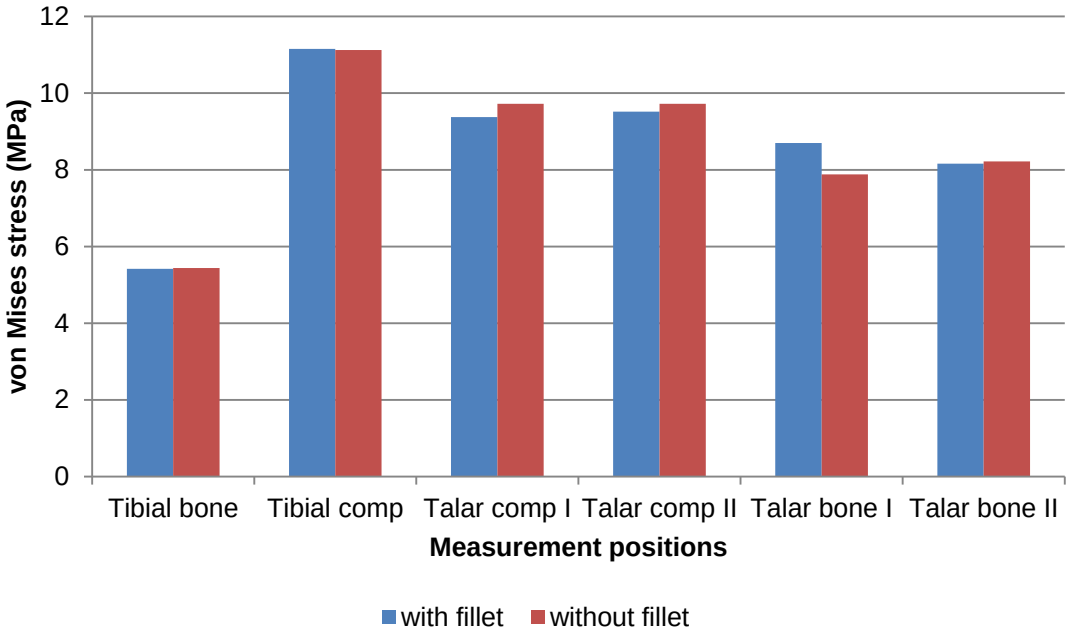

Figure 3-11 von Mises stress (MPa) measured at all locations of interest on the models with and without fillets

The differences in minimum principal strain and vertical displacement were less than 8% and 1% at all locations respectively (Figure 3-12 and 3-13). Moreover, as expected, the computational time of the model without the fillet was considerably less, with a reduction of approximately 19%.

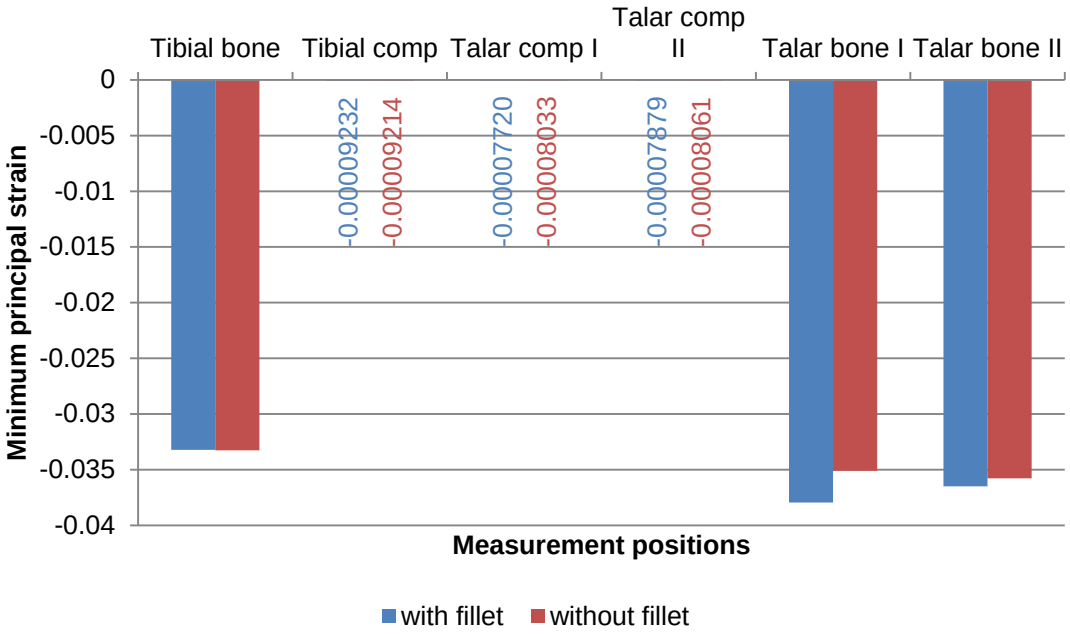

Figure 3-12 Minimum principal strain measured at all locations of interest on the models with and without fillets

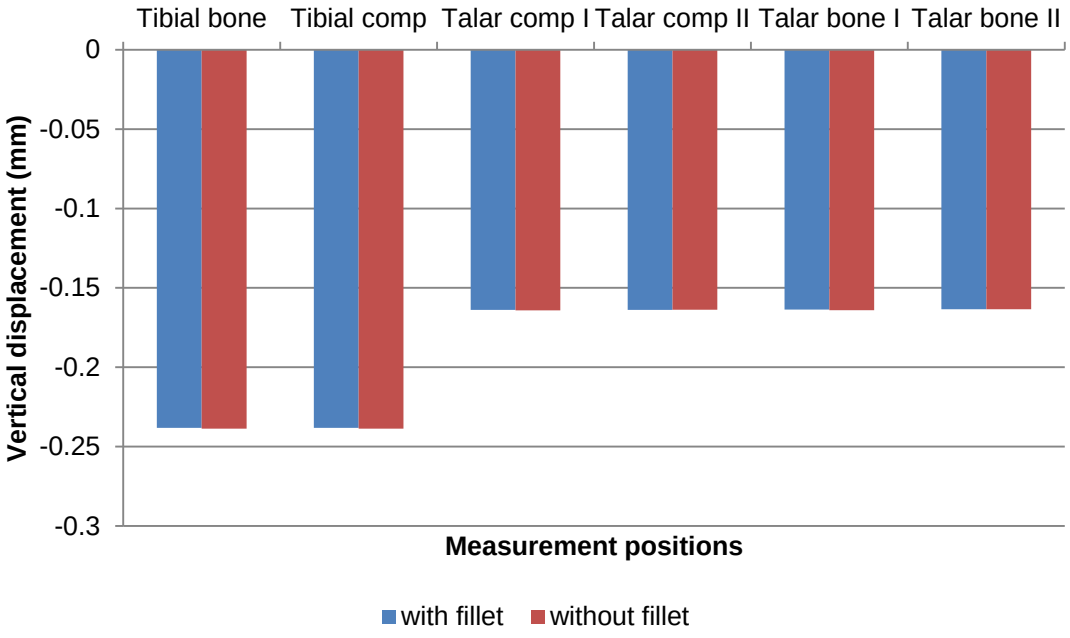

Figure 3-13 Vertical displacement (mm) measured at all locations of interest on the models with and without fillets

3.3.3 Verification: Mesh Convergence Study

The mesh convergence study showed that the model with ~226,000 elements, FE model #5 (from Table 3-6), was the most suitable for further analyses. Compared to the model with twice as many elements, the differences in von Mises stress, minimum principal strain, and vertical displacement measured at the locations of interest on the tibial synthetic bone were 1.22%, 0.42%, and 0.08% respectively (Figure 3-14). The running time of this model was about three hours, while the model with twice as many elements needed about 11 hours using four processors of an Intel® Xeon® Processor X5560.

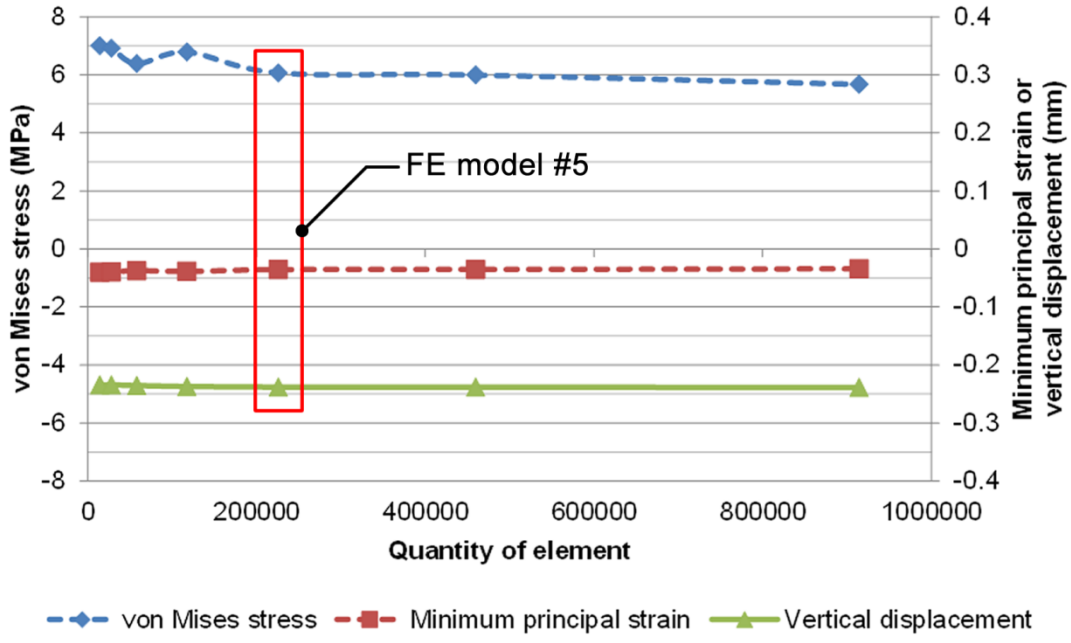

Figure 3-14 All output variables measured at the locations of interest on the tibial synthetic bone in the mesh convergence study

3.3.4 Sensitivity Study: Material Properties

The Young's modulus had considerable effect on both minimum principal strain and vertical displacement, but negligible effect on von Mises stress. The differences in von Mises stress at all measured locations caused by the variation in the Young's modulus were less than 1% (Figure 3-15). However, the differences in minimum principal strain were about 19% at all nodes located on the tibial and talar bones (Figure 3-16). The percentage differences in vertical displacement were close to 18% at all measured locations (Figure 3-17).

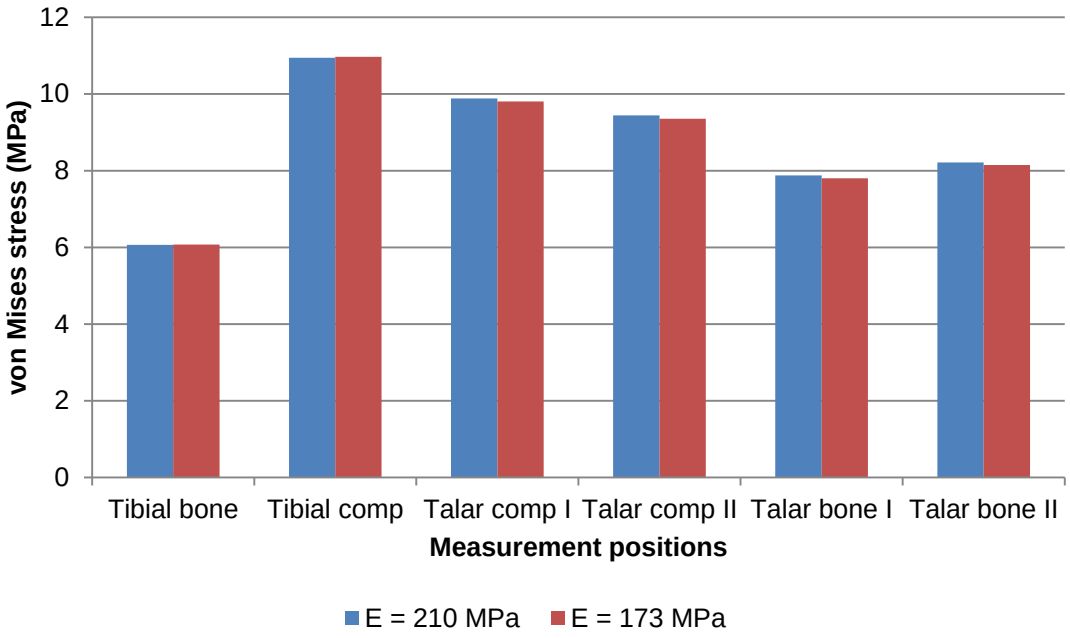

Figure 3-15 von Mises stress (MPa) measured at all locations of interest on the models with different elastic moduli

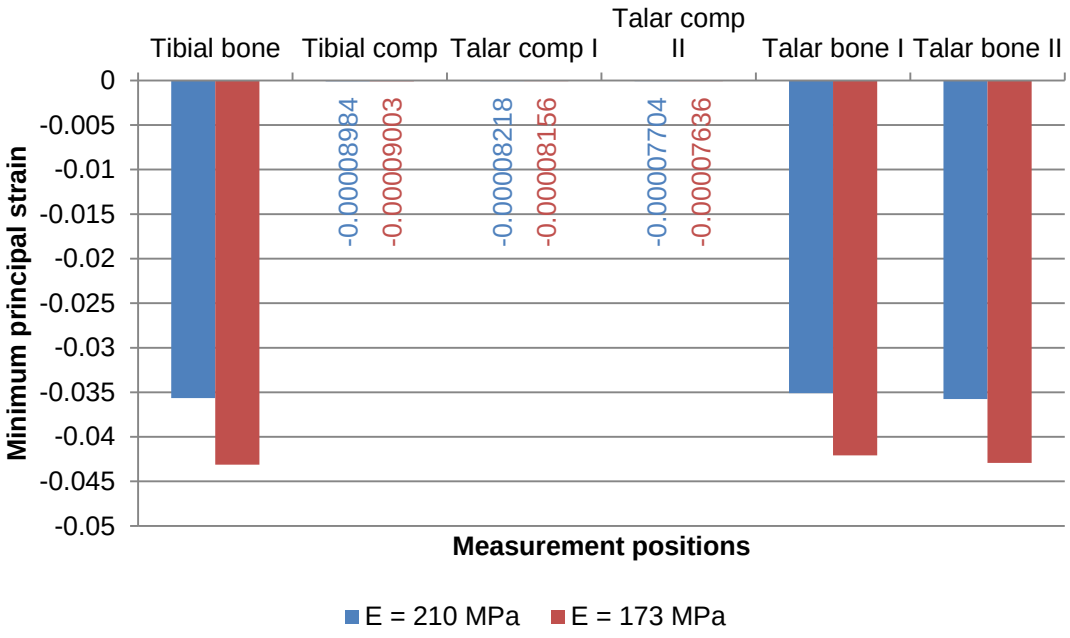

Figure 3-16 Minimum principal strain measured at all locations of interest on the models with different elastic moduli

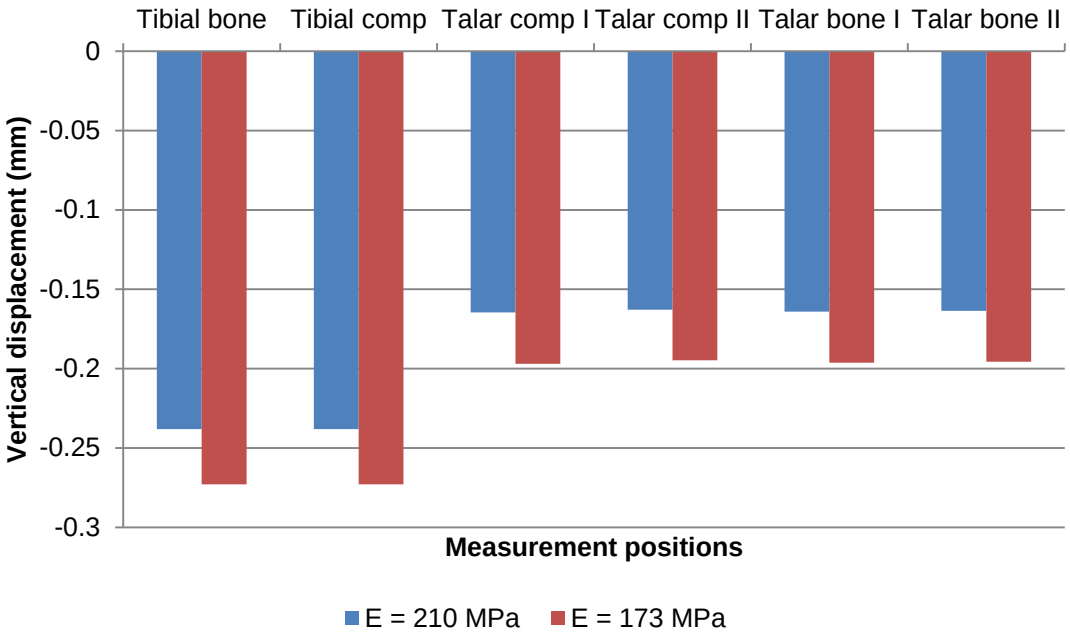

Figure 3-17 Vertical displacement (mm) measured at all locations of interest on the models with different elastic moduli

3.3.5 Sensitivity Study: Interactions

The interaction between the bone and implant had a considerable effect on the outputs except at two nodes located on the talar bone. The predictions of the FE model with frictionless interaction and those of the model with coefficient of friction of 1.3 were exactly same. Compared to the tie interaction, the von Mises stress, minimum principal strain, and vertical displacement at the node located in the tibial bone of the model with frictionless interaction increased by about 315%, 212%, and 10% respectively (Figure 3-18).

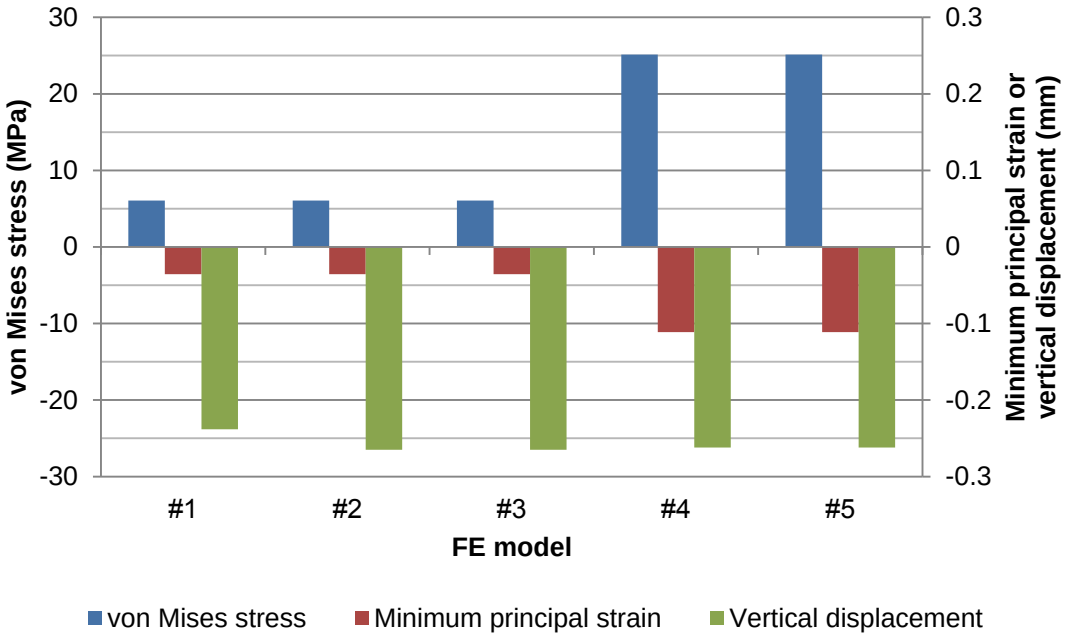

Figure 3-18 All output variables measured at the locations of interest on the tibial synthetic bone in the models with different bone-implant interface conditions (from Table 3-8)

3.3.6 Sensitivity Study: Bone Structure

The results of the study with the inclusion of the cortical bone layer are presented in Table 3-11. The fully constrained bone-implant interface model with the weight-bearing cortical structure was not successful in analysis due to an overconstraint problem. Therefore, FEA results were obtained from only eight different FE models.

The existence of the cortical structure had considerable effect on reducing von Mises stress and minimum principal strain in the synthetic cancellous bone, especially when the cortical structure was weight-bearing (i.e. overlapping the implant). As with the results obtained in Section 3.3.5, the predictions of the FE model with the frictionless interaction and those of the model with coefficient of friction of 1.3 were exactly same, and higher than the models with tie constraints. Compared to the FE model without the cortical structure, both the von Mises stress and minimum principal strain at a node located in the tibial bone decreased by about 47% (non-weight-bearing) and 75% (weight-bearing) respectively.

Table 3-11 The output variables measured at the node in the tibial bone obtained from the analyses of the FE model with and without cortical structure

Bone-implant interface condition	von Mises stress (MPa)			Minimum principal strain		
	Bone without cortical structure	Bone with cortical structure		Bone without cortical structure	Bone with cortical structure	
		Non-weight-bearing	Weight-bearing		Non-weight-bearing	Weight-bearing
Tie	5.46	2.71	n/a	-0.0317	-0.0158	n/a
Frictionless	22.21	11.8	5.57	-0.0981	-0.0521	-0.0246
Coefficient of 1.3	22.21	11.8	5.57	-0.0981	-0.0521	-0.0246

3.3.7 Validation: Plastic Deformation of Synthetic Bone

Good agreement was found in the location of damage and average depth of plastic deformation in the synthetic bone. The largest deformations in both experimental and FE models were in the same location which was on the talar synthetic bone at the region where the most posterior edge of the talar component was located (Figure 3-19).

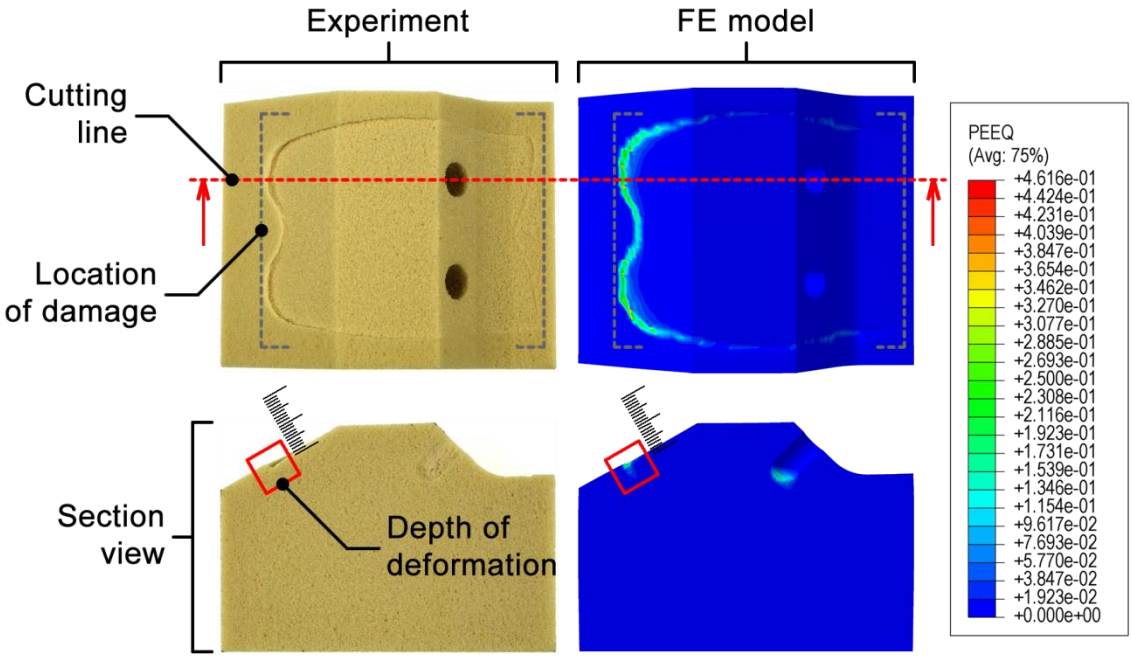

Figure 3-19 The locations of deformation of talar synthetic bone obtained from both experimental and FE models

The average deformation depths at the most posterior region of the talar bone-implant interface of both experimental and FE models were compared. The difference between both results was approximately 3.10%, and these results are presented in Table 3-12.

Table 3-12 The depth of deformation measured from both experimental and FE models

#	Location of measurement - distance from the mid-plane (mm)	Depth of deformation (mm)					
		Experiment			Finite element analysis		
		Left	Right	Average	Left	Right	Average
1	7	0.2700	0.2200	0.2450	0.2482	0.2499	0.2491
	8	0.2700	0.2200	0.2450	0.2492	0.2496	0.2494
	9	0.2700	0.2200	0.2450	0.2500	0.2489	0.2495
2	7	0.2600	0.2200	0.2400	-	-	-
	8	0.2600	0.2200	0.2400	-	-	-
	9	0.2600	0.2200	0.2400	-	-	-
3	7	0.2700	0.2100	0.2400	-	-	-
	8	0.2700	0.2100	0.2400	-	-	-
	9	0.2700	0.2100	0.2400	-	-	-
	Average	0.2667	0.2167	0.2417	0.2491	0.2495	0.2493
	SD	0.0050	0.0050	0.0025	0.0009	0.0005	0.0002

Moreover, the average contact pressure measured at the interface between the tibial and bearing components obtained from the fully constrained bone-implant interface model without cortical structure in Section 3.3.5 (4.091 MPa) was close to the corresponding value obtained from the non-destructive test in section 2.3.2.2 (3.997 MPa). The difference between both values was 2.32%.

3.4 Discussion

Only a few FEA studies have been undertaken previously to analyse the mechanical effects of ankle replacement surgery. Due to limited studies of TAR using FEM to date, there is potential for a wide variety of investigations in this field to fill the knowledge gap compared to studies of hip and knee replacements. Finite element analysis of the TAR can be used to understand the mechanism of failure of the current prostheses or to predict the possibility of failure to improve new designs. To ensure that the FE model is robust, verification, sensitivity studies, and validation are necessary. Therefore, in this study, a FE model was developed for a TAR and a series of verification and sensitivity studies were performed to prepare for further more clinically relevant studies.

3.4.1 Verification

3.4.1.1 Code Verification

Code verification for commercial software is usually expected to be accomplished by the developer. However, to ensure that the meshed model is analysed correctly, code verification in this study was performed by comparing the contact radius and maximum pressure between the results obtained from the FEA and Hertzian contact theory, which was also used in other studies in the same field (Elliot et al. 2014). The negligible difference (1.95%) in contact radii between the FE model and Hertzian contact theory provides verification not only for the code but also for the procedure that is used in the present study to solve contact problems. The larger difference (16.46%) in maximum contact pressure prediction obtained between both methods was thought to be an effect of the Young's modulus. The relatively low elastic modulus caused the large contact area, which breaches the assumption of Hertzian theory that assumes small strain conditions. To explain this, another test was undertaken. The elastic modulus of the UHMWPE component was artificially increased and both the FE and Hertzian analyses repeated. It was found that the difference between the FE-predicted contact pressure and Hertzian theory became less than 5% when the UHMWPE modulus was increased ten-fold. A further ten-fold increase in modulus caused the contact region to become very small, meaning that errors due to mesh resolution also became a factor, so the difference did not continue to decrease, as shown in Table 1-3.

Table 3-13 The output data predicted by the Hertzian contact theory and FE model

Young's modulus (MPa)		Radius of contact circle (mm)			Maximum contact pressure (MPa)		
Ti-6Al-4V	UHMWPE	Hertzian theory	FEA	Diff (%)	Hertzian theory	FEA	Diff (%)
113800	850	7.26	7.12	1.95	30.94	36.49	16.46
113800	8500	3.45	3.74	8.07	137.26	144.03	4.81
113800	85000	1.89	1.92	1.57	455.32	484.51	6.21

3.4.1.2 Mesh Convergence Study

The mesh verification was used to identify the most appropriate mesh scheme for the system. In this case, an element size in range of approximately 0.8-2.5 mm was found to be optimum because doubling the mesh density only introduced a very small change in the results. Similarly, Terrier et al. used an element with average size of 0.7 mm to mesh their TAR model in the regions of interest and larger elements elsewhere (Terrier et al. 2014).

3.4.2 Validation

3.4.2.1 Plastic Deformation of Synthetic Bone

There was good agreement, not only the contact pressures, but also in the location and size of plastic deformation when the FE model was compared to the experimental results reported in Chapter 2. There was a little difference (2.32%) in contact pressures obtained between the FE model and pressure mapping sensor. In this case, the difference was thought to be affected by small inaccuracies in the sensor. This is because the interface between the tibial and bearing components was not such a complex system. The entire compressive force (3416 N) was assumed to be transmitted over all area of the top surface of the bearing component (832.3 mm^2), therefore, the contact pressure at this region can be simply calculated by dividing the load by contact area. The calculated value is 4.104 MPa that is closer to the FEA output (0.32%) than experimental measurement (2.64%).

The locations of plastic deformation on the FE and experiment models were similar at the posterior region of the talar bone-prosthesis interface. As described in Section 2.4.2.3, there were not any fixing parts to provide support in this region. The fixation not only provides constraint of the component in a certain plane, but also shares the load over a larger area using the tip and the

skin friction. Therefore, the large damage on the talar synthetic bone could be a result of the lack of fixation features in this region.

Although the sizes of plastic deformation between each side of the mid-plane of the FE model were expected to be the exactly same, there was a very small difference between both values (0.16%). This was the effect of the geometries of the elements of the model on each side, which differed slightly. Therefore, it was better to use average values for comparison. Average depths of deformation obtained from both the FE and experimental models were close (with a difference of only 3.10%). The value obtained from the experimental testing was the lower. This can be explained because the material was modeled as elastic-perfectly plastic in the FE model, where there was not any resistance to the load applied after reaching the yield point, but the material behavior of the experimental model was different, with the elastic modulus gradually increasing after the yield point due to densification of the foam material. Therefore, a smaller plastic deformation in the experimental model was expected by the real-world behavior of the foam material.

Overall, these good agreements provide assurance that the model is able to predict the synthetic bone behavior and likely location of failure, and give confidence that the model can be extended to examine more clinically relevant cases.

3.4.3 Sensitivity Studies

3.4.3.1 Geometry

The present study has also identified the importance of some parameters of the Zenith TAR system for future studies. For example, since the fillets of the TAR only had a negligible effect on the outputs, it is reasonable not to consider them in the model. Such a simplification not only makes the mesh procedure easier but also considerably reduces the computational cost. Although these fillets were located at the regions of bone-prosthesis interface, their small sizes compared to the entire area of load-bearing had not much effect on the overall output variables and did not affect the load distribution. However, the effect of removal of these features appeared larger on the talar bone than the tibial bone. This might be because the measured nodes on the talar bone from the models with and without fillets could not be taken at exactly the same coordinates.

3.4.3.2 Material Properties

In this study, it was found that the stress in the model was relatively insensitive to the Young's modulus of the Sawbones®. This is not surprising because for the studied load-driven case, the effective stress is approximately a measure of the internal force experienced per unit cross section area, so would not be affected by the Young's modulus. Moreover, since the strain is the product of the stress and the Young's modulus, it would therefore be expected to be approximately proportional to the Young's modulus. This explains the 19% difference in the strain between the results obtained from the two Young's moduli because the difference between the two Young's moduli is approximately 19%. Therefore, an accurate measure of the modulus is necessarily required to avoid the error caused by material uncertainty.

3.4.3.3 Interactions

In this sensitivity study, the output variables measured in the tibial bone were of greatest interest. Therefore, in the first three cases, any changes of properties of the talar bone-prosthesis interface had little effect on the results. The highest von Mises stress concentration on the tibial bone was located around the tip of the stem for the fully constrained case, but at the tip of the stem for the non-constrained (frictionless and $\mu = 1.3$) cases. The fully bonded properties could maintain the geometry of tibial bone-implant interface during load application to continue to distribute load onto the entire interface. The non-constrained cases were different, with the full bone-prosthesis interface failing to be maintained. Therefore, an amount of load was only borne by the tip of the stem that was perpendicular to the direction of the load causing a high concentration of stress at this location. In a like manner, the reduction of area of the load-bearing region led to higher magnitudes of stress experienced. This was also the reason for the increase in minimal principal (compressive) strain. The similar results obtained between the frictionless and coefficient of friction of 1.3 cases, might be because some of the surface was relatively parallel to the direction of load applied (around the stem), and the deformation of the materials meant there would be a separation at this interface, so therefore the addition of friction had little effect.

The high sensitivity of the stress and strain in the tibial bone to the types of bone-component interface has important clinical and experimental implications. First, it is likely that the bones are not fully bonded to the components immediately after the surgery. If this is the case, the stress and strain in the bone will be considerably higher than the ideal case (i.e. fully bonded) shown in the present study. Such an increase in the stress and strain in the bone may have a severe adverse effect on the performance of the replacement. Second, since the constraint at the bone-component interface considerably affects the results, the method by which the bones and components are secured should be carefully considered in future experimental studies.

However, the severity in the clinical cases may be lower. This is because the structure of the surrounding compact bone, which is much higher in stiffness, may better maintain the shape of bone-prosthesis interface and improve the distribution of the load or share load-bearing directly. The effect of the cortical bone was therefore considered in an additional sensitivity study.

3.4.3.4 Bone Structure

The results of the addition of the cortical bone layer demonstrated that the cortical bone clearly affects the mechanical response. The effect is greatest when the bone is in contact with the implant, providing a direct load transfer into the cortical bone, but even when it is not, it still provides some support by preventing the cancellous bone from displacing outwards laterally. This was similar to the existence of the fully bonded tibial bone-implant interface that helped to maintain the geometry of the interface as the bone deforms. In this study, the cortical bone geometry was not modelled realistically, but now that the effect has been shown, more realistic geometry should be considered. Therefore it is important that the cortical shell is included in future models and consideration given to whether or not the implant is in contact.

3.5 Summary

A simplified FE model of TAR with synthetic bone was developed. A series of verification, validation, and sensitivities studies were then used to determine the degree to which the model is a sufficiently accurate representation of the real-world for its intended use and to identify the effect of altering the input parameters upon the FEA results. The mesh convergence study was performed to determine appropriate element size for meshing. The contact pressure and location and size of deformation obtained from Chapter 2 were compared with the corresponding FEA results for validation. Some input parameters (material properties, interactions, and bone structures) were evaluated to assess their importance. The following conclusions can be drawn from this study:

1 The code verification ensured that both the software and the procedures used in model development were suitable for this type of study. The mesh verification was also used to determine the appropriate element size for meshing the FE model.

2 Some dominant input parameters and their effects were identified. The small features on the FE model that were proven to have little effect on the results were removed to optimize the computational expense. The material properties, interactions, and bone structures that have considerable effect on the results were assigned to the FE model with care to mimic the real-world situation as much as possible.

3 Clinically, if the bones are not fully bonded to the components after the surgery, the stress and strain in the bone may be considerably higher than the ideal case leading to failure in implantation. This finding may be useful for the patient during rehabilitation.

4 Good agreement between the experimental and FEA results in location and size of the plastic deformation provides assurance that the model is able to predict the synthetic bone behavior and likely location of failure, and gives confidence that the model can be extended to examine more clinically relevant cases.

Chapter 4 Construction of the FE Model of the Natural Ankle Geometry

4.1 Introduction

The development of an anatomical FE model of the ankle is introduced in this chapter. The model includes three ankle bones: the tibia, fibula, and talus. Although the fibula is considered to be a non-weight-bearing structure in this study and is not included in the FE model, it is necessary to create this bone as an anatomical landmark to locate an appropriate position for the talus to represent the physical posture of the foot during gait. The methods of developing realistic geometries and the material properties of the ankle joint in terms of cortical and cancellous bones and cartilage are detailed. The boundary and loading conditions used in the FE model are also presented. The various positions of the talus in the ankle are considered to illustrate the effect of the different positions of the talus on the FEA results of the ankle bones.

4.2 Material and Methods

4.2.1 3-D Model Construction of Natural Ankle

4.2.1.1 Medical Imaging Data

The medical imaging data used to create 3-D model of ankle bones in this study were cryosectional images downloaded with permission from the National Library of Medicine's Visible Human Project® (https://www.nlm.nih.gov/research/visible/visible_human.html).

The ankle bone of the male cadaver was selected for this study. The cadaver was from a 38 year old white male who died of court-ordered lethal injection. His height and weight were 1.8 m and 90 kg respectively. The cadaver was embedded in a gelatin solution and then frozen to provide stability for the transverse cryomacrotoming process at 1 mm interval. A full colour image was captured after each cutting, and there are consequently 1878 anatomic slices in total (Spitzer et al. 1996).

The database contains several formats of 3D images, such as .raw, .rgb, and .png formats. A total of 615 slices of the leg region of the male cadaver, in 24 bit RGB colour in .raw format, were chosen to develop the ankle bone models. The resolution of each slice was 2048 pixels by 1216 pixels, and the width and height of each pixel and the separation were 0.33 mm, 0.33 mm, and 1.00 mm respectively. The reason for choosing the anatomical images (.raw) was because their resolution was better than both the MRI (256 × 256 pixels) and

CT images (512 × 512 pixels), and their type of file was compatible with the existing software used. A sample of the imaging data is illustrated in Figure 4-1.

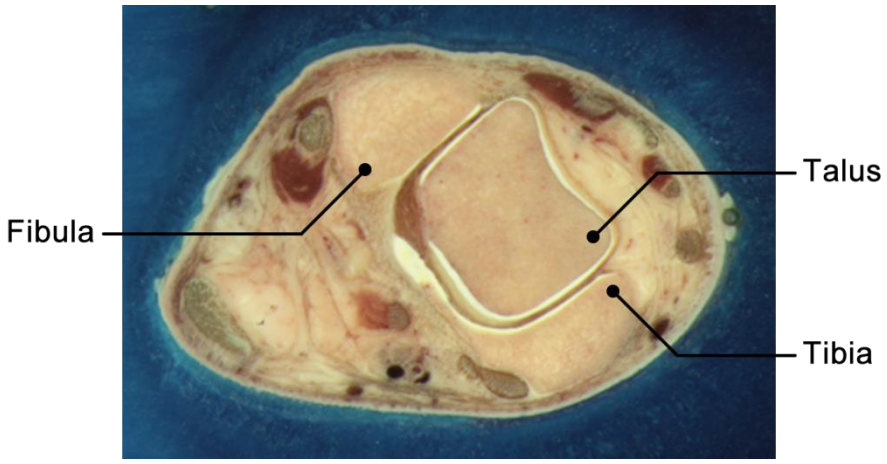

Figure 4-1 Sample of medical imaging data collected from database of the Visible Human Project® showing a section through the ankle bone

4.2.1.2 Image Processing

The models of natural ankle were created from the cryosectional images with the aid of image processing software, ScanIP™ (version 5.1, Simpleware Ltd, Exeter UK), and 3-D modeling software, Geomagic Studio® (version 2014.0.1, Geomagic Inc, North Carolina USA). Although the ScanIP™ software could be used to create a 3-D model for further development using CAD software, a 3-D model with NURBS (non-uniform rational B-splines) surface that was thought to provide better quality for meshing was preferable. There was not the capability to generate NURBS surfaces in the available version of the ScanIP™ software at the time of this study, therefore, the Geomagic Studio® software that included this function was used for this purpose.

4.2.1.2.1 Creating Surface Model Using ScanIP™ Software

A typical workflow within the ScanIP™ software includes importing 3-D images, segmenting regions of interest, assigning desired output parameters, and exporting generated model. The software creates geometry of 3-D surface model from a set of 2-D data by combining pixels on adjacent images into voxels (volumetric pixels). The width and height of each pixel and the separation of the slices identify the three dimensions of the voxel. The segmenting of each slice defines the boundary of the model.

In this study, the 3-D surface models of ankle bones were generated from medical imaging data with the aid of the ScanIP™ software through the following steps.

1 The stack of raw images were imported with assigned spacing (size of each voxel) values and volume settings corresponding to the input data.

2 Because the images obtained from the National Library of Medicine's Visible Human Project® were the scanned data of whole legs, excessive data other than the region of right ankle were eliminated using the crop function. In this case, 370 and 680, 160 and 770, and 400 and 570 were assigned to lower and upper boundaries of X, Y, and Z respectively. Only 170 slices of cryosectional images were necessary to be used to create the ankle surface model instead of 615 slices imported. After cropping the excessive data, the file size was dramatically reduced from approximately 1.24 GB to 0.04 GB.

3 The original resolution of (width, height, and separation) 0.33 × 0.33 × 1.00 mm was resampled to the same resolution in all dimensions (0.33 × 0.33 × 0.33 mm) to improve the quality of the elements. This technique is suggested in the ScanIP™ reference guide to resample the spacing to be a cubic to obtain the best element qualities.

4 The segmentation of the region of interest was simply performed using the threshold function to set a range of greyscale values to be added to the segmentation mask. In this case, a range of greyscale could not be perfectly differentiated using the threshold function, therefore, segmentation on almost all image slices needed to be performed manually with the aid of the paint function. The initial mask was created using threshold segmentation function with upper and lower values of 255 and 210 respectively. After the mask had been created, the paint function was then used manually to select the region of interest by both paint and unpaint commands on each slice. The sections related to the tibia throughout the set of slices were masked in this step.

5 Basic filters, such as morphological and smoothing filters, were then used to enhance the quality of the data. In this case, a morphological filter with the close option (the structuring element (ball) radius of 2 pixels in all directions) was used to get rid of small holes on the segmentation mask, and smoothing using a recursive gaussian filter (with the gaussian sigma of 1.98 mm in all directions) was used to reduce detail, making the edge of segmentation mask smoother (Figure 4-2b).

6 It was found that there was not sufficient image contrast between the cancellous and cortical bone to use the images to segment one region from the other. Instead, the cortical shell was assumed to be a constant thickness of 1 mm. The same value was also used for the thickness of the cortex in the study of Miller et al. (Miller et al. 2004). Similarly, in the study of Burghardt et al., the average thickness of cortical bone of the distal tibia of 40 subjects measured using high-resolution peripheral quantitative computed tomography (HR-pQCT) was 1.25 ± 0.26 mm (Burghardt et al. 2010). Although this was a simplification, the effect of cortical stiffness was considered further in a sensitivity study (Section 5.2.4). In order to generate the two bone regions, a morphological 'erode' filter (with a structuring element (ball) radius of 3 pixels in all directions) was applied to the segmentation mask to shrink the outer surface of the model by approximately 1 mm to represent the boundary of the cancellous geometry (Figure 4-2c). The outer geometry lost by the shrinkage was assumed to be the cortical structure, and this structure was constructed later using CAD software based on the model of ankle trabecular bone.

7 In this study, only the surface geometry was exported from ScanIP™, so a new surface model was created from the corresponding mask, and the parameters used to enhance the quality of the model left at their default settings.

8 After finishing the model configuration, the surface mesh was generated (Figure 4-2d). Then, the model of the tibia was exported as point cloud data.

9 To create the point cloud data for the fibula and the talus, the steps 4 to 8 were repeated using a separate mask and model.

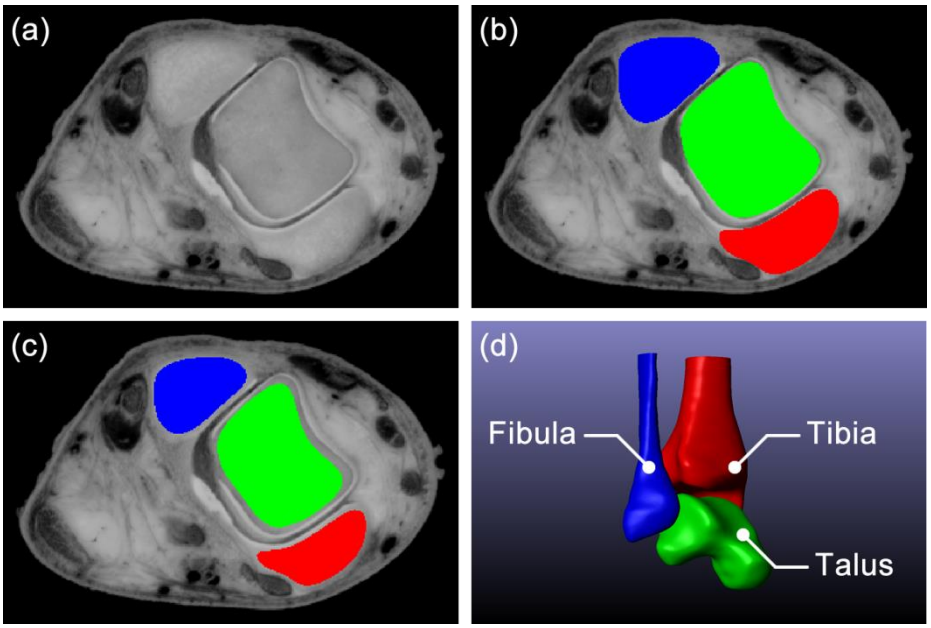

Figure 4-2 The process for creating the 3-D surface model (a) imported cryosectional image, (b) manual segmentation using 'paint' tool, (c) 'morphological erode' filter applied on segmentation, (d) 3-D surface model of ankle joint

For creating the 3-D models of the tibial and talar cartilage from the medical imaging data, the procedure was similar to that described for the ankle bone construction except for steps 5 and 6. In this case, the surface model of the cartilage did not need to be enhanced (Figure 4-3). This is because only the boundary of the cartilage was needed in order to identify the region of the cartilage on the corresponding bone. The outline of the cartilage was then projected on the outer surface of the bone and the 3-D model of the cartilage was created from that surface and outline projected using CAD software.

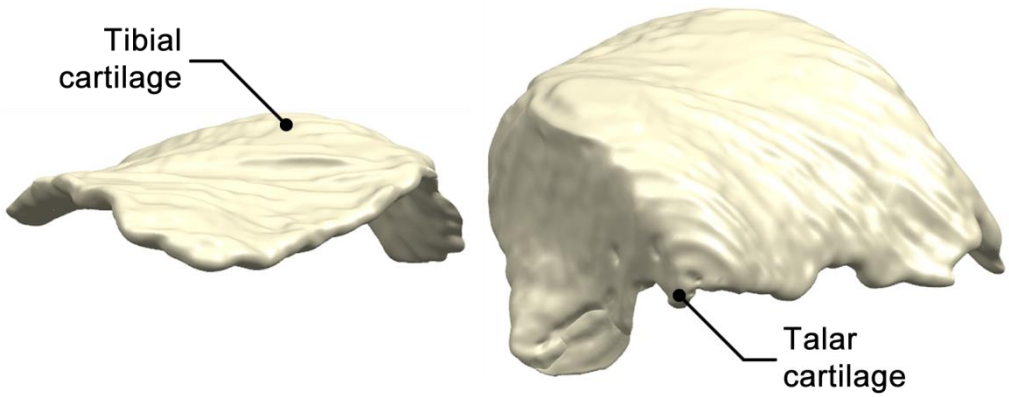

Figure 4-3 3-D surface model of tibial and talar cartilages

All of the 3-D surface models created using the ScanIP™ software were consequently exported as point cloud data to continue to create the 3-D solid model using the Geomagic Studio® software (Figure 4-4).

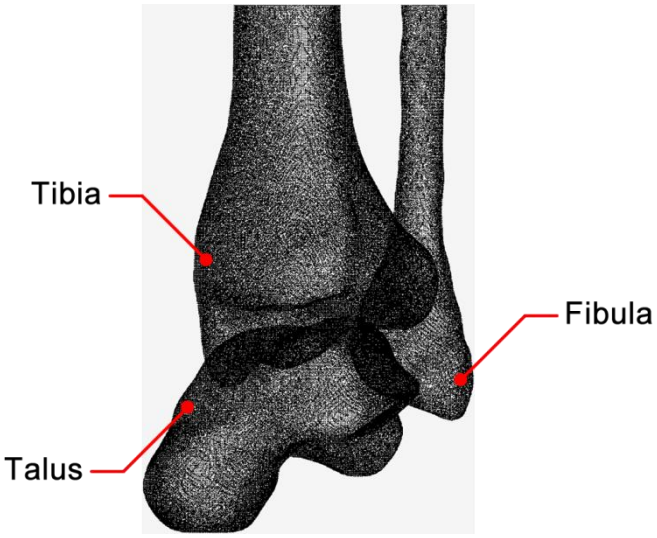

Figure 4-4 Point cloud data of ankle joint

4.2.1.2.2 Creating 3-D Solid Model Using Geomagic Studio® Software

A fundamental workflow within the Geomagic Studio® software includes three main phases which are point, polygon, and surface phases. In the point phase, there are several functions to enhance the point cloud distribution, for example to reduce noise by moving points to statistically more likely locations), and then wrap those points by drawing a triangular surface between every three data points. The surface of polygon object is refined using various functions in the polygon phase, such as the removal of spikes and filling of holes. In the surface phase, the polygon mesh is converted to a CAD object by generating surfaces that match the object exactly as it is constructed.

In this study, the 3-D solid models of the tibia, fibula, and talus bones and the corresponding cartilage regions were generated with the aid of the Geomagic Studio® software through the application of the following steps for each component:

1 The point cloud data of component was imported into the software (Figure 4-5a).

2 The reduce noise command was used to move points to statistically more likely locations making the point object smoother. The parameter in this command was set as free-form shapes (with smoothness level 1) because this option reduces the noise with respect to surface curvature. For the smoothness level, the manufacturer suggests to use the degree of noise reduction as low as acceptable.

3 The point object was then converted to a polygon object using wrap command (Figure 4-5b). The automatic noise reduction setting was also chosen to reduce noise on the original point object during the wrapping process. Small groups of points that may interfere with smooth wrapping were automatically deleted by choosing delete small components option. The degree of data reduction was determined by the target maximum number of triangles in the resulting object which was 2,500,000. These settings were the default by software.

4 The polygon mesh was enhanced by use of functions in the polygon phase. In this case, the proximal region of the tibia was trimmed by a horizontal plane using trim with plane command to remove the original top surface of the bone and create a flat surface for more controllable application of loading. The remove spike command (smoothness level 50) was also used to detect and flatten single-point spikes on a polygon mesh making the surface smoother.

5 In the surface phase, the polygon object (Figure 4-5c) was converted to be an exact surfaces object using the following commands. Firstly, the detect contours command was applied on the polygon object to detect and manipulate the borders between individually distinguishable regions of the object. All parameter settings used with this command were computed automatically which was the software default. Secondly, the edit contours command was used to add, modify, and removes contour lines created automatically by the previous command because it was found that the algorithm did not always generate an optimum solution and a degree of manual intervention was necessary to improve the quality in some cases. Thirdly, the construct patches command (with auto estimate patch count) was applied on the object to generate a patch (a four-sided subdivision of a surface that is approximately equilateral) boundary structure from the contour lines. Then, the construct grids command with the default grid density (resolution: 20) was applied on the model to create an ordered u-v grid (a quadrangular mesh of user-specified density) in every patch on the object. A finer grid caused greater precision in the eventual NURBS (non-uniform rational B-splines) surface, and a coarser grid yielded less precision. Finally, the fit surfaces command with adaptive

fitting method was applied on the object to generate and manipulate NURBS surfaces on the prepared objects.

6 The 3-D solid model of the bone (Figure 4-5d) was exported as a parasolid file for further construction using CAD and FEA software.

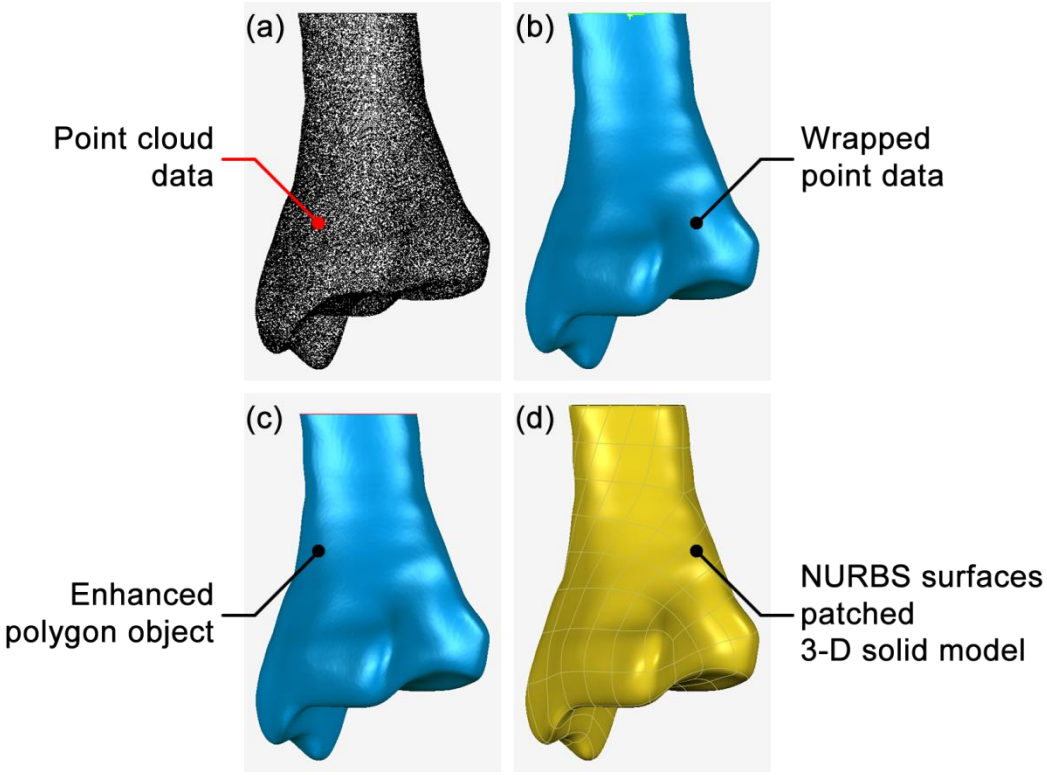

Figure 4-5 3-D solid model creating process showing the imported point cloud (a), the wrapped point data (b), the enhanced polygon object (c), and the NURBS surfaces patched 3-D solid model (d)

4.2.1.3 Model Construction

The parasolid models of the ankle cancellous bones and corresponding cartilage regions were imported into CAD software, NX (version 7.5.4.4, Siemens Product Lifecycle Management Software Inc, Texas USA) for creating cortical bone and cartilage structures. Because the right leg and the foot of the male cadaver did not appear to have been in a neutral position during image acquisition, the ankle bones in the model had to be rearranged into the proper anatomical position first, as described in the following section. In order to obtain more realistic FEA results, physiological alignment was necessarily required to better represent *in vivo* load transmission.

4.2.1.3.1 Anatomical Position of Ankle

By examining the position of ankle bones in the frontal plane, the leg of the cadaver at the time of imaging appeared to be in an abduction posture (Figure 4-6) and the foot seemed to be in a plantar flexion posture (Figure 4-7) compared to images of the leg and ankle obtained from various published papers and anatomical books (Yoshioka et al. 1989, Martini et al. 2012, Tortora and Nielsen 2012).

To rotate the ankle bone into a neutral position in the frontal plane, the approximate angle of abduction needed to be determined. The image collected from various published papers and anatomical books was overlaid with the image of the 3-D solid model of the ankle which was made to be translucent to enable comparison between both images (Figure 4-6a). After rotating the image of the 3-D solid model about 5° of adduction, the outlines of the ankle bone in both images were approximately sited in the same location (Figure 4-6b).

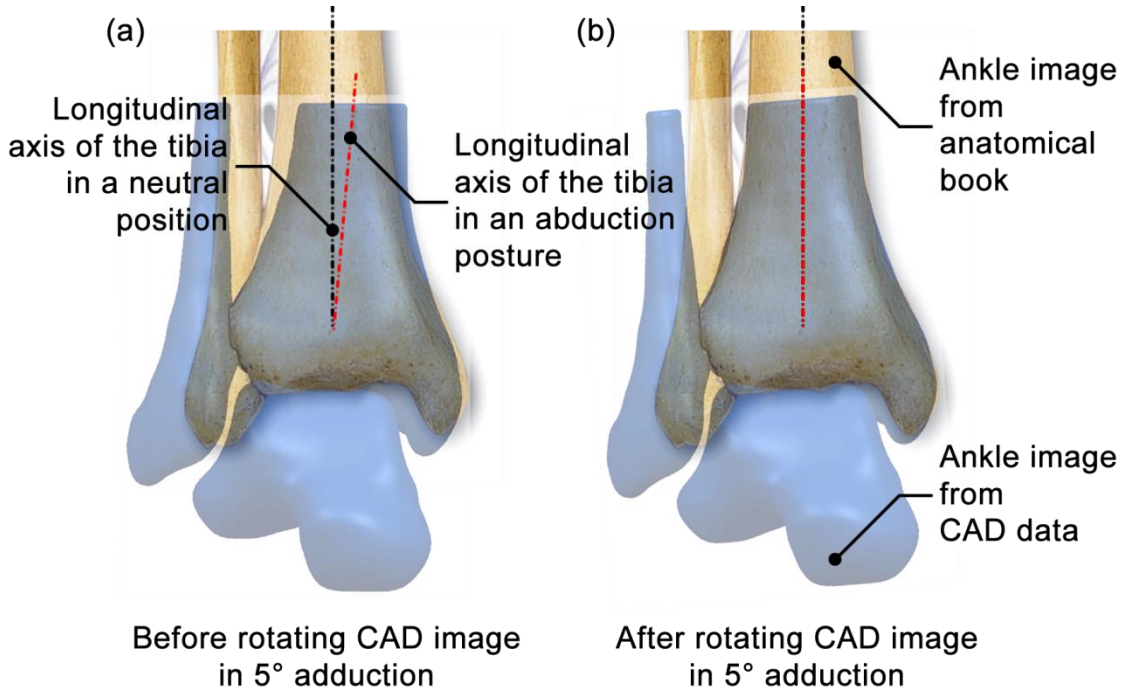

Figure 4-6 Comparison between ankle images collected from anatomical book (Martini et al. 2012) and exported from CAD software, (a) before rotating, (b) after rotating in 5° adduction

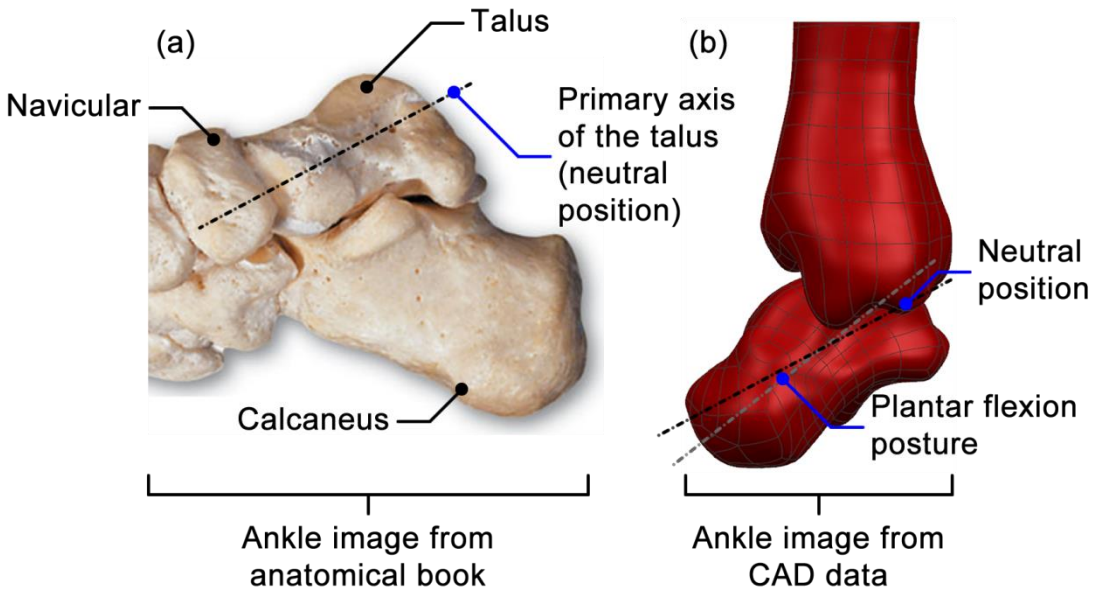

Figure 4-7 Comparison between ankle images collected from anatomical book (Martini et al. 2012) (a) and exported from CAD software (b) in the sagittal plane

The 3-D solid model of the ankle was therefore adjusted by rotating 5° (using 'Move Object' command) in adduction to provide the best approximation of the neutral position in the frontal plane (Figure 4-8). The top surface of the tibia and fibula were then cut to maintain the horizontal level corresponding to the new location after rotating (using 'Trim Body' command).

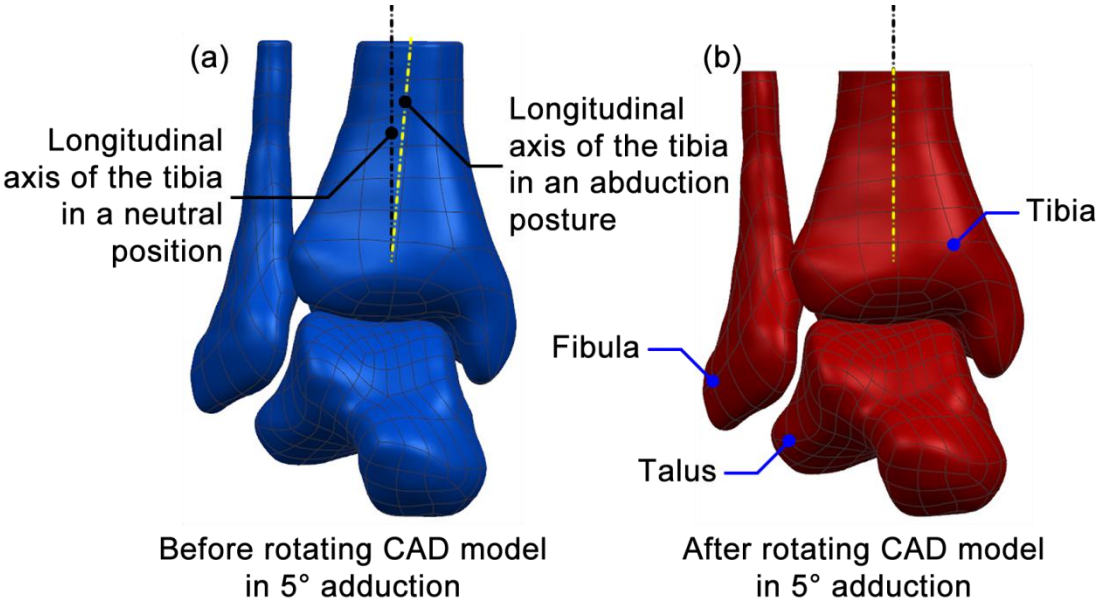

Figure 4-8 3-D solid model of the ankle before (a) and after (b) rotating in 5° adduction

In the sagittal plane, the talus required rotation in dorsiflexion to maintain the neutral position of the ankle. Because the articular surface of the ankle joint might be affected by moving the talus, the rotation of the talus needed to mimic the physiological movement as much as possible. This was different from the previous re-positioning of the ankle bones in frontal plane where all the bones were moved together, while only the talus was moved in the sagittal plane. The movement of talus depended on the geometry of the mortise. Therefore, to rotate the talus into the neutral position, the axis of rotation of the talus had to be identified.

As reported in the Literature Review, the axis of rotation of this joint passes below the tips of the lateral and medial malleoli, which runs from lateral to medial towards with approximately 6° in the transverse plane and ascending with approximately 8° in the frontal plane (Figure 4-9). This is because the medial malleolus is anterior and superior to the lateral malleolus (Zwipp and Randt 1994).

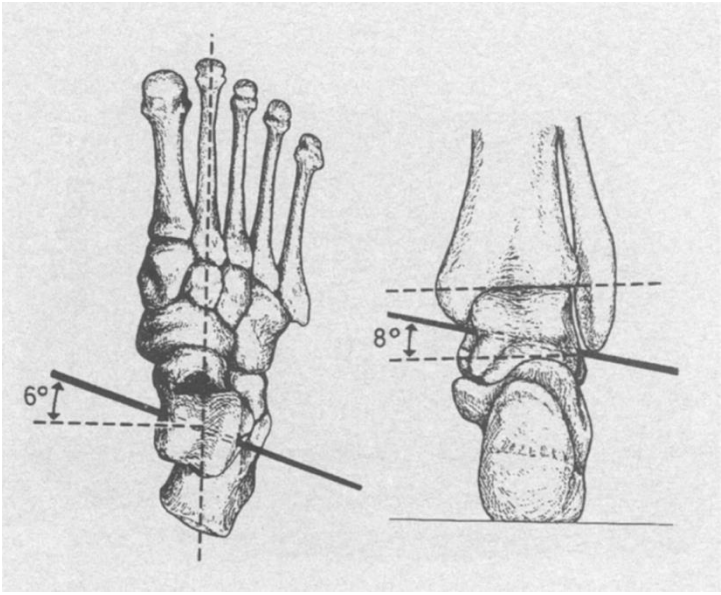

Figure 4-9 Axis of rotation of the ankle joint (Image taken from Zwipp and Randt 1994, page 23)

The rotational axis of the ankle joint has been found to be highly variable from one individual to another. In a study of 46 cadaver legs, Isman and Inman identified the locations of the medial and lateral ends of the axis of rotation (Figure 4-10). The medial end of this axis was found to be positioned at 1 ± 5 mm posterior and 16 ± 4 mm inferior to the most medial point of the tibial malleolus, while the lateral end of the axis located at 11 ± 4 mm anterior and 12 ± 4 mm inferior to the most lateral point of fibular malleolus (Isman and Inman 1969).

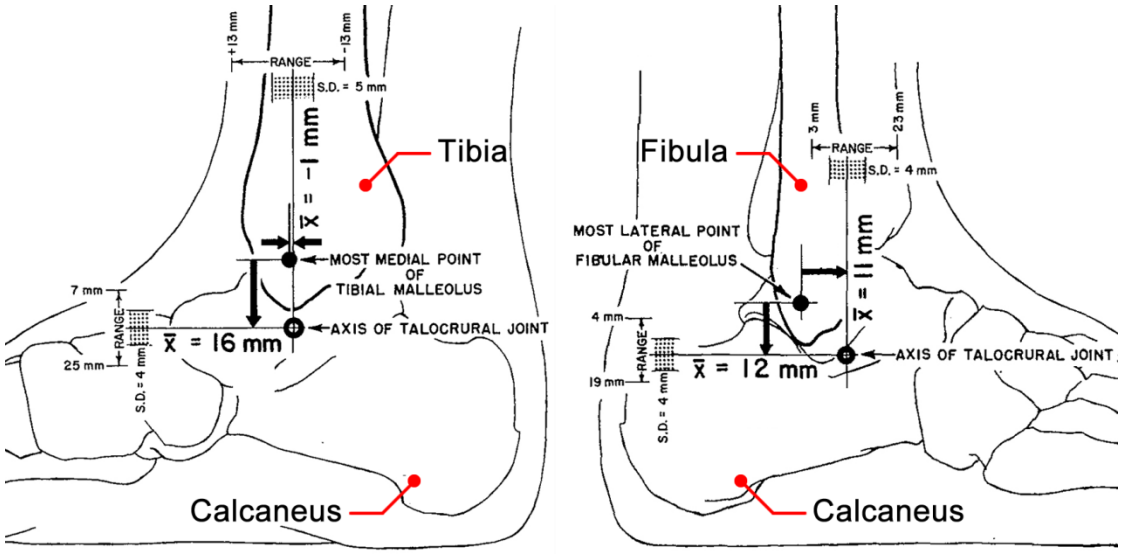

Figure 4-10 Location of axis of rotation of the ankle joint measured from 46 cadaver legs (Image taken from Isman and Inman 1969, page 124 and 126)

The average measurement values obtained from the study of Isman and Inman could only be used as a guideline to identify the axis of rotation of the ankle because of the high standard deviations of some measuring points, revealing the degree of uniqueness of the rotational axis location. Therefore, the method described in the study of Anderson et al. was chosen to be used to identify the axis of rotation because it was suitable for individual geometry of the joint.

The main concept of this method was to create circles to fit to the arcs of the trochlea of the talus at both the medial and lateral talar facets, and the line connecting between the centers of both circles was defined as the rotational axis of the ankle (Anderson et al. 2006).

To identify the axis of rotation of the ankle joint using NX software, straight lines over the talar trochlea at both the medial and lateral talar facets were created first (using 'Basic Curves' command, Figure 4-11a). Secondly, both straight lines were projected onto the curve surface of the trochlea of the talus (using 'Project Curve' command). The curves were now lain on the curved surface of the trochlea at both talar facets. Thirdly, three points were created on each previously defined curve projected using 'Point' command (Figure 4-11b). Then, arcs from each three points on the corresponding facets were created (using 'Basic Curves' command, Figure 4-11c). These arcs were parts of circles which were created to fit the shape of the talar trochlea. Finally, points were created at the center of each arc (circle), and straight lines were then created to connect between the centers of the circles (using 'Point' and 'Basic Curve' commands respectively, Figure 4-11d). This connecting line was assumed to be the axis of rotation of the ankle joint for further use in this study.

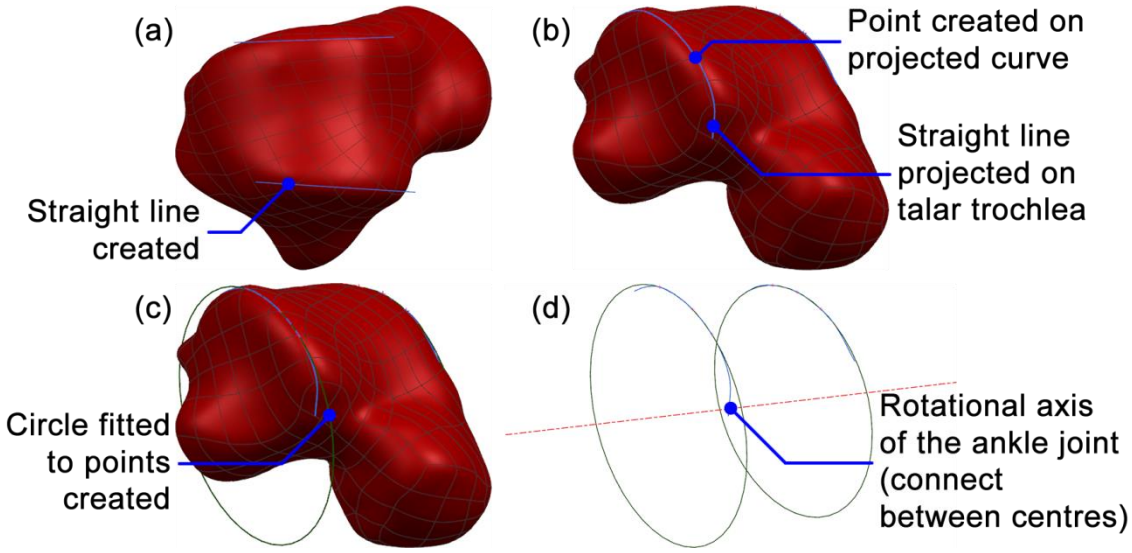

Figure 4-11 The process of identifying the axis of rotation of the ankle joint showing the straight lines created over the talar trochlea (a), the three points created on each projected curve (b), the circles created to fit each set of the three points (c), the rotational axis of the ankle joint created to connect between the centres of the circles (d)

The image of the ankle joint in the sagittal plane was exported from NX software for comparison with several corresponding images obtained from published papers and anatomical books using the same method as for the frontal plane adjustment. The comparison revealed that the right of the cadaver was in approximately 10° plantar flexion during image acquisition time.

Therefore, the 3-D solid model of the talus was adjusted by rotating in 10° dorsiflexion around the rotational axis identified previously to align the ankle bone is in an approximately neutral position in the sagittal plane (Figure 4-12).

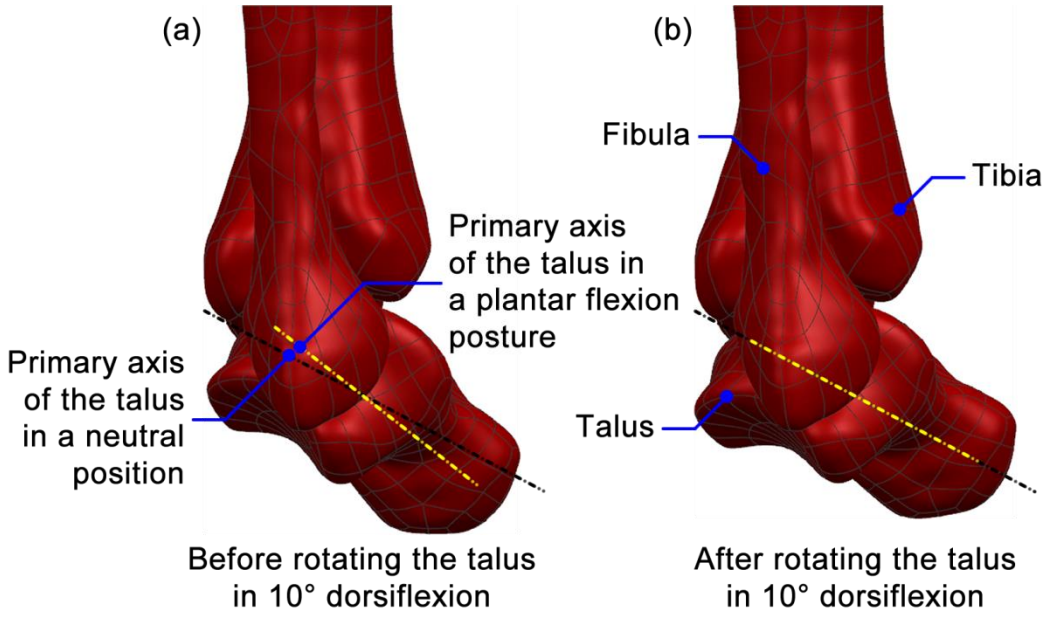

Figure 4-12 3-D solid model of the ankle before (a) and after (b) rotating in 10° dorsiflexion

4.2.1.3.2 Creating Cortical Structure of the Ankle Bone Using NX Software

Due to the difficulty in differentiating between the structure of the cortical and cancellous bones on the cryosectional data, the structure of the cortical bone in this study was assumed to be a shell with constant thickness of 1 mm covering the entire structure of the cancellous bone, as explained in Section 4.2.1.2.1.

After the parasolid models of the ankle bones were imported into NX software, the cortical structures were then created by extending the outer surface of the cancellous geometry by 1 mm using the following steps. First, the CAD models of the ankle cancellous bones were duplicated. Second, the outer surfaces of the duplicated models were entirely extended by 1 mm (using ‘Offset Face’ command, Figure 4-13a). Finally, the ‘Subtract’ command was used to remove the intersecting volume between the cortical and cancellous structures on the cortical models (Figure 4-13b). All CAD models of the ankle bones were exported as parasolid files for further construction.

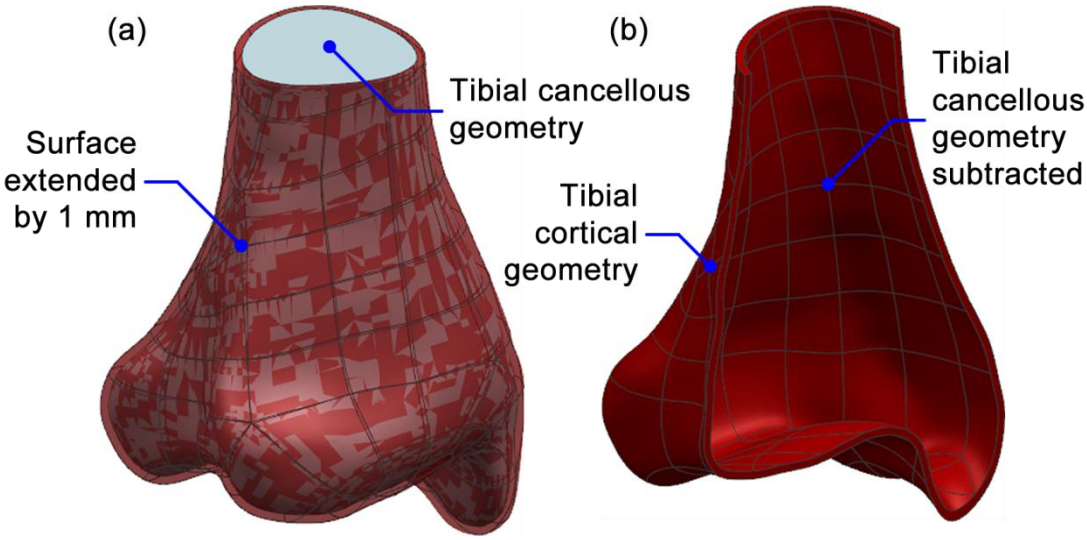

Figure 4-13 Cortical structure creating process using NX software

Several approaches were investigated to generate the FE model of the whole structure. Exporting both cancellous and cortical as separate parts, which then required a tie interaction to be implemented between them was found to increase computational expense and risk of overconstraint problems. If using the merge function in Abaqus software instead of the tie constraint, it was always possible to use the function with complex morphologies.

It was also found that sometimes the cortical shell created using NX software could not be successfully combined with the cancellous structure using 'Merge Instances' command in Abaqus software. Therefore, the final step of hollowing the corticall shell was not performed in the NX software, but instead two fully solid parts were exported and then the subtract function was used in Abaqus software to hollow out the cortical shell.

The merge command was found to be the best function for combining models together whilst maintaining their individual properties. After combining, the interaction between each model did not need to be assigned, and meshing could be applied continuously on the entire combined model.

4.2.1.3.3 Creating Cartilage Geometry Using NX Software

The ankle cartilages used in this study were simply created based on the geometry of the ankle bones created previously. The boundaries of the cartilage regions were identified based of the cryosectional data obtained from the database of the Visible Human Project®. The thickness of the cartilages created was constant throughout and the value was collected from several published papers.

In the study of Athanasiou et al., who biomechanically evaluated the articular surfaces of 14 fresh-frozen normal ankles obtained from seven cadavers, the average thickness of the ankle cartilage (distal tibia and proximal talar cartilages) was 1.18 ± 0.29 mm (Athanasiou et al. 1995). Eleven sets of cadaveric human ankle joints were collected for measuring the thickness of the cartilage in the study of Shepherd and Seedhom, and the average measuring values reported were in the range of 1.00 ± 0.20 mm to 1.62 ± 0.25 mm (Shepherd and Seedhom 1999). The average thicknesses of the tibial, fibular, and talar cartilages obtained from fresh-frozen ankles of 12 male cadavers, which were measured using a high resolution stereophotography system in the study of Millington et al., were 1.16 ± 0.14 mm, 0.85 ± 0.13 mm, and 1.10 ± 0.18 mm respectively (Millington et al. 2007). Adam et al., who measured the thickness of the left and right ankle joint cartilages harvested from 10 cadavers using ultrasound measurement technique, reported in their published paper that the average thicknesses of the left and right ankle joint cartilages were 0.94 ± 0.16 mm and 0.97 ± 0.17 mm respectively (Adam et al. 1998).

As can be seen, the average thicknesses of the ankle cartilage collected from several published papers were approximately 1 mm. Therefore, in this study, the constant thickness of 1 mm throughout was then used for simplified cartilages created.

In this case, cartilage was simply created based on the original boundary outline taken from the cryosectional data. The reasons for this procedure were the creation of a full cartilage model using the ScanIP™ was considered to be a time consuming process, and several features used to enhance the quality of the model might change bone-cartilage interface making both surfaces to be an inexact match and consequently cause difficulties in the assembly process. Therefore, the cartilage was created from the outer surface of the corresponding bone together with the original boundary outline taken from the cryosectional data.

The process of creating simplified ankle cartilage was started by importing the 3-D solid models of the tibial and talar cartilages created previously using Geomagic Studio® software into NX software. The outer surfaces of the tibial and talar cortical bones in the cartilage covering region were copied as sheets using ‘Extract Body’ command, which was typically used to create a new model by copying either existing surface or solid model (Figure 4-14a). Then, edges of the cartilage models were copied as curves and projected onto the corresponding sheets copied previously using ‘Extract Curve’ and ‘Project Curve’ respectively. The curves projected were enhanced to be smoother

curves using several commands, such as ‘Curve Length’, ‘Bridge Curve’, and ‘Join Curves’, and were then re-projected on the same sheets using ‘Project Curve’ command (Figure 4-14b). After that, the sheets were cut following the curves projected and the areas outside the cartilage regions were removed using ‘Trimmed Sheet’ command, which was typically used to cut off a portion of a sheet using curves, surfaces, or planes (Figure 4-14c). Finally, the simplified cartilages were created from the sheets cut previously by thickening the sheets to be solid models with the thickness of 1 mm throughout using ‘Thicken’ command, which was generally used to create a solid model from a surface by adding thickness (Figure 4-14d). All CAD models of the ankle cartilages were exported as parasolid files for further constructing of a FE model using Abaqus/CAE software.

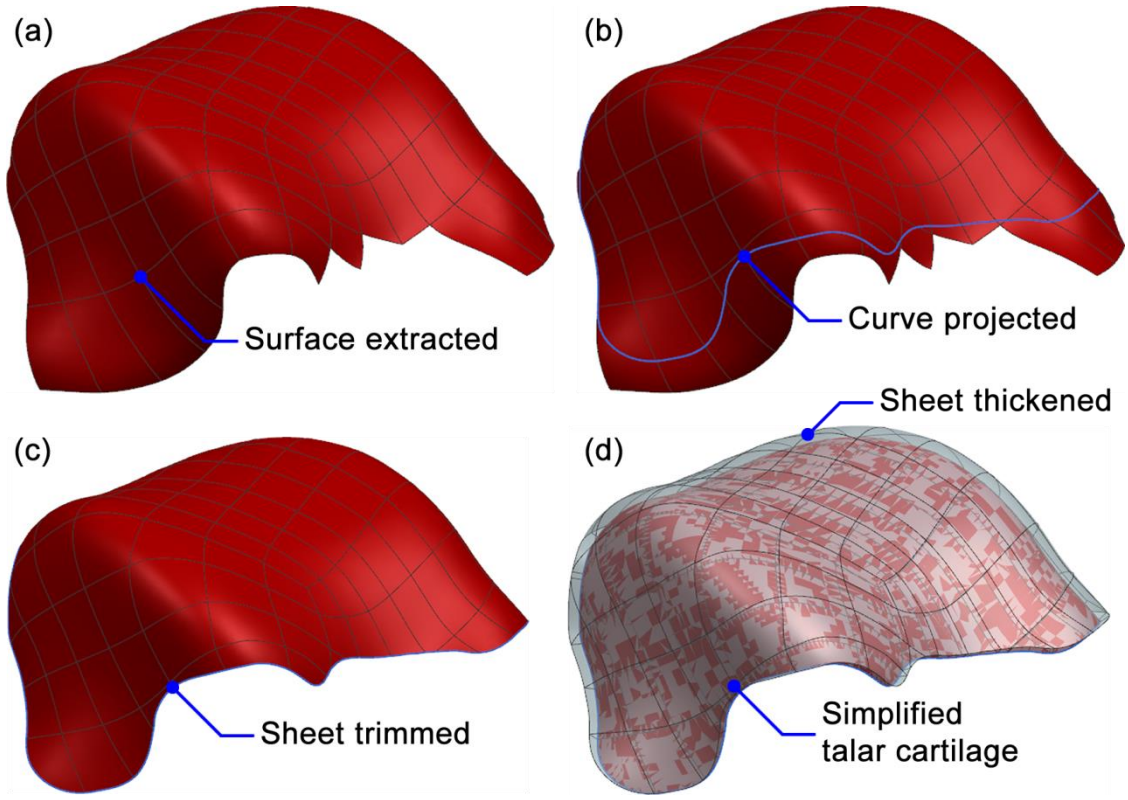

Figure 4-14 Ankle cartilage creating process using NX software

4.2.1.3.4 Creating FE Model of Natural Ankle Using Abaqus/CAE Software

The CAD models of the ankle bones and their cartilage layers were imported as parasolid files into Abaqus/CAE software (version 6.12-2, Dassault Systèmes Simulia Corp, Rhode Island USA). In this case, the models of the cortical bones imported were fully solid models instead of hollow structures. A 30 × 30 mm square analytical rigid plate was created to enable loading over the whole of the cross section at the top of the tibial bone. A reference point was located at the center of the analytical rigid plate and the plate was aligned on the top of the tibial bone.

Instances of all parts except the cancellous bones were created as one set for each part, while instances of cancellous bones were created as two sets in order to use one to cut the solid cortical geometry by applying the 'Cut Instances' tool (Figure 4-15a). After that, the instances of cortical shells were combined together with another set of cancellous geometries to make single instances of bone using 'Merge Instances' tool (Figure 4-15b). When applying this tool in this study, both geometries and meshes were combined together, but inherent material properties were still maintained. Finally, the analytical rigid plate was positioned onto the top of the tibial bone (Figure 4-16).

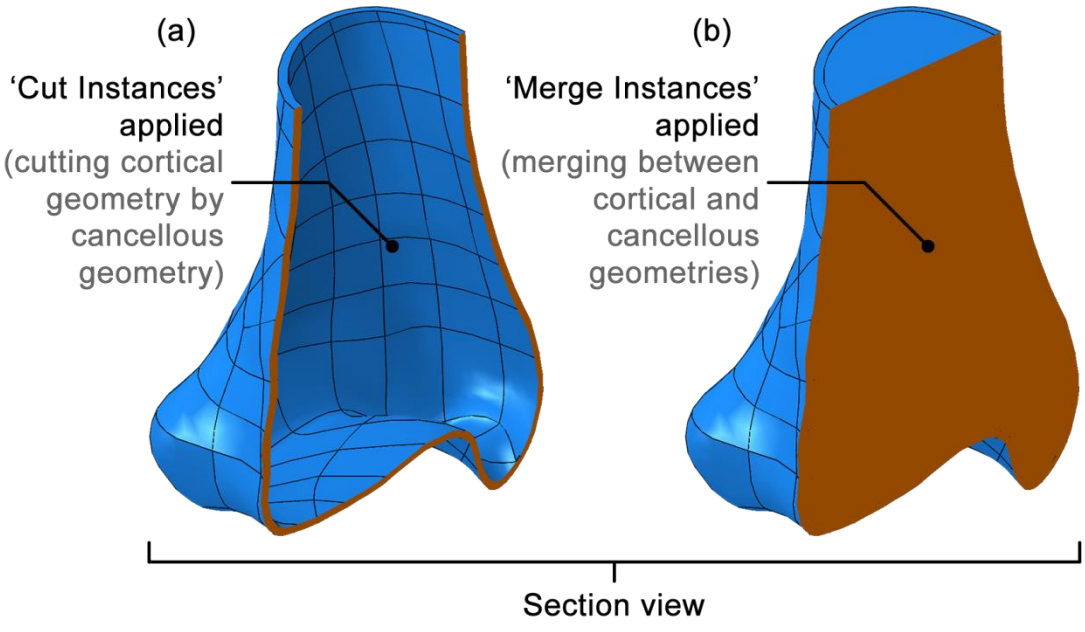

Figure 4-15 Cortical structure after applying 'Cut Instances' tool (a) and 'Merge Instances' tool (b)

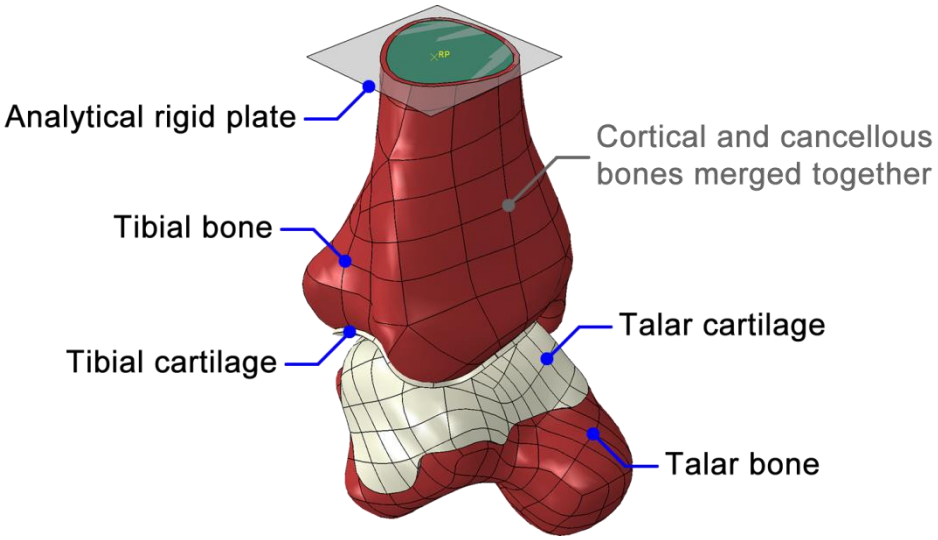

Figure 4-16 Assembly of all instances

Three steps were used for applying boundary conditions and loads. The boundary condition on the talus was applied in the initial step, then a displacement was applied to close the gap between articular surfaces of the ankle joint, and finally a concentrated force was applied in the third step to represent load applied during gait cycle. Both displacement and concentrated force were applied through a reference point on the analytical rigid plate, as was the boundary condition. The analysis was then run sequentially following the steps created.

In this study, the ten-node quadratic tetrahedron (C3D10) and the eight-node linear brick (C3D8R) were chosen to mesh the bone and the cartilage structures respectively. The tetrahedron was thought to be a geometrically versatile element that was suitable for automatic meshing complex geometry like a bone, while the hexahedron perform better in contact problems so were more suitable for meshing the articulating structures like the cartilage. The meshing of the bone structures was achieved through the standard automated meshing tool (‘Mesh Part Instance’), while the meshing of the cartilage structures required the use of a bottom-up approach (using ‘Create Bottom-Up Mesh’ tool with the ‘Sweep’ method), it was first necessary to combine several faces on the surface of the cartilage into a single face to improve the bottom-up mesh. The element type, approximate element size, and the element number of each instance in the initial FE model were shown in the Table 4-1.

Table 4-1 Meshing information of the initial FE model of the natural ankle

Instance	Element type	Approximate element size	Element number
Tibial cortical bone	C3D10	0.96	284987
Tibial cancellous bone	C3D10		
Tibial cartilage	C3D8R	0.75	11988
Talar cartilage	C3D8R	0.52	40228

In this initial model, the talar bone was not included due to unsuccessful merging of the talar cortical and cancellous bones in the subsequent study (the FE model of TAR with natural ankle geometry). There was not another FE model to compare to the FEA results of the talar bone. Therefore, the talar bone was removed from this FE model to reduce computational expense such a running time of analysis.

4.2.1.4 Material Properties

Material properties of the ankle bones and cartilages in this study were assumed to be linear, homogenous, and isotropic. The values of Young's modulus and Poisson's ratio were derived from several published papers.

The Young's moduli of the cortical and cancellous bones used in this study were 17.58 GPa and 280 MPa respectively, and their Poisson's ratios were both 0.30. These values were taken from the study of Miller et al., who use FEA to investigate effect of geometry of talar component on stress in polyethylene liner (Miller et al. 2004). The values were similar to a number of experimental papers. For example, Aitken et al., who assessed elastic modulus of cancellous bone in the distal tibia of 15 amputation specimens harvested from patients with amputation of a lower limb using an indentation method, reported that the elastic moduli of cancellous bone in the distal tibia at the level of the subchondral bone were in a range of 150-300 MPa (Aitken et al. 1985). Another study in the mechanical properties of the tibial trabecular bone by Goldstein et al., determined the tibial trabecular bone mechanical properties at the metaphyseal portion using an electromechanical testing machine. The average elastic moduli of the five human tibial metaphyses obtained from five autopsy subjects ranged from 31 ± 18 MPa to 336 ± 86 MPa (the values taken from the first transverse section of the proximal tibia) (Goldstein et al. 1983). In the study of Reilly and Burstein, who investigated the compressive elastic properties of the human femoral specimens harvested from four subjects using uniaxial compression testing, the average longitudinal elastic modulus and Poison's ratio were 18.2 ± 0.85 GPa and 0.38 ± 0.154 respectively (Reilly and Burstein 1975). Snyder and Schneider also investigated the elastic modulus of

the tibial cortical bone at the mid-diaphyseal location obtained from seven subjects using three point bending tests. In their published papers, the moduli of elasticity investigated were in a range of 14.3-21.1 GPa and the average value of which was 17.5 ± 1.62 GPa (Snyder and Schneider 1991).

For the cartilage, a Young's modulus of 12 MPa and Poisson's ratio of 0.42 were chosen. These values were taken from several studies of Anderson et al., who investigated the contact stress at the ankle joint using FEA (Anderson et al. 2006, Anderson et al. 2007, Li et al. 2008). Similar results were found in the study of Shepherd and Seedhom using an indentation methods to test eleven sets of cadaveric human ankle joints, with the average values reported in the range of 10.6 ± 5.6 MPa to 18.6 ± 6.3 MPa (Shepherd and Seedhom 1999).

4.2.1.5 Interactions, Loads, and Boundary Conditions

A frictionless contact was defined between articular cartilage surfaces of the ankle joint. The interface between the tibial bone and cartilage and between the analytical rigid plate and the tibial bone were defined with a tie constraint. The talar cartilage was coupled to another reference point located at the origin coordinate (0, 0, 0).

A boundary condition was assigned to the inferior reference point to fully fix the talar cartilage in all directions.

The displacement and rotation of the analytical rigid plate was constrained in all directions except the vertical displacement (Y-axis).

In order to load the joint, a two-stage process was used. First, a vertical displacement was applied to the analytical rigid plate to move the tibial bone down by a distance of 3.50 mm to close the gap between the articular surfaces of the ankle joint. This allowed the cartilage surfaces to come into contact and the contact algorithms in Abaqus to be initiated.

In the second step, an axial concentrated force was applied to the superior reference point of the analytical rigid plate. The rigid plate was used to distribute concentrated force over the entire cross sectional area at the top of the tibia. The concentrated force applied to the tibial bone used in this study was the compressive axial load of 3416 N, which was approximately the maximum axial load applied on the ankle joint during a gait cycle same as the previous study.

The structure of the FE model created in this study is illustrated in the Figure 4-17.

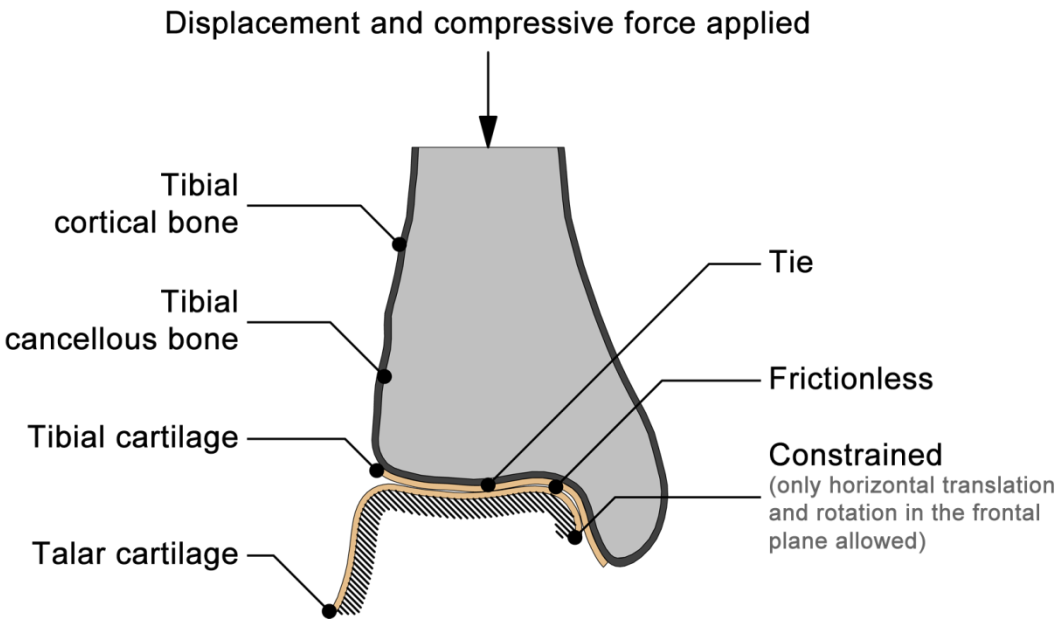

Figure 4-17 FE model of natural ankle

4.2.2 Finite Element Analysis of Natural Ankle

4.2.2.1 Evaluation of Different Loads and Boundary Conditions

Initial attempts to run the full model indicated that there were difficulties in reaching convergence due to the large strains in the cartilage and size of the FE model. To examine the effects of different magnitudes of applied load and different boundary conditions, a number of models were evaluated using a model representing only the cartilage, with the bone replaced by rigid surfaces.

There were seven FE models in total in this study. These models were divided into two sets and all models in each set were run simultaneously. The second set models were performed after the first set models were completed and their results were identified. The model configurations, and the results where solutions were achieved, are shown in Table 4-2. The Displacement/Rotation boundary conditions were applied to the inferior reference point to constrain the talar cartilage, while the displacement and load were applied to the superior reference point to control the tibial cartilage.

Table 4-2 Various FE models of cartilage analyzed to identify optimum loads and boundary conditions and their results

Set		**1**				**2**		
Model		**1**	**2**	**3**	**4**	**5**	**6**	**7**
BCs	**X**	×	×	×	×	×	×	×
	Y	×	×	×	×	×	×	×
	Z	×	✓	✓	✓	✓	✓	✓
	UX	×	✓	✓	×	✓	✓	✓
	UY	×	×	×	×	×	×	×
	UZ	×	×	×	×	×	×	×
Step-1	**Applied displace-ment**	3.50	3.50	3.30	3.30	3.45	3.35	3.35
	Result	×	×	n/a	✓	×	✓	✓
	RF-X	-5.48	46.92	n/a	7.69	n/a	n/a	n/a
	RF-Y	12.01	355.99	n/a	53.29	n/a	n/a	n/a
	RF-Z	-43.03	0	n/a	0	n/a	n/a	n/a
Step-2	**Applied load**	3416	3416	n/a	3416	350	350	360
	Result	-	-	n/a	×	-	✓	×
	RF-X	-	-	n/a	37.56	n/a	n/a	n/a
	RF-Y	-	-	n/a	286.23	n/a	n/a	n/a
	RF-Z	-	-	n/a	0	n/a	n/a	n/a

The following conclusions could be drawn from the analyses of the models in the first set: The full constraint of the inferior reference point resulted in interference at the malleolar articulation leading to failure of the analysis (Model 1). The applied displacement of 3.50 mm was too high and caused excessive strain in the cartilage, leading to failure of the analysis (Model 2), while the displacement of 3.30 mm was too low to full engage the cartilage leading to the consequent separation of the tibial and talar cartilage layers and error in the output variables (Model 3). The model could be solved with a higher load when allowing rotation about X-axis to allow the two convex shapes of talar cartilage to share load bearing (Model 2 and 4).Therefore, the boundary conditions that allowed translation along the Z-axis and rotation about the X-axis, displacement in a range between 3.30 mm and 3.50 mm, and a load of approximately 355 N were then assigned to the subsequent models in the second set.

According to the analysis of the second set of models, the optimum loads and boundary conditions were identified. The boundary conditions applied at the inferior reference point allowed displacement along the Z-axis to avoid interference at the malleolar articulation and rotation about the X-axis to share the load between to convex shapes of talar articular surface for increasing the magnitude of load bearing. The vertical displacement of 3.35 mm was used to move the tibial bone down in the first step, and the concentrated force of 350 N was applied to the tibial bone in the second step. These parameters were then applied to all subsequent FE models.

4.2.2.2 FEA of Natural Ankle

The boundary conditions and loads in the original FE model of the natural ankle were modified to those found to be optimum as described in Section 4.2.2.1. Other parameters assigned were the same as the original model.

4.2.2.3 Mesh Convergence Study

The models described previously were composed of approximately 337,000 elements, which included ~285,000 tetrahedral elements of the tibial bone and ~52,000 hexahedral elements of the cartilage layers. The cartilage-only model required a running time of only approximately 10 minutes using four processors of an Intel® Xeon® Processor E5-2670, while the whole model required as long as approximately 122 hours. An alteration in the meshing of the tibial bones was therefore considered to reduce the computational expense. The approximate element size was doubled from 0.96 mm to 1.92 mm, reducing its number of elements to approximately 64,000. Similarly, the analysis time was significantly reduced down to approximately four hours. The output variables obtained from both models were compared in terms of the maximum magnitudes of the von Mises stress and minimum principal strain on the tibial cancellous bone and the vertical displacement at loading point as shown in Table 4-3.

Table 4-3 All output variables measured at the locations of interest on the tibial cancellous bone in the mesh convergence study, showing the magnitude and location of the variables

Number of element	von Mises stress - maximum magnitude (MPa)			Minimum principal strain - maximum magnitude			Vertical displacement (mm)
~337,000	1.07758			-0.00435565			-3.47532
	Coordinate			Coordinate			
	X	Y	Z	X	Y	Z	
	5.12409	33.2639	-1.10403	4.77153	32.3123	-0.509219	
~116,000	1.08827			-0.00438876			-3.47527
	Coordinate			Coordinate			
	X	Y	Z	X	Y	Z	
	5.27171	33.6845	0.30407	4.37118	32.3098	0.0325609	

The locations of the maximum magnitudes of the von Mises stress and minimum principal strain on the tibial cancellous bone between the two models were very similar. The differences in the von Mises stress, minimum principal strain, and vertical displacement were 0.99%, 0.76%, and 0.0014% respectively. Therefore, an element size of approximately 1.92 mm for meshing of tibial bone was found to be optimum because tripling the mesh density only introduced a very small change in the results.

4.3 Results

The contour plots of the von Mises stress distribution in the tibial cancellous bone are presented in both the frontal (Figure 4-18) and sagittal planes (Figure 4-19). The region of the highest concentration of stress was located closest to the articular surface, while the magnitude of the stress gradually reduced in a direction away from the contact location.

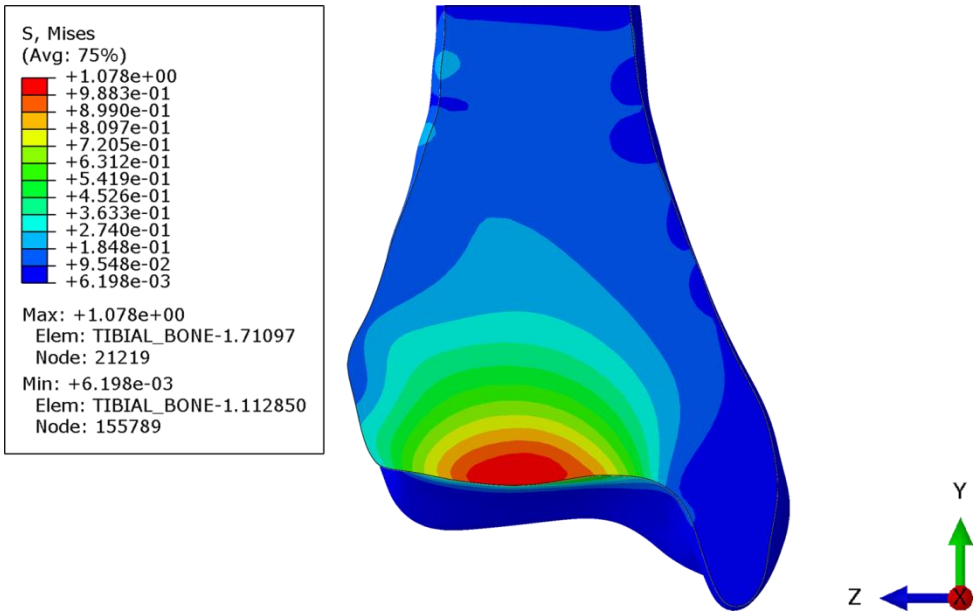

Figure 4-18 The contour plots of the von Mises stress (MPa) distribution in the tibial cancellous bone, showing in the frontal plane

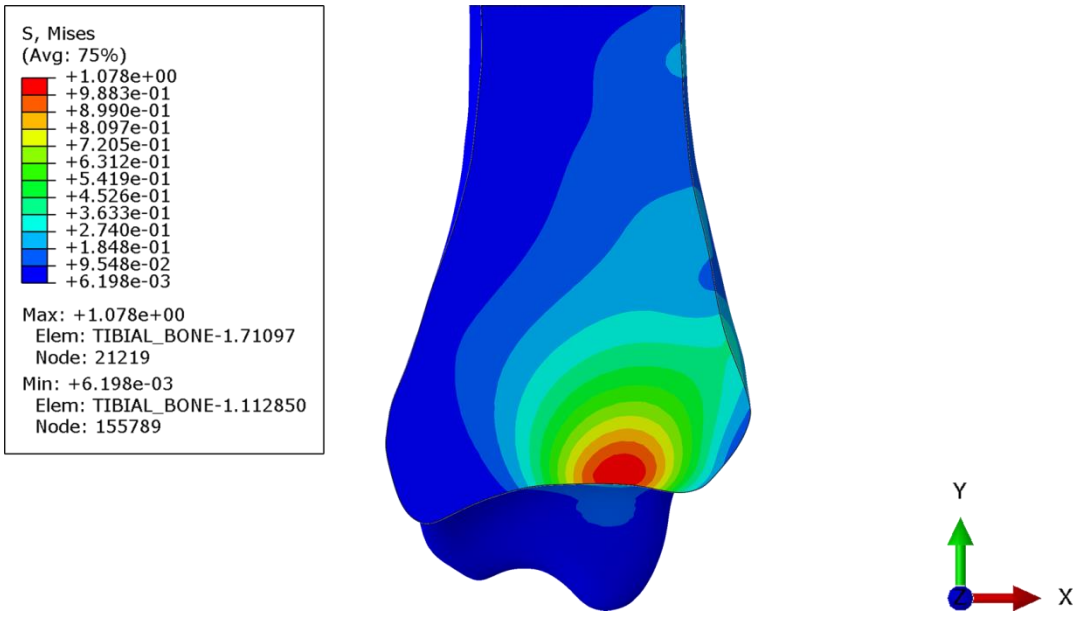

Figure 4-19 The contour plots of the von Mises stress (MPa) distribution in the tibial cancellous bone, showing in the sagittal plane

4.4 Discussion

The cartilage layers with elastic material properties assigned in this study could not withstand a typical load experienced by the ankle. Therefore, the simple linear elastic behavior was considered to be not appropriate for the cartilage. This is likely to be for two reasons: first, the cartilage is fibre-reinforced and gets stiffer at higher strains, so the linear elastic model allows the cartilage to deform more than it does in reality, increasing local stress/strain in cartilage and adjacent bone. Second, the boundary conditions almost certainly over-constrain the model compared to reality where much of the constraint is provided by soft tissues. Both of these factors are likely to cause greater localized stresses in the adjacent bone in the model than in reality. In several finite element analysis studies that focus on cartilage, a biphasic fibre-reinforced behaviour was adopted instead of isotropic elastic material properties (García and Cortés 2007, Julkunen et al. 2007, Shirazi et al. 2008). This method might provide a solution for the problem of excessive strain leading to failure of the analysis.

Although a full mesh convergence study was not undertaken, the mesh verification study was used to identify the most appropriate mesh scheme for the system. In this case, an element size of approximately 1.92 mm for meshing of tibial bone was found to be optimum because tripling the mesh density only introduced a very small change in the results and the running time required for the analysis was considerably lower.

One of the primary aims of this study was to enable comparison between the natural ankle and the TAR case presented in the next chapter. Although the full axial load could not be applied due to convergence issues, the lower load did converge and provides a case to compare to the TAR model in the next chapter. It was not surprising that the region of high concentration of the stress was located at the region closest to the articular surface because the load was transmitted to both cortical bone and cartilage via that location. The magnitude of the compressive load used in this study was approximately 10% of the typical load experienced by the ankle. If the finite element analysis result was considered to be linear, then the behavior under larger loads could be determined using interpolation. This would indicate that, the maximum magnitude of the von Mises stress in the cancellous bone might be as high as 10 MPa, which exceeds an average value of the compressive yield strength of cancellous bone. In reality, the bone would not be damaged partly because the stiffer subchondral region would maintain its shape and prevent it from severe deformation. This indicates that the peak stress in the region around the

cartilage is therefore likely to be an overestimation of reality, however, the main purpose here is to compare this model to that with a TAR, where the region of interest is around the TAR stem, away from the cartilage. Several factors were considered to be likely to affect the contact area of the ankle joint leading to a subsequent increasing of the stress. For example, some functions used in creating the 3-D model from medical imaging data changed the geometry of the articular surface of the ankle joint; the positioning of the talus in the ankle mortise might be slightly different from the physiological; and a lateral moving of the talus to avoid interference at the medial malleolus might not represent the corresponding complex movement of the talus in reality well enough.

4.5 Summary

A FE model of natural ankle was developed and some verification and sensitivity studies were undertaken to determine the optimum mesh density and to identify appropriate loads and boundary conditions. The following conclusions can be drawn from this study:

1 The FE model of natural ankle was successfully created from the cryosectional images with the aid of several commercial softwares.

2 The most appropriate loads and boundary conditions were identified for analysis of the FE model of natural ankle in which the cartilage was represented by elastic material properties.

3 The mesh verification was used to determine the appropriate element size for meshing the FE model to maintain accuracy while reducing the computational expense.

4 The FE model of natural ankle was successfully solved, and although the results in the region of the cartilage contact may not be realistic, the model can be used to compare the bone behaviour away from the contact zone to the FE model of TAR in the next Chapter.

Chapter 5 Finite Element Analysis of TAR with Natural Ankle Geometry

5.1 Introduction

The small inclination angle of the TAR components in the experiment in Chapter 2 were shown to cause substantial differences in the contact pressures between each side of the mid-plane, and this may have an effect on the potential for bone damage. In addition, cases of malalignment are reported in the literature as being a reason for TAR failure, as discussed in Chapter 1. Therefore, the main purpose of this chapter was to investigate the effect of clinically relevant misalignment of TAR on surrounding bone. Moreover, an analysis of the FE model of the TAR within the natural ankle geometry using the same load condition as the analysis of the FE model of natural joint in Chapter 4 was also performed for comparison between the results.

5.2 Materials and Methods

5.2.1 FE Model of TAR with Natural Ankle Geometry

The 3D models of the TAR that were simplified and used for verification, validation, and sensitivity studies in Chapter 3 were virtually inserted into the 3-D models of natural ankle created in Chapter 4 following surgical technique provided by manufacturer.

5.2.1.1 Model Construction

The models of tibial and talar bones created and adjusted into realistic anatomical positions as described in Chapter 4 and the simplified models of TAR components as described in Chapter 3 were imported into CAD software, NX (version 7.5.4.4, Siemens Product Lifecycle Management Software Inc, Texas USA) for creating a model of a TAR within the natural ankle geometry.

The models of the TAR components were virtually inserted into the models of the ankle bones following the surgical technique provided by the manufacturer. The gap between the tibia and the talus was used to determine the joint line, which was a starting point to define appropriate positions of components. Clinically, a spacer inserted into the joint gap, which is used to define the joint line, and a tibial alignment jig aligned parallel to the longitudinal axis of the tibia, are mainly used to determine the proper position of implanting (Figure 5-1). Therefore, in this study, the TAR was positioned by referring to the joint line that was located in the joint gap and aligned perpendicular to the longitudinal axis of the tibia. In this case, the joint line was used to adjust the position of

implant vertically, while the longitudinal axis of the tibia was used to arrange the position of implant horizontally. The position of the TAR in the transverse plane was defined to cover the articular surface of the ankle joint as much as possible and based on the rotational axis described in Chapter 4. After the TAR components had been positioned, the articular surface of the tibia and the talus were cut to match with the surfaces of the tibial and talar components respectively using ‘trim body’ and ‘subtract’ functions for creating conformable bone-component interfaces (Figure 5-2). The CAD model of the TAR within the ankle bone was then exported as a parasolid file for further generation of the FE model.

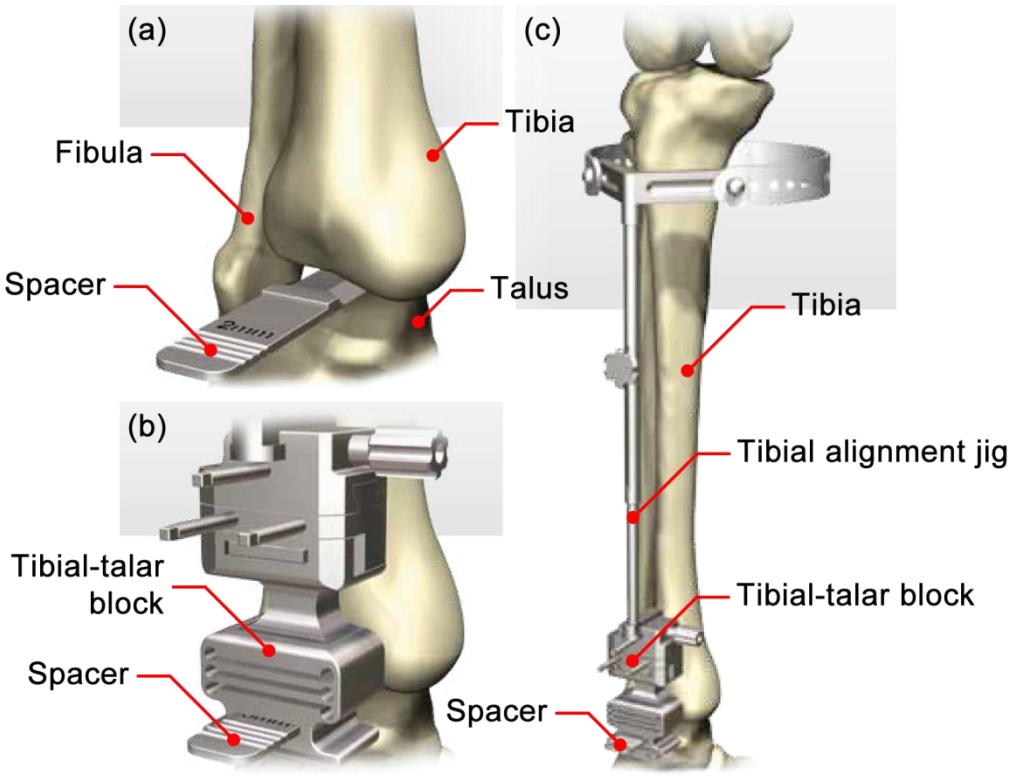

Figure 5-1 Defining implant position process, (a) defining joint line using spacer to adjust the implant position vertically, (b) and (c) installing the tibial-talar block and the tibial alignment jig to adjust the implant position horizontally (Image taken from http://www.coringroup.com [cited 25 May 2015])

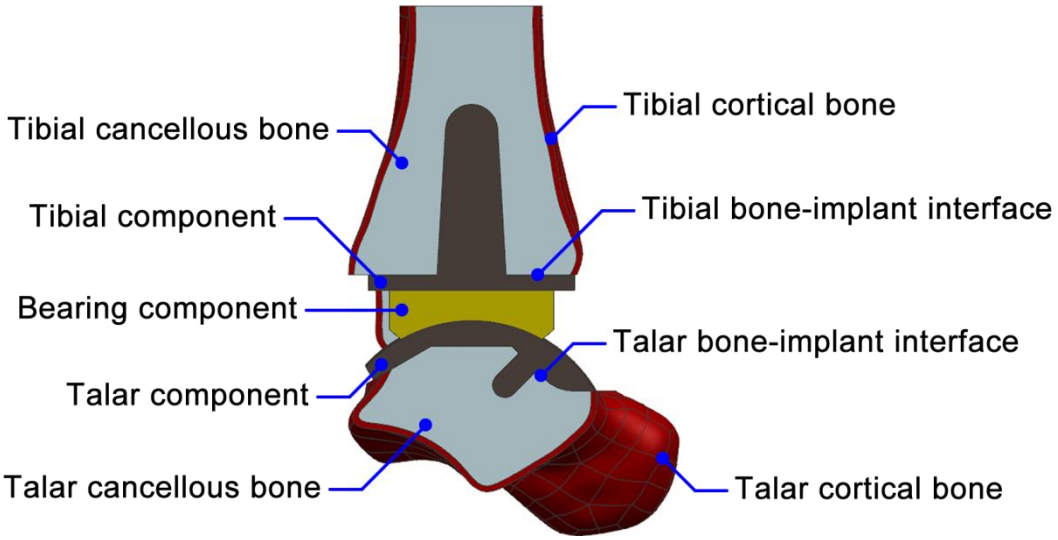

Figure 5-2 Cutting the tibia and talus to conform to the surfaces of tibial and talar components

The CAD model was then imported into the FEA software, Abaqus/CAE (version 6.12-2, Dassault Systèmes Simulia Corp, Rhode Island USA). In this initial model, the talus was not included because it was not possible to use the automated tools to merge the instances of the cortical and cancellous bones together. The merge function was necessary to avoid an overconstraint problem that always occurred at a region of more than two components tied together and to reduce computational expense as described in Chapter 4. The tibial cortical bone was tied to the tibial cancellous bone using the 'merge instances' function as described in Chapter 4. Although both types of bone were merged into one object, they still maintained their inherent material properties.

5.2.1.2 Material Properties

The Young's moduli of the cortical and cancellous bones used in this study were 17.58 GPa and 280 MPa respectively, and their Poisson's ratios were both 0.30. These values were taken from the study of Miller et al. who use FEA to investigate effect of geometry of talar component on stress in polyethylene liner as described in Chapter 4 (Miller et al. 2004). The similar values of the moduli also appear on several published papers (Reilly and Burstein 1975, Goldstein et al. 1983, Aitken et al. 1985, Snyder and Schneider 1991). As in Chapter 3, the tibial and talar components were assumed to be titanium alloy (Ti-6Al-4V) (Young's modulus of 113.8 GPa and Poisson's ratio of 0.342), while the bearing component ultra-high-molecular-weight polyethylene (UHMWPE) (Young's modulus of 850 MPa, Poisson's ratio of 0.4, and yield strength of 13.8 MPa).

5.2.1.3 Interactions, Loads, and Boundary Conditions

The tibial TAR component was tied to the tibial bone to model the fully constrained bone-component interfaces. The contacts between tibial, talar, and bearing components were assumed to be frictionless replicating the simplified model used for validation in Chapter 3.

The bottom surface of the talar component was fully fixed similar to the full constraint of the talar cartilage in Chapter 4. A compressive force of 3416 N, which is approximately the maximum axial load applied on the ankle joint during a gait cycle, was applied to the tibial bone (Figure 5-3). At the loading point, another boundary condition was applied to restrict displacement and rotation in all directions except vertical translation. The method of applying loads and boundary conditions through an analytical rigid plate and a reference point were the same as described in Chapter 4, but, in this study, the previous step of applying a displacement to bring the surfaces into contact was not needed due to there being no gap between each component.

Ten-node quadratic tetrahedron elements were used to mesh both the bones and TAR components as in the previous FE models. All models in this study were run with at least ~120,000 elements, and some initial models were run with a higher mesh density during the development phase of the study.

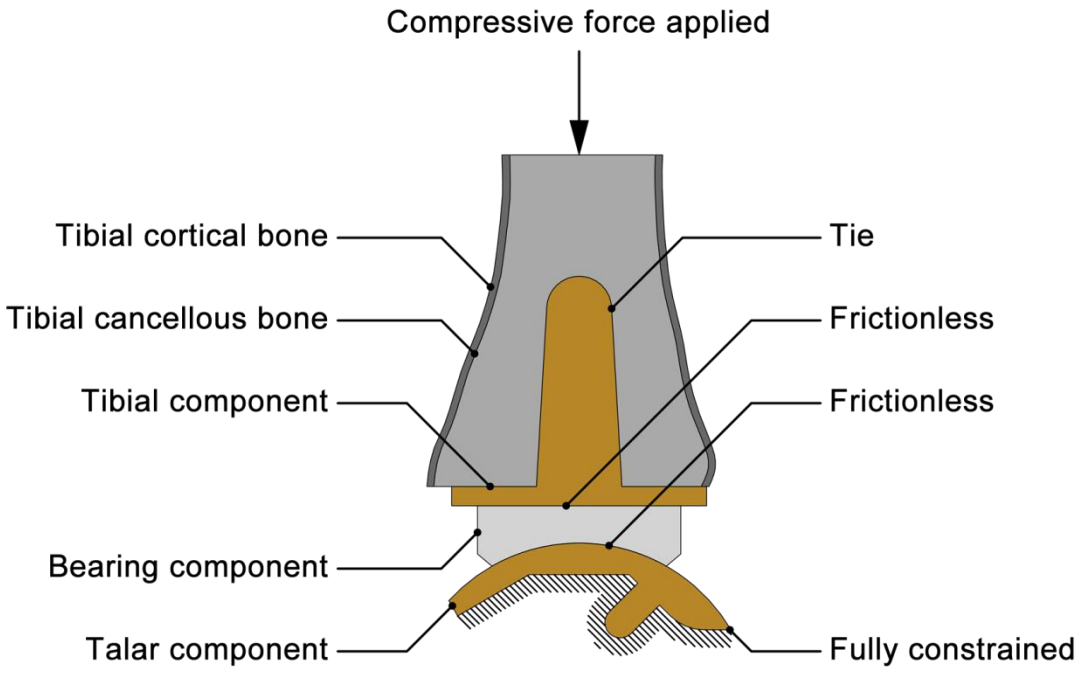

Figure 5-3 FE model of TAR with natural ankle geometry

5.2.2 Mesh Convergence Study

A mesh convergence study was performed on the model in Section 5.2.1 to choose an optimal mesh density for further studies. Three mesh schemes were used with the element number approximately doubled up each time from ~120,000 to 460,000. The element sizes of the model with ~120,000 elements were the default option of the FEA software, while the model with ~460,000 elements were based on the mesh convergence study done in Chapter 3. The element number of an intermediate model was ~230,000, which was twice the number of the model with default element sizes.

Three output variables: maximum von Mises stress (σ_{vm}), maximum minimum principal strain (ε_{min}), and vertical displacement (u_y) obtained from each model were compared.

5.2.3 Sensitivity Study – Tibial Geometry

It was found that the geometry of the medial malleolus in some misalignment cases meant that the models of the tibial cortical and cancellous bones could not be automatically merged together. It was not possible to obtain any clarification from the software to explain the reason for this failure. Therefore, a study of the effect of malleolus geometry on the FEA result was undertaken to establish if it could be removed from the FE model without affecting the results of interest.

Tibial models with and without malleolus geometry were created originally from the same model, but the malleolus of the latter model was removed by cutting at the same level as when preparing the surface for installing the tibial component (Figure 5-4). Both models were meshed using a similar element size, which was chosen from the mesh convergence study in Section 5.2.2. All analysis components in Section 5.2.1 were applied on both models, and both analysis results were compared to study the effects of malleolus geometry on the tibial FE model.

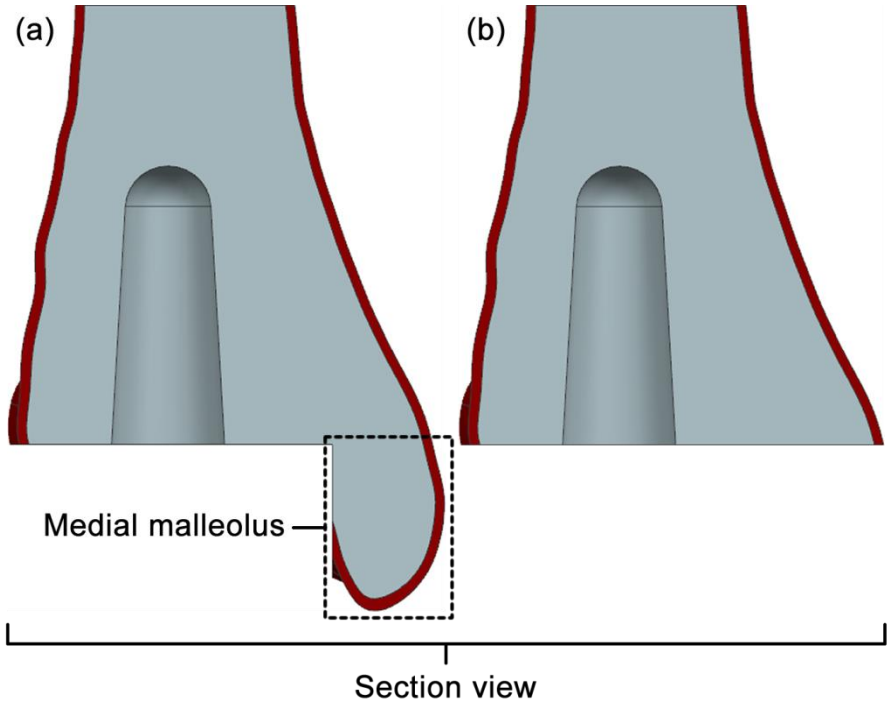

Figure 5-4 Model of the tibia, (a) with malleolus, (b) without malleolus

5.2.4 Sensitivity Study – Elastic Modulus of Cortical Shell

From the results of the previous simplified model, it is clear that the cortical shell is important. In the real patient population, the stiffness of the cortex varies because of differences in its thickness and material properties. Here, it was difficult to alter the thickness because sometimes the software was unable to estimate the new boundary of the complex geometry, but it was easy to change the material properties. Therefore, the effect of cortex stiffness was examined through changing the material properties. The modulus of the tibial cortical bone may vary over a wide range depending on its composition, for example the elastic modulus reported in the study of Lee et al. measured from 11 different subjects, varied by approximately 51% (11.3±5.8 GPa) (Lee et al. 1997). In three other studies by Mather, Choi and Goldstein, and Snyder and Schneider, the modulus value was found to vary by approximately 37%, 25%, and 9% respectively (Mather 1967, Snyder and Schneider 1991, Choi and Goldstein 1992).

Three FE models were used in this study. All analysis conditions were exactly the same except the Young's modulus of the cortical bone. Here, two additional values were investigated, with the modulus reduced to be 75% and half of the original value. The changes in output variables were investigated and compared.

5.2.5 Initial FEA of TAR with Natural Ankle Geometry

The FE model of the TAR with natural ankle geometry created following the procedures described previously was analysed to obtain the results for comparison to the outcomes obtained from the analysis of the FE model of natural ankle in Chapter 4. However, for comparison, the compressive force applied onto the tibia needed to be reduced to 350 N which was same as the magnitude of load used in Chapter 4. Both the location and magnitude were then compared in this study.

5.2.6 FEA of TAR with Different Positions of Implantation

Considering the surgical technique provided by the manufacturer, there were various cases of misalignment of implantation which are likely to occur clinically. In the surgical procedure, the method of locating the TAR position starts by defining the joint line located between the articular surfaces of the tibia and the talus, and several types of jig are installed to locate the positions of all components with reference to that joint line. If the position of the joint line is defined incorrectly, then misalignment of whole TAR components will occur. Another type of misalignment that could occur is the misalignment between each component. Because the talus can be moved in a certain range in a loose mortise formed by the tibia and fibula, defining the correct position of the bones of ankle joint is challenging. If the ankle bones before installation of the location jigs are not in their natural alignment, the bones will then return to their normal position after removal of the jigs, yielding a misalignment between each component.

Therefore, misalignment of the TAR in this study was divided into two types of cases: whole and partial prosthesis misalignments.

Translational and rotational misalignments were considered on two anatomical planes: the frontal and the sagittal, for the whole prosthesis misalignment. All of the TAR components were translated together 5 mm in distance from the ideal position in each of the medial, lateral, anterior, and posterior directions, and rotated together ±5° in angle in the frontal and sagittal planes (Figure 5-5). All analysis conditions of all models were the same as the models described in the previous sections. There were a total of eight FE models which were performed and compared in this study.

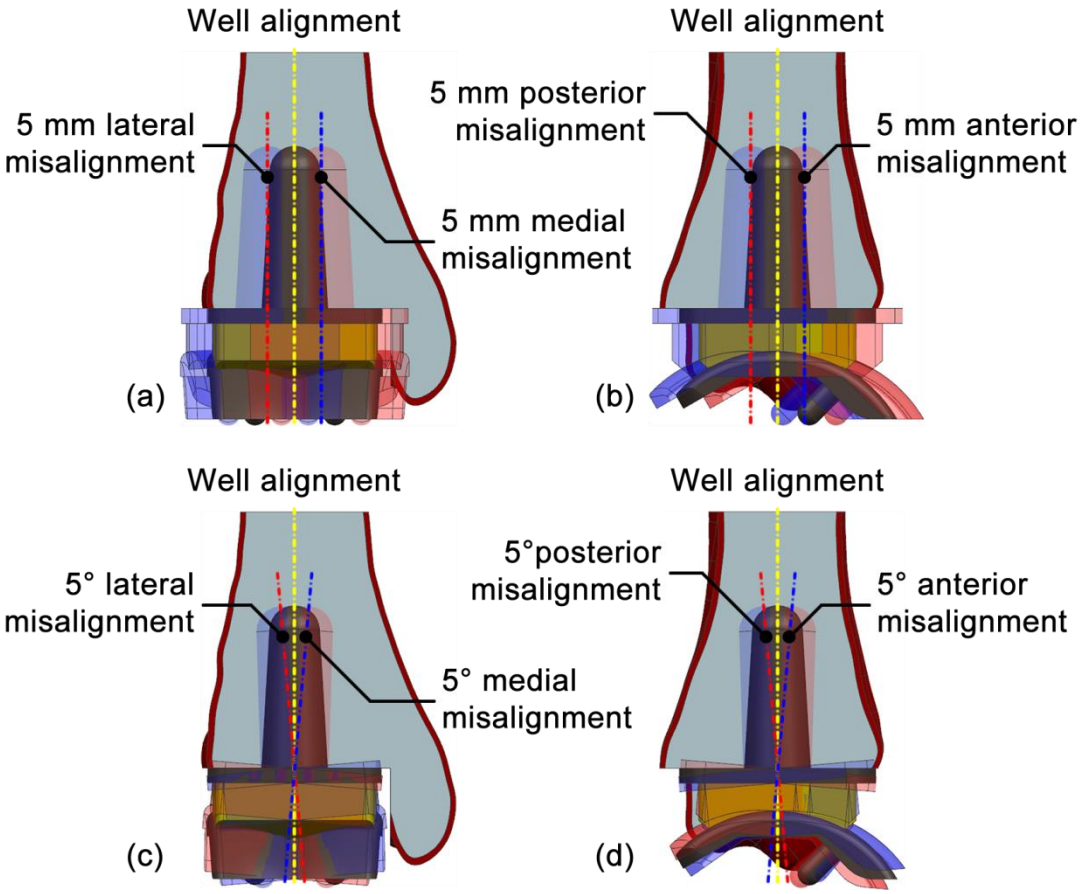

Figure 5-5 FE model of TAR with whole component misalignment, (a) medial and lateral translation, (b) anterior and posterior translation, (c) medial and lateral rotation, (d) anterior and posterior rotation

For the partial prosthesis misalignment cases, all conditions were the same as the whole component misalignment models except the number of misaligned parts. For the former study, all components were misalignment together, while in this study only the bearing and talar components were misaligned (Figure 5-6). However, the rotational misalignment of the partial prosthesis was not considered because the human body is freer than the experimental set-up and this type of misalignment can be compensated by a slight change in positioning of the joint as discussed in Section 2.4.2.3 in Chapter 2. Therefore, there were only a total of four FE models of only translational misalignment of the partial prosthesis (Figure 5-6a and 5-6b) which were performed and compared in this study.

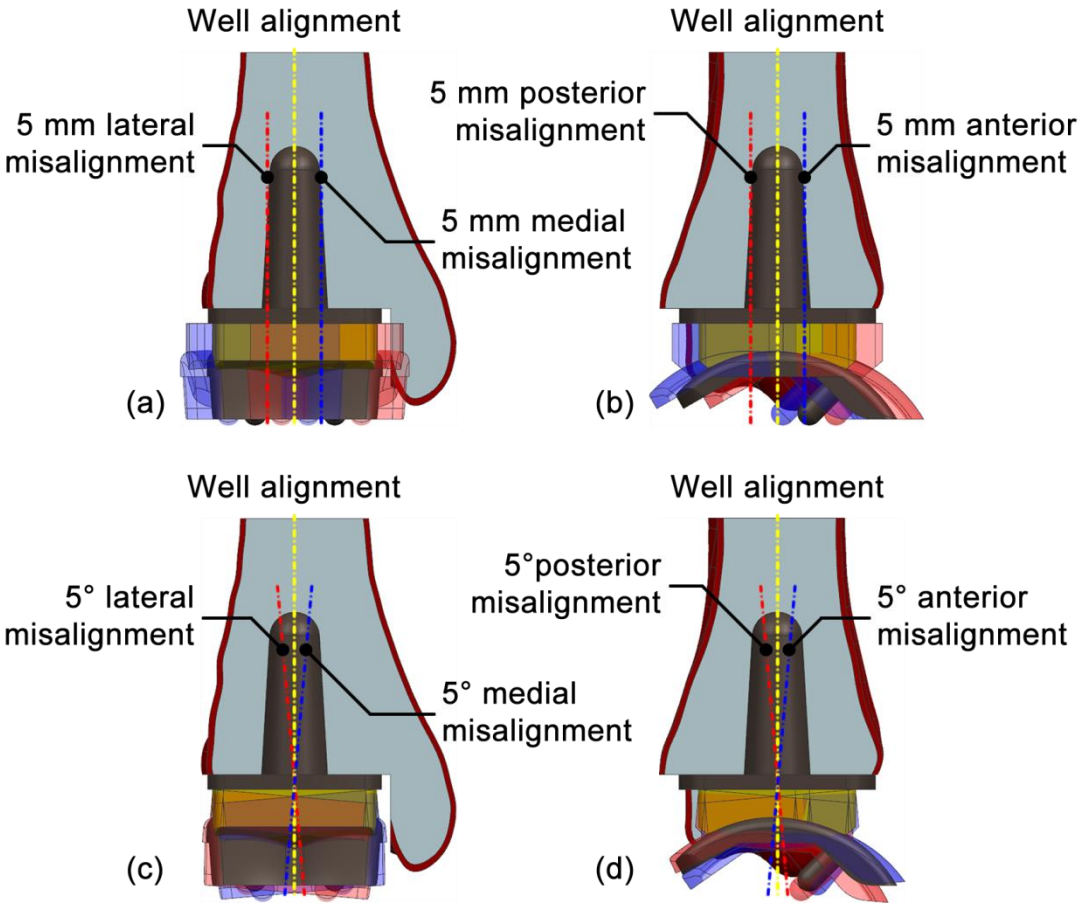

Figure 5-6 FE model of TAR with partial component misalignment, (a) medial and lateral translation, (b) anterior and posterior translation, (c) medial and lateral rotation, (d) anterior and posterior rotation

5.3 Results

5.3.1 Mesh Convergence Study

The mesh convergence study showed that all models undertaken have very similar values for the outputs selected (Figure 5-7). Comparing between the model with ~120,000 elements and the model with a doubled mesh (~230,000 elements), the differences in the maximum σ_{vm} and ε_{min} measured at tibial bone and u_y measured at the point of load application were 1.93%, 0.28%, and 0.01% respectively. The running time of the former model was about four hours, while the latter needed about 11.5 hours using four processors of an Intel® Xeon® Processor X5560. Comparing the model with the finest mesh (~460,000 elements) to the model with a half mesh (~230,000 elements), the differences in the maximum σ_{vm} and ε_{min} and u_y were 0.19%, 0.33%, and 0.47% respectively. This model required 36.5 hours of running time for the analysis.

Therefore, the model with ~120,000 elements was selected for all further studies.

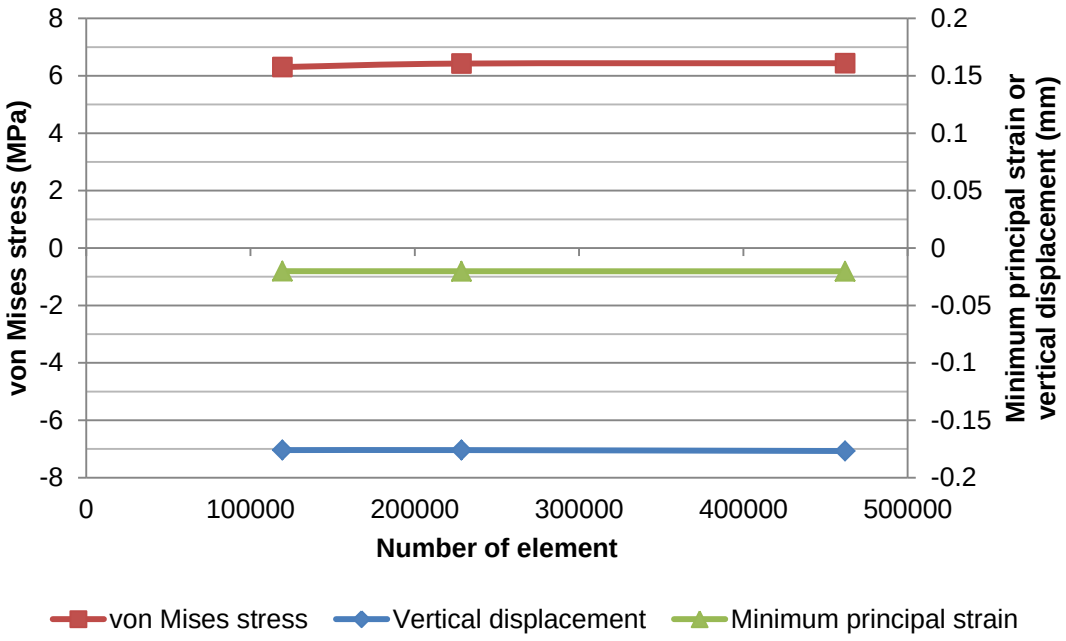

Figure 5-7 Mesh convergence study (measuring at tibial bone)

The locations of the maximum σ_{vm} and ε_{min} on all models were not the exactly same, but were close together within a range of 0.9-3.4 mm in the region of the tip of the tibial stem (Figure 5-8). This is because all models were meshed using different average element size.

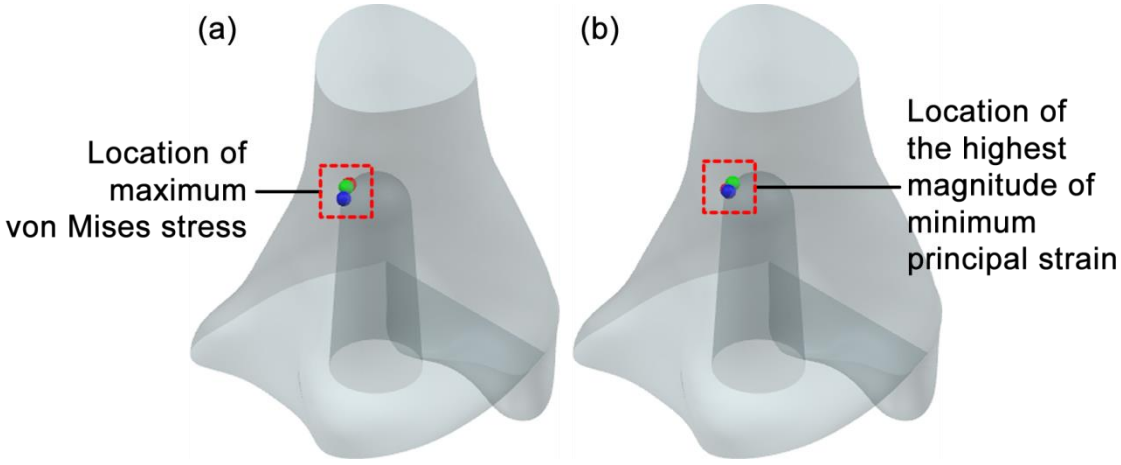

Figure 5-8 Location of maximum von Mises stress (a) and the highest magnitude of minimum principal strain (b) on tibial bone

Although this study mainly focused on the risk of bone damage, mesh convergence study was also performed on the TAR component to investigate the suitable meshing for it. The model with ~120,000 elements was compared to the model with a doubled mesh, and the differences in the maximum σ_{vm} and ε_{min} measured at bearing component and u_y measured at the same point as in previous mesh convergence study were 0.06%, 0.12%, and 0.01% respectively. The model with the finest mesh (~460,000 elements) was also compared to the model with a half mesh (~230,000 elements), and the differences in the maximum σ_{vm} and ε_{min} and u_y were 0.09%, 0.12%, and 0.47% respectively (Figure 5-9).

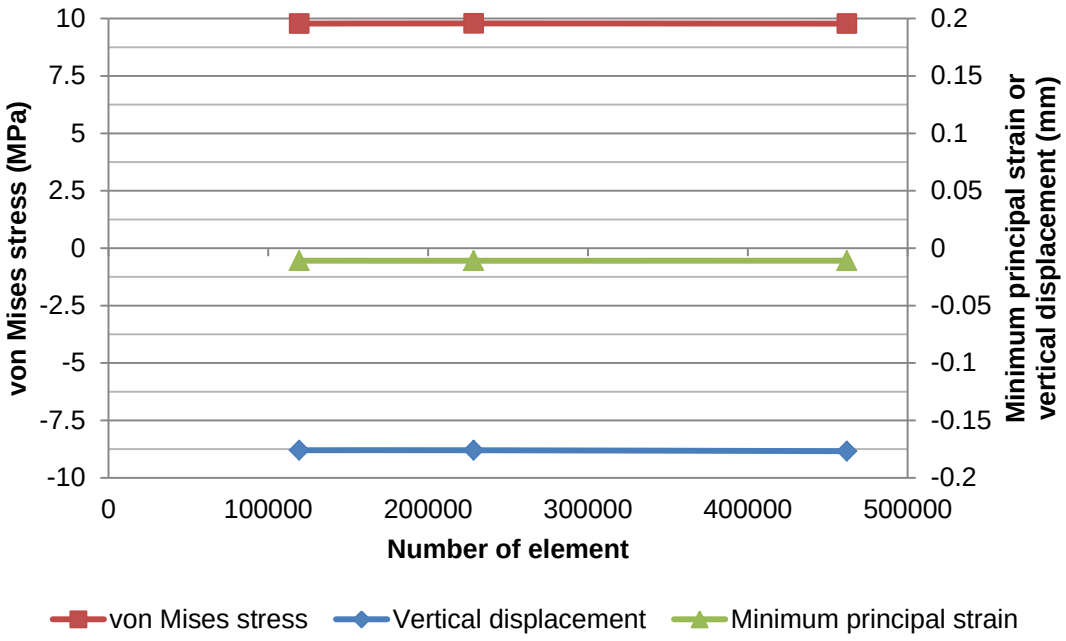

Figure 5-9 Mesh convergence study (measuring at bearing component)

The locations of the maximum σ_{vm} and ε_{min} on all models were not the exactly same as well, but were close together within a range of 0.02-1.40 mm in the region of the lower articulation surface of the bearing component (Figure 5-10).

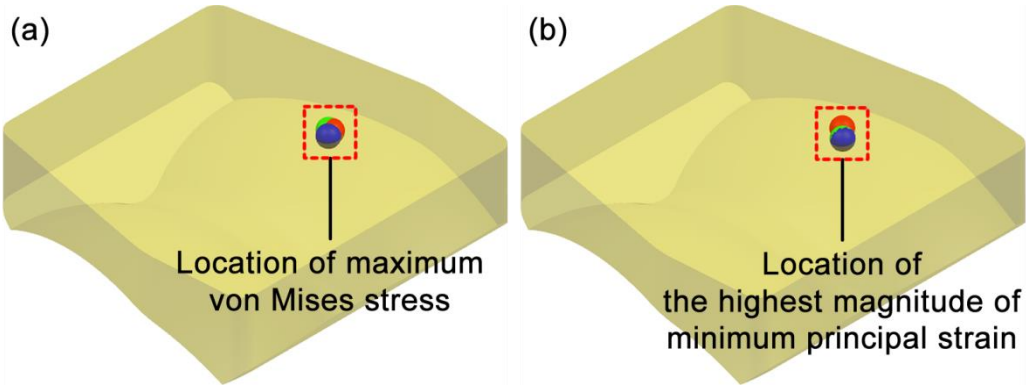

Figure 5-10 Location of maximum von Mises stress (a) and the highest magnitude of minimum principal strain (b) on bearing component

5.3.2 Sensitivity Study – Tibial Geometry

The results obtained from the FE models with and without malleolus geometry were compared in terms of three output variables: von Mises stress (σ_{vm}), minimum principal strain (ε_{min}), and vertical displacement (u_y). These outputs were measured only on the tibial bone. The σ_{vm} and ε_{min} were measured at the nodes where the highest magnitudes were located, while the u_y was measured at the point of load application. The presence of the medial malleolus of the tibia had little effect on the outputs (Figure 5-11, 5-12, and 5-13).

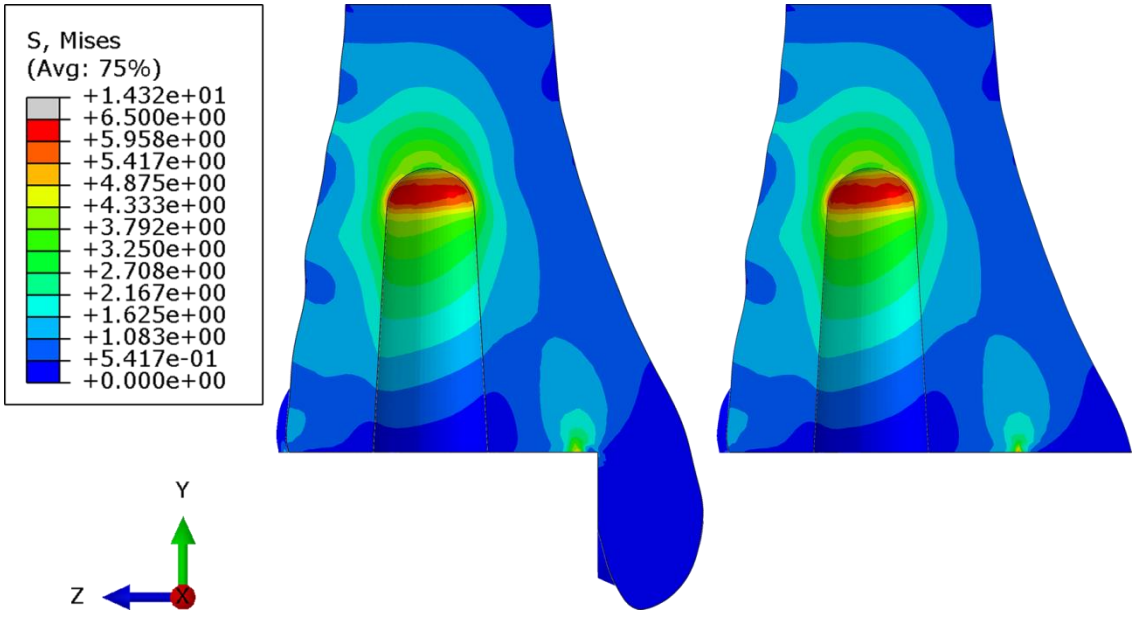

Figure 5-11 Plot of von Mises stress (MPa) distribution in the model with and without tibial malleolus

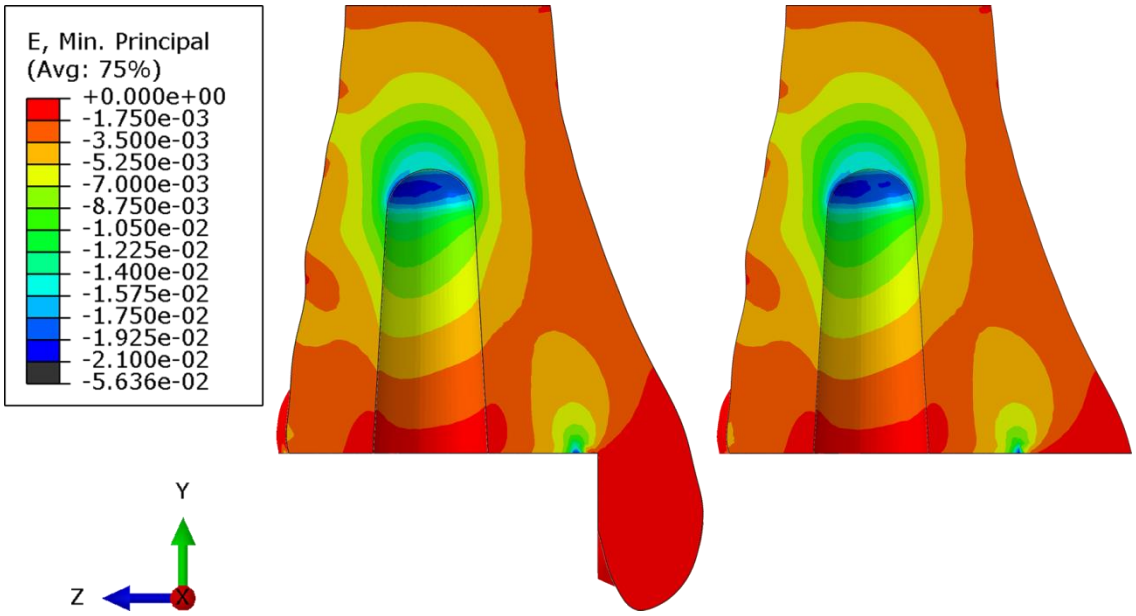

Figure 5-12 Plot of minimum principal strain distribution in the model with and without tibial malleolus

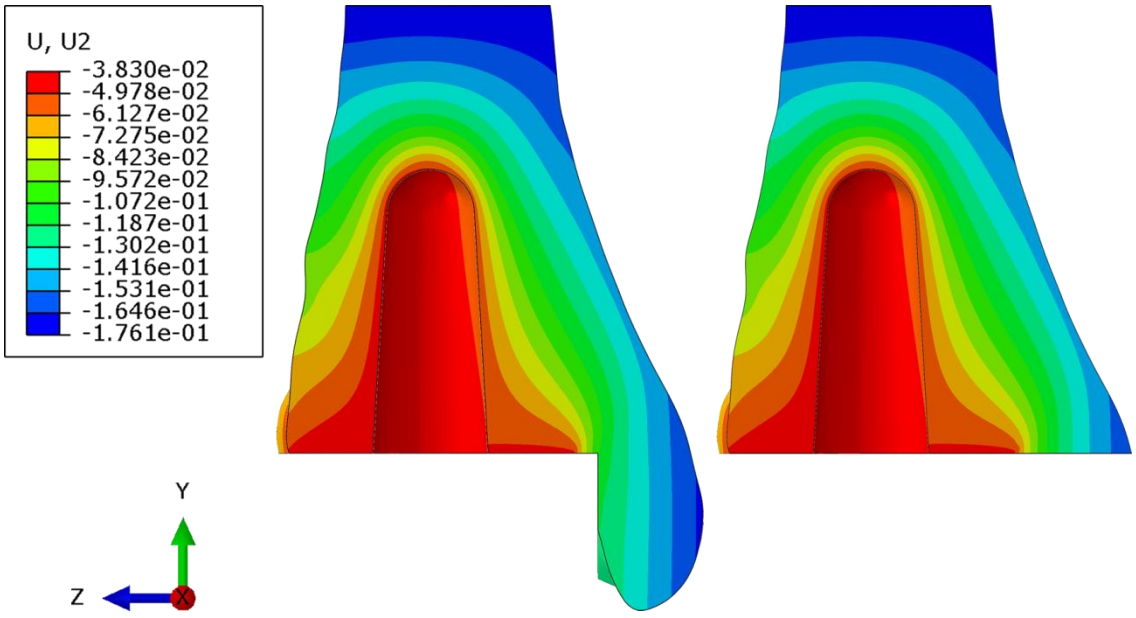

Figure 5-13 Plot of vertical displacement (mm) distribution in the model with and without tibial malleolus

The location of the maximum von Mises stress and minimum principal strain of the models with and without tibial malleolus were found to be located at exactly the same coordinates. The differences in the maximum σ_{vm} and highest magnitude ε_{min} between the two models were 1.05% and 0.26% respectively, and the difference in the u_y was 0.04%.

5.3.3 Sensitivity Study – Elastic Modulus of Cortical Shell

The results obtained from the FE models with three different elastic moduli of cortical shell were compared in terms of three output variables: von Mises stress (σ_{vm}), minimum principal strain (ε_{min}), and vertical displacement (u_y). These outputs were measured only on the tibial bone. The σ_{vm} and ε_{min} were measured at the nodes which their highest magnitudes were located, while the u_y was measured at the point of load application (Table 5-1). After reducing the Young's modulus of the cortical bone by 25%, the maximum von Mises stress, highest magnitude minimum principal strain, and vertical displacement were increased by between 8% and 11%, while doubling the reduction of the elastic modulus to 50%, the increasing of these outputs were more than two-fold (in a range of 2.60-2.68).

Table 5-1 Changing of three outputs on cancellous bone after reducing elastic modulus of cortical bone

Model	Elastic modulus		von Mises stress – maximum		Minimum principal strain – maximum magnitude		Vertical displacement	
	Value (GPa)	Diff (%)	Value (MPa)	Diff (%)	Value	Diff (%)	Value (mm)	Diff (%)
1	17.580	-	6.426	-	-0.0202	-	-0.176	-
2	13.185	25.00	6.954	-8.22	-0.0221	-9.41	-0.195	-10.80
3	8.790	50.00	7.798	-21.35	-0.0252	-24.75	-0.227	-28.98

The results were also plotted to show the linearity of the relationships between reducing elastic moduli and increasing of the outputs (Figure 5-14). The increasing of the outputs was not perfect linear, with coefficient of determination (R^2) of all outputs about 0.98.

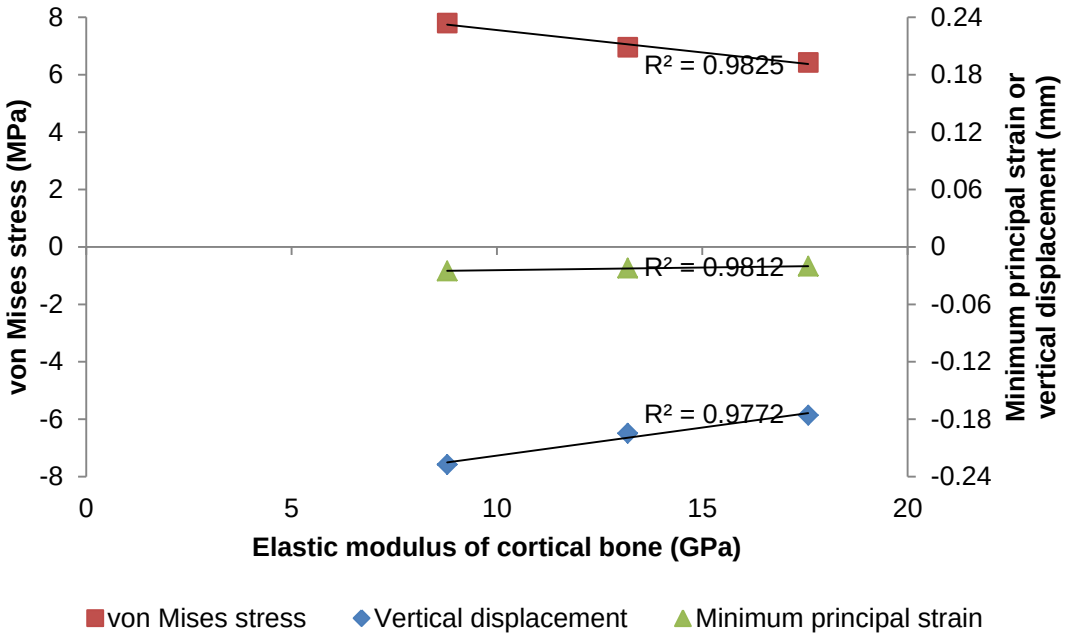

Figure 5-14 Relationship between reducing elastic moduli and increasing of the outputs (maximum von Mises stress, highest magnitude of minimum principal strain, and vertical displacement) with linear regression line

5.3.4 FEA of TAR for Comparison with FEA of Natural Ankle

The contour plots of the von Mises stress distribution in the tibial cancellous bone for the FE model of natural ankle and the FE model of TAR with natural ankle geometry were illustrated in Figure 5-15 and 5-16 respectively. The region of high concentration of stress distribution was located at the region that was close to the articular surface for the former FE model, while located at the region surrounding the tip of the tibial stem for the latter FE model.

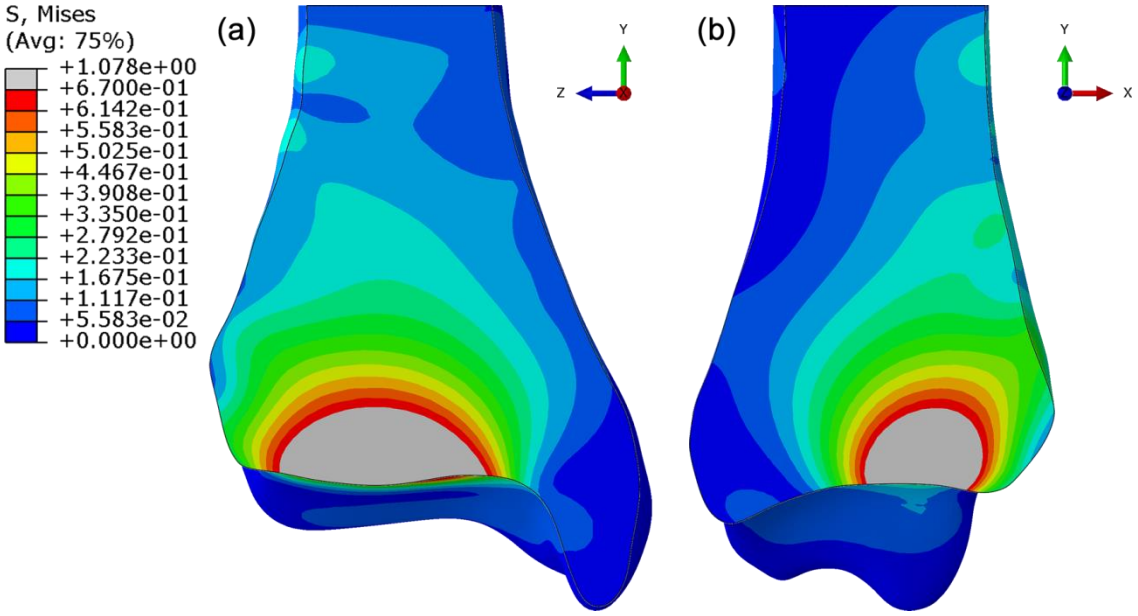

Figure 5-15 The contour plots of the von Mises stress (MPa) distribution in the tibial cancellous bone of the FE model of natural ankle, (a) showing the cross section in the frontal plane, and (b) showing the cross section in the sagittal plane

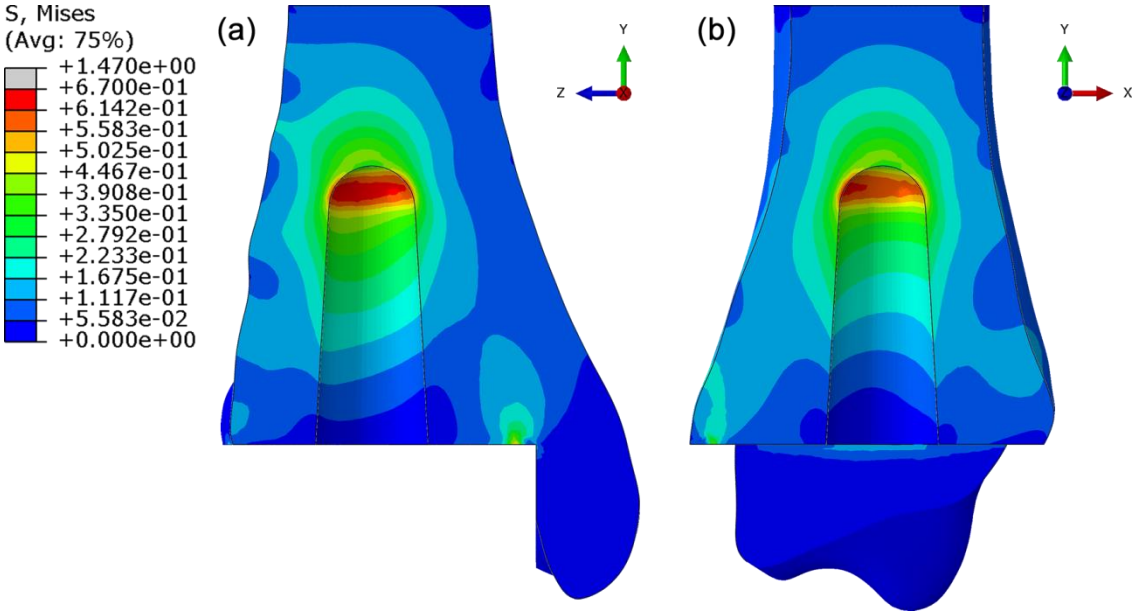

Figure 5-16 The contour plots of the von Mises stress (MPa) distribution in the tibial cancellous bone of the FE model of TAR with natural ankle geometry, (a) showing the cross section in the frontal plane, and (b) showing the cross section in the sagittal plane

In this study, only the stress distributions in the region located at level of the tip of the tibial stem on both FE models were of interest and compared. In the FE model of natural ankle, the magnitude of the stress was gradually reduced corresponding to the distance away from the contact location, and the stress at the region of interest was approximately in a range of 0.06-0.17 MPa. At the similar region in the FE model of the TAR within the natural ankle geometry, the stress was approximately in a range of 0.39-0.67 MPa, and the maximum magnitude of von Mises stress was 0.66 MPa.

5.3.5 FEA of TAR with Different Positions of Implantation

The FEA results obtained from the FE models with different positions of implantation were compared in terms of the distribution of von Mises stress (σ_{vm}) as well as the location and magnitude of the maximum value in the cancellous bone.

5.3.5.1 Translation of Whole Component of TAR

The maximum von Mises stress on the cancellous bone at around the tip of the stem of the model with normal position of TAR was about 6.43 MPa (Figure 5-17a). The maximum von Mises stress of the model with the TAR moved medially by a distance of 5 mm was 6.40 MPa, which was little different from the model with the normal position (Figure 5-17b). For the other three misalignment models, in which all the components were moved laterally, anteriorly, and posteriorly by a distance of 5 mm, the maximum von Mises stresses were 9.77, 8.77, and 10.28 MPa respectively (Figure 5-17).

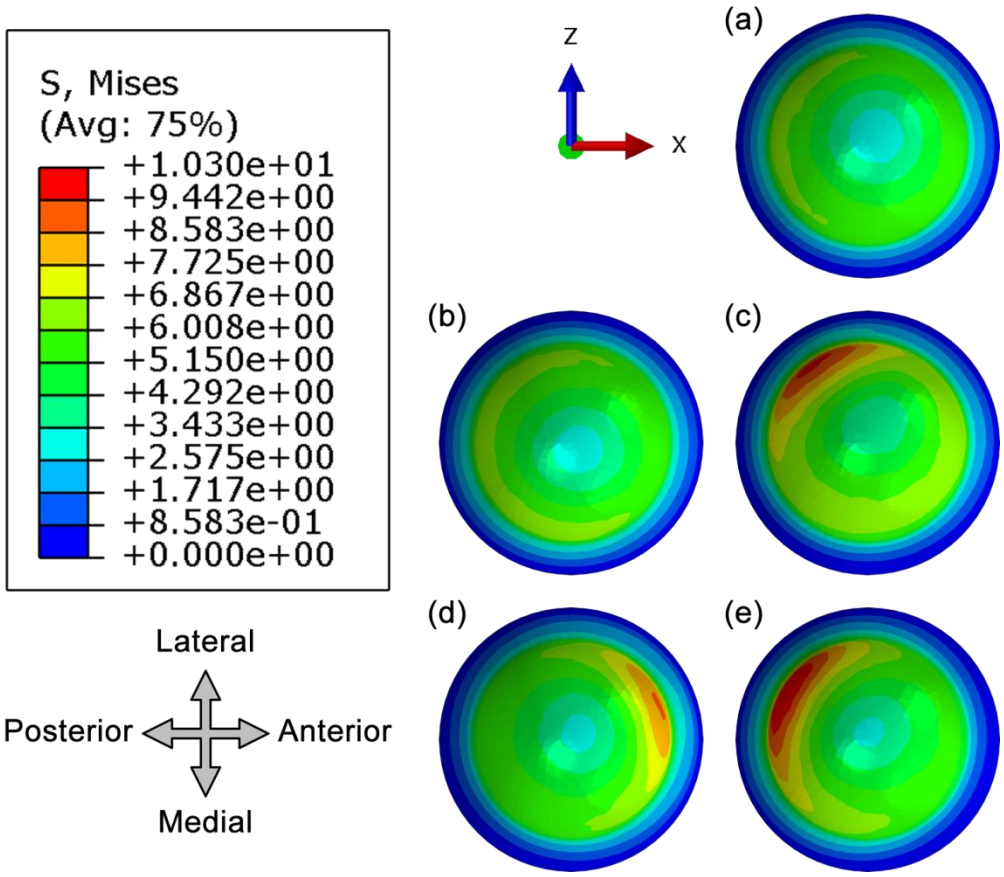

Figure 5-17 von Mises stress (MPa) in cancellous bone around the tip of the stem, (a) well aligned position, (b) medial misalignment, (c) lateral misalignment, (d) anterior misalignment, (e) posterior misalignment

The position of the maximum von Mises stress in the cancellous bone was always located in the same region as the misaligned components were moved towards (Figure 5-17). For example, when the misaligned components moved anteriorly, the maximum von Mises stress was located at the anterior side of the tip of the stem (Figure 5-17d).

With regards the shear stress, it was found to be difficult to obtain useful visual plots because of the 3-D nature of the structure, and the contour plots of shear stress in a particular direction at a particular cross-section were not very informative. Although difficult to present in a contour plot, the location of the peak shear stresses were found to generally match the location of the peak von Mises stress. The higher shear stresses generally extended down the interface between the stem and the bone rather than into the bone.

Considering the relationship between the magnitude of the maximum von Mises stress and the misalignment, the value of the magnitude was inversely proportional to the distance between the stem and the outer surface of the cancellous bone. In this case, the shorter the distance, the higher the von Mises stress. Their relationship was plotted and also modeled using the linear regression method with coefficient of determination (R^2) of 0.93 (Figure 5-18).

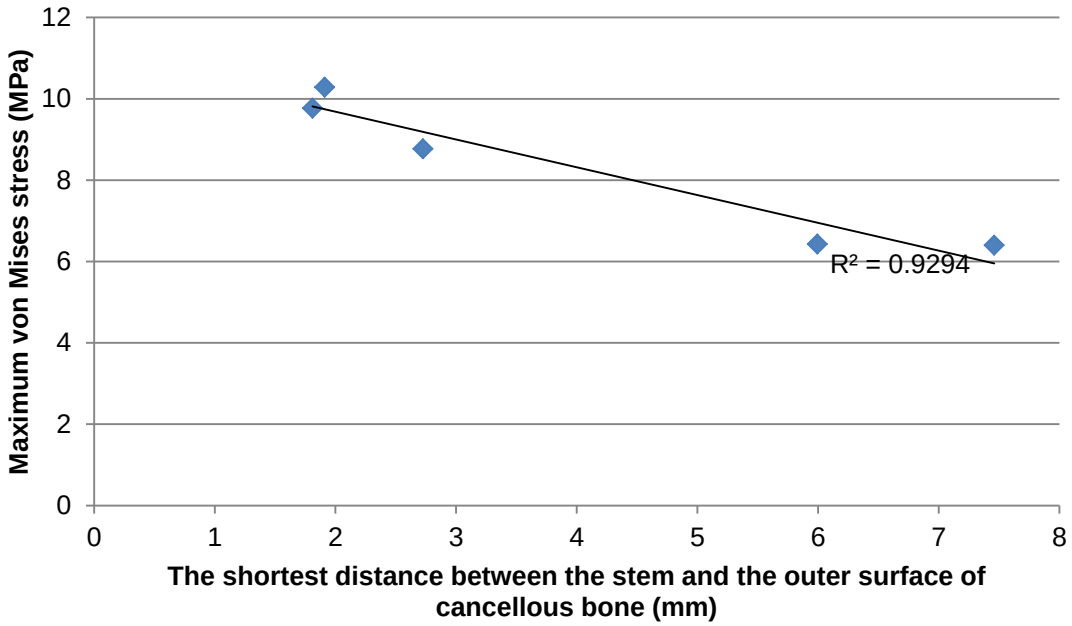

Figure 5-18 The maximum von Mises stress (MPa) versus the shortest distance between the stem and the outer surface of cancellous bone (mm) measured at the region surrounding the tip of the stem, with linear regression line

Further into the cancellous bone, the distribution of higher von Mises stress values was moved toward the thinner side of the cancellous bone, between the tip of the stem and outer surface of the bone, and in the same direction as the misalignment of the component (Figure 5-19). However, the distribution of the higher stresses on the model with medial misalignment did not shift toward the medial side, it was just around the tip of the stem (Figure 5-19b). In this case, the cancellous bone is thicker on the medial side in the well-aligned case, so the medially misaligned component was now effectively sitting nearer the middle of the bone.

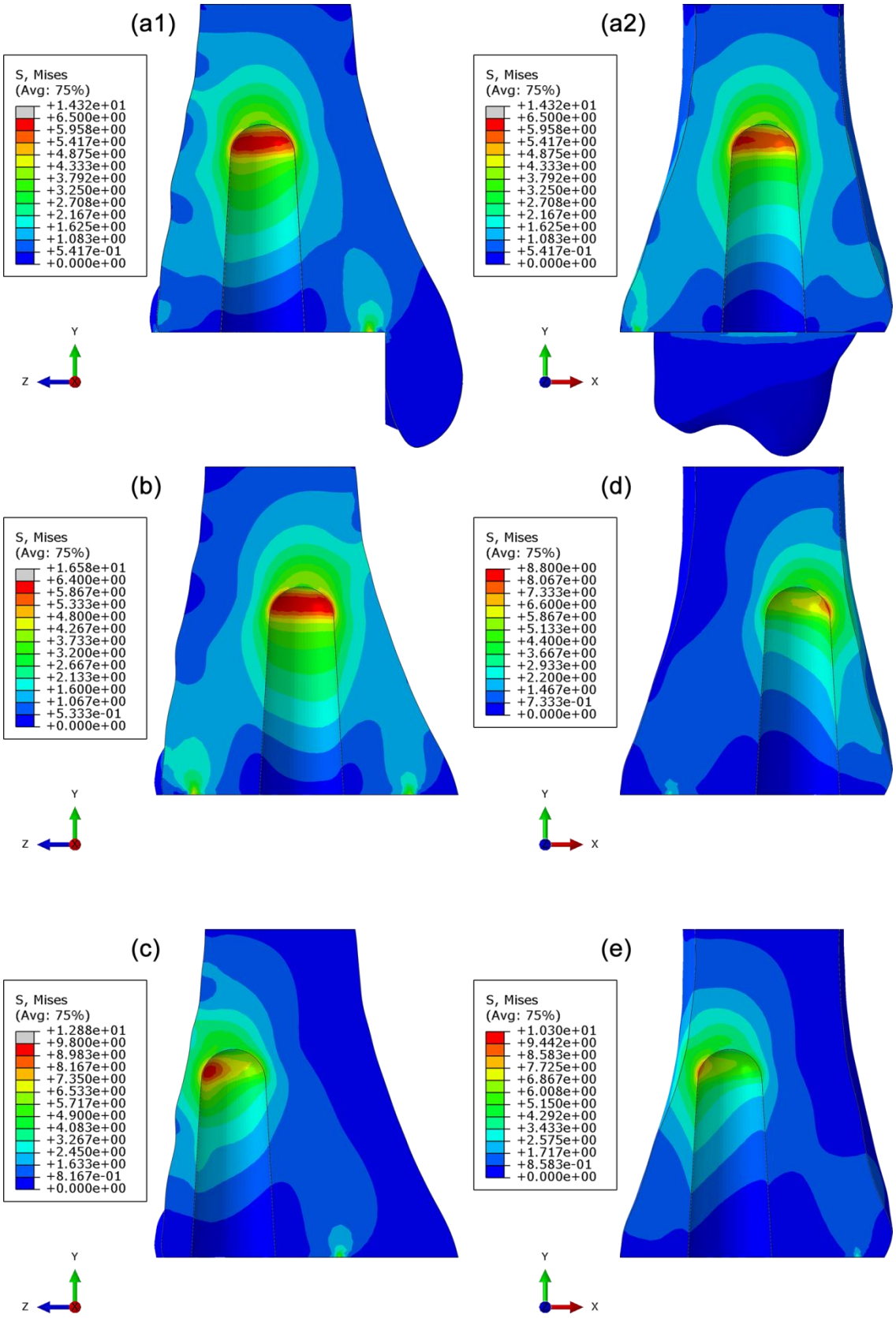

Figure 5-19 Distribution of von Mises stress (MPa) in cancellous bone around the tip of the stem, (a1) and (a2) well aligned position, (b) medial misalignment, (c) lateral misalignment, (d) anterior misalignment, (e) posterior misalignment

5.3.5.2 Rotation of Whole Component of TAR

The maximum von Mises stress in the cancellous bone of the models where the whole TAR implant was tilted were 6.01 MPa (medial tilt), 7.43 MPa (lateral tilt), 6.98 MPa (anterior tilt), and 7.95 MPa (posterior tilt). The location of the maximum von Mises stress on all models was located in the region that the stem tilted towards, except the model with medial rotation. The maximum von Mises stress of this model was located at the posterior region of the tip of the stem (Figure 5-20a). The region of higher von Mises stress shifted toward the thinner side between the tip of the stem and outer surface of the cancellous bone, and this was similar to the direction of the misalignment of the component (Figure 5-20).

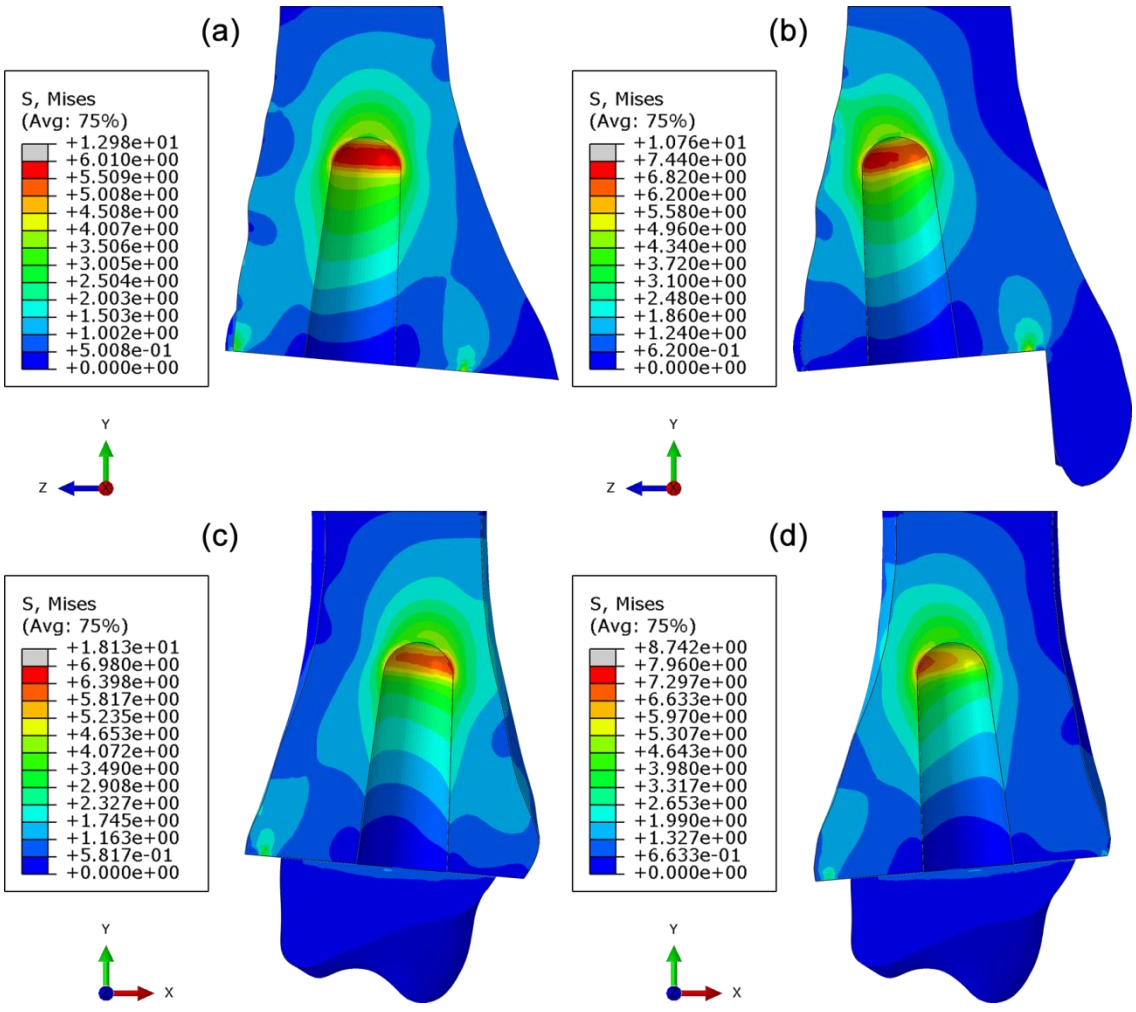

Figure 5-20 Distribution of von Mises stress (MPa) in cancellous bone around the tip of the stem, (a) medial misalignment, (b) lateral misalignment, (c) anterior misalignment, (d) posterior misalignment

The distance between the stem and the outer surface of the cancellous bone was plotted against the magnitude of the maximum von Mises stress to show their relationship and also modeled using the linear regression method with coefficient of determination (R^2) of 0.81 (Figure 5-21).

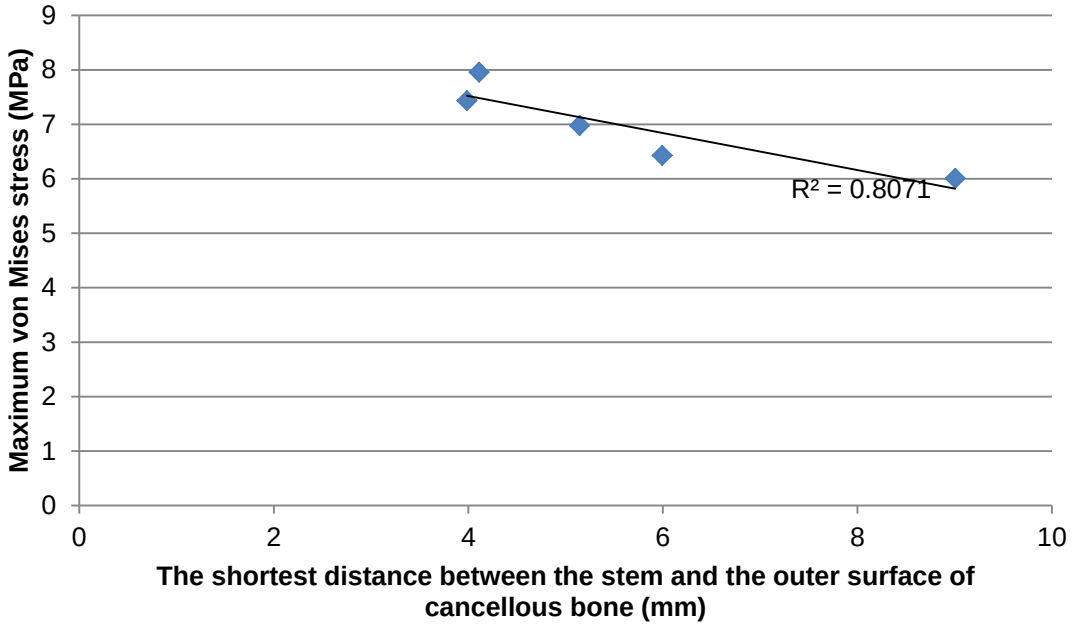

Figure 5-21 The maximum von Mises stress (MPa) versus the shortest distance between the stem and the outer surface of cancellous bone (mm) measured at the region surrounding the tip of the stem, with linear regression line

5.3.5.3 Translation of Partial Component of TAR

The maximum von Mises stress in the cancellous bone of the models where the partial TAR implant was moved were 6.56 MPa (medial move), 6.69 MPa (lateral move), 6.78 MPa (anterior move), and 7.89 MPa (posterior move). The stresses of all partial misalignment cases were similar except for the posterior partial misalignment case that was much higher. The location of the maximum von Mises stress on all models was located on the region that the bearing and talar components moved to, and the main region of higher von Mises stress was shifted towards that direction as well (Figure 5-22). Compared to the well aligned model where the maximum von Mises stress was 6.43 MPa, the differences were less than 5.3% except for the posterior misalignment case. The change in the stress for this type of misalignment was low because the tibial component was in the same location in all cases. Only the varying position of the bearing and talar components affected the results.

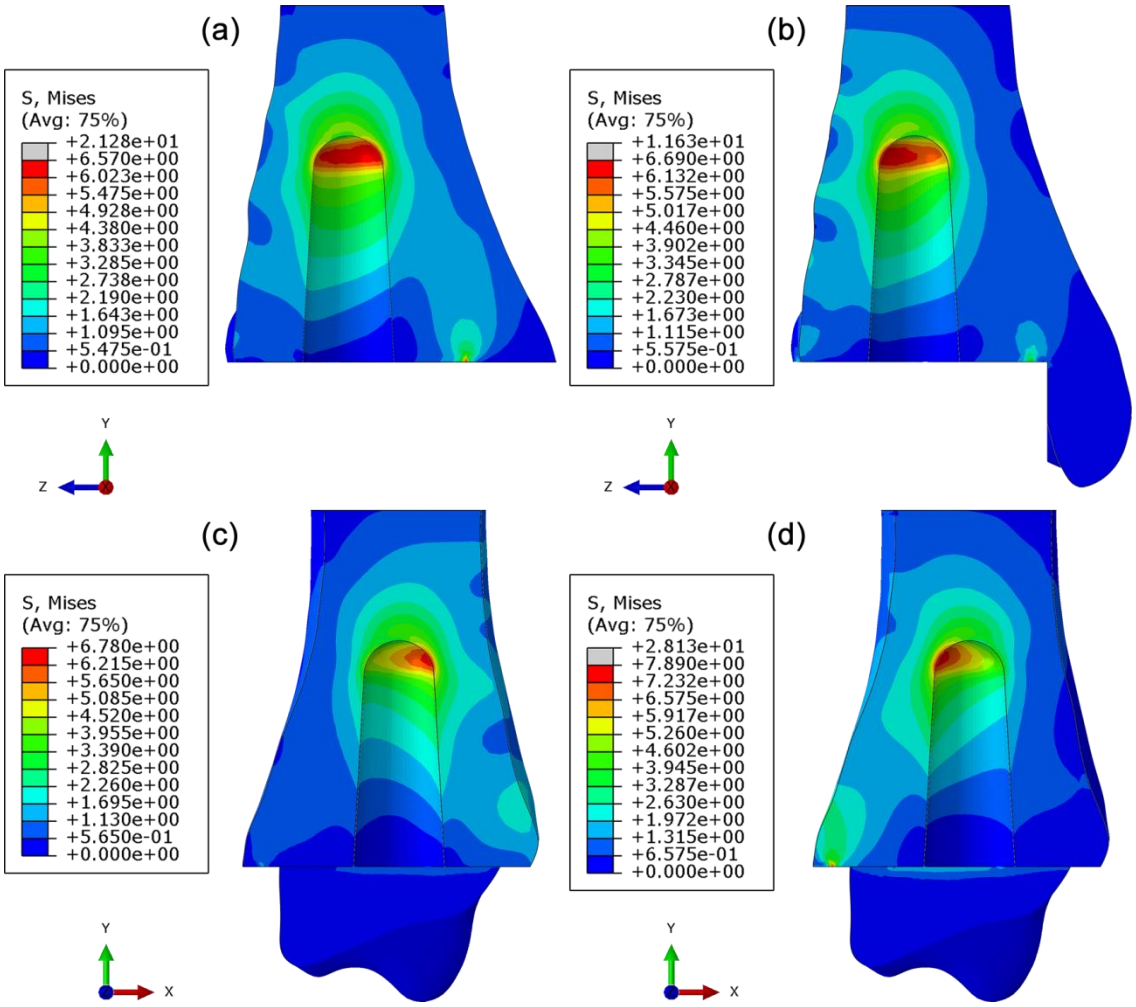

Figure 5-22 Distribution of von Mises stress (MPa) in cancellous bone around the tip of the stem, (a) medial misalignment, (b) lateral misalignment, (c) anterior misalignment, (d) posterior misalignment

5.4 Discussion

5.4.1 Mesh Convergence Study

The mesh convergence study was used to identify the most appropriate mesh scheme for the system. The predicted outputs obtained from the models with three different mesh schemes can be used for further analyses with respect to the accuracy of the results. However, when considering the aspect of computational cost together, the model with ~120,000 elements which requires the shortest running time of analysis was found to be the most suitable.

The mesh sensitivity study indicated that the models had sufficiently converged for all of the output measures of interest in this study.

5.4.2 Removing of the Tibial Malleolus Geometry

The tibial malleolus was found to cause difficulties in merging the cortical and cancellous instances on some models because of its complex geometry. After removing the malleolus geometry, the merging procedure could be performed successfully. Because the malleolus overhangs the TAR and does not bear load, it was not expected to cause any major effect on the load transmission. However, before removing the malleolus geometry from the ankle model, the study of the effect of the existing of medial malleolus was required.

Considering the FEA results obtained from the model with and without malleolus, the differences of almost of all outputs in the region of interest were less than 1%. There was only the maximum von Mises stress that was little higher than 1%. Considering the plot of the distribution of von Mises stress, minimum principal strain, and vertical displacement, the plot on both models were very similar (Figure 5-11, 5-12, and 5-13). Therefore, the geometry of tibial malleolus can be excluded from the FE model without significant effect on the results. However, malleolus geometry was included in some models in this study which has already been created and analysed prior to the issues in the merging instances processes.

In this study, there was only one axial force applied on the top surface of the tibial bone (as shown in Figure 5-3), and tibial bone was support and stabilized by the boundary condition, which was different from the real-world condition as described in Section 5.2.1.3. In the real-world, there are ligaments that connect to the medial malleolus providing some force transmission to support and stabilize the ankle. If future studies include the ligaments, then the malleolus clearly cannot be removed. The placement position of the tibial component in the real-world situation should be performed with care with this regard since the structure of malleolus left after implanting the TAR needs to be strong enough to withstand the force provided by the ligaments to prevent a risk of malleolus fracture.

5.4.3 Changing of the Stiffness of the Cortical Structure

According to the study in Chapter 3, the cortical shell plays an important role in reducing the stress in the cancellous bone in the region of interest. However, in the real-world, the stiffness of the cortical shell may vary in a range. A study of the effect of the stiffness of cortical structure on the output variables in the cancellous bone was therefore investigated. Generally, the stiffness of the cortex can be affected by the two means: changes in its thickness and changes in its material properties. Changing the thickness in the model was thought to be a difficult and time consuming procedure due to its complex shape and the

problems encountered in merging the geometry with the cancellous bone, therefore, changing elastic modulus of the cortical bone was chosen to be performed instead. The changing of the modulus is not only representing a change in stiffness, but also give some indication of what would likely happen if the cortex was either thinner or thicker.

After reducing the Young's modulus of the cortical shell by 25%, the von Mises stress and minimum principal strain on the cancellous bone were increased by about 9%. When reducing the elastic modulus by 50%, both outputs were increased by about 25%. The reduction and increase were not perfectly proportional, because the bone where the elastic modulus was reduced (i.e. the cortex) was not the same bone that was measured in the output (the cancellous bone).

Although the strong linear regression plot (coefficient of determination (R^2) = 0.98) representing the relationship between the stiffness of cortical bone and its effect on the cancellous bone cannot be used to entirely predict the real-world cases due to more complex structure of the real bone, the trend of this relationship is clear with changes in the stress and strain being inversely proportional to the stiffness of the cortex. This can be used to confirm that the quality of the bone is one of the important factors causing the success or failure of the TAR implantation. Therefore, clinically, surgeons should assess the quality of the bone carefully before making a decision to treat patients with the TAR.

5.4.4 Comparison between the Results of FEA of TAR and FEA of Natural Ankle

Compared to the natural ankle, the von Mises stress in the well aligned and fully bonded implanted ankle at the region of the tip of the tibial stem was at least two and may be as much as approximately six times as high. In this case, the stress might not exceed the compressive yield strength of cancellous bone, but, in inappropriate alignment and constraint, the stress might significantly increase leading to bone damage and consequently failure in implantation.

In natural ankle, this region was far from the region of maximum magnitude of the von Mises stress located close to the articular surface, and the stress gradually reduced in magnitude corresponding to the distance from that surface to a low level in the region of interest. In the implanted ankle case, the stress distribution was different, the tibial TAR component was much stiffer compared to the cancellous bone and transmitted the load to the cancellous bone at the tip of the stem directly, leading to the high stress on the cancellous bone in this region.

The existence of the tibial component of TAR shifted the position of high concentration of stress from the location close to the articular surface in the epiphyseal region to the higher location around the tip of the stem in the metaphyseal region. In the real-world, the bones are heterogeneous, and the region of the highest in magnitude of the strength of the tibial cancellous bone is at the epiphysis is close to the articular surface. The strength of the distal tibial cancellous bone is likely to decline further away from the articular surface (Hvid et al. 1985, Harada et al. 1988). In other words, the highest magnitude of von Mises stress was moved from the region of high strength to the region of lower strength. Therefore, in the prosthesis design, the length of the stem of the tibial component should be taken into account. An appropriate tibial stem should not reach the region of lowest strength to reduce risk of bone damage due to exceeding the yield strength of the cancellous bone.

5.4.5 Effect of Misalignment of TAR

The study of misalignment of the TAR components was divided into two main cases that were likely to occur clinically. One was the misalignment of the whole components, while the other was the partial misalignment where only the position of bearing and talar components was changed. Each case was subdivided into translation and rotation misalignments. Therefore, there were totally 12 different models created in this study.

5.4.5.1 Misalignment of the Whole TAR Component

For the misalignment of the whole components, the magnitudes of the maximum von Mises stress around the tip of the stem varied in a range of 6.40 to 10.28 MPa (translation misalignment) and 6.01 to 7.95 MPa (rotation misalignment) depending on the distance between the stem and the outer surface of the cancellous bone (Figure 5-17 and 5-22). In some misalignment cases, the compressive yield stress for cancellous bone was likely to be exceeded, and may lead to the failure of implantation. The yield stress of tibial trabecular bone may vary due to its individually complex structure, and its average value seen in several published papers is approximately in a range of 6-9 MPa. For example, the average compressive yield stress of tibial cancellous bone reported in the study by Morgan and Keaveny was 5.83 ± 3.42 MPa, while a value of 8.975 ± 7.568 was reported in the study by Rincón-Kohli and Zysset (Morgan and Keaveny 2001, Rincón-Kohli and Zysset 2009). Although there have been limited studies of tibial bone, these values overlap those measured at other sites, e.g. the compressive yield stress of the specimen collected from the femoral neck reported in the study by Morgan and Keaveny was 17.45 ± 6.15 MPa, while, in the another study by Homminga et

al., the yield stresses of the femoral trabecular bone reported were 6.7 ± 2.7 MPa (control group) and 8.2 ± 2.6 MPa (fracture group) (Homminga et al. 2002). Therefore, according to the yield strength obtained from these published papers, the cancellous bone is likely to be damaged due to excessive stress experienced in some misalignment cases.

The relationship between the magnitude of the maximum von Mises stress and the distance between the stem and the outer surface of the cancellous bone obtained from the study of the whole TAR component misalignment was inversely proportional with coefficient of determination (R^2) of 0.85 (Figure 5-23). It can be initially concluded that the main factor that affects the magnitude of the stress is the distance between the stem and the outer surface of cancellous bone. The shorter the distance, the greater the likelihood of failure.

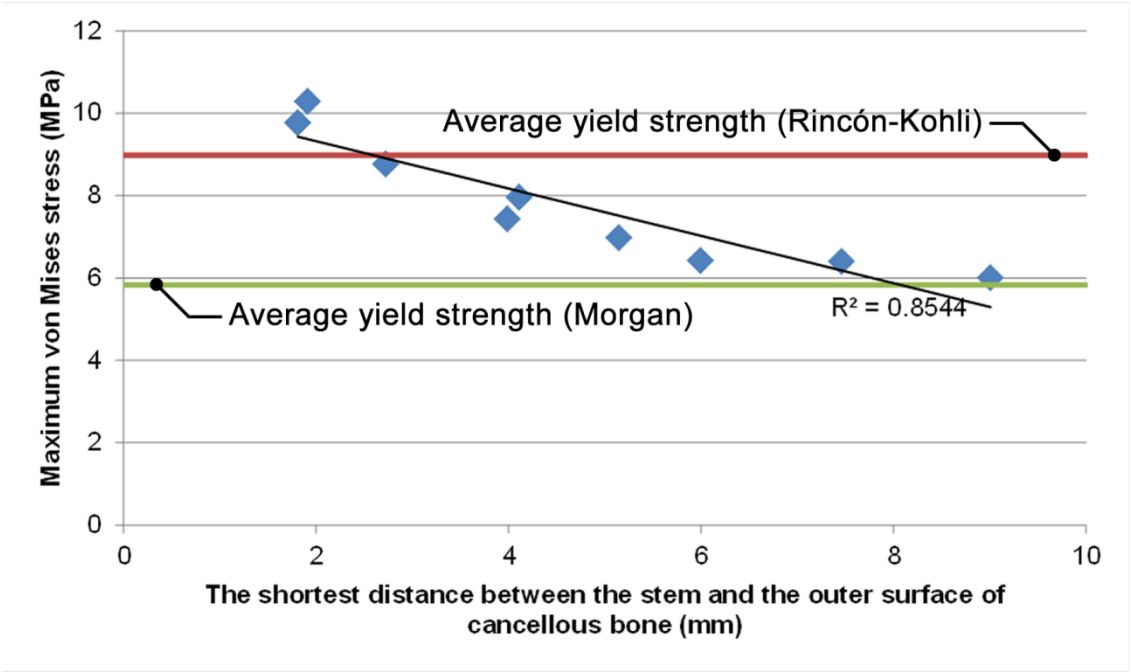

Figure 5-23 The maximum von Mises stress (MPa) versus the shortest distance between the stem and the outer surface of cancellous bone (mm) measured at the region surrounding the tip of the stem, with linear regression line

However, as seen in Figure 5-23, there are two data points that do not obey this relationship. This means that, there are other factors that might also affect the magnitude of the maximum von Mises stress. Considering the deformed shape of the cancellous bone, the deformation of the cancellous bone in the region that the cortical shell overlaps with the tibial component was less than in the region where the shell and the component were not overlapping (Figure 5-24). In the overlapping region, the cortical shell helps the cancellous bone to withstand the load transmitted and reduces the deformation of the bone in that region. The difference in deformation of the bone between the regions with and without the overlapping cortical bone causes a slight rotation of the tibial bone around the axis that lies between the regions (Figure 5-25). This rotation causes an increase in the magnitude of the von Mises stress around the tip of the stem in the opposite direction to the tilting of the tibial bone. Although the distance between the stem and the outer surface of cancellous bone is longer, the stress involved by the supporting location of the cortical shell can be added to make the overall magnitude of the von Mises stress to be higher.

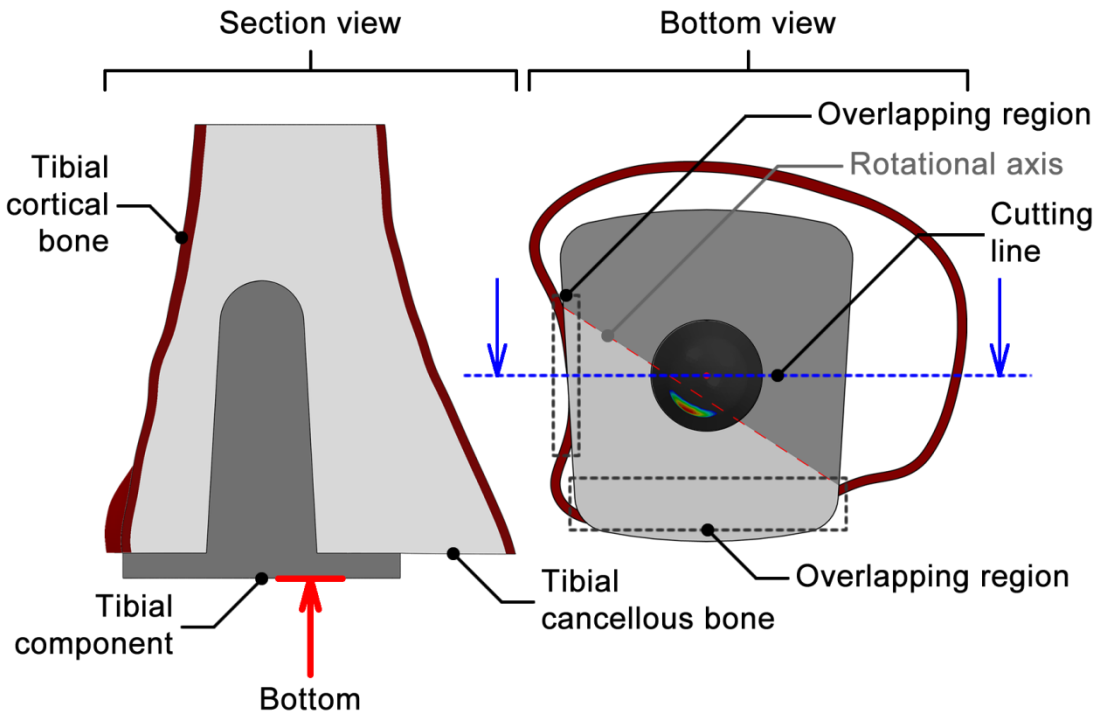

Figure 5-24 The bottom view shows the overlapping region between cortical structure (shown in dark red) and tibial component. There are two colors on the tibial component: light grey (with cortical structure support) and dark grey (without cortical structure support). The red dash line acts like a rotational axis.

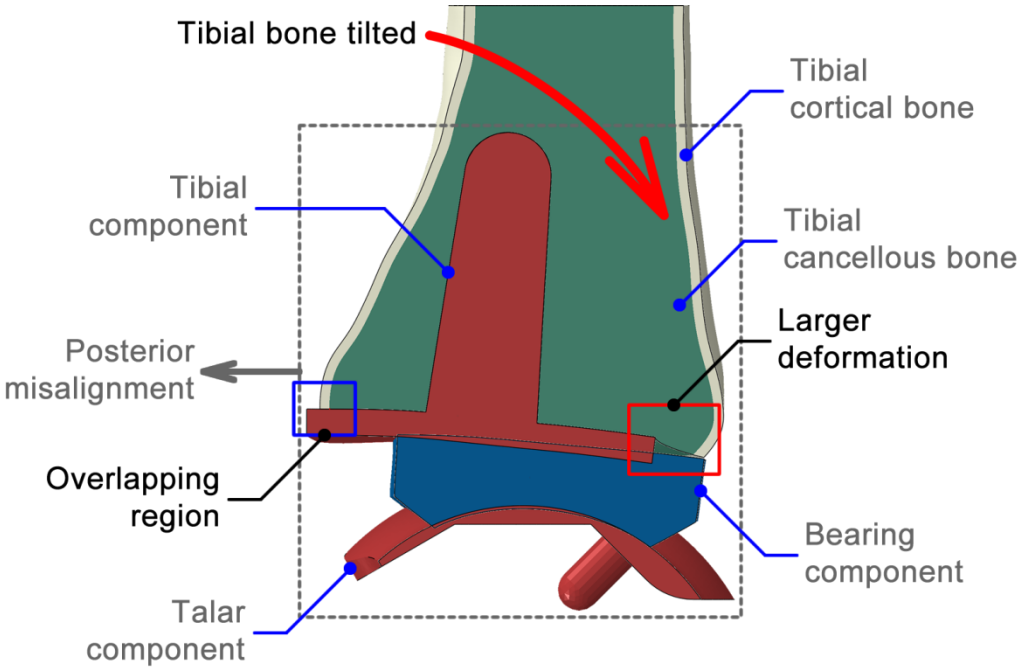

Figure 5-25 The deformation plot (displacements have been exaggerated by a factor of 30 to highlight the deformation) of a posterior misalignment (whole TAR component) FE model showing the different degrees of deformation between the regions with and without cortical structure support

The locations of the maximum von Mises stress on all models were in the same direction that the whole components moved/tilted toward, except the model with medial rotation of whole TAR component. The location of the maximum stress on this model was located at the posterior region instead of the medial region of the stem. This is because the distance between the stem and the outer surface of the cancellous bone in the posterior region is the shorter even if the TAR component is tilted medially. In this case, the cancellous bone is thicker on the medial side before tilting, so the medially misaligned component is now effectively sitting nearer the middle of the bone. In summary, the location of the maximum von Mises stress is dependent on the distance between the stem and the outer surface of the cancellous bone, and is always located at the position of the shortest distance.

Similarly, the distribution of the region of higher von Mises stress values was shifted toward the thinner side between the tip of the stem and the outer surface of the cancellous bone, and in the same direction as the misalignment of the component. However, the distribution on the model with medial misalignment (both medially move and tilt) was not moved toward the medial side, it was just around the tip of the stem. This is because an adequate space remained after the component moving/tilting for the stress to distribute

completely. In this case, the cancellous bone is thicker on the medial side before moving/tilting, so the medially misaligned component is now effectively sitting nearer the middle of the bone. So the distribution of the maximum von Mises stress is also dependent on the distance between the stem and the outer surface of the cancellous bone. If there is not an adequate space, there will be an increase in stress applied onto the outer surface of the cancellous bone.

In summary, the main factor that affects the magnitude, the location, and the distribution of the von Mises stress is the distance between the stem and the outer surface of the cancellous bone following implantation. The magnitude of the maximum stress is inversely proportional to the distance, and its location is always located at the position of the shortest distance. The distribution of the higher stress value is shifted toward the outer surface of the cancellous bone. Moreover, another factor that also affects the magnitude of the maximum von Mises stress is the overlap between the cortical shell structure and the tibial component. This causes different deformations between the regions with and without cortical bone support, making a slight tilting of the tibial bone, and increasing the magnitude of the stress in the opposite direction.

Clinically, other than the location of the articular surface, the location of the stem should also be carefully taken into account when defining the implanted position. An inadequate thickness of cancellous bone surrounding the stem may cause the failure of implantation.

5.4.5.2 Misalignment of the Partial TAR Component

For the misalignment of the partial component, the magnitudes of the maximum von Mises stress around the tip of the stem on all models were similar (varying in a range of 6.56 to 6.78 MPa) except the posterior misalignment (7.89 MPa). The stress was higher following posterior misalignment because the stress in this region is higher in well aligned model. This is because the distance between the tip of the stem and the outer surface of the cancellous bone in this region was the shortest. In this type of misalignment, the locations of the tibial component were the same on all misalignment models, therefore, the inherent stresses involved by the thickness of the cancellous bone around the tip of the stem were also the same on all model. The partial misalignment causes increasing of the magnitude of the stress by making more deformation of the cancellous bone in the region that the bearing and the talar components moved toward (Figure 5-26). In other words, the compressive load was higher in the region of misalignment. Comparing with the well aligned case, the increasing of the magnitude of maximum von Mises stress involved by this type of misalignment at the same location varies in a range of 0.36 to 1.46 MPa. The

difference in the increase in the stress was affected by the overlapping between the cortical shell and the tibial component.

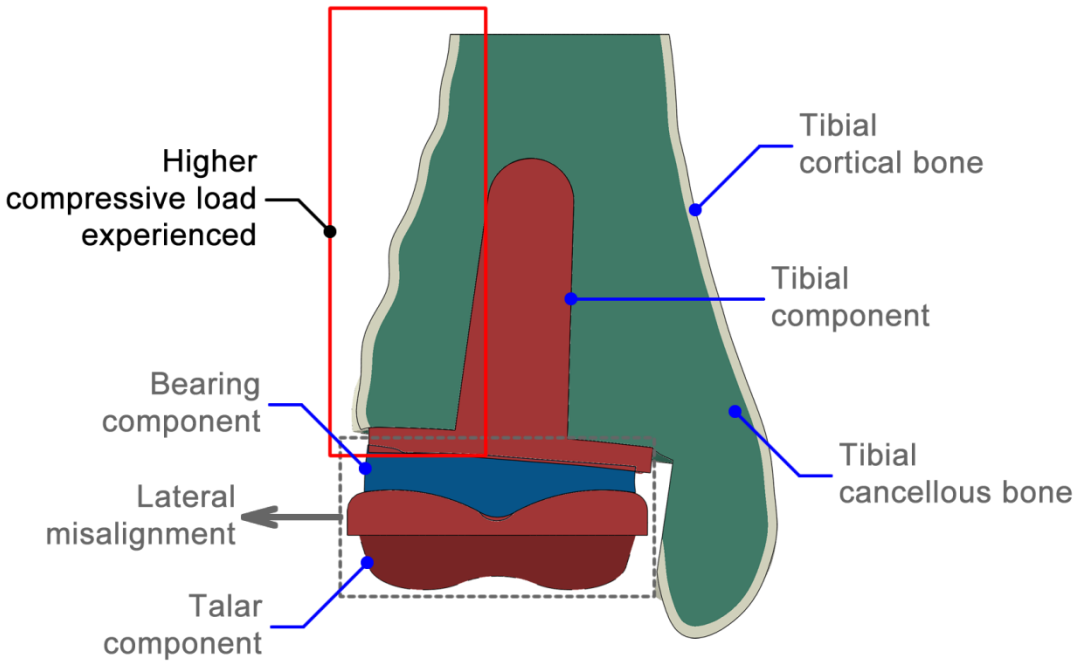

Figure 5-26 The deformation plot (displacements have been exaggerated by a factor of 30 to highlight the deformation) of a lateral misalignment (partial TAR component) FE model showing the different degrees of deformation between the regions that the bearing and talar component move toward and outward

The location of the maximum stress on all models was at the same region as the component moved toward. The distribution of the higher stress value is also shifted to the direction that the component moved towards, except the medial misalignment where the distribution was just around the tip of the stem. This is because there is an adequate cancellous bone at the medial side in this case.

Clinically, the posture of the ankle joint before placing the location jig during surgery should represent the physiological position. If not, the bones will return to the normal position after removing jig and misalignment between each component will then occur. This type of misalignment can increase the magnitude of the stress on the cancellous bone, and may cause more risk of failure of the implantation.

5.5 Summary

A general methodology of creating the FE model of TAR with natural ankle geometry was developed, and a series of verification and sensitivity studies were undertaken. The effect of misalignment on the cancellous bone leading to the failure of implantation was analyzed. The following conclusions can be drawn from this study:

1 The existence of the tibial component of the TAR shift the position of the highest magnitude of the von Mises stress from the region of the high strength of the tibial cancellous bone to the region of the lower strength. So, in the prosthesis design, the length of the stem of the tibial component should not reach the region of the lowest strength to reduce risk of bone damage due to exceeding the yield strength of the cancellous bone.

2 The trend of the relationship between the stiffness of cortical bone and its effect on the cancellous bone can be identified. The relationship is inversely proportional. This can be used to confirm that the quality of the bone is an important factor in the success or failure of the implantation. Therefore, clinically, surgeons should assess the quality of the bone carefully before making a decision to treat patients with the TAR.

3 There are at least two main factors that affect the magnitude, location, and distribution of the maximum von Mises stress on the tibial cancellous bone. One is the distance between the stem and the outer surface of the cancellous bone, and another is the amount of overlap between the cortical structure and the tibial component. The relationship between the former factor and the magnitude of the maximum stress is inversely proportional. Clinically, other than the location of the articular surface, the location of the stem should also be carefully taken into account when defining the implanted position. An inadequate thickness of cancellous bone surrounding the stem may cause the failure of implantation.

4 The misalignment between each component of the TAR can increase the stress on the cancellous bone and may exceed the yield strength leading to the failure of implantation. Clinically, the posture of the ankle joint before placing the jig to locate the implant should well represent the physiological position to maintain the alignment of the TAR component after removing the jig.

Chapter 6 Overall Discussion and Conclusions

6.1 Overall Discussion

A finite element model (FE) of a total ankle replacement (TAR) was developed in this thesis. A series of verification, validation, and sensitivity studies were undertaken, including comparison of the model results to a corresponding experimental test, to determine the robustness of the model. A FE model of a natural ankle geometry was also developed to represent the real-world condition with greater accuracy. The validated method of representing the TAR design was then used together with the natural ankle FE model to investigate stress distribution in the bone and how it was affected by possible misalignments of the TAR implantation seen clinically. This initial study provided insight into the mechanisms of failure of existing designs of prosthesis, and could be used to predict likelihood of failure of novel designs.

6.1.1 Experimental Studies and Initial FE Model of a TAR with Synthetic Bones

The experimental model of the TAR implanted in synthetic bone was used to investigate the depth of plastic deformation at various locations (Chapter 2). Deformation was found to occur on both the tibial and talar synthetic bones in the region of the bone-implant interface, but the largest deformation was located at the most posterior region of the talar bone-implant interface. At that location, the depth of plastic deformation was measured for comparison to the FEA results in Chapter 3. Good agreement was found in the location of damage and average depth of plastic deformation in the synthetic bone. The largest deformations in both experimental and FE models were in the same location on the talar synthetic bone at the region where the most posterior edge of the talar component was located. The average deformation depths at the most posterior region of the talar bone-implant interface of both experimental and FE models were compared and there was found to be excellent agreement with the difference between both the results being approximately 3%. The reason why the deformation at this location was the largest might be because there was not any fixing peg located in this area for sharing the load. The two fixing pegs of the talar component were located in the anterior region, and the deformation of the synthetic bone in that region was considerably smaller. In addition to constraining the prosthesis components onto the bones, in the aspect of load bearing, the importance of the fixing peg may be comparable to that of a pile in a building structure, that is, it increases the area of the bone-implant interface to share the load using both the tip and the side friction.

Actually, there were failure zones in both the tibial and talar synthetic bone after destructive testing where a load of more than two-fold the maximum axial load measured during gait was applied onto the model. The ease of removal of the press-fit components indicated that there was also plastic deformation of the synthetic bone at the fixing hole, causing the hole to expand. Although the damage occurred on both synthetic bones, the plastic deformation in the talar synthetic bone was easier to observe by eye and more convenient to measure using a vernier caliper. That was why this damage was chosen for comparison to the result of the corresponding FE model for a validation step.

However, subsequently, this thesis was focusing on only the failure zone in the tibial bone due to a number of reasons. First, there were difficulties in modeling the natural talus due to the automated merging function being unsuccessful for this geometry. Second, the strength of the tibial cancellous bone has been reported to be considerably weaker (by approximately 40%) than the talar cancellous bone (Hvid et al. 1985). Therefore although the magnitude of von Mises stress at the location of the tip of the fixing part in the tibial cancellous bone was approximately 32% lower than the corresponding value in the talar cancellous bone (Section 3.3.2), the weaker tibial cancellous structure might make the degree of failure in this bone likely to be more severe. Therefore, in this thesis, only the effect on tibial cancellous bone was considered.

In addition to the deformation, the average contact pressure measured on the FE model at the interface between the tibial and bearing components (Section 3.3.5) was close to the corresponding value obtained from the non-destructive test (Section 2.3.2.2), and the difference between both values was approximately 2.3%.

These high levels of agreement illustrated that the FE model was capable of predicting the location of damage and magnitude of plastic deformation in the synthetic bone and the contact pressure between the TAR components. Therefore, the method used to model the TAR in bone developed in this thesis was deemed to be sufficiently robust to use for further predictions in a more realistic bone model.

6.1.2 Sensitivity Studies of Initial FE Model

A series of sensitivity studies was undertaken in Chapter 3 to identify the importance of some parameters of the TAR system used in this thesis for further studies. In this case, the bone structures and interaction properties of bone-implant interface were investigated.

The study to identify the importance of the cortical bone using a simplified cortical layer (section 3.3.6) illustrated that this structure had considerable effect on reducing stress in the synthetic cancellous bone, especially when it was weight-bearing. In the case where the cortical bone was in direct contact with the prosthesis component, the stress in the cancellous bone was reduced significantly since this allowed a direct load transfer from the TAR into the cortical structure. However, even in the non-overlapping case, the stress in cancellous bone was also decreased. This is because the stiffer cortical bone layer provided some support by preventing the cancellous bone from displacing outwards laterally. This showed that the cortical structure is important both in FEA studies and in clinical cases. Appropriate clinical assessment of the quality and geometry of the cortical structure before locating the prosthesis may therefore reduce the risk of failure of the implantation.

The investigation of the effect of the bone-implant interface properties on the stress in the cancellous bone (section 3.3.5 and 3.3.6) showed that there was not a difference in the FEA results between the frictionless case and the interface with a coefficient of friction of 1.3. In comparison to the tied constraint case that represents the full ingrowth of the bone into the TAR, the magnitude of the von Mises stress in these cases was approximately 300% higher. These conditions may represent a situation in the period after the operation when the bone has not fully ingrown into the TAR, and there is only some compressive forces applied onto the prosthesis due to the press fit method. The reason for the lack of difference between the frictionless case and the interface with a coefficient of friction of 1.3, might be because in some of the region, the friction force was relatively parallel to the direction of the load applied (around the stem). Therefore, this could not much help to withstand load during the lateral deformation of the bone. From a clinical rehabilitation perspective, this suggests that the patient should be prohibited in applying full loads onto the implanted joint until the bone has full ingrowth to prevent excessive stress occurring in the cancellous bone that could consequently lead to failure of the implantation.

6.1.3 Stress Distribution in Natural Ankle FE Model

In the FE model of the natural ankle (Chapter 4), the region of high stress concentration in the cancellous bone was located closest to the articular surface because the load was transmitted to both cortical bone and cartilage via this location. Although the maximum magnitude of the von Mises stress might exceed an average value of the compressive yield strength of the cancellous bone (Morgan and Keaveny 2001, Rincón-Kohli and Zysset 2009),

the bone in reality would not be damaged partly because the stiffer subchondral region would maintain its shape and prevent it from severe deformation. However, the peak stress in the region around the cartilage seemed to be an overestimation of reality. Several factors were considered to be likely to affect the contact area of the ankle joint leading to a subsequent increasing of the stress. For example, some functions used in creating the 3-D model from medical imaging data changed the geometry of the articular surface of the ankle joint; the positioning of the talus in the ankle mortise might be slightly different from the physiological; and a lateral moving of the talus to avoid interference at the medial malleolus might not represent the corresponding complex movement of the talus in reality well enough. This result did not have an effect on this study because the main purpose here was to compare this model to that with a TAR, where the region of interest was around the tip of the stem, away from the cartilage.

Compared to the FE model of the natural ankle, in the FE model of TAR (Section 5.3.4), the magnitude of the von Mises stress in the region of interest was at least two and may be as much as approximately six times as high. Although in the well aligned and fully bonded implanted ankle, the peak stress might not exceed the compressive yield strength of the cancellous bone, in inappropriate alignment and constraint, the stress might considerably increase leading to bone damage and consequent failure of the implantation.

Considering the heterogeneous nature of bone in reality, the strength of the cancellous bone is likely to decline further away from the articular surface (Hvid et al. 1985, Harada et al. 1988). In other words, the strength of the epiphyseal cancellous bone is higher than the metaphyseal cancellous bone. The existence of the tibial component of the TAR shifted the location of the high concentration of stress from the epiphysis to the metaphysis. Therefore, this shifting might increase the risk of bone damage even in the well aligned and fully boned condition. In a prosthesis design aspect, the length of the stem of the tibial component should be taken into account. Its positioning should avoid the region of lowest strength to reduce risk of the stress experienced by cancellous bone exceeding yield.

6.1.4 Effect of Misalignment of TAR on Stress Distribution in Bone

It was found that a few degrees of inclination in the experimental model in Chapter 2 induced large effects on the contact pressure between the prosthesis components and on the deformation of the synthetic bones. An experimental inclination of only 0.28° between the TAR components in the frontal plane was found to cause a difference of 27% in the contact pressures experienced by the

two sides of the component and 21% in the depths of deformation on either side of the synthetic bone. Therefore, the alignment of the TAR components is likely to be one of the important factors determining the success or failure of the implantation. Nevertheless, the severity of the effect of inclination of the TAR may be lower in reality. This is because the movement of each part of the human body is freer than the experimental set-up, and they can slightly change their positioning to compensate a misalignment of the prosthesis and better share the load, but associated problems due to alterations in physiological movement may occur instead. These results prompted the simulation of possible clinical misalignment cases to investigate the failure mechanisms and identify factors that cause that failure using a more realistic model of the full TAR in natural bone model (Chapter 5).

From the results in Chapter 5, it was found that one of the main factors that affects the location and magnitude of the stress in the cancellous bone is the distance between the stem and the outer surface of the cancellous bone. The location of the maximum von Mises stress is also dependent on the distance between the stem and the outer surface of the cancellous bone, and was found to be always located at the position of the shortest distance. The relationship between the magnitude of the maximum von Mises stress and the distance between the stem and the outer surface of cancellous bone obtained from all of the misalignment scenarios investigated in the FE study was found to be inversely proportional, with coefficient of determination (R^2) of 0.85. It was concluded that the distance between the stem and the outer surface of cancellous bone is a main factor in affecting the magnitude of the stress. The shorter the distance, the greater the likelihood of failure. Several designs of TAR reviewed in Chapter 1 that have a fixing part that is relatively large compared to the size of the distal tibia, faced problems of bone failure such as aseptic loosening and subsidence. Considering medical images in all anatomical planes to define an appropriate implant position, choosing an appropriate size of the TAR, and adjusting the ankle joint to represent its uniquely natural posture as much as possible before installing the devices following the recommendation of manufacturer strictly may help to improve the alignment problem and prevent the occurrence of excessive stress in the cancellous bone. Therefore, clinically, other than the location of the articular surface, the location of the stem should also be carefully taken into account when defining the implanted position. An inadequate thickness of cancellous bone surrounding the stem may cause the failure of implantation.

6.2 Overall Conclusions

In summary, the following major conclusions can be made from this study.

Good agreement in the location of damage and magnitude of plastic deformation was obtained between experimental and FEA studies, indicating that the methods used for the FE model of the TAR were suitable for further prediction in a more realistic ankle model with good levels of accuracy.

The cortical bone layer was found to significantly reduce the stress in the cancellous bone, especially when overlapping with the implant to transfer load directly. Therefore, the cortical structure is important and should be taken into account when considering the prosthesis location.

The properties of the bone-implant interface were another important factor that affects the magnitude of stress in the cancellous bone considerably. Applying load on the implanted joint while the bone has not full ingrown may cause excessive stress in the bone leading to early failure of the implantation. This may be useful information to be provided to patients for appropriate rehabilitation after treatment.

Compared to the natural ankle, the location of the highest stress concentration was shifted from the region of high strength of the tibial cancellous bone to the region of lower strength. Carefully considering the location to position the TAR with the aid of medical imaging in all anatomical planes and choosing the appropriate size of the TAR may help to improve the problem of excessive stress clinically. In the prosthesis design aspect, the geometry of any fixing parts should be located within a region of adequate strength within the cancellous bone.

Only a few degrees of inclination of the TAR in the frontal plane had a significant effect on the contact pressure in the prosthesis component and the damage to synthetic bone. The twin convex shape of the talar component was intended to share load equally, but when an inclination occurs, the bone that supports the higher load-bearing side may experience an excessive stress. This factor should be taken into account either in prosthesis design or the clinical operation.

Location and magnitude of the stress concentration at the tip of the stem were dependent on the distance between the stem and the outer surface of the cancellous bone. The highest stress was always located where the stem was closest to the cortical bone, and the magnitude of the stress was inversely proportional to the length of the shortest distance

between the stem and the cortical bone. An inadequate thickness of cancellous bone surrounding the stem may cause the failure of implantation. This factor should be also taken into account both in prosthesis design and in the clinical operation procedure. In the prosthesis design aspect, the stem and fixing jig should be designed for easier installation and prevention of human errors, and have more features to appropriately support the alignment of the prosthesis. In the clinical aspect, the location of the stem should also be carefully taken into account when defining the implanted position.

6.3 Future Work

A FE model of a TAR was developed in this thesis, and various processes were undertaken to confirm that the model can be used for further predictions with adequate accuracy. However, there are a few limitations in this thesis that need to be addressed in future work.

The natural ankle in this study was created from a set of cryosectional images whose quality was limited. The boundary of the bone could not be differentiated automatically using available functions in a commercial image processing software. Therefore, using of a set of CT images is recommended in the future for easier and more accurate model generation. In this case, a good contrast of the greyscale level of the medical image is considered to be the most important factor. The better contrast the image is, the easier the software will be able to automatically differentiate the tissues. Another important factor is an adequate resolution, and a very high resolution such a microCT image is not always preferable. In this case, only the exact geometry of the ankle bone is required, but the fine texture of bone surface and microstructure is not necessary. An initial investigation of developing a model from a microCT scan was undertaken in this study. The high resolution of this type of the data caused the high degree of roughness of the surface of the model when using the automatic segmentation tool within the software. To smooth the surface of the model, a high number of the smoothen parameters were necessarily required. It was difficult for the software to distinguish between small unwanted details and the complex geometry, therefore the generated model lost some small but important geometrical features. To solve this problem at that time, manual segmentation was required to be performed on each slice after automatic segmentation to remove unwanted small details while

maintaining small geometric features. This was a time consuming process similar to that of using the cryosectional images. Therefore, choosing the appropriate image resolution to meet the need for the particular use of the model is important for future model generation methods.

The thickness of cortical bone layer in the real-world is not constant, and the bone properties depend on many factors including the microstructure and the mineral composition. The use of CT images may also enable the bone properties to be more realistically represented, for example, the bone can be created as a single part and an element-specific method used to define heterogeneous material properties that depend on the local intensity of the CT images. As stated in Chapter 1, this method has the disadvantage that it represents only the properties of a single patient and may not be representative of the whole population. However, this method is recommended to be examined in future studies to obtain different FEA results for comparison between the procedures. Additionally, if the heterogeneous method can be automated, then it would be possible to examine the performance of many different ankles.

The material properties of bones are also non-linear and orthotropic, however, in this initial study, the bone material was assumed to be linearly elastic and isotropic. Assigning more realistic material behavior for the bone in the FE model may alter the results. This study may be suitable to be included in the future sensitivity studies to investigate how this parameter affects the analysis result.

The loads and boundary conditions used in this study represented only the maximum axial load measured from one experimental study and one of various postures during the gait cycle, with the case selected representing a standing posture similar to that in the midstance and the terminal stance phases in the gait cycle. Additionally, a typical position of the ankle bone in several textbooks was used for reference when adjusting the ankle model to the anatomical position in this posture. The two reasons of choosing this magnitude of the load were that the extreme load condition is likely to provides the worst case and this maximum magnitude of load occurred during those two phases of the gait cycle described. Considering several postures together with the corresponding loads in future studies may provide more insight into the likelihood of failure of the implantation.

The main study in this thesis was focused on the FE model development process, therefore, the study of the effects of misalignment considered only a limited number of cases for a single TAR design. Now that the method has been developed, the final recommendation for future study is to investigate more realistic misalignment cases and other TAR designs to determine other factors that affect the failure of implantation and examine how TAR fixation could be improved.

References

Adam, C., F. Eckstein, S. Milz and R. Putz (1998). "The distribution of cartilage thickness within the joints of the lower limb of elderly individuals." Journal of Anatomy **193**(2): 203-214.

Aitken, G. K., R. B. Bourne, J. B. Finlay, C. H. Rorabeck and P. R. Andreae (1985). "Indentation stiffness of the cancellous bone in the distal human tibia." Clinical orthopaedics and related research **201**: 264-270.

Anderson, D. D., J. K. Goldsworthy, W. Li, M. James Rudert, Y. Tochigi and T. D. Brown (2007). "Physical validation of a patient-specific contact finite element model of the ankle." Journal of Biomechanics **40**(8): 1662-1669.

Anderson, D. D., J. K. Goldsworthy, K. Shivanna, N. M. Grosland, D. R. Pedersen, T. P. Thomas, Y. Tochigi, J. L. Marsh and T. D. Brown (2006). "Intra-articular Contact Stress Distributions at the Ankle Throughout Stance Phase–patient-specific Finite Element Analysis as a Metric of Degeneration Propensity." Biomechanics and Modeling in Mechanobiology **5**(2): 82-89.

Arakilo, M., D. Thewlis, G. Paul and J. Rasmussen (2009). Simulation of ankle joint forces to optimize total ankle replacement design. 7th Australasian Biomechanics Conference. Griffith University, Goaldcoast.

Asgari, S. A., A. M. S. Hamouda, S. B. Mansor, H. Singh, E. Mahdi, R. Wirza and B. Prakash (2004). "Finite element modeling of a generic stemless hip implant design in comparison with conventional hip implants." Finite Elements in Analysis and Design **40**(15): 2027-2047.

Athanasiou, K. A., G. G. Niederauer and R. C. Schenck Jr (1995). "Biomechanical topography of human ankle cartilage." Annals of biomedical engineering **23**(5): 697-704.

Baldwin, M. A., C. W. Clary, C. K. Fitzpatrick, J. S. Deacy, L. P. Maletsky and P. J. Rullkoetter (2012). "Dynamic finite element knee simulation for evaluation of knee replacement mechanics." Journal of Biomechanics **45**(3): 474-483.

Bandak, F. A., R. E. Tannous and T. Toridis (2001). "On the development of an osseo-ligamentous finite element model of the human ankle joint." International Journal of Solids and Structures **38**(10–13): 1681-1697.

Barnett, C. H. and J. R. Napier (1952). "The axis of rotation at the ankle joint in man. Its influence upon the form of the talus and the mobility of the fibula." Journal of anatomy **86**(Pt 1): 1.

Bauer, G., O. Eberhardt, D. Rosenbaum and L. Claes (1996). "Total ankle replacement. Review and critical analysis of the current status." Foot and Ankle Surgery **2**(2): 119-126.

Baumhauer, J. (2013). "Ankle Arthrodesis Versus Ankle Replacement for Ankle Arthritis." Clinical Orthopaedics and Related Research® **471**(8): 2439-2442.

Behnke, R. S. (2006). Kinetic anatomy. Champaign, IL, Human Kinetics (ISBN: 9780736059091 (softcover)

0736059091 (softcover)).

Benedetti, M. G., A. Merlo and A. Leardini (2013). "Inter-laboratory consistency of gait analysis measurements." Gait & Posture.

Berentey, G., J. Feczkó and A. Sárváry (1994). "Open reduction of lateral ankle fractures and internal fixation with the gripper plate." Orthopedics and Traumatology **3**(1-2): 114-121.

Berlet, G. C., L. A. DiDomenico, V. K. Panchbhavi and J. K. Steck (2008). "Roundtable Discussion: Ankle Arthritis." Foot & Ankle Specialist **1**(2): 108-111.

Bernstein, J. and J. Ahn (2010). "In Brief: Fractures in Brief: Calcaneal Fractures." Clinical Orthopaedics and Related Research® **468**(12): 3432-3434.

Bhavikatti, S. S. (2005). Finite Element Analysis, New Age International (P) Limited, Publishers (ISBN: 9788122415896).

Bianchi, A., N. Martinelli, E. Sartorelli and F. Malerba (2012). "The Bologna–Oxford total ankle replacement A mid-term follow-up study." Journal of Bone & Joint Surgery, British Volume **94**(6): 793-798.

Bonasia, D. E., F. Dettoni, J. E. Femino, P. Phisitkul, M. Germano and A. Amendola (2010). "Total ankle replacement: why, when and how?" The Iowa orthopaedic journal **30**: 119.

Bonnin, M., F. Gaudot, J.-R. Laurent, S. Ellis, J.-A. Colombier and T. Judet (2011). "The Salto Total Ankle Arthroplasty: Survivorship and Analysis of Failures at 7 to 11 years." Clinical Orthopaedics and Related Research® **469**(1): 225-236.

Bonnin, M., T. Judet, J. A. Colombier, F. Buscayret, N. Graveleau and P. Piriou (2004). "Midterm results of the Salto total ankle prosthesis." Clinical orthopaedics and related research **424**: 6-18.

Brekelmans, W. A. M., H. W. Poort and T. Slooff (1972). "A new method to analyse the mechanical behaviour of skeletal parts." Acta Orthopaedica **43**(5): 301-317.

Buechel, F. F., Sr., F. F. Buechel, Jr. and M. J. Pappas (2004). "Twenty-Year Evaluation of Cementless Mobile-Bearing Total Ankle Replacements." Clinical orthopaedics and related research **424**.

Burdett, R. G. (1982). "Forces predicted at the ankle during running." Medicine and Science in Sports and Exercise **14**(4): 308-316.

Burghardt, A. J., H. R. Buie, A. Laib, S. Majumdar and S. K. Boyd (2010). "Reproducibility of direct quantitative measures of cortical bone microarchitecture of the distal radius and tibia by HR-pQCT." Bone **47**(3): 519-528.

Cailliet, R. (1968). Foot and ankle pain. Philadelphia,, F. A. Davis Co.

Canseco, K., C. Albert, J. Long, M. Khazzam, R. Marks and G. F. Harris (2011). "Postoperative Foot and Ankle Kinematics in Rheumatoid Arthritis." Journal of Experimental & Clinical Medicine **3**(5): 233-238.

Choi, K. and S. A. Goldstein (1992). "A comparison of the fatigue behavior of human trabecular and cortical bone tissue." Journal of Biomechanics **25**(12): 1371-1381.

Chu, T. M., N. P. Reddy and J. Padovan (1995). "Three-dimensional finite element stress analysis of the polypropylene, ankle-foot orthosis: static analysis." Medical Engineering & Physics **17**(5): 372-379.

Conti, S. F. and Y. S. Wong (2001). "Complications of Total Ankle Replacement." Clinical orthopaedics and related research **391**.

Cook, R. A. and M. J. O'Malley (2001). "Total ankle arthroplasty." Orthopaedic Nursing **20**(4): 30-37.

Cook, R. D., D. S. Malkus and M. E. Plesha (1989). Concepts and applications of finite element analysis. New York, Wiley (ISBN: 0471847887).

Datir, A., M. Xing, A. Kakarala, M. Terk and S. Labib (2013). "Radiographic evaluation of INBONE total ankle arthroplasty: a retrospective analysis of 30 cases." Skeletal Radiology **42**(12): 1693-1701.

Dawe, E. J. C. and J. Davis (2011). "(vi) Anatomy and biomechanics of the foot and ankle." Orthopaedics and Trauma **25**(4): 279-286.

DeOrio, J. K. (2010). "INBONE Total Ankle Arthroplasty." Seminars in Arthroplasty **21**(4): 288-294.

DiStefano, J. G. and S. Pinney (2010). "Ankle Arthritis: Etiology and Epidemiology." Seminars in Arthroplasty **21**(4): 218-222.

Easley, M. E., J. S. B. Adams, W. C. Hembree and J. K. DeOrio (2011). "Results of Total Ankle Arthroplasty." The Journal of Bone & Joint Surgery **93**(15): 1455-1468.

Easley, M. E., C. J. Vertullo, W. C. Urban and J. A. Nunley (2002). "Total Ankle Arthroplasty." Journal of the American Academy of Orthopaedic Surgeons **10**(3): 157-167.

Elliot, B. J., D. Gundapaneni and T. Goswami (2014). "Finite element analysis of stress and wear characterization in total ankle replacements." Journal of the Mechanical Behavior of Biomedical Materials **34**(0): 134-145.

Ellis, S. and J. K. DeOrio (2010). "The INBONE Total Ankle Replacement." Operative Techniques in Orthopaedics **20**(3): 201-210.

Espinosa, N., M. Walti, P. Favre and J. Snedeker (2010). "Misalignment of Total Ankle Components Can Induce High Joint Contact Pressures." The Journal of Bone and Joint Surgery **92**(5): 1179-1187.

Fallat, L., D. J. Grimm and J. A. Saracco (1998). "Sprained ankle syndrome: Prevalence and analysis of 639 acute injuries." The Journal of Foot and Ankle Surgery **37**(4): 280-285.

Falsig, J., I. Hvid and N. C. Jensen (1986). "Finite element stress analysis of some ankle joint prostheses." Clinical Biomechanics **1**(2): 71-76.

Fernandez, D. L. (1984). "Transarticular fracture of the calcaneus." Archives of orthopaedic and traumatic surgery **103**(3): 195-200.

Fischer-Cripps, A. C. (2007). Introduction to contact mechanics. New York, Springer (ISBN: 0387681876

9780387681870).

Fong, D., Y.-Y. Chan, K.-M. Mok, P. Yung and K.-M. Chan (2009). "Understanding acute ankle ligamentous sprain injury in sports." Sports Medicine, Arthroscopy, Rehabilitation, Therapy & Technology **1**(1): 1-14.

Fong, D. T.-P., Y. Hong, L.-K. Chan, P. S.-H. Yung and K.-M. Chan (2007). "A systematic review on ankle injury and ankle sprain in sports." Sports Medicine **37**(1): 73-94.

Froes, F. H. (2015). Titanium: physical metallurgy, processing, and applications, ASM International (ISBN: 1627080805).

García, J. J. and D. H. Cortés (2007). "A biphasic viscohyperelastic fibril-reinforced model for articular cartilage: Formulation and comparison with experimental data." Journal of Biomechanics **40**(8): 1737-1744.

Giannini, S., R. Buda, C. Faldini, F. Vannini, M. Romagnoli, G. Grandi and R. Bevoni (2007). "The treatment of severe posttraumatic arthritis of the ankle joint." The Journal of Bone & Joint Surgery **89**(suppl_3): 15-28.

Giannini, S., A. Leardini and J. J. O'Connor (2000). "Total ankle replacement: review of the designs and of the current status." Foot and Ankle Surgery **6**(2): 77-88.

Giannini, S., M. Romagnoli, M. Cadossi and A. Leardini (2013). "The Box Ankle Replacement: Results at a Minimum Follow-up of 5 Years." Orthopedic & Muscular System: Current Research.

Giannini, S., M. Romagnoli, J. J. O'Connor, F. Catani, L. Nogarin, B. Magnan, F. Malerba, L. Massari, M. Guelfi, L. Milano, A. Volpe, A. Rebeccato and A. Leardini (2011). "Early Clinical Results of the BOX Ankle Replacement Are Satisfactory: A Multicenter Feasibility Study of 158 Ankles." The Journal of Foot and Ankle Surgery **50**(6): 641-647.

Golanó, P., J. Vega, P. A. J. de Leeuw, F. Malagelada, M. C. Manzanares, V. Götzens and C. N. van Dijk (2010). "Anatomy of the ankle ligaments: a pictorial essay." Knee Surgery, Sports Traumatology, Arthroscopy **18**(5): 557-569.

Goldstein, S. A., D. L. Wilson, D. A. Sonstegard and L. S. Matthews (1983). "The mechanical properties of human tibial trabecular bone as a function of metaphyseal location." Journal of Biomechanics **16**(12): 965-969.

Gougoulias, N. E., A. Khanna and N. Maffulli (2009). "History and evolution in total ankle arthroplasty." British Medical Bulletin **89**(1): 111-151.

Grimston, S. K., B. M. Nigg, D. A. Hanley and J. R. Engsberg (1993). "Differences in Ankle Joint Complex Range of Motion as a Function of Age." Foot & Ankle International **14**(4): 215-222.

Guyer, A. J. and E. G. Richardson (2008). "Current Concepts Review: Total Ankle Arthroplasty." Foot & Ankle International **29**(2): 256-264.

Hall, R. L. and M. J. Shereff (1993). "Anatomy of the calcaneus." Clinical orthopaedics and related research **290**: 27-35.

Halloran, J. P., A. J. Petrella and P. J. Rullkoetter (2005). "Explicit finite element modeling of total knee replacement mechanics." Journal of Biomechanics **38**(2): 323-331.

Hamill, J. and K. Knutzen (2009). Biomechanical basis of human movement. Philadelphia ; London, Wolters Kluwer Health/Lippincott Williams and Wilkins (ISBN: 9780781791281

0781791286).

Harada, Y., H. W. Wevers and T. D. V. Cooke (1988). "Distribution of bone strength in the proximal tibia." The Journal of Arthroplasty **3**(2): 167-175.

Henninger, H. B., S. P. Reese, A. E. Anderson and J. A. Weiss (2010). "Validation of computational models in biomechanics." Proceedings of the Institution of Mechanical Engineers, Part H: Journal of Engineering in Medicine **224**(7): 801-812.

Henricson, A., A. Skoog and Å. Carlsson (2007). "The Swedish Ankle Arthroplasty Register: an analysis of 531 arthroplasties between 1993 and 2005." Acta Orthopaedica **78**(5): 569-574.

Hernández-Díaz, C., M. Á. Saavedra, J. E. Navarro-Zarza, J. J. Canoso, P. Villaseñor-Ovies, A. Vargas and R. A. Kalish (2012). "Clinical Anatomy of the Ankle and Foot." Reumatología Clínica **8, Supplement 2**(0): 46-52.

Hicks, J. H. (1953). "The mechanics of the foot: I. The joints." Journal of Anatomy **87**(Pt 4): 345.

Hintermann, B. (2005). Total Ankle Arthroplasty: Historical Overview, Current Concepts and Future Perspectives, Springer (ISBN: 9783211212523).

Hintermann, B., M. Knupp, L. Zwicky and A. Barg (2012). "Total Ankle Replacement for Treatment of End-Stage Osteoarthritis in Elderly Patients." Journal of Aging Research **2012**: 8.

Hintermann, B., V. Valderrabano, G. Dereymaeker and W. Dick (2004). "The HINTEGRA ankle: rationale and short-term results of 122 consecutive ankles." Clinical orthopaedics and related research **424**: 57-68.

Hintermann, B., L. Zwicky, M. Knupp, H. B. Henninger and A. Barg (2013). "HINTEGRA revision arthroplasty for failed total ankle prostheses." The Journal of Bone & Joint Surgery **95**(13): 1166-1174.

Homminga, J., B. R. McCreadie, T. E. Ciarelli, H. Weinans, S. A. Goldstein and R. Huiskes (2002). "Cancellous bone mechanical properties from normals and patients with hip fractures differ on the structure level, not on the bone hard tissue level." Bone **30**(5): 759-764.

Hopkins, A. R., A. M. New, F. Rodriguez-y-Baena and M. Taylor (2010). "Finite element analysis of unicompartmental knee arthroplasty." Medical Engineering & Physics **32**(1): 14-21.

Hubbard, T. and J. Hertel (2006). "Mechanical Contributions to Chronic Lateral Ankle Instability." Sports Medicine **36**(3): 263-277.

Hubbard, T. J. and M. Cordova (2009). "Mechanical Instability After an Acute Lateral Ankle Sprain." Archives of Physical Medicine and Rehabilitation **90**(7): 1142-1146.

Huiskes, R. and E. Y. S. Chao (1983). "A survey of finite element analysis in orthopedic biomechanics: The first decade." Journal of Biomechanics **16**(6): 385-409.

Hulsker, C. C., S. Kleinveld, C. L. Zonnenberg, M. Hogervorst and M. J. Bekerom (2011). "Evidence-based treatment of open ankle fractures." Archives of Orthopaedic and Trauma Surgery **131**(11): 1545-1553.

Hutton, D. V. (2004). Fundamentals of finite element analysis. Boston, McGraw-Hill (ISBN: 0072395362 (acid-free paper)

0071122311 (ISE)).

Hvid, I., O. V. E. Rasmussen, N. C. Jensen and S. Nielsen (1985). "Trabecular bone strength profiles at the ankle joint." Clinical orthopaedics and related research **199**: 306-312.

Ingrosso, S., M. G. Benedetti, A. Leardini, S. Casanelli, T. Sforza and S. Giannini (2009). "GAIT analysis in patients operated with a novel total ankle prosthesis." Gait & Posture **30**(2): 132-137.

Isman, R. E. and V. T. Inman (1969). "Anthropometric studies of the human foot and ankle." Bulletin of Prosthetics Ressearch **10**(11): 97-129.

Jackson, M. P. and D. Singh (2003). "Total ankle replacement." Current Orthopaedics **17**(4): 292-298.

Jagota, V., A. P. S. Sethi and K. Kumar (2013). "Finite Element Method: An Overview." Walailak Journal of Science and Technology (WJST); Vol 10, No 1 (2013).

Julkunen, P., P. Kiviranta, W. Wilson, J. S. Jurvelin and R. K. Korhonen (2007). "Characterization of articular cartilage by combining microscopic analysis with a fibril-reinforced finite-element model." Journal of Biomechanics **40**(8): 1862-1870.

Kettunen, J. and H. Kröger (2005). "Surgical treatment of ankle and foot fractures in the elderly." Osteoporosis International **16**(2): S103-S106.

Knecht, S. I., M. Estin, J. J. Callaghan, M. B. Zimmerman, K. J. Alliman, F. G. Alvine and C. L. Saltzman (2004). "The Agility Total Ankle ArthroplastySeven to Sixteen-Year Follow-up." The Journal of Bone & Joint Surgery **86**(6): 1161-1171.

Kofoed, H. (2004). "Scandinavian Total Ankle Replacement (STAR)." Clinical orthopaedics and related research **424**.

Kong, A., R. Cassumbhoy and R. M. Subramaniam (2007). "Magnetic resonance imaging of ankle tendons and ligaments: Part I – Anatomy." Australasian Radiology **51**(4): 315-323.

Kopp, F. J., M. M. Patel, J. T. Deland and M. J. O'Malley (2006). "Total Ankle Arthroplasty With the Agility Prosthesis: Clinical and Radiographic Evaluation." Foot & Ankle International **27**(2): 97-103.

Labib, S. A., S. M. Raikin, J. T. Lau, J. G. Anderson, N. F. SooHoo, S. Carette and S. J. Pinney (2013). "Joint Preservation Procedures for Ankle Arthritis." Foot & Ankle International **34**(7): 1040-1047.

Lawrence, I. and K. Lin (1989). "A concordance correlation coefficient to evaluate reproducibility." Biometrics: 255-268.

Lee, S. C., B. S. Coan and M. L. Bouxsein (1997). "Tibial ultrasound velocity measured in situ predicts the material properties of tibial cortical bone." Bone **21**(1): 119-125.

Lee, W.-C., J.-S. Moon, K. Lee, W. J. Byun and S. H. Lee (2011). "Indications for Supramalleolar Osteotomy in Patients with Ankle Osteoarthritis and Varus Deformity." The Journal of Bone & Joint Surgery **93**(13): 1243-1248.

Li, W., D. D. Anderson, J. K. Goldsworthy, J. L. Marsh and T. D. Brown (2008). "Patient-specific finite element analysis of chronic contact stress exposure after intraarticular fracture of the tibial plafond." Journal of Orthopaedic Research **26**(8): 1039-1045.

Lin, L. (2007). "Overview of Agreement Statistics for Medical Devices." Journal of Biopharmaceutical Statistics **18**(1): 126-144.

Lundberg, A., O. K. Svensson, G. Nemeth and G. Selvik (1989). "The axis of rotation of the ankle joint." Journal of Bone & Joint Surgery, British Volume **71**(1): 94-99.

Martini, F., M. J. Timmons, R. B. Tallitsch, W. C. Ober, C. W. Garrison, K. Welch and R. T. Hutchings (2012). Human anatomy. Boston, Mass. ; London, Benjamin Cummings (ISBN: 9780321732668 (Human anatomy)

0321732669 (Human anatomy)).

Mather, B. S. (1967). "Correlations between strength and other properties of long bones." Journal of Trauma and Acute Care Surgery **7**(5): 633-638.

Michael, J. M., A. Golshani, S. Gargac and T. Goswami (2008). "Biomechanics of the ankle joint and clinical outcomes of total ankle replacement." Journal of the Mechanical Behavior of Biomedical Materials **1**(4): 276-294.

Millar, T. and S. Garg (2013). "THE ZENITH TOTAL ANKLE REPLACEMENT: EARLY RESULTS OF THE FIRST 50 CASES IN A NON-INVENTOR SERIES." Bone & Joint Journal Orthopaedic Proceedings Supplement **95**(SUPP 21): 11-11.

Miller, A., E. Carroll, R. Parker, D. Helfet and D. Lorich (2010). "Posterior Malleolar Stabilization of Syndesmotic Injuries is Equivalent to Screw Fixation." Clinical Orthopaedics and Related Research® **468**(4): 1129-1135.

Miller, M. C., P. Smolinski, S. Conti and K. Galik (2004). "Stresses in Polyethylene Liners in a Semiconstrained Ankle Prosthesis." Journal of Biomechanical Engineering **126**(5): 636-640.

Millington, S. A., M. Grabner, R. Wozelka, D. D. Anderson, S. R. Hurwitz and J. R. Crandall (2007). "Quantification of ankle articular cartilage topography and thickness using a high resolution stereophotography system." Osteoarthritis and Cartilage **15**(2): 205-211.

Morgan, E. F. and T. M. Keaveny (2001). "Dependence of yield strain of human trabecular bone on anatomic site." Journal of Biomechanics **34**(5): 569-577.

Moskowitz, R. W. (1987). "Primary osteoarthritis: Epidemiology, clinical aspects, and general management." The American Journal of Medicine **83**(5, Supplement 1): 5-10.

Muir, D., J. Aoina, T. Hong and R. Mason (2013). "The outcome of the Mobility total ankle replacement at a mean of four years Can poor outcomes be predicted from pre-and post-operative analysis?" Bone & Joint Journal **95**(10): 1366-1371.

Netter, F. H. (2010). Atlas of human anatomy. Philadelphia, PA, Saunders/Elsevier (ISBN: 9781416059516

1416059512

9781437709704 (hbk.)

1437709702 (hbk.)

9780808924234 (International ed.)

0808924230 (International ed.)

9780808924227 (enhanced international ed.)

0808924222 (enhanced international ed.)).

Nodzo, S. R., M. P. Miladore, N. B. Kaplan and C. A. Ritter (2014). "Short to Midterm Clinical and Radiographic Outcomes of the Salto Total Ankle Prosthesis." Foot & Ankle International **35**(1): 22-29.

Osborne, M. D. and T. D. Rizzo Jr (2003). "Prevention and treatment of ankle sprain in athletes." Sports Medicine **33**(15): 1145-1150.

Park, J. S. and K. J. Mroczek (2011). "Total ankle arthroplasty." Bull NYU Hosp Jt Dis **69**(1): 27-35.

Parr, W. C. H., U. Chamoli, A. Jones, W. R. Walsh and S. Wroe (2013). "Finite element micro-modelling of a human ankle bone reveals the importance of the trabecular network to mechanical performance: New methods for the generation and comparison of 3D models." Journal of Biomechanics **46**(1): 200-205.

Petersen, W., I. Rembitzki, A. Koppenburg, A. Ellermann, C. Liebau, G. Brüggemann and R. Best (2013). "Treatment of acute ankle ligament injuries: a systematic review." Archives of Orthopaedic and Trauma Surgery **133**(8): 1129-1141.

Procter, P. and J. P. Paul (1982). "Ankle joint biomechanics." Journal of Biomechanics **15**(9): 627-634.

Pyevich, M. T., C. L. Saltzman, J. J. Callaghan and F. G. Alvine (1998). "Total Ankle Arthroplasty: a Unique Design. Two to Twelve-Year Follow-up*." The Journal of Bone & Joint Surgery **80**(10): 1410-1420.

Ranawat, C. S. and R. G. Positano (1999). Disorders of the heel, rearfoot, and ankle. New York, Churchill Livingstone (ISBN: 0443078386).

Rancourt, D., A. Shirazi-Adl, G. Drouin and G. Paiement (1990). "Friction properties of the interface between porous-surfaced metals and tibial cancellous bone." Journal of Biomedical Materials Research **24**(11): 1503-1519.

Rao, S., S. J. Ellis, J. T. Deland and H. Hillstrom (2010). "Nonmedicinal therapy in the management of ankle arthritis." Current opinion in rheumatology **22**(2): 223.

Reggiani, B., A. Leardini, F. Corazza and M. Taylor (2006). "Finite element analysis of a total ankle replacement during the stance phase of gait." Journal of Biomechanics **39**(8): 1435-1443.

Reilly, D. T. and A. H. Burstein (1975). "The elastic and ultimate properties of compact bone tissue." Journal of Biomechanics **8**(6): 393-405.

Reuver, J. M., N. Dayerizadeh, B. Burger, L. Elmans, M. Hoelen and N. Tulp (2010). "Total Ankle Replacement Outcome in Low Volume Centers: Short-Term Followup." Foot & Ankle International **31**(12): 1064-1068.

Riegger, C. L. (1988). "Anatomy of the Ankle and Foot." Physical Therapy **68**(12): 1802-1814.

Rincón-Kohli, L. and P. Zysset (2009). "Multi-axial mechanical properties of human trabecular bone." Biomechanics and Modeling in Mechanobiology **8**(3): 195-208.

Ritterman, S. A., T. A. Fellars and C. W. Digiovanni (2012). "Current thoughts on ankle arthritis." Rhode Island medical journal **96**(3): 30-33.

Rockar Jr, P. A. (1995). "The subtalar joint: anatomy and joint motion." The Journal of orthopaedic and sports physical therapy **21**(6): 361.

Saltzman, C. L., R. A. Mann, J. E. Ahrens, A. Amendola, R. B. Anderson, G. C. Berlet, J. W. Brodsky, L. B. Chou, T. O. Clanton, J. T. Deland, J. K. DeOrio, G. A. Horton, T. H. Lee, J. A. Mann, J. A. Nunley, D. B. Thordarson, A. K. Walling, K. L. Wapner and M. J. Coughlin (2009). "Prospective Controlled Trial of STAR Total Ankle Replacement versus Ankle Fusion: Initial Results." Foot & Ankle International **30**(7): 579-596.

Saltzman, C. L., M. L. Salamon, G. M. Blanchard, T. Huff, A. Hayes, J. A. Buckwalter and A. Amendola (2005). "Epidemiology of Ankle Arthritis: Report of a Consecutive Series of 639 Patients from a Tertiary Orthopaedic Center." The Iowa Orthopaedic Journal **25**: 44-46.

San Giovanni, T. P., D. J. Keblish, W. H. Thomas and M. G. Wilson (2006). "Eight-Year Results of a Minimally Constrained Total Ankle Arthroplasty." Foot & Ankle International **27**(6): 418-426.

Sawatari, T., H. Tsumura, K. Iesaka, Y. Furushiro and T. Torisu (2005). "Three-dimensional finite element analysis of unicompartmental knee arthroplasty–the influence of tibial component inclination." Journal of Orthopaedic Research **23**(3): 549-554.

Schie-Van der Weert, E. M., E. M. M. Lieshout, M. R. Vries, M. Elst and T. Schepers (2012). "Determinants of outcome in operatively and non-operatively treated Weber-B ankle fractures." Archives of Orthopaedic and Trauma Surgery **132**(2): 257-263.

Schmitt, S., M. Melnyk, W. Alt and A. Gollhofer (2009). "Novel approach for a precise determination of short-time intervals in ankle sprain experiments." Journal of Biomechanics **42**(16): 2823-2825.

Schouwenaars, B. and J. C. Mulier (1979). "The conservative treatment of ankle fractures." Archives of orthopaedic and traumatic surgery **94**(3): 161-166.

Scott, R. T., B. L. Witt and C. F. Hyer (2013). "Design Comparison of the INBONE I Versus INBONE II Total Ankle System." Foot & Ankle Specialist **6**(2): 137-140.

Seireg, A. and R. J. Arvikar (1975). "The prediction of muscular load sharing and joint forces in the lower extremities during walking." Journal of Biomechanics **8**(2): 89-102.

Seth, A. (2011). "A review of the STAR prosthetic system and the biomechanical considerations in total ankle replacements." Foot and Ankle Surgery **17**(2): 64-67.

Shepherd, D. E. and B. B. Seedhom (1999). "The 'instantaneous' compressive modulus of human articular cartilage in joints of the lower limb." Rheumatology **38**(2): 124-132.

Shepherd, D. E. T. and B. B. Seedhom (1999). "Thickness of human articular cartilage in joints of the lower limb." Annals of the Rheumatic Diseases **58**(1): 27-34.

Shirazi, R., A. Shirazi-Adl and M. Hurtig (2008). "Role of cartilage collagen fibrils networks in knee joint biomechanics under compression." Journal of Biomechanics **41**(16): 3340-3348.

Snyder, S. M. and E. Schneider (1991). "Estimation of mechanical properties of cortical bone by computed tomography." Journal of Orthopaedic Research **9**(3): 422-431.

Spirt, A. A., M. Assal and S. T. HansenJr (2004). "Complications and Failure After Total Ankle Arthroplasty." The Journal of Bone & Joint Surgery **86**(6): 1172-1178.

Spitzer, V., M. J. Ackerman, A. L. Scherzinger and D. Whitlock (1996). "The Visible Human Male: A Technical Report." Journal of the American Medical Informatics Association **3**(2): 118-130.

Sproule, J. A., T. Chin, A. Amin, T. Daniels, A. S. Younger, G. Boyd and M. A. Glazebrook (2013). "Clinical and Radiographic Outcomes of the Mobility Total Ankle Arthroplasty System: Early Results From a Prospective Multicenter Study." Foot & Ankle International **34**(4): 491-497.

Stauffer, R. N., E. Y. Chao and R. C. Brewster (1977). "Force and motion analysis of the normal, diseased, and prosthetic ankle joint." Clinical orthopaedics and related research **127**: 189-196.

Struijs, P. A. A. and G. M. M. J. Kerkhoffs (2010). "Ankle sprain." Clinical evidence **2010**.

Summers, J. C. and H. S. Bedi (2013). "Reoperation and patient satisfaction after the Mobility total ankle arthroplasty." ANZ Journal of Surgery **83**(5): 371-375.

Taddei, F., S. Martelli, B. Reggiani, L. Cristofolini and M. Viceconti (2006). "Finite-Element Modeling of Bones From CT Data: Sensitivity to Geometry and Material Uncertainties." Biomedical Engineering, IEEE Transactions on **53**(11): 2194-2200.

Terrier, A., X. Larrea, J. Guerdat and X. Crevoisier (2014). "Development and experimental validation of a finite element model of total ankle replacement." Journal of Biomechanics **47**(3): 742-745.

Thomas, R. H. and T. R. Daniels (2003). "Ankle arthritis." The Journal of Bone & Joint Surgery **85**(5): 923-936.

Tortora, G. J. and M. T. Nielsen (2012). Principles of human anatomy. Hoboken, NJ, John Wiley & Sons (ISBN: 9780470567050

0470567058

9780470917466

0470917466).

Tuncer, M., J. P. Cobb, U. N. Hansen and A. A. Amis (2013). "Validation of multiple subject-specific finite element models of unicompartmental knee replacement." Medical Engineering & Physics **35**(10): 1457-1464.

Valderrabano, V., B. Hintermann and W. Dick (2004). "Scandinavian Total Ankle Replacement: A 3.7-Year Average Followup of 65 Patients." Clinical orthopaedics and related research **424**.

Valderrabano, V., B. Hintermann, M. Horisberger and T. S. Fung (2006). "Ligamentous Posttraumatic Ankle Osteoarthritis." The American Journal of Sports Medicine **34**(4): 612-620.

Valderrabano, V., M. Horisberger, I. Russell, H. Dougall and B. Hintermann (2009). "Etiology of Ankle Osteoarthritis." Clinical Orthopaedics and Related Research® **467**(7): 1800-1806.

Van, A., S. V. A. N. Heuvel and G. Dereymaeker (2010). "Total ankle replacement Design evolution and results." Acta Orthopædica Belgica **76**: 150-161.

van Jonbergen, H.-P., B. Innocenti, G. Gervasi, L. Labey and N. Verdonschot (2012). "Differences in the stress distribution in the distal femur between patellofemoral joint replacement and total knee replacement: a finite element study." Journal of Orthopaedic Surgery and Research **7**(1): 28.

Vickerstaff, J. A., A. W. Miles and J. L. Cunningham (2007). "A brief history of total ankle replacement and a review of the current status." Medical Engineering & Physics **29**(10): 1056-1064.

Weatherall, J. M., K. Mroczek, T. McLaurin, B. Ding and N. Tejwani (2013). "Post-Traumatic Ankle Arthritis." Bulletin of the Hospital for Joint Diseases **71**(1): 104-112.

Whittle, M. (2007). Gait analysis : an introduction. Edinburgh ; New York, Butterworth-Heinemann (ISBN: 9780750688833

0750688831).

Witjes, S., F. Gresnigt, M. P. J. van den Bekerom, J. G. Olsman and N. C. van Dijk (2012). "The ANKLE TRIAL (ANKLE treatment after injuries of the ankle ligaments): what is the benefit of external support devices in the functional treatment of acute ankle sprain?: a randomised controlled trial." BMC Musculoskeletal Disorders **13**(1): 21.

Wood, P. L. R., T. M. Clough and S. Jari (2000). "Clinical Comparison of Two Total Ankle Replacements." Foot & Ankle International **21**(7): 546-550.

Wood, P. L. R. and S. Deakin (2003). "Total ankle replacement." JOURNAL OF BONE AND JOINT SURGERY-BRITISH VOLUME- **85**(3): 334-341.

Wood, P. L. R., M. T. Karski and P. Watmough (2010). "Total ankle replacement THE RESULTS OF 100 MOBILITY TOTAL ANKLE REPLACEMENTS." Journal of Bone & Joint Surgery, British Volume **92**(7): 958-962.

Yalamanchili, S., R. Abboud and W. Weijie (2009). A model to calculate the joint movements and forces in the foot. Electronic Measurement & Instruments, 2009. ICEMI '09. 9th International Conference on.

Yoshioka, Y., D. W. Siu, R. A. Scudamore and T. D. V. Cooke (1989). "Tibial anatomy and functional axes." Journal of Orthopaedic Research **7**(1): 132-137.
Zwipp, H. and T. Randt (1994). "Ankle joint biomechanics." Foot and Ankle Surgery **1**(1): 21-27.

Appendix A Engineering Drawings

A.1 Engineering Drawings of Synthetic Bones

A.1.1 Tibial Synthetic Bone

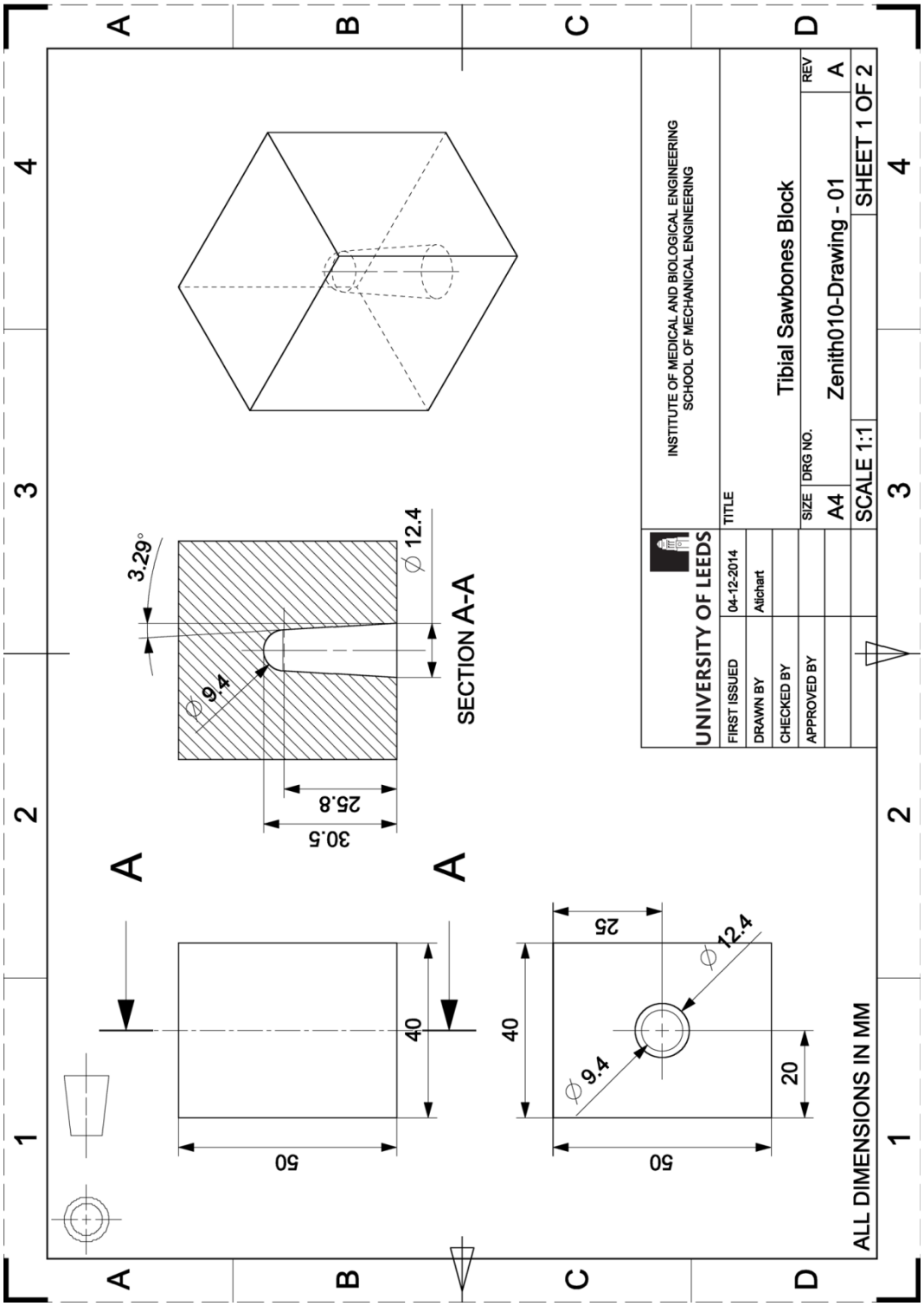

A.1.2 Talar Synthetic Bone

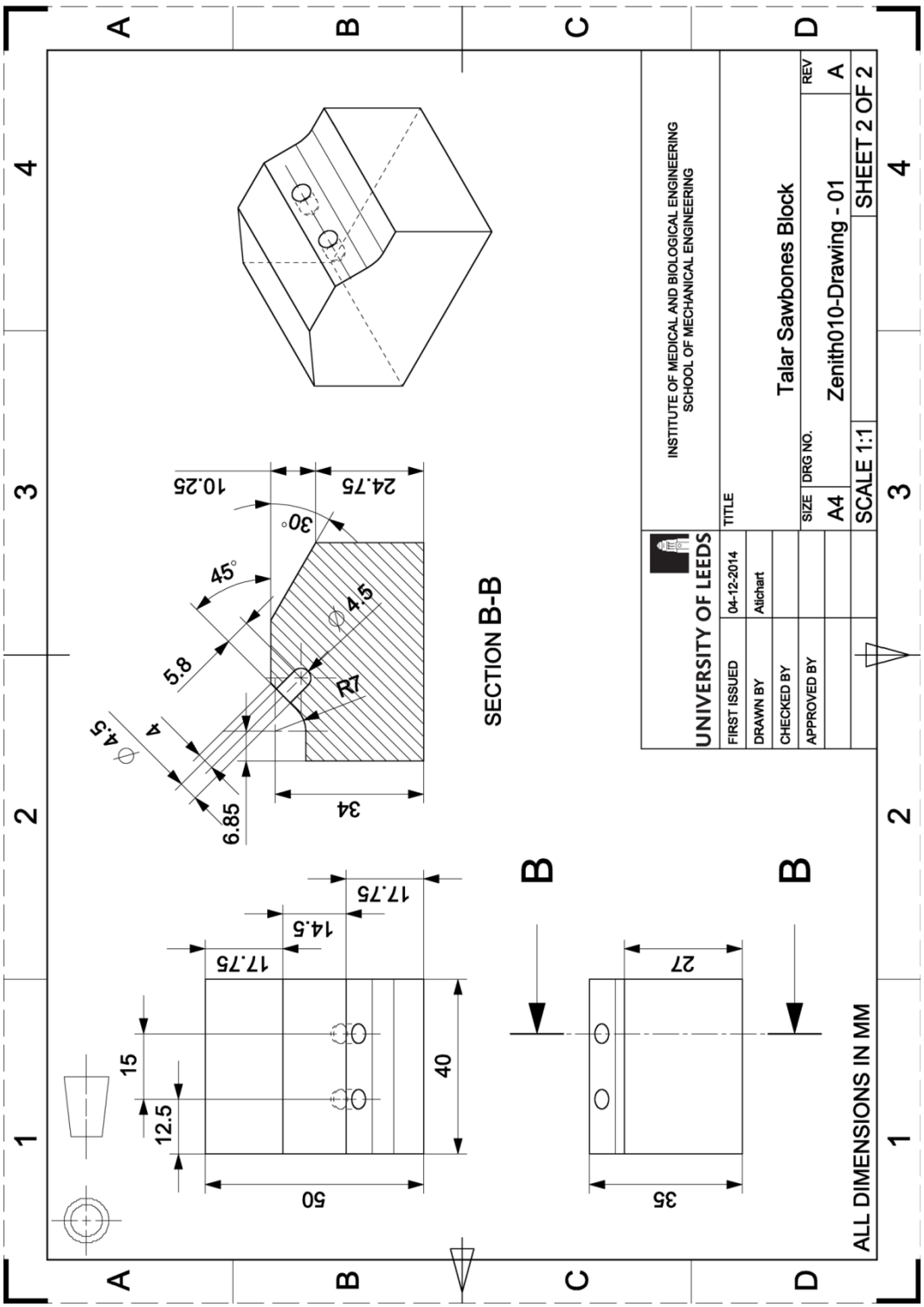

A.1.3 Cutting of Sawbones Block

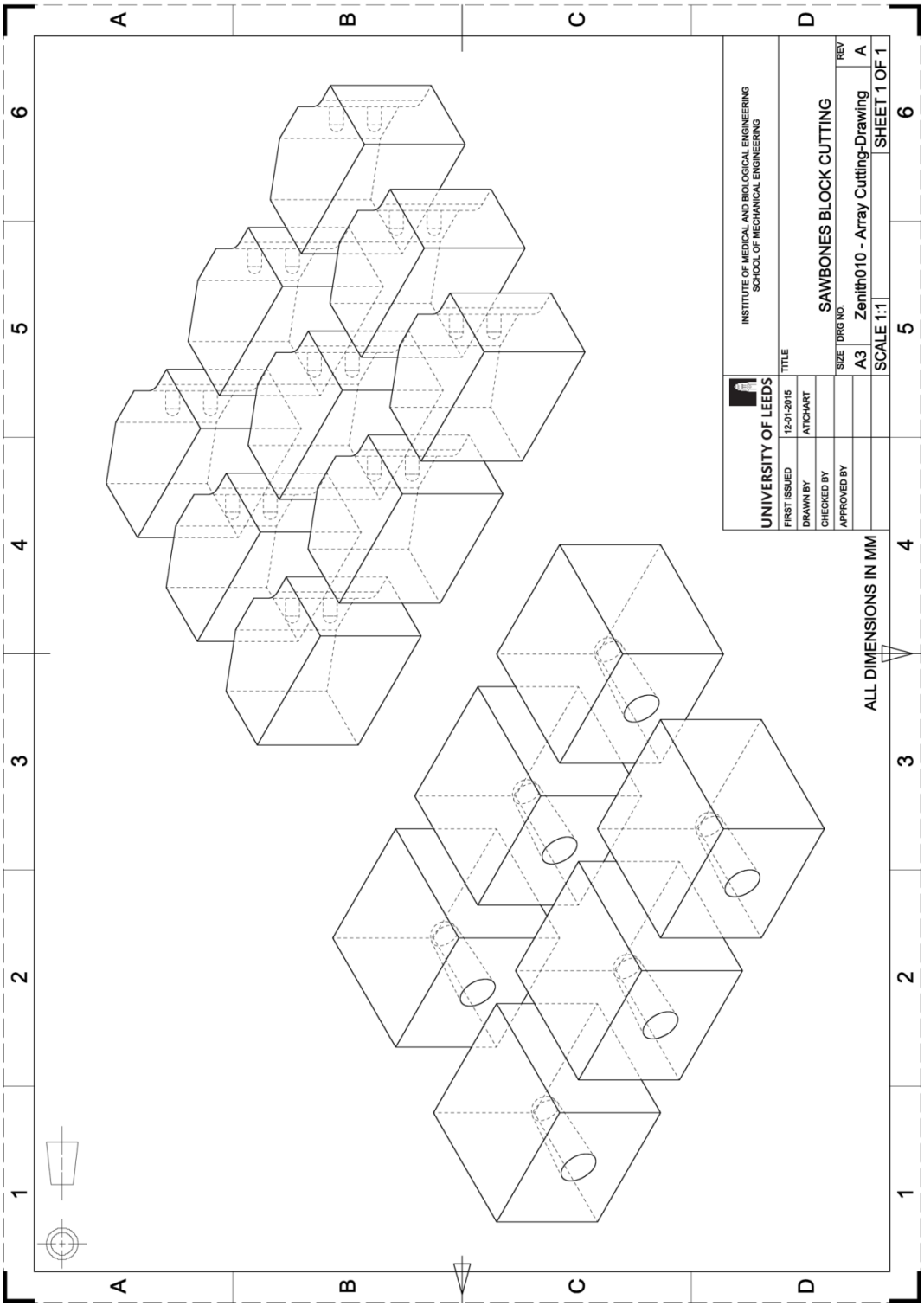

A.2 Engineering Drawings of Jigs

A.2.1 Assembly of Jigs

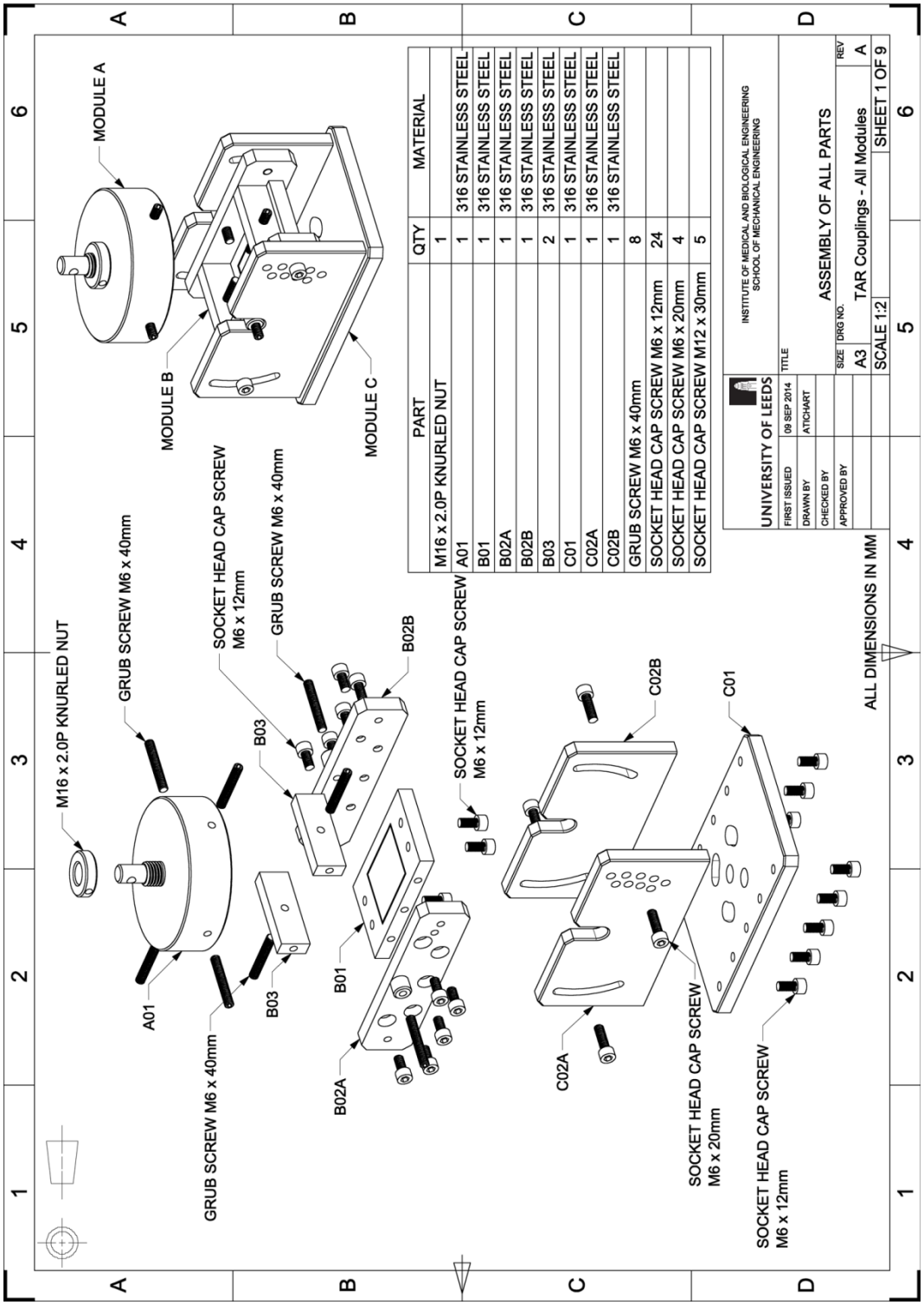

A.2.2 Upper Jig

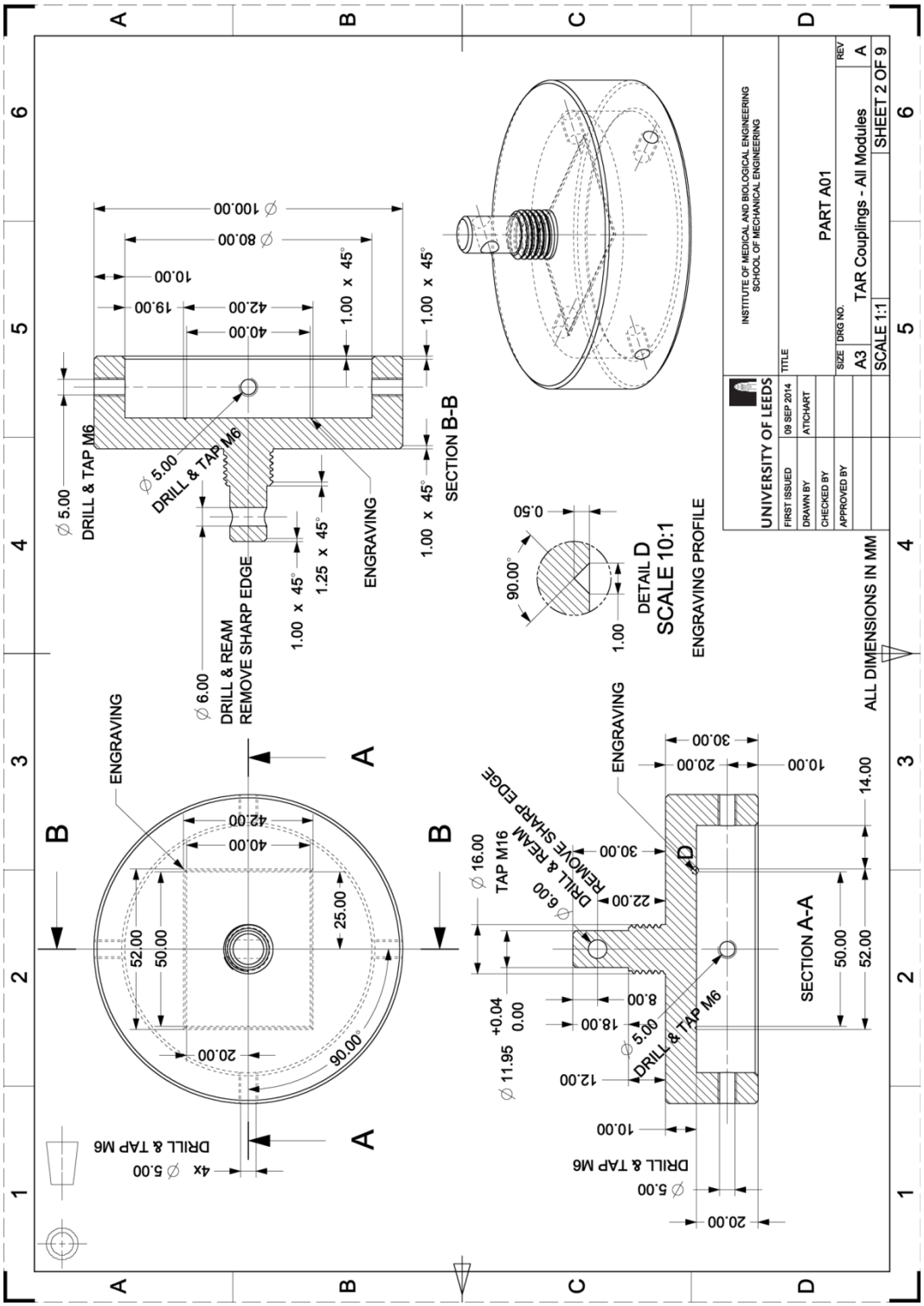

A.2.3 Lower Jig

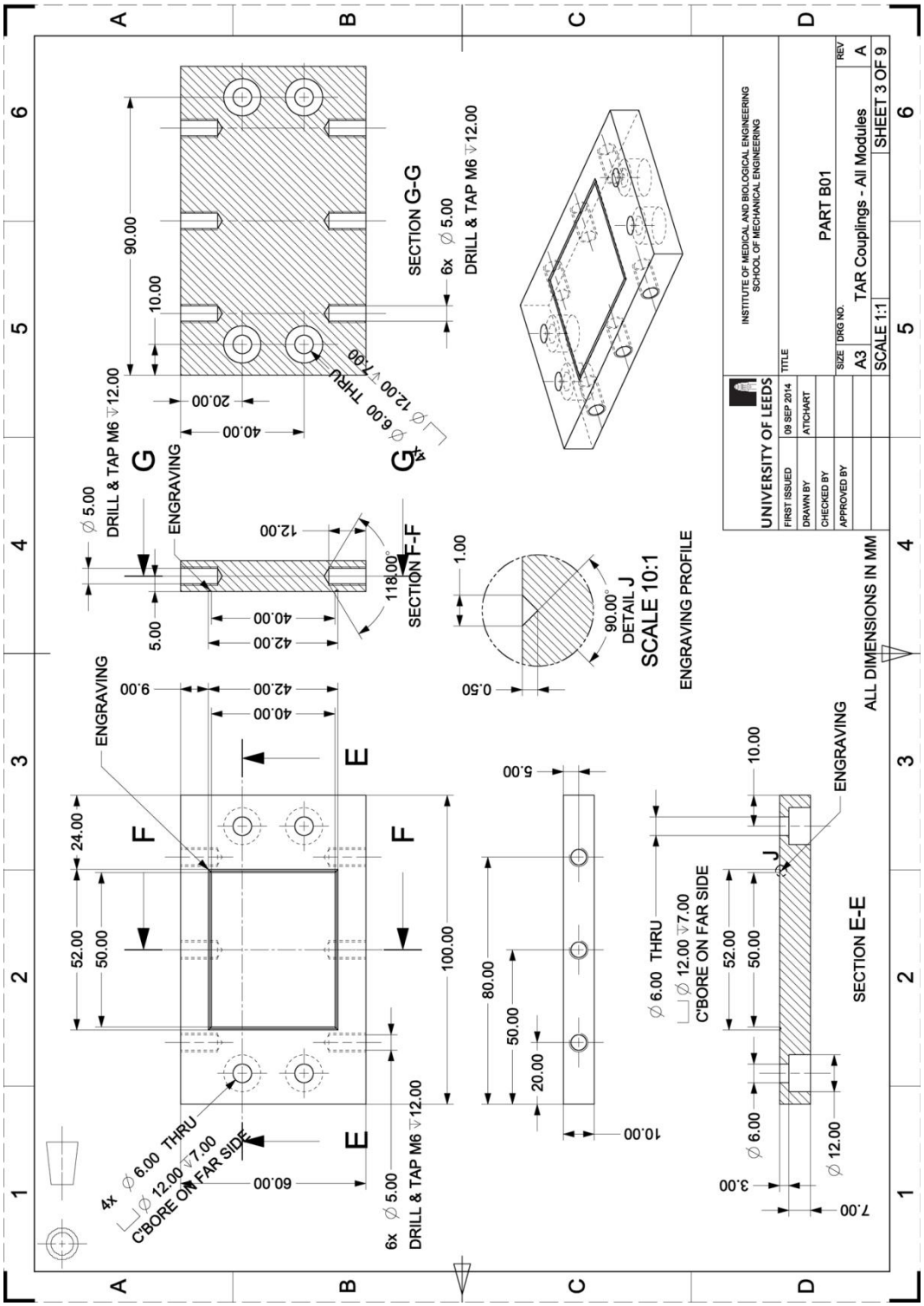

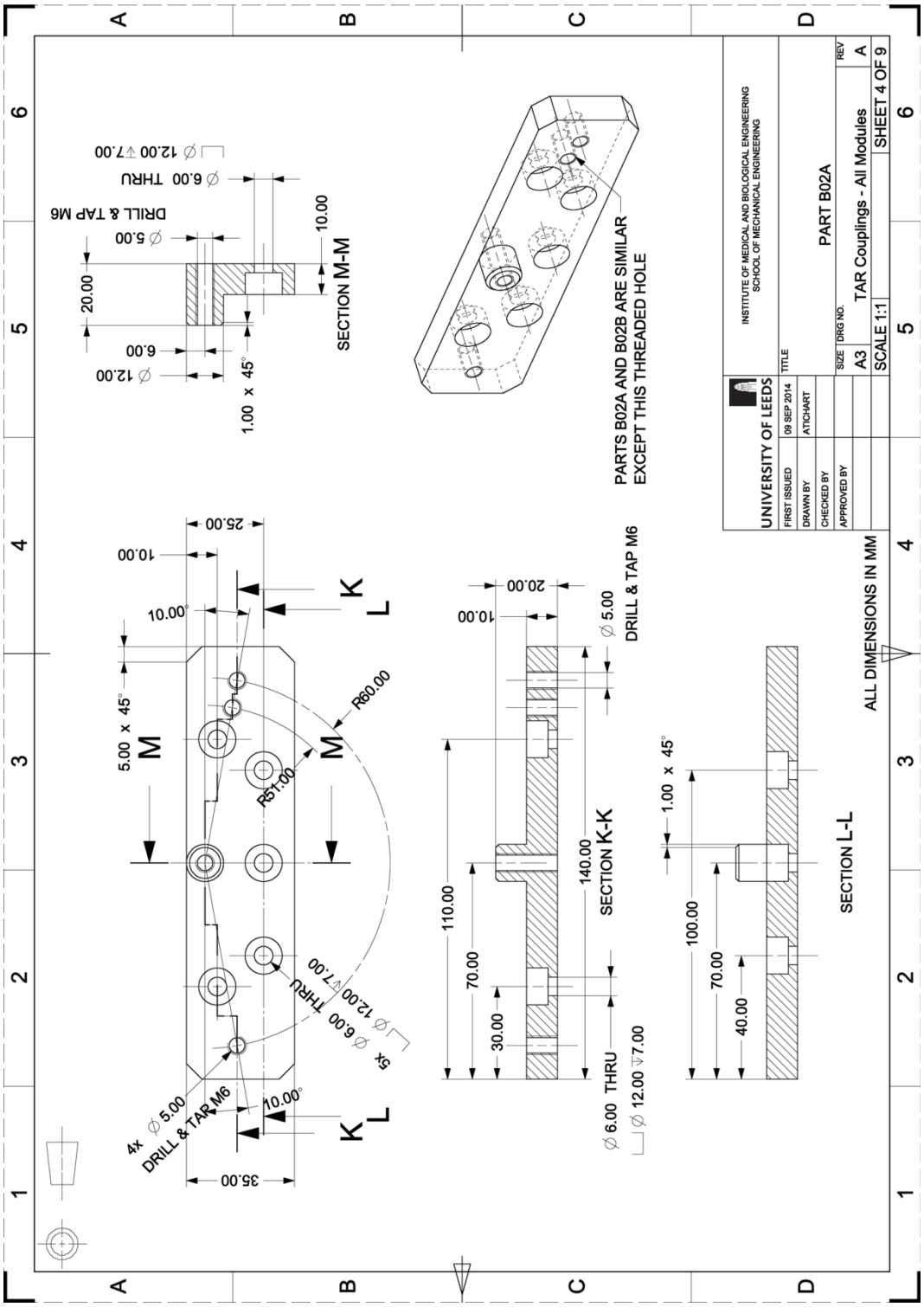
A
B
C
D
1
2
3
4
5
6
SECTION M-M
DRILL & TAP M6
⌀ 6.00 THRU
⌴ ⌀ 12.00 ↧7.00
⌀ 5.00
⌀ 12.00
6.00
20.00
10.00
1.00 x 45°
PARTS B02A AND B02B ARE SIMILAR
EXCEPT THIS THREADED HOLE
25.00
10.00
10.00°
5.00 x 45°
R60.00
R57.00
5x ⌀ 6.00 THRU ⌴ ⌀ 12.00 ↧7.00
4x ⌀ 5.00 DRILL & TAP M6
10.00°
35.00
K
L
M
20.00
10.00
⌀ 5.00
DRILL & TAP M6
110.00
70.00
30.00
140.00
SECTION K-K
⌀ 6.00 THRU
⌴ ⌀ 12.00 ↧7.00
1.00 x 45°
100.00
70.00
40.00
SECTION L-L
ALL DIMENSIONS IN MM
UNIVERSITY OF LEEDS
INSTITUTE OF MEDICAL AND BIOLOGICAL ENGINEERING
SCHOOL OF MECHANICAL ENGINEERING
FIRST ISSUED 09 SEP 2014
DRAWN BY ATICHART
CHECKED BY
APPROVED BY
TITLE
PART B02A
SIZE A3
DRG NO.
TAR Couplings - All Modules
SCALE 1:1
REV A
SHEET 4 OF 9

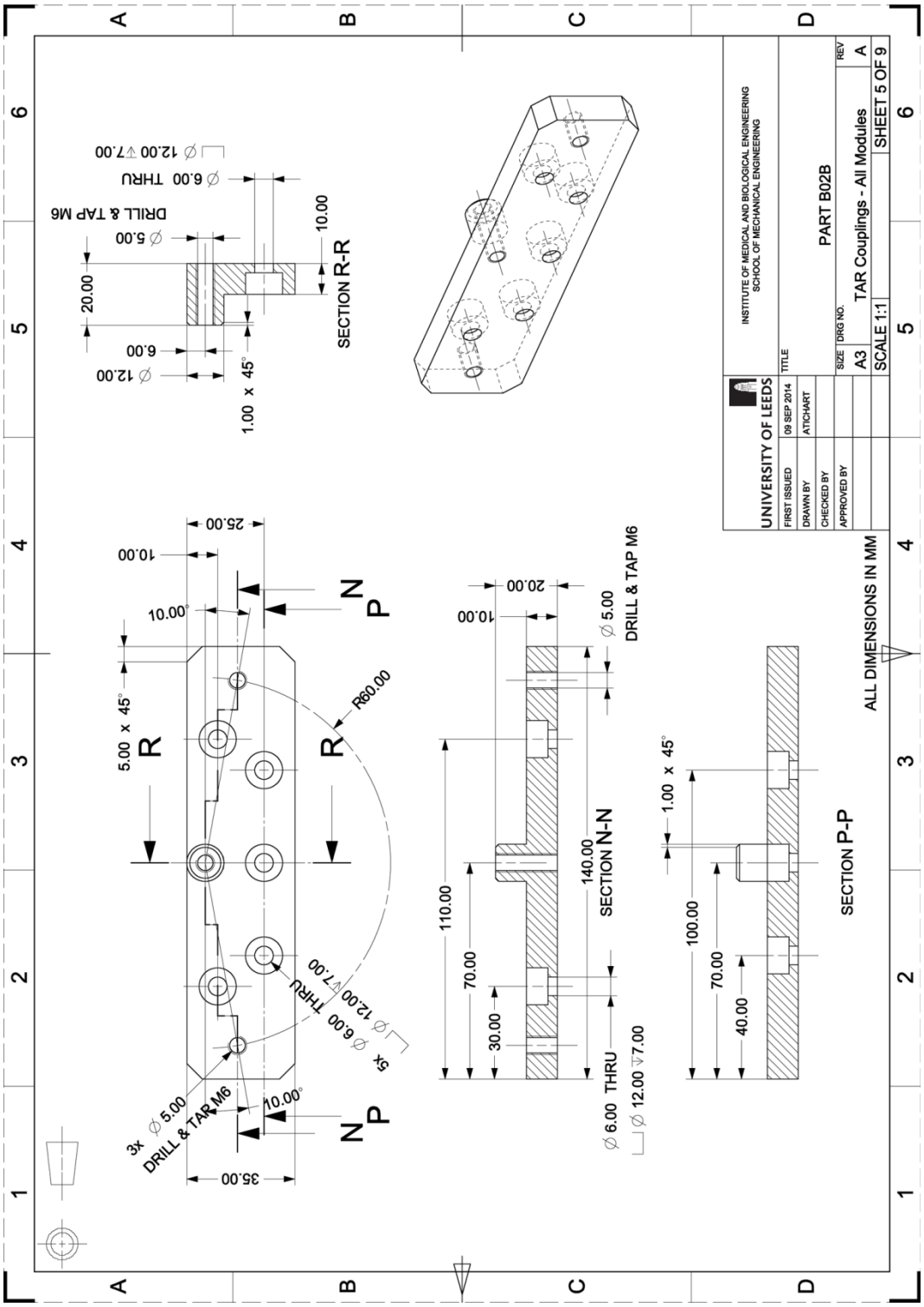
SECTION R-R
DRILL & TAP M6
SECTION N-N
SECTION P-P
DRILL & TAP M6
THRU
ALL DIMENSIONS IN MM
UNIVERSITY OF LEEDS
INSTITUTE OF MEDICAL AND BIOLOGICAL ENGINEERING
SCHOOL OF MECHANICAL ENGINEERING
PART B02B
TAR Couplings - All Modules
SCALE 1:1
SHEET 5 OF 9

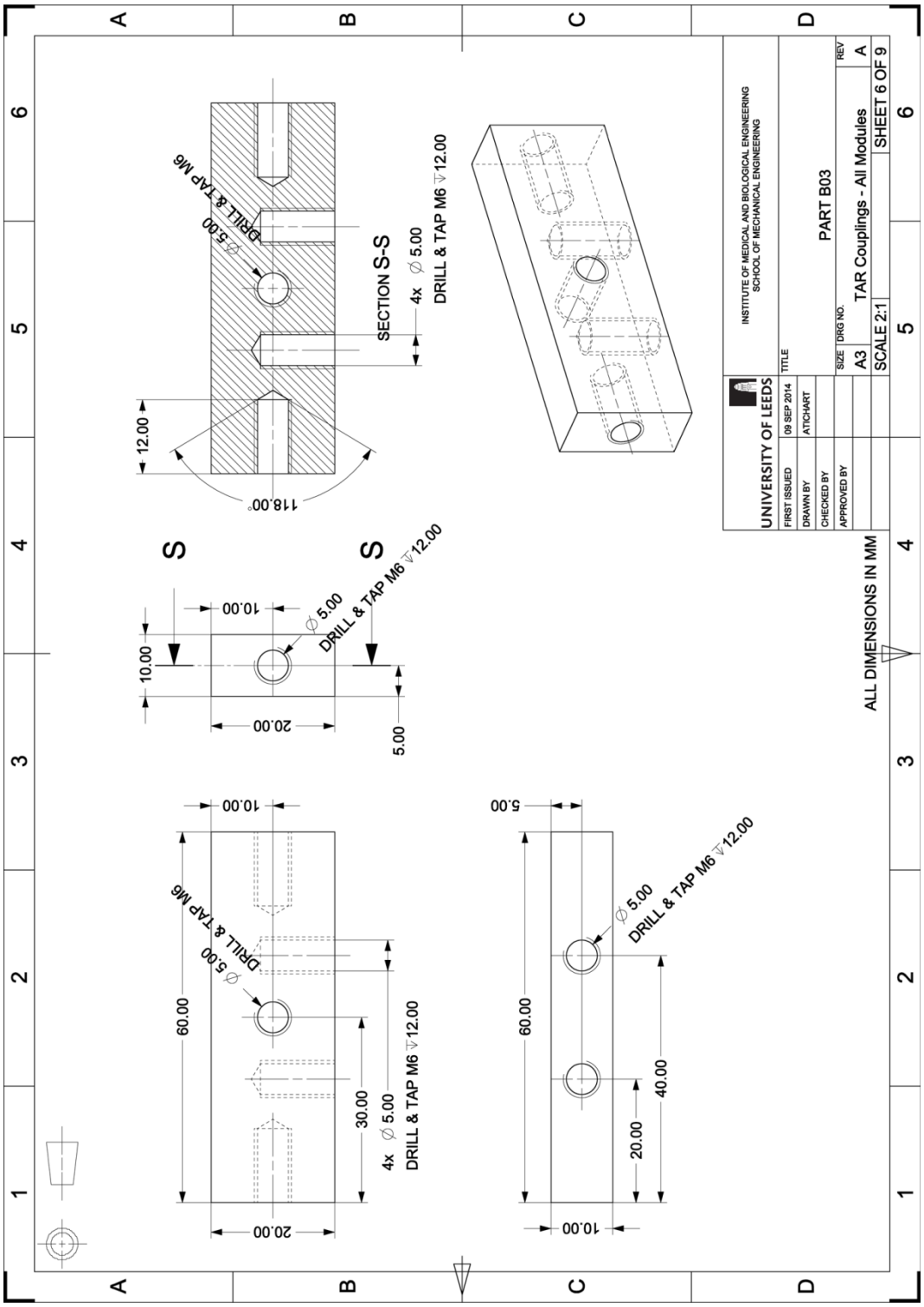
SECTION S-S
4x ∅ 5.00
DRILL & TAP M6 ▽12.00
∅5.00
DRILL & TAP M6
12.00
118.00°
10.00
20.00
5.00
60.00
30.00
40.00
ALL DIMENSIONS IN MM
UNIVERSITY OF LEEDS
INSTITUTE OF MEDICAL AND BIOLOGICAL ENGINEERING
SCHOOL OF MECHANICAL ENGINEERING
FIRST ISSUED 09 SEP 2014
DRAWN BY ATICHART
CHECKED BY
APPROVED BY
TITLE
PART B03
SIZE A3
DRG NO.
TAR Couplings - All Modules
REV A
SCALE 2:1
SHEET 6 OF 9

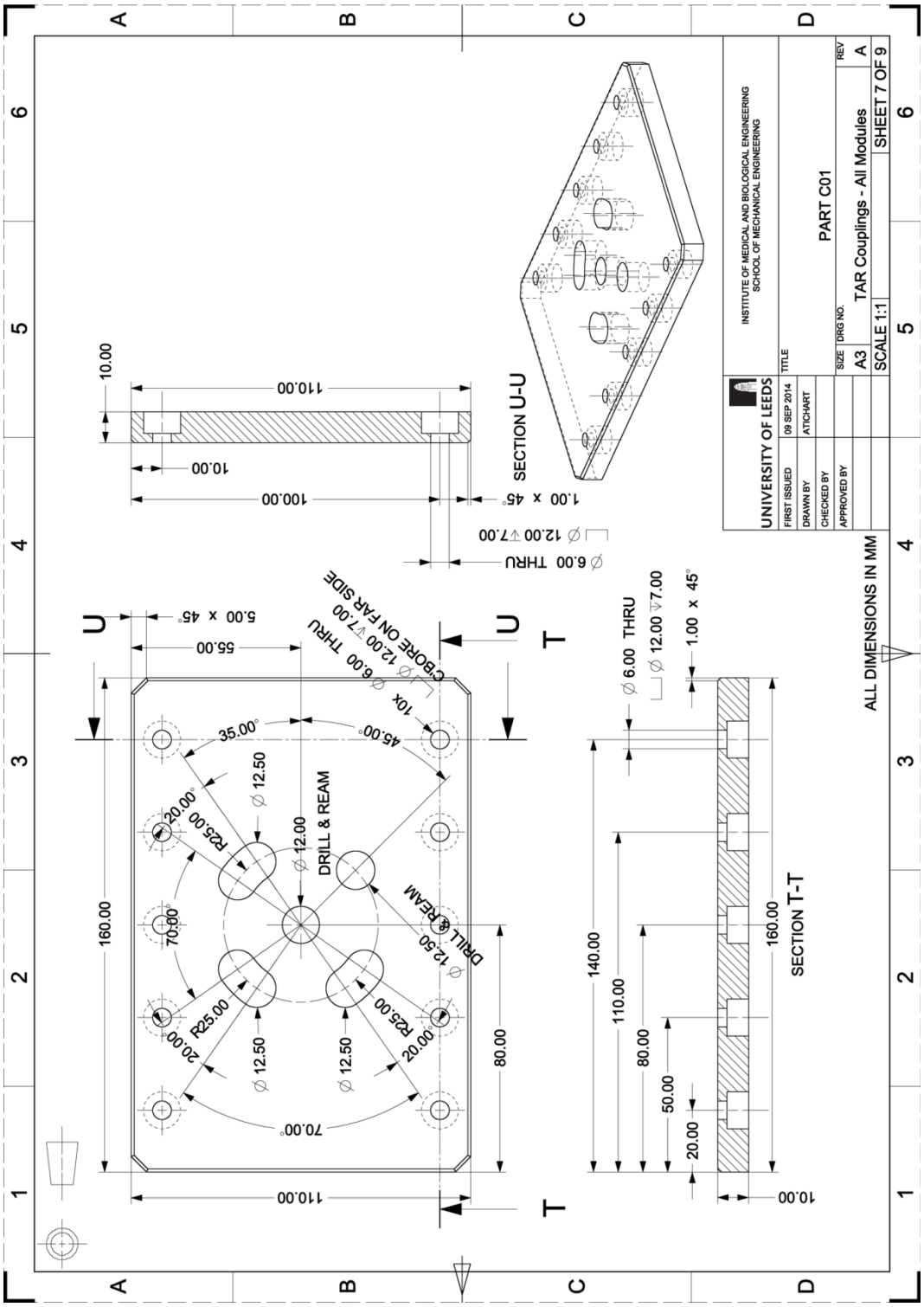
INSTITUTE OF MEDICAL AND BIOLOGICAL ENGINEERING
SCHOOL OF MECHANICAL ENGINEERING
UNIVERSITY OF LEEDS
FIRST ISSUED 09 SEP 2014
DRAWN BY ATICHART
CHECKED BY
APPROVED BY
TITLE
PART C01
SIZE A3
DRG NO.
REV A
TAR Couplings - All Modules
SCALE 1:1
SHEET 7 OF 9
ALL DIMENSIONS IN MM
SECTION U-U
SECTION T-T
DRILL & REAM
C'BORE ON FAR SIDE
THRU

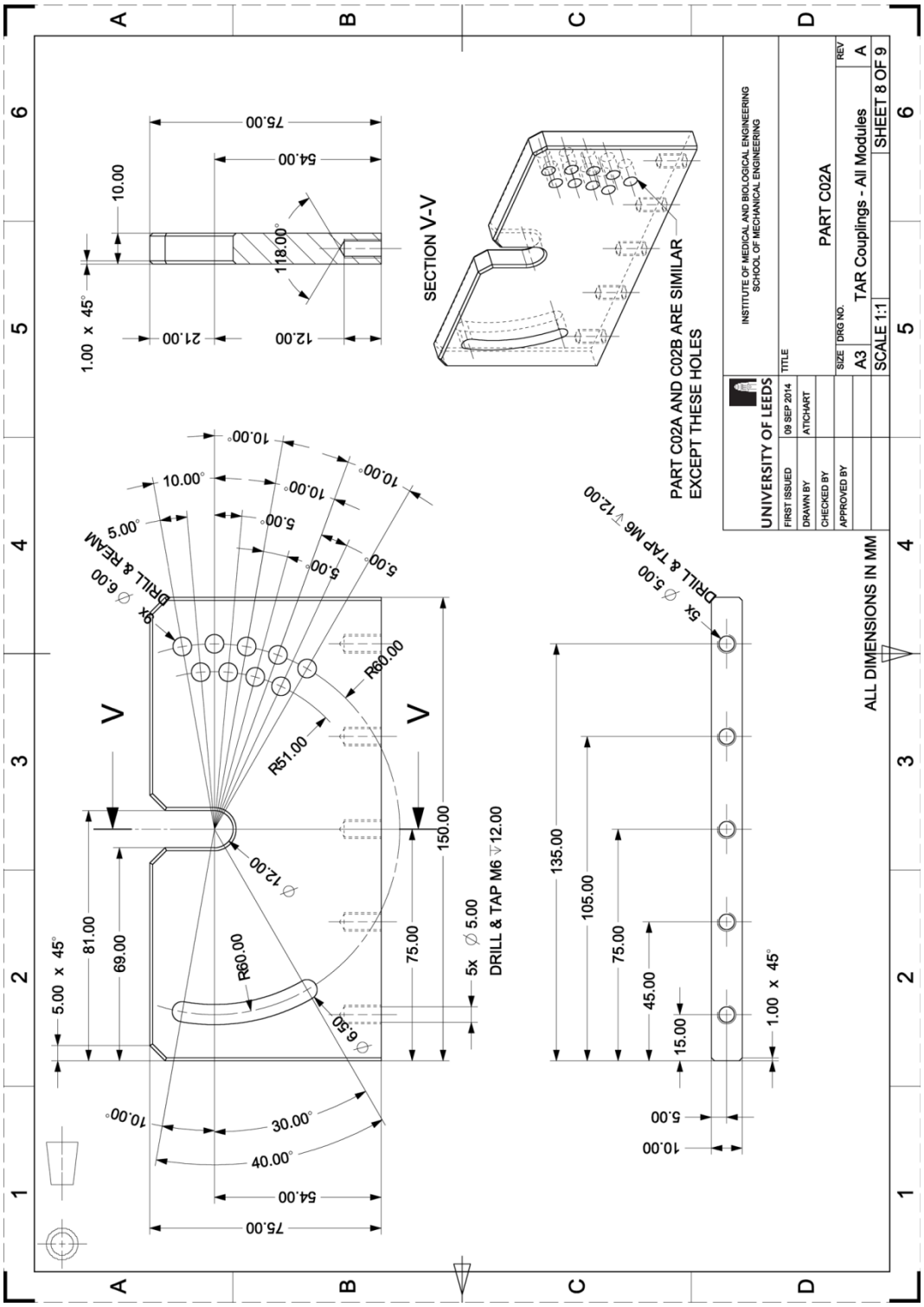
SECTION V-V
PART C02A AND C02B ARE SIMILAR
EXCEPT THESE HOLES
DRILL & REAM 9x ∅6.00
DRILL & TAP M6 ▽12.00
5x ∅5.00
DRILL & TAP M6 ▽12.00
ALL DIMENSIONS IN MM
UNIVERSITY OF LEEDS
INSTITUTE OF MEDICAL AND BIOLOGICAL ENGINEERING
SCHOOL OF MECHANICAL ENGINEERING
PART C02A
TAR Couplings - All Modules
SCALE 1:1
SHEET 8 OF 9
A3
09 SEP 2014
ATICHART

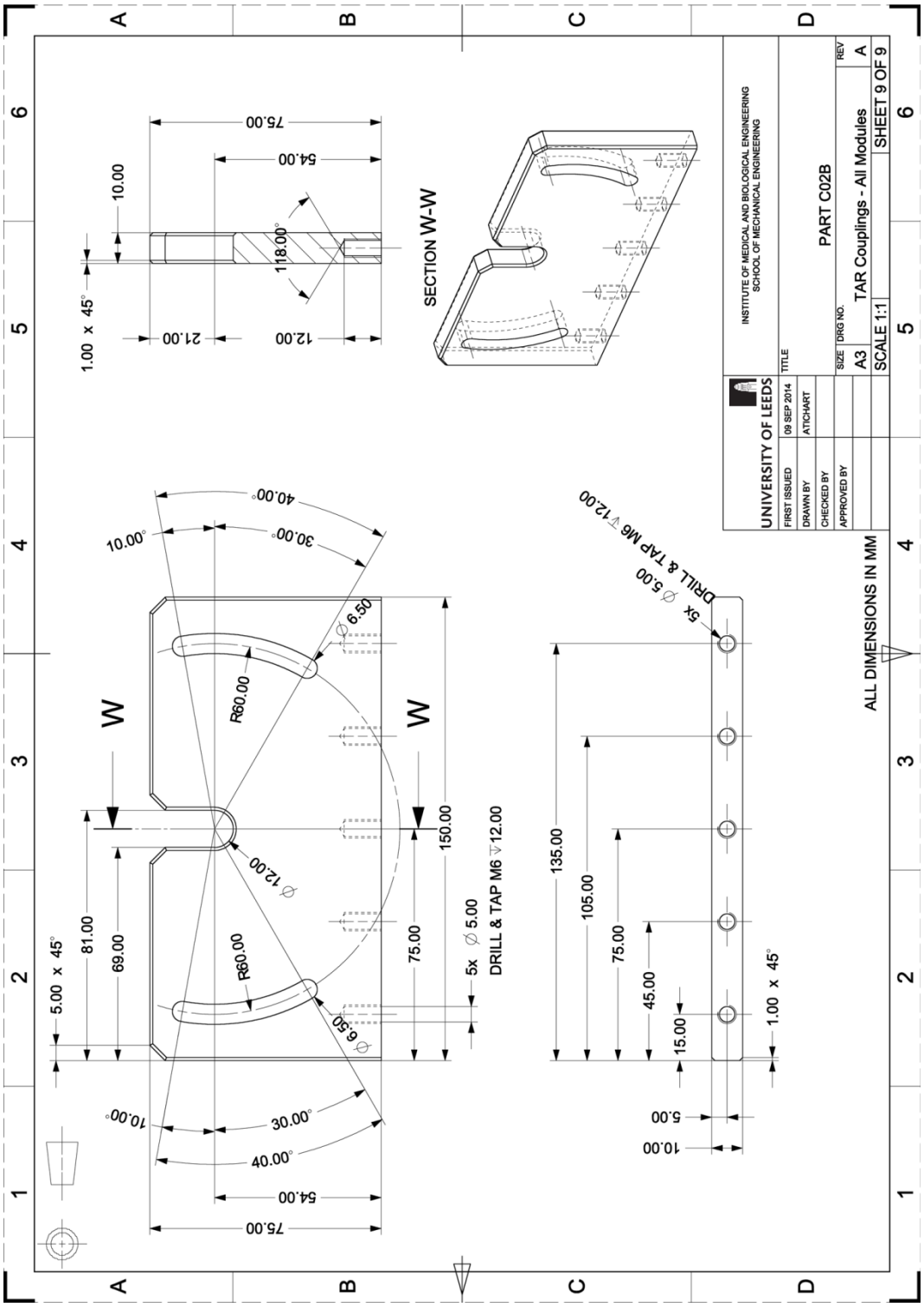
SECTION W-W
75.00
54.00
10.00
118.00°
1.00 x 45°
21.00
12.00
40.00°
30.00°
10.00°
Ø 6.50
R60.00
W
Ø 12.00
5.00 x 45°
81.00
69.00
150.00
75.00
5x Ø 5.00
DRILL & TAP M6 ▽12.00
135.00
105.00
45.00
15.00
5.00
10.00
DRILL & TAP M6 ▽12.00
5x Ø 5.00
1.00 x 45°
ALL DIMENSIONS IN MM
INSTITUTE OF MEDICAL AND BIOLOGICAL ENGINEERING
SCHOOL OF MECHANICAL ENGINEERING
UNIVERSITY OF LEEDS
FIRST ISSUED 09 SEP 2014
DRAWN BY ATICHART
CHECKED BY
APPROVED BY
TITLE
PART C02B
SIZE A3
DRG NO.
TAR Couplings - All Modules
REV A
SCALE 1:1
SHEET 9 OF 9

Appendix B Conference Proceedings and Presentations

B.1 Conference Proceedings

Kwanyuang, A., Meng, Q., Brockett, C. L., Fisher, J., & Wilcox, R. K. (2015). 46 Development of a finite element model of total ankle replacement to examine bone failure following implantation. British Journal of Sports Medicine, 49(Suppl 1), A19-A19.

Kwanyuang, A., Meng, Q., Brockett, C., Fisher, J., & Wilcox, R. (2016). Development of a finite element model of TAR to examine bone failure following implantation. Foot and Ankle Surgery, 22(2), 41.

B.2 Conference Oral Presentations

Kwanyuang, A., Meng, Q., Brockett, C.L., Fisher, J., and Wilcox, R.K. Development of a Finite Element Model of TAR to Examine Bone Failure Following Implantation. FOOT International Congress 2016, Berlin, Germany. June 23-25, 2016.

B.3 Conference Poster Presentations

Kwanyuang, A., Meng, Q., Brockett, C.L., Fisher, J., and Wilcox, R.K. Development of a Finite Element Model of Total Ankle Replacement to Examine Bone Failure Following Implantation. 6th International Ankle Symposium, Dublin, Ireland. October 16-18, 2015.

Kwanyuang, A., Meng, Q., Brockett, C.L., Fisher, J., and Wilcox, R.K. Development of a FE Model of Total Ankle Replacement to Examine Bone Failure Following Implantation. 22nd Congress of the European Society of Biomechanics (ESB 2016), Lyon, France. July 10-13, 2016.

B.4 Conference Abstracts

B.4.1 6th International Ankle Symposium

Title: Development of a finite element model of total ankle replacement to examine bone failure following implantation

[1]Kwanyuang A, [1]Meng Q, [1]Brockett CL, [1]Fisher J, [1]Wilcox RK

[1]Institute of Medical and Biological Engineering, School of Mechanical Engineering, University of Leeds, Leeds, UK

Background: Globally, 1% of the population is affected by arthritis of the foot and ankle. Post-traumatic osteoarthritis, resulting from ankle injury or chronic ankle instability, accounts for more than 50% of these cases. Total ankle replacement (TAR) was developed as an alternative to fusion to treat end-stage arthritis whilst preserving some natural biomechanics. However failure rates are relatively high and are often related to bony damage. Finite element (FE) analysis may be used to investigate the damage to the bone surrounding the TAR implant.
Objective: The objective of this study was to develop a FE model of a TAR, which is a sufficiently accurate representation of the real world for further use to examine the failure mechanisms.
Design: Experimental.
Setting: Not applicable.
Patients (or Participants): Not applicable.
Interventions (or Assessment of Risk Factors): Zenith™ TARs (Corin, UK) were inserted into polyurethane foam blocks (Sawbones, USA) representing the tibial and talar bones. The constructs were loaded in an electromechanical testing machine (Instron, USA) with increasing compressive force until reaching plastic deformation. A corresponding FE model was generated and analyzed using Abaqus (Dassault Systèmes, France).
Main Outcome Measurements: Experimental contact pressure, which was captured by pressure mapping sensor (Tekscan, USA), and deformation data were used to validate the FE results.
Results: Good agreement was found in the location of damage and average depth of plastic deformation in the synthetic bone (experimental depth was 2.8% smaller than the similar value obtained from analysis). Experimentally, there was some difference in deformation laterally, which corresponded to a difference in contact pressures measured on either side of the mid-plane, illustrating that there was some degree of inclination between the interfaces of the TAR.
Conclusions: The good agreement indicates the FE model can be used for further predictions of bone failure. Importantly, the model will be used to investigate clinically relevant misalignment, which this study shows may have an effect on bone damage.

B.4.2 FOOT International Congress 2016

Abstract title: Development of a Finite Element Model of Total Ankle Replacement to Examine Bone Failure Following Implantation

Authors: Atichart Kwanyuang, Qingen Meng, Claire Brockett, John Fisher, and Ruth Wilcox

Institute of Medical and Biological Engineering, School of Mechanical Engineering, University of Leeds, Leeds LS2 9JT, UK

Background: Globally, 1% of the population is affected by arthritis of the foot and ankle. Total ankle replacement (TAR) was developed as an alternative to fusion to treat end-stage arthritis whilst preserving some natural biomechanics, however failure rates are relatively high and are often related to bony damage. Finite element (FE) analysis may provide insight into the reasons for failure under different patient and surgical conditions.

Aim: The aim of this study is to develop a FE model of a TAR to examine risk of bone failure.

Methods: A FE model of the natural ankle was created from cryosectional images obtained from the Visible Human Project®, and virtually implanted with a Zenith™ TAR (Corin, UK). The model was generated and analyzed using Abaqus (Dassault Systèmes, France). Compressive axial load and boundary conditions were applied on the FE model to represent the real-world conditions. The surgical positioning of the TAR and cortical stiffness were varied to represent relevant ranges seen clinically.

Results: The magnitudes of maximum von Mises stress on the cancellous bone were mainly affected by two factors: the stiffness of cortical shell and the distance between the fixing stem and the outer surface of cancellous bone. Their relationships were inversely proportional. The locations of maximum stresses were also dependent on both factors.

Conclusions: Clinically, other than the location of the articular surface, the location of the fixing stem should be carefully taken into account when defining the implanted position. An inadequate thickness of cancellous bone may cause the failure of implantation.

B.4.3 22nd Congress of the European Society of Biomechanics (ESB 2016)

DEVELOPMENT OF A FE MODEL OF TOTAL ANKLE REPLACEMENT TO EXAMINE BONE FAILURE FOLLOWING IMPLANTATION

Atichart Kwanyuang (1), Qingen Meng (1), Claire Brockett (1), John Fisher (1), and Ruth Wilcox (1)

1. Institute of Medical and Biological Engineering, School of Mechanical Engineering, University of Leeds, Leeds LS2 9JT, United Kingdom

Introduction

Globally, 1% of the population is affected by arthritis of the foot and ankle [1]. Total ankle replacement (TAR) was developed as an alternative to fusion to treat end-stage arthritis whilst preserving some natural biomechanics, however failure rates are relatively high and are often related to bony damage [2]. Knowledge of the failure mechanisms of TAR is limited to date, therefore, finite element (FE) analysis may provide insight into the reasons for failure under different patient and surgical conditions.

The aim of this study is to develop a FE model of a TAR to examine risk of bone failure.

Methods

A FE model of the natural ankle was created from cryosectional images obtained from the Visible Human Project®, and virtually implanted with a Zenith™ TAR (Corin Group PLC, UK). The model was generated and analyzed using Abaqus (Dassault Systèmes Simulia Corp, USA). Material properties of both bones and prostheses were assumed to be homogeneous, isotropic, and linearly elastic. Compressive axial load and boundary conditions were applied on the FE model to represent the ankle joint during standing with the midstance phase. Both the surgical positioning of the TAR and the cortical stiffness were varied to represent relevant ranges seen clinically.

Results

The maximum von Mises stress on the cancellous bone was primarily affected by two factors: the stiffness of cortical shell and the distance between the fixing stem and the outer surface of the cancellous bone (Figure 1). Their relationships were inversely proportional (Figure 2). In some misalignment cases, the yield stress for cancellous bone was likely to be exceeded [3].

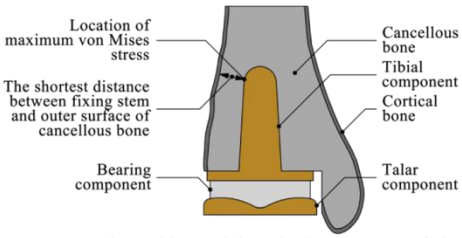

Figure 1: The ankle model with the location of the maximum von Mises stress on the cancellous bone

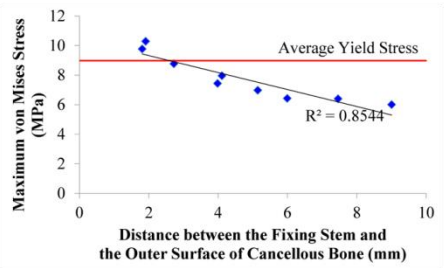

Figure 2: Plot of relationship between the distance between the fixing stem and the outer surface of cancellous bone and the magnitude of maximum von Mises stress

The distance between the fixing stem and the outer surface of cancellous bone also affected the locations of maximum stresses. The highest magnitudes of the stresses were always located at the positions of the shortest distance.

Discussion

The inversely proportional relationship between the stiffness of the cortex and the stress in the trabecular bone can be used to confirm that the quality of the bone is one of the important factors causing the success or failure in implantation due to the risk of bony failure. Therefore, surgeons should assess the quality of the bone carefully before making a decision to treat patients with TAR.

As seen in Figure 2, the thickness of the trabecular bone surrounding the fixing stem of the implant is another important factor that can cause the excessive stress in bone. Clinically, other than the location of the articular surface, the location of the fixing stem should also be carefully taken into account when defining the implanted position. An inadequate thickness of cancellous bone may cause the failure of implantation.

References

1. Hintermann et al, J Aging Research, 2012:1-8, 2012.
2. Bestic et al, AJR, 190:1112-1123, 2008.
3. Rincón-Kohli and Zysset, Biomech Model Mechanobiol, 8:195-208, 2009.

Acknowledgements

Funding for this project was received from the Office of the Civil Service Commission and the ERC (grant 2012-StG 306615).